Report

R-19-14

February 2019

Modelling of concrete degradation – influence of concrete mix design

Report for the safety evaluation SE-SFL

Andrés Idiart

Javier Olmeda

Marcelo Laviña

SVENSK KÄRNBRÄNSLEHANTERING AB

SWEDISH NUCLEAR FUEL
AND WASTE MANAGEMENT CO

Box 3091, SE-169 03 Solna
Phone +46 8 459 84 00
skb.se

SVENSK KÄRNBRÄNSLEHANTERING

ISSN 1402-3091
SKB R-19-14
ID 1610830

February 2019

Modelling of concrete degradation – influence of concrete mix design

Report for the safety evaluation SE-SFL

Andrés Idiart, Javier Olmeda, Marcelo Laviña
Amphos 21 Consulting S. L.

This report concerns a study which was conducted for Svensk Kärnbränslehantering AB (SKB). The conclusions and viewpoints presented in the report are those of the authors. SKB may draw modified conclusions, based on additional literature sources and/or expert opinions.

Summary

Engineered barriers in the BHK vault of the SFL repository are primarily made of cementitious materials. Long-term performance of these barriers has been assessed in previous studies (Idiart and Shafei 2019, Idiart and Laviña 2019) using reactive transport models. The concrete composition was assumed to be similar to the construction concrete employed in the SFR repository. In this work, the performance of alternative cementitious systems has been assessed. To this end, reactive transport simulations of concrete degradation in the BHK vault have been performed using iCP, a software interface between Comsol Multiphysics (version 5) and PHREEQC (version 3). This report presents the results of two-dimensional (2D) and one-dimensional (1D) reactive transport simulations over 100 000 and 1 million years, respectively.

Consideration of alternative compositions of the concrete mix design implies the ability to predict the phase assemblage of the hydrated mix. State-of-the-art models of cement hydration have been used to estimate the mineralogical and porewater composition of the different mixes. The hydration simulations have been based on thermodynamic modelling coupled to kinetically-controlled dissolution of the cement clinker and mineral additions, when present. The output of the hydration models after full hydration (10 000 days) have been used as input for the reactive transport simulations, defining the initial composition of intact concrete. The different concrete compositions analysed consist of:

- *Anläggningscement* (i.e. CEM I 42.5 N – SR 3 MH/LA) with a w/c ratio of 0.47.
- *Anläggningscement* with a w/c ratio of 0.63 and 320 kg/m^3 concrete.
- *Anläggningscement* with a w/c ratio of 0.63 and 280 kg/m^3 concrete.
- *Bascement Slite* (i.e. CEM II/A-V 52.5 N) with a w/c ratio of 0.47 and 12.3 wt% fly ash.
- *Anläggningscement* containing limestone and dolomite addition with w/c of 0.49.

A literature review of how these different mix designs are expected to alter the chemical and physical properties is also presented. Based on this, the transport properties of the intact composition of each mix are proposed.

Degradation of concrete in the SFL repository has been studied using 1D and 2D reactive transport models of a cross-section of the BHK vault. A total of five models are presented considering different concrete compositions. The main concrete degradation process is driven by leaching of calcium in all cases, leading to gradual dissolution of the main cement hydrates. Calcite precipitation is another important process. The rate of degradation is shown to be low after 100 000 years in all simulated cases. This is due to the small flow rates of water into the vault, together with a low initial diffusion coefficient of the backfill. Comparison of the results of the different cases over 100 000 years shows that the impact of changing the concrete composition to the studied alternatives does not have a significant effect on its performance. The depth of the degradation front is relatively sensitive to concrete composition, although the results indicate that the governing factors are the initial porosity and transport properties.

A set of 1D reactive transport models of the same five cases considers an extended period of 1 million years. The differences between different modelled cases are much larger over this time scale in terms of penetration of degradation fronts. After 1 million years, the full thickness of the concrete backfill is near complete degradation in all cases. Extended calcite precipitation is predicted across almost the entire backfill. In the 1D models, a constant increase in the Darcy velocity is observed with time, which is due to the boundary conditions. As a result, fluid flow increases with time.

The case which considers the addition of limestone filler is the concrete mix that has the best performance. According to the model results, this improvement is more related with the initially lower porosity compared to the rest of cases than to the chemical composition of the cementitious system.

Sammanfattning

Tekniska barriärer i BHK-salen i SFL utgörs primärt av cementbaserade material. Dessa barriärers långsiktiga funktion har tidigare utvärderats (Idiart och Shafei 2019, Idiart och Laviña 2019) med hjälp av reaktiva transportmodeller. Betongsammansättningen antogs likna konstruktionsbetongen som använts i SFR. I detta arbete så har funktionen för alternativa cementbaserade system utvärderats. För detta ändamål har reaktiva transportsimuleringar av betongdegradering i BHK-salen utförts med iCP, vilket är en programvara som sammankopplar Comsol Multiphysics (version 5) med PHREEQC (version 3). I denna rapport presenteras resultaten för två- (2D) och endimensionella (1D) reaktiva transportsimuleringar under 100 000 respektive 1 miljon år.

En förutsättning för att överväga alternativa betongsammansättningar är att fassammansättningen för de hydratiserade formerna kan predikteras. ”State-of-the-art”-modeller för cementhydratisering har använts för att skatta sammansättning av mineralfaser och porvatten för de olika blandningarna. Simuleringarna har baserats på termodynamisk modellering, i kombination med kinetiskt styrd upplösning, av cementklinker och eventuella mineraltillsatser. Simuleringsresultaten för fullständig hydratisering (10 000 dagar) har använts som indata för de reaktiva transportsimuleringarna, vilket därmed definierat sammansättningen för ursprunglig intakt betong. De undersökta betongsammansättningarna består av:

- *Anläggningscement* (dvs CEM I 42.5 N – SR 3 MH/LA) med ett vct på 0,47.
- *Anläggningscement* med ett vct på 0,63 och 320 kg/m^3 betong.
- *Anläggningscement* med ett vct på 0,63 och 280 kg/m^3 betong.
- *Bascement Slite* (dvs CEM II/A-V 52,5 N) med ett vct på 0,47 och 12,3 vikt% flygaska.
- *Anläggningscement* med ett vct på 0,49 och med tillsats av kalksten och dolomit.

Även en litteraturöversikt presenteras över hur dessa olika blandningsförhållanden förväntas förändra betongens kemiska och fysikaliska egenskaper. Baserat på detta har transportegenskaper föreslagits för de ursprungliga betongsammansättningarna.

Betongdegradering i SFL har studerats med hjälp av 1D och 2D reaktiva transportmodeller för ett tvärsnitt av BHK-salen. Totalt presenteras fem modeller där olika betongsammansättningar beaktas. I samtliga fall är lakning av kalcium den huvudsakliga drivkraften för nedbrytning av betong, vilket leder till gradvis upplösning av de huvudsakliga cementhydraten. En annan viktig process är utfällning av kalkspat. I samtliga simulerade fall visar sig nedbrytningshastigheten vara låg efter 100 000 år. Detta beror på låga flöden av inträngande vatten, tillsammans med en låg initial diffusionskoefficient för återfyllnaden. Resultaten visar att byte till de nu undersökta betongsammansättningarna inte har en betydande inverkan på funktionen under 100 000 år. Degraderingsdjupet är relativt känsligt för betongsammansättningen, men resultaten tyder på att de styrande faktorerna är initial porositet och transportegenskaper.

En uppsättning av 1D reaktiva transportmodeller för motsvarande fem fall har även utförts för en utökad period på 1 miljon år. Skillnaderna, vad det gäller degraderingsdjup, är mycket större mellan modellerade fall på denna tidsskala. I samtliga fall är betongen, efter 1 miljon år, nästan fullständigt nedbruten genom hela dess tjocklek. Utökad utfällning av kalkspat förväntas i nästan hela återfyllnaden. För 1D-modellerna observeras en monoton ökning av Darcy-hastigheten med tiden, vilket beror på randvillkoren. Som ett resultat av detta ökar vattenflödet genom betongen med tiden.

Det fall som utvärderar betong med kalksten som utfyllnad ger den bäst funktion jämfört med övriga fall. Enligt resultaten spelar en initialt lägre porositet större roll för förbättringen än skillnaderna i den kemiska sammansättningen av det cementbaserade systemet.

Abbreviations and notations

AFm – Group of calcium aluminate hydrates ($Al_2O_3 - Fe_2O_3$ – mono) with general formula $[Ca_2(Al,Fe)(OH)_6] \cdot X \cdot nH_2O$. The most important phases are hydroxy-AFm, monosulfoaluminate (or monosulfate) and monocarboaluminate (X in these cases denote hydroxyl, sulfate and carbonate, resp.).

AFt – Group of calcium aluminate hydrates ($Al_2O_3 - Fe_2O_3$ – tri) with general formula $[Ca_3(Al,Fe)(OH)_6 \cdot 12H_2O]_2 \cdot X_3 \cdot nH_2O$. Ettringite is the most important member (X in this case denote sulfate).

A/S – Aluminium-to-silica molar ratio.

ASR – Alkali-silica reaction.

BHK – Repository concept for metallic wasted based on cementitious materials as engineered barrier.

BSE – Backscattered electrons.

C – Calcium oxide = CaO

C_2S – Dicalcium silicate or belite = $2CaO \cdot SiO_2$

C_3A – Tricalcium aluminate = $3CaO \cdot Al_2O_3$

C_3S – Tricalcium silicate or alite = $3CaO \cdot SiO_2$

C_4AF – Tetracalcium aluminoferrite = $4CaO \cdot Al_2O_3 \cdot Fe_2O_3$

Ca/Si – Calcium-to-silica molar ratio (or C/S in cement chemistry notation).

C-A-S-H – Calcium aluminium silicate hydrates.

CEC – Cation exchange capacity.

CH – Portlandite = $Ca(OH)_2$

C-S-H – Calcium silicate hydrates.

FA – Fly ash.

HCP – Hydrated cement paste.

MCL – Mean chain length.

MIP – Mercury intrusion porosimetry.

OPC – Ordinary Portland cement.

PLC – Portland limestone cement.

RH – Relative humidity.

S – Silica = SiO_2

SCC – Self-compacting concrete.

SCM – Supplementary cementitious materials.

SEM – Scanning electron microscopy.

SFL – Repository for long-lived radioactive waste.

SFR – Repository for short-lived radioactive waste.

w/b – Water-to-binder mass ratio.

w/c – Water-to-cement mass ratio.

Cement chemistry notation: abbreviation of oxides

$A = Al_2O_3$

$C = CaO$

$F = Fe_2O_3$

$H = H_2O$

$K = K_2O$

$M = MgO$

$N = Na_2O$

$S = SiO_2$

$\hat{S} = SO_3$

Contents

1 Introduction 9
1.1 Cement with fly ash additions 9
1.2 Cement with limestone replacement 9
1.3 Effect of water-to-cement ratio 10

2 Objectives, scope and methodology 11

3 Literature review 13
3.1 Effect of fly ash addition on the properties of concrete 13
  3.1.1 Impact on the properties of fresh concrete 14
  3.1.2 Chemical aspects 16
  3.1.3 Impact on the properties of hardened concrete 19
3.2 Effect of limestone addition on OPC and fly ash blended cements 24
  3.2.1 Impact on the properties of fresh concrete 24
  3.2.2 Chemical aspects 26
  3.2.3 Impact on the properties of hardened concrete 27
3.3 Effect of water-to-cement ratio on concrete properties 31
  3.3.1 Porosity 31
  3.3.2 Permeability 33
  3.3.3 Effective diffusion coefficient 34
3.4 Conclusions 36

4 Thermodynamic modelling of cement hydration 39
4.1 Conceptual models and numerical implementation 39
  4.1.1 Cementitious initial phase composition 41
  4.1.2 Fly ash 43
  4.1.3 Cement with limestone and dolomite additions 44
  4.1.4 Selected phase assemblage 45
  4.1.5 Alkali uptake approach 47
  4.1.6 Porosity and concrete composition 47
4.2 Results 48
  4.2.1 Hydration models 1 and 2 (CEM-I 42.5 N – SR, w/c ratio 0.47 and 0.63) 49
  4.2.2 Hydration model 3 (CEM II/A-V 52.5 N) 53
  4.2.3 Hydration model 4 (CEM I 42.5 N - SR with limestone/dolomite addition) 55
  4.2.4 Evolution of porosity 57
  4.2.5 Final mineral assemblages 59

5 Modelling of reactive transport processes 61
5.1 Conceptual models and numerical implementation 61
  5.1.1 2D models of a BHK cross-section 62
  5.1.2 1D models of concrete backfill 66
5.2 Results for 2D models of a BHK cross-section 68
  5.2.1 Case I 68
  5.2.2 Case II 72
  5.2.3 Case III 73
  5.2.4 Case IV 74
  5.2.5 Comparison of results 74
5.3 Results for 1D models of concrete backfill 79
  5.3.1 Case I 79
  5.3.2 Case II 83
  5.3.3 Case III 87
  5.3.4 Case IV 89
  5.3.5 Comparison of results 91

6 Summary and conclusions 97

References 99
Appendix A Verification of the cement hydration model 107
Appendix B Minerals 109
Appendix C Tabulated key parameter results 111
Appendix D Porosity calculations 115

1 Introduction

SKB plans to dispose of long-lived low and intermediate level waste (LILW) in a deep geological repository, named SFL. The total capacity of SFL is estimated to 16 000 m^3. Approximately one third of the waste originates from nuclear power plants in the form of neutron-irradiated components and control rods. The remainder comes from AB SVAFO and Studsvik Nuclear AB, who manage the legacy waste and the waste from hospitals, industry and research. Possible repository concepts for SFL have been evaluated and Elfwing et al. (2013) proposed a repository concept to be analysed in an evaluation of post-closure safety (SE-SFL). This study focusses on the repository concept proposed for metallic waste, denoted BHK, which relies on the extensive use of cementitious materials for constructing the engineered barrier system. The BHK vault will be backfilled with concrete, which acts as a barrier against groundwater flow and contributes to a low diffusion rate and high sorption of many radionuclides. The concrete in the barrier will furthermore create an alkaline environment, reducing the corrosion rate of the steel and thus limiting the release rate of radionuclides.

1.1 Cement with fly ash additions

The constructions in BHK rely to a large extent on the use of cement as binder material. As a first assumption, the Degerhamn Anläggningscement has been considered in modelling. Anläggningscement has been used in the construction of the SFR repository and consists of CEM I Portland cement with the following characteristics:

- It complies with the requirements of EN 197-1:2011 focused on composition, specifications and conformity criteria for common cements.
- It has a low C_3A content (2.0 wt%) and satisfies the requirements for sulfate resistance of SR 3 type cement in EN 197-1:2011.
- It satisfies the requirements for cement with moderate heat development in accordance with SS 134202:2006 and for low alkali cement in accordance with SS 134203:2014.

The cement provider, CEMENTA (Heidelberg Group), has communicated to SKB that at the time of construction of the SFL repository the Anläggningscement cement may no longer be available in the market. Instead, another cement composition, a CEM II/A-V Portland Cement named Bascement, manufactured in Slite, will be provided by CEMENTA. Bascement (CEMENTA 2015) complies with EN 197-1:2011 standard requirements for Portland cement with a siliceous fly ash content of up to 20 wt%.

A consequence of this change in cement composition for future construction works is that the numerical models of concrete degradation performed so far, for the yet to be constructed repository components, may need to be revised. This revision needs to account for the different chemical compositions of both cements and the resulting physical properties of the hardened cementitious material. The expected changes in water-to-cement ratio and aggregate volume fraction of the concrete mix as a result of the change in cement composition need to be quantified. In addition, the differences in the cement hydrates resulting from the hydration of both cements also needs to be modelled. A key issue for modelling the hydration of ordinary Portland cement (OPC) or blended cements is the knowledge of the rate of reaction of the clinker phases and the supplementary cementitious materials (silica fume, fly ash, etc).

1.2 Cement with limestone replacement

In addition, SKB is currently developing and testing a new type of concrete for the 2BMA of the future SFR3 repository (Lagerblad et al. 2017). In this concrete mix, crushed ballast is used. In this new mix, finely ground limestone is added to allow for low cement content together with a low amount of superplasticiser. It is therefore relevant to assess how the addition of limestone ($CaCO_3$) affects the hydration process (cement hydrates) and physical properties of the hardened concrete (porosity, permeability, diffusivity, etc).

1.3 Effect of water-to-cement ratio

All calculations of the performance of concrete structures in the SFR and SFL repositories have been based so far on the use of a water-to-cement ratio (w/c) of 0.47 (Jacobsen and Gjörv 1987, cited in Höglund 2001). This w/c ratio has also been used by Idiart and Shafei (2019) to study the long-term performance of the concrete barriers in the BHK vault of the future SFL repository. Here, the effect of changing the w/c from 0.47 to 0.63 (i.e. a 34 % increase) on the long-term performance of concrete is assessed.

Concrete degradation in the BHK vault is expected to be mainly driven by interaction with groundwater. Thus, concrete transport properties are the most important parameters to assess the vault durability. These transport properties, namely hydraulic conductivity, effective diffusivity and porosity, are highly dependent on the w/c ratio. Therefore, these dependencies need to be quantified and their impact on long-term performance needs to be addressed.

The amount of cement hydrates also depends on the w/c ratio. Increasing the w/c ratio is associated with a higher porosity and therefore a decrease in volume fraction of cement hydrates. The impact of this decrease on the long-term performance and pH buffering capacity of the concrete backfill also need to be studied.

2 Objectives, scope and methodology

The objective of the present work is to assess the effect of changing the cement composition and w/c ratio on long-term concrete degradation in BHK. The concrete compositions considered are:

- A "reference" OPC concrete with a water-to-cement ratio of 0.47,
- an OPC concrete with a water-to-cement ratio of 0.63 and 320 kg/m^3 concrete,
- an OPC concrete with a water-to-cement ratio of 0.63 and 280 kg/m^3 concrete,
- a concrete with fly ash as a supplementary cementitious material, and
- a concrete with partial replacement of limestone and dolomite filler.

Reactive transport models account for (1) cement hydration, (2) groundwater flow, (3) solute transport, and (4) chemical reactions between the concrete barriers and incoming groundwater. Mechanical effects are not considered in this study. Their impact and couplings with reactive transport processes are addressed in a separate work (Idiart et al. 2019).

The scope of the project is to study long-term concrete degradation of new concrete compositions using 1D and 2D reactive transport models of a cross-section of the BHK vault. Two-dimensional reactive transport models are used to assess the performance over the first 100 000 years. In addition, one-dimensional models are used to study concrete degradation over longer time-scales, considering a period of 1 million years. The results of these models are compared with the outcomes of the base case defined in Idiart and Shafei (2019) in 2D and Idiart and Laviña (2019) in 1D. In those studies, it was assumed that the composition of concrete to be used in SFL is the same as the one used in SFR for construction concrete (see e.g. Höglund 2014).

The first task has been to conduct a literature review to assess the impact of different cement and concrete compositions on chemical and physical properties of hardened concrete. Based on the main outcomes of this literature review, conceptual models of each concrete composition are developed, including physical as well as chemical properties.

To model long-term degradation of hardened concrete using reactive transport models, the mineralogical composition of the material after hydration is needed. Idiart and Shafei (2019) considered the same hydrated composition as Höglund (2014). That composition was calculated using a cement hydration model presented by Höglund (1992), developed for OPC. In the present work, more up-to-date cement hydration models are used, which are based on thermodynamic modelling coupled to the kinetically controlled dissolution of the clinker and cement additions (Lothenbach et al. 2008b). This modelling approach has the advantage that it can be applied to any cementitious system, provided the required input data is available. Moreover, it makes use of the same geochemical calculations as in traditional reactive transport models (e.g. Idiart and Shafei 2019) and can therefore be consistently simulated using the same thermodynamic database. A set of cement hydration models have been developed and simulated in the geochemical simulator PHREEQC (Parkhurst and Appelo 2013) using the approach proposed by Lothenbach and Winnefeld (2006). A total of four hydration models (see Table 2-1) have been developed to study the effects of changing the w/c ratio, adding fly ash, and replacing cement with limestone ($CaCO_3$) and dolomite ($CaMg(CO_3)_2$) filler. Furthermore, a validation exercise of the hydration model implementation is presented in Appendix A. The fourth model considers the same cementitious system used for SFR construction concrete (see Höglund 2014 for more details), for comparison purposes. In addition, a verification case is also presented (Appendix A) to compare the new implementation with the results of Lothenbach and Winnefeld (2006).

The composition of each cementitious system after full hydration is used as input to the reactive transport models. The development of these long-term degradation models follows exactly the same methodology as previously by Idiart and Shafei (2019) and Idiart and Laviña (2019).

In total, fifteen (15) simulations have been carried out, as detailed in Table 2-1. These include five batch (i.e. 0D) models of cement paste hydration, five reactive transport models of concrete degradation in two dimensions (2D), and five reactive transport models of concrete degradation in one dimension (1D). The 2D simulations consider a time span of 100 000 years, while an extended period of 1 million years is considered in the 1D models.

Table 2-1. Numerical models of the hydration and long-term degradation of different concrete mixes in the BHK vault of SFL presented in this report. A total of fifteen (15) simulations have been carried out.

Process modelled	Dimension	Simulated time	Model ID	Main features
Cement paste hydration	Batch (0D)	10 000 days (27.4 years)	Model 1	Anläggningscement OPC CEM I cement (w/c ratio 0.47)
			Model 2	Anläggningscement OPC CEM I cement (w/c ratio 0.63)
			Model 3	Bascement Slite CEM II (fly ash) cement (w/c ratio 0.47)
			Model 4	Anläggningscement CEM I with limestone+dolomite replacement (w/c ratio 0.49)
			Verification case	OPC system from Lothenbach and Winnefeld (2006). See Appendix A
Concrete degradation	2D	100 000 years	Case I	Hydrated system from Model 1
			Case IIa	Hydrated system from Model 2, cement = 320 kg/m^3
			Case IIb	Hydrated system from Model 2, cement = 280 kg/m^3
			Case III	Hydrated system from Model 3
			Case IV	Hydrated system from Model 4
Concrete degradation	1D	1 000 000 years	Case I	Hydrated system from Model 1
			Case IIa	Hydrated system from Model 2, cement = 320 kg/m^3
			Case IIb	Hydrated system from Model 2, cement = 280 kg/m^3
			Case III	Hydrated system from Model 3
			Case IV	Hydrated system from Model 4

3 Literature review

3.1 Effect of fly ash addition on the properties of concrete

Fly ash (FA) is used as a supplementary cementitious material (SCM) in the production of Portland cement. Fly ash is a by-product produced in large amounts from the combustion of coal in power plants. The physical and chemical properties of fly ash depend on several factors, such as type of coal combustion, type of furnace, method for off-gas desulfurization, etc. All these factors serve to determine its behaviour in the cement system.

Differences in oxide composition of fly ashes are the base of their classification. The European Standard EN 197-1:2011 divides fly ashes in accordance to the content of CaO:

- Siliceous fly ash (CaO content < 10 wt% – labelled as V) and
- Calcareous fly ash (CaO content >10 wt% – labelled as W).

In this framework, FA can be categorised as a SCM with pozzolanic or latent hydraulic properties, respectively.

The Bascement Slite CEM II/A-V consists of a Portland cement with a siliceous fly ash addition of 12.3 wt%, according to data provided by the manufacturer (CEMENTA 2015), see Table 3-1. Note that FA composition is not provided by the manufacturer and thus the one reported by De Weerdt et al. (2011), based on class F siliceous fly ash, has been used instead.

Table 3-1. Chemical composition (wt. %) of Bascement Slite and Fly ash (after De Weerdt et al. 2011).

Component	Bascement Slite CEM II/A-V 52.5 N	Fly ash Class F siliceous FA
Nomenclature	Content by weight (%)	
CaO	56.3	6.3
SiO_2	23.5	50.0
Al_2O_3	6.4	23.9
Fe_2O_3	3.4	6.0
MgO	2.6	2.1
K_2O	1.2	1.36
Na_2O	0.3	0.58
SO_3	3.5	0.40
Cl	<0.1	–
Fly Ash	12.3	

The siliceous FA has pozzolanic properties, meaning that in the presence of moisture, it will chemically react with calcium hydroxide at room temperature to form compounds having cementitious properties (cement hydrates). According to literature, the averaged composition of this type of FA shows low content of unburned elements with silicon (> 25 wt%), aluminium and iron as the major oxides (Table 3-2). Crystalline compounds are quartz, mullite and hematite. FA can also be comprised of significant amounts of alkalis.

Table 3-2. Averaged chemical composition of siliceous type FA (from Taylor 1997).

Composition	Oxide wt%	Composition	Oxide wt%
SiO_2	48.7	MgO	1.6
Al_2O_3	27.9	Na_2O	1.5
Fe_2O_3	9.5	SO_3	1.2
K_2O	4.2	TiO_2	0.9
CaO	2.4	P_2O_5	0.2

3.1.1 Impact on the properties of fresh concrete

Workability, water demand, and water segregation (bleeding)

The workability and, especially, the compactability, flowability, and plasticity of fresh concrete are generally improved when fly ash is added to the mix (Wesche 2004). Likewise, the use of fly ash permits the use of a lower water content compared to OPC of the same workability. The degree of improvement of the rheological properties of concrete with FA addition can vary significantly depending on the nature of the SCM and other parameters of the mix. Nonetheless, as a rule of thumb, the amount of water reduction can be approximated to at least 3 % for every 10 % of fly ash added to the mix (Thomas 2007).

After concrete casting, there is a tendency for the solids (aggregates and cement paste) to settle and displace the water, which is pushed upwards. Excessive bleeding may result in cracking of the concrete surface due to plastic settlement. It can also lead to segregation in the cementitious matrix. The tendency of a concrete to bleed is controlled by the constituents and their proportions, particularly the grading of the fine aggregate, the water content and the use of admixtures.

Concrete containing FA shows a reduced rate and amount of bleeding primarily due to the reduced water demand (Gebler and Klieger 1986). An exception is when FA is used without appropriate water reducers, in which case bleeding (and segregation) will increase compared to OPC concrete.

Setting time and kinetics of hydration

Low-calcium fly ashes are reported to extend both the initial and final setting time of concrete (Thomas 2007, Rahhal and Talero 2004). The increasing addition of FA induces a retardation in the setting times up to 70 % of replacement. Beyond this level, rapid setting has been observed (Brooks et al. 2000, Naik and Singh 1997). In general, FA addition can delay the hydration of cement. Several works have studied the evolution of the heat of cement hydration in cement blends at different FA additions (Deschner et al. 2012, De Weerdt et al. 2011, Rahhal and Talero 2004). The results coincide in pointing out a delayed appearance of the peak corresponding to the maximum rate of heat of hydration (Figure 3-1).

This fact is related to a decrease of Ca^{2+} concentration in solution due to the surface retention of this cation by the FA, which forms AFt during the first hours of hydration. The low Ca aqueous content delays the formation of Ca-rich layers in clinker minerals, and thus the precipitation of reaction products, such as portlandite and C-S-H phases (Puertas et al. 2005, Fajun et al. 1985, He et al. 1984).

Shrinkage

Shrinkage of cement-based materials can occur at either early or later ages. The early-age shrinkage takes place within the first days, while the cement is setting (Holt 2001). At rapid drying conditions, early-age shrinkage becomes relevant as it can lead to large tensile stresses when the mix has not gained significant strength to withstand them, leading in some to cases severe cracking (Nehdi and Soliman 2011, Holt 2001).

The most important types of shrinkage strains affecting cementitious materials are the external drying shrinkage and the autogenous shrinkage. Drying shrinkage is the reduction of volume due to water loss by evaporation. Saha (2018) observed a decrease in drying shrinkage of concrete samples with increasing FA replacement (Figure 3-2a).

Plastic shrinkage is associated with a very rapid loss of moisture from freshly laid cement, within a few hours after placement (Khairallah 2009). The use of fly ash reduces plastic shrinkage due to the combination of decreased bleeding and the filler effect (Wesche 2004). The causes of the early-age shrinkage are also attributed to some additional parameters such as particle size distribution, cement and aggregate content, and w/c ratio (Nehdi and Soliman 2011, Wesche 2004). Some research studies indicate that the use of FA reduces the water requirement, thus reducing drying shrinkage (Malhotra and Mehta 2005, Atiş 2003). In turn, for samples with the same w/b ratio, recent studies attribute such effect to the reduction of the rate of hydration as a result of lime content decrease in the mix (Saha 2018). In addition to these, environmental factors such as air and concrete temperature and relative humidity (RH) also have an influence on drying shrinkage at early-age (Nehdi and Soliman 2011, Wesche 2004, Holt 2001).

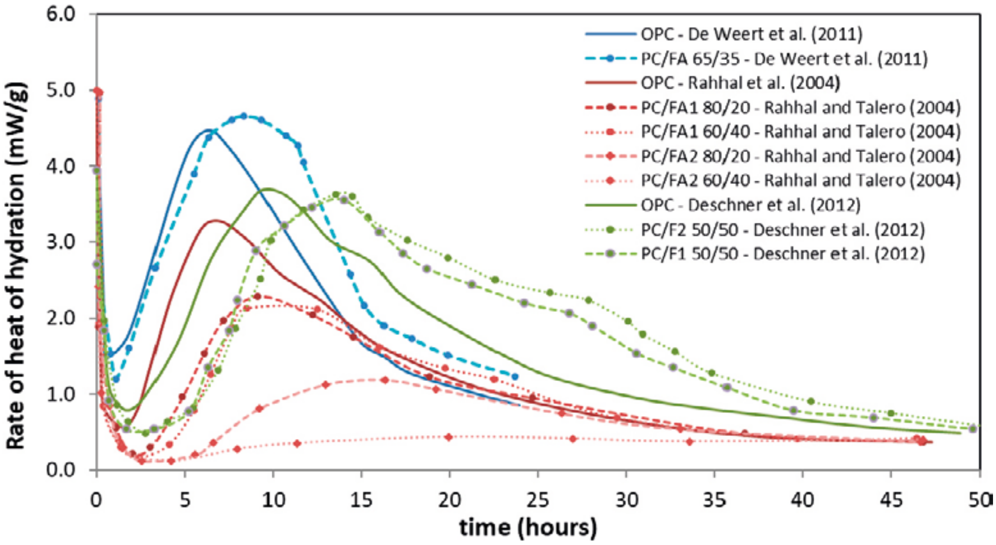

Figure 3-1. *Rate of heat of hydration (mW/g) of different FA blended cements as a function of time (hours) from different sources (OPC results are also shown for comparison). Data from: De Weerdt et al. (2011) – 35 wt% siliceous FA addition and w/c ratio = 0.5 (blue lines); Rahhal and Talero (2004) 20 and 40 wt% of two types of siliceous FA addition and w/c ratio ~ 0.3 (red lines); Deschner et al. (2012) – 50 wt% of siliceous FA addition and w/c ratio = 0.5 (green lines).*

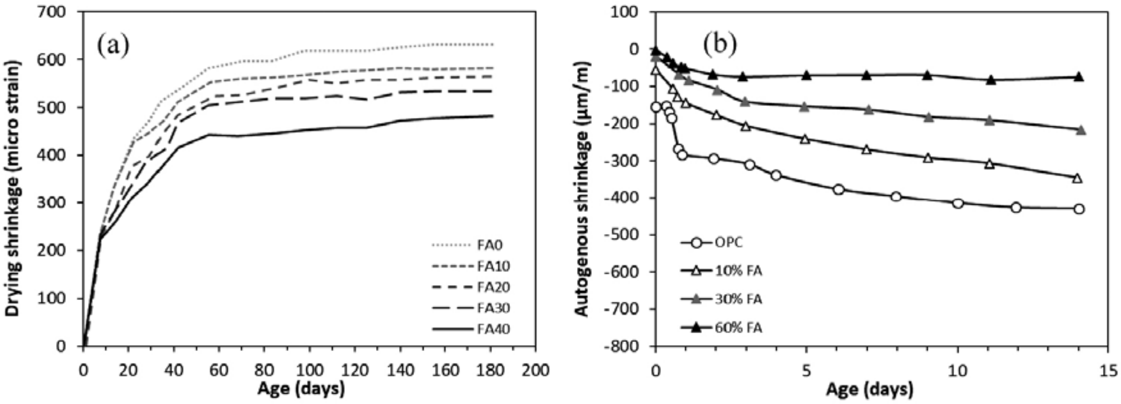

Figure 3-2. *(a) Effect of fly ash (FA) weight percent (0, 10, 20, 30 and 40 wt%) on drying shrinkage of concrete with w/b ratio of 0.35 (adapted from Saha 2018); (b) Effect of fly ash weight percent on autogenous shrinkage of mortar with a w/b ratio of 1.0 by volume (adapted from Lura et al. 2003).*

Autogenous shrinkage is the macroscopic volume reduction associated with cement hydration. It results from internal chemical reactions leading to unsaturated conditions and capillary forces within the cementitious matrix and does not involve moisture transfer to the environment (Jensen and Hansen 2001a, Nehdi and Soliman 2011). Contribution of autogenous shrinkage to total shrinkage becomes important in mixtures with reduced w/c ratio (Nehdi and Soliman 2011). In these mixes, water availability for hydration reactions is limited, resulting in self-desiccation.

Chemical shrinkage is also associated with cement hydration reactions, although in this case it occurs under water saturated conditions. It is defined as the volumetric difference between hydration products and the unhydrated cement and water before hydration (Tazawa 2014). Some authors relate autogenous shrinkage to an external volume change while chemical shrinkage is considered as an internal volume reduction or change in porosity (Jensen and Hansen 2001a, Holt 2001, Tazawa 2014).

Recent studies have demonstrated that the FA-containing cements have a higher total chemical shrinkage than OPC due to the filler effect and the pozzolanic reaction of FA, which progresses with time (Deschner et al. 2012, De Weerdt et al. 2011 – Figure 3-13). In turn, the addition of FA is found to reduce autogenous shrinkage for a given w/b ratio (Lura et al. 2003 – Figure 3-2). Nevertheless, as the addition of FA can reduce the water requirement, autogenous shrinkage can drastically increase in blended mixtures of w/c ratio below 0.4 (Lura et al. 2003).

3.1.2 Chemical aspects

Portlandite content (pozzolanic reaction) and bound water

The presence of pozzolanic additions modifies the normal development of cement hydration. A blended or pozzolanic cement is a mixture of Portland cement and a pozzolanic material. Examples of artificial pozzolanic materials include fly ash, silica fume or blast furnace slag. Blended cements release calcium hydroxide at first hydration stages and is later consumed through pozzolanic reactions, from ~ 7 days and onwards. This effect is reported to increase with the extent of replacement (Figure 3-3).

Portlandite content depends on several factors such as the degree of clinker hydration, the progress of the pozzolanic reaction, the composition of the hydrates, the FA soluble silica content and particle fineness, or the water-to-cement and pozzolana-to-clinker ratios, among others (Bouzoubaâ et al. 1999, Sánchez de Rojas et al. 1993, Sharma et al. 1993).

Similarly, the bound water is also increased in FA-containing cements, mainly due to the filler effect of the SCM. This confirms the promotion of the OPC hydration by a seeding effect whereby the FA provides new nucleation sites within the pore space away from the particle surfaces (Thomas et al. 2009).

Hydration products

It is generally accepted that, in the pozzolanic reaction of fly ash, the $Ca(OH)_2$ produced during cement hydration reacts with the silicate and aluminate phases to produce calcium silicate and aluminate hydrates (Taylor 1997). Thus, hydrated cements with SCM additions are generally characterised by a higher content of C-S-H phases and a lower content of portlandite compared to OPC (Massazza 1993, Fajun et al. 1985). C-S-H phases are composed of silicate chains held together by calcium oxide layers forming the so-called dreierketten structure, a repeating chain of three silica tetrahedra (Taylor 1997). The length of these chains depends on the composition of the C-S-H phases and is typically characterised by the mean chain length (MCL). Two of these silica tetrahedra are linked to the calcium oxide layer (pairing tetrahedra), while the third one, the bridging tetrahedron, is linked to two pairing tetrahedra (L'Hôpital et al. 2015). The structure of C-S-H is amorphous in nature, but it keeps some structural order within a short range which is analogous to tobermorite and jennite.

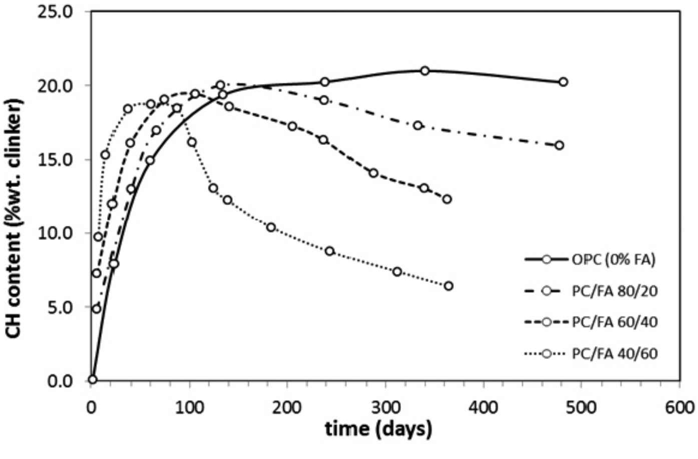

Figure 3-3. *Calcium hydroxide (portlandite) contents of Portland-fly ash cement mixes containing 0, 20, 40 and 60 wt% of low-CaO fly ash (adapted from Taylor 1997).*

The SiO_2 released from the FA is partly consumed in forming additional C-S-H to that formed by clinker dissolution, and partly in lowering the C/S ratio of the C-S-H. This leads to a gradual evolution from a jennite-like towards a tobermorite-like structure (Lothenbach et al. 2011, Wesche 2004), with an associated proliferation of bridging tetrahedra that results in an increase of the C-S-H mean chain length (MCL - Table 3-3) (L'Hôpital et al. 2015, Taylor 1997).

The chemical composition of SCM generally exhibits lower lime content than OPC, and therefore differences in the amount and type of hydrates formed are expected (Figure 3-4a).

For cements with SCM additions with significant amounts of alumina, such as FA, an increased formation of Al-bearing phases such as hydrogarnet, strätlingite and other hydrated calcium aluminates is expected (Figure 3-4b). Hydrogarnet phases (C_3AH_6) have been detected in young blended cements with high Al_2O_3 (Deschner et al. 2012), but especially in older cement pastes and under high curing temperature (Nagataki et al. 1982). The presence of strätlingite (C_2ASH_8) has been identified at high quantities of FA replacement when portlandite content is depleted (Figure 3-5). According to Damidot and Glasser (1995), these two phases are not compatible, however, the presence of strätlingite has been observed with portlandite for a one-year old cement with 30 wt% of FA (Escalante-Garcia and Sharp 2004).

Furthermore, experimental studies indicate that aluminium is incorporated into C-S-H tobermorite-like structures, forming the so-called C-A-S-H phases (e.g. L'Hôpital et al. 2015, García-Lodeiro et al. 2011, Andersen et al. 2006, Sun et al. 2006). A different mechamism of substitution has been reported, i.e., tetrahedrally coordinated Al(IV) substitution at low Ca/Si ratios whereas octahedrally coordinated Al(VI) at high ratio (L'Hôpital et al. 2015, Pardal et al. 2012, Sun et al. 2006). According to García-Lodeiro et al. (2011), C-A-S-H phases show a compositional range of $0.72 < C/S < 1.94$ and $0 < A/S < 0.1$ (Figure 3-4b), being compatible with portlandite, mono-/hemi-carbonates and strätlingite. The same A/S ratio was reported by L'Hôpital et al. (2015) as the maximum limit for C-A-S-H phases, even though other authors observed higher A/S ratios up to 0.19 approx. (Pardal et al. 2009, Sun et al. 2006).

Aluminium incorporation leads to modification of the C-S-H structure, mainly entering in the bridging position of the silica dreierketten structure and increasing the MCL (L'Hôpital et al. 2015, Manzano et al. 2009 – Table 3-3). The impact of different FA addition on C-S-H composition in blended cements has been evidenced by several authors (Figure 3-5).

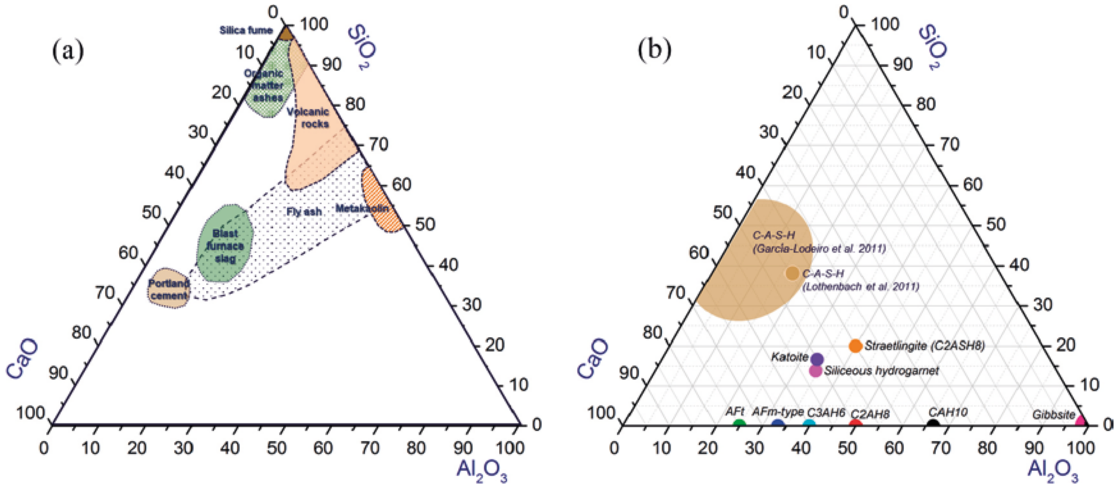

Figure 3-4. *(a) Ternary diagram (wt% based) situating the chemical constitution of the major SCM groups (modified after Glasser et al. 1987); (b) Ternary diagram including the most common aluminium-bearing phases occurring in cementitious materials (data from several sources). Light brown shaded area corresponds to stability zones of C-A-S-H phases proposed by the experimental work conducted by García-Lodeiro et al. (2011), while the brown point corresponds to the suggested limits of the C-A-S-H solid solution after Lothenbach et al. (2011).*

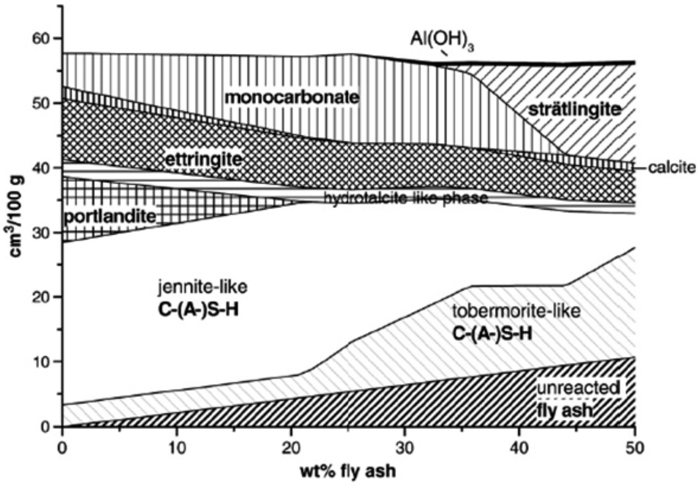

Figure 3-5. Modelled changes in hydrated Portland cement upon blending with fly ash, assuming complete reaction of the Portland cement (after Lothenbach et al. 2011).

Table 3-3. Experimental parameters and characterization of experimentally obtained cement blends with FA additions in accordance with consulted literature. Data of OPC is also included for comparison.

System	FA (wt%)	Age (d)	w/c (wt/wt)	C/S (mol/mol)	A/S (mol/mol)	MCL	Source
OPC	0	28–550	0.4	1.7–1.8	0.05–0.07	3.3–5.0	(a, b, c)
OPC-FA	50	28–90	0.5	1.4–1.6 ± 0.4	0.15–0.16 ± 0.03	–	(b)
OPC-FA	50	250–550	0.5	1.3–1.4 ± 0.2	0.17 ± 0.03	–	(b)
OPC-FA	30	30	–	1.57	0.2	15.6	(c)
OPC-FA	20	8	0.5	1.55	0.12	–	(d)

(a) Taylor (1997).
(b) Deschner et al. (2012).
(c) Girão et al. (2010).
(d) Rayment (1982).

Pore solution

In general, the pH of the pore solution of hydrated cement pastes containing fly ash depends on the composition of the latter in terms of alkalis, calcium, and silica (Shehata et al. 1999). The higher the silica the higher the amount of alkalis removed from solution by the hydrates and thus the lower the pH of the porewater. On the other hand, the higher the calcium concentration the lower the amount of alkalis removed from the solution and therefore the higher the resulting pH.

The evolution of the composition of the pore solution of FA blended cements with hydration time is in general similar to that of an OPC mix. However, several authors coincided in indicating important differences that need to be considered:

- Decrease of Ca concentration in the pore solution (and the pH) after some time of hydration compared to the reference OPC. This is related to the consumption of portlandite by the pozzolanic reaction with fly ash (Deschner et al. 2012, De Weerdt et al. 2011, Shehata et al. 1999).
- Decrease of alkalis (Na and K) and OH^- concentration (i.e. pH) after some time of hydration (from 7 days onwards). This is due to the enhanced binding of alkalis in the C-S-H structure (see above) (Deschner et al. 2012, De Weerdt et al. 2011, Diamond 1981).
- Decrease of SO_4^{2-} concentrations compared to OPC not directly related to the dilution effect, possibly due to the increase of the Al_2O_3/SO_3 ratio in the FA-containing cement (Deschner et al. 2012, De Weerdt et al. 2011).
- Increase of Al and Si concentrations compared to OPC at longer hydration time, which is attributed to the FA dissolution (Deschner et al. 2012, Shehata et al. 1999).

Due to the change of C-S-H composition towards lower C/S ratios and higher A/S ratios, the pore solution shows a decreased Ca and increased Al and Si concentrations, as governed by the solubility of C-(A)-S-H phases.

3.1.3 Impact on the properties of hardened concrete

Porosity

It is generally accepted that the pore sizes become finer as hydration proceeds (e.g. Zeng et al. 2010). The extent of hydration and the formation of cement hydrates play a key role in the evolution of the pore structure in cement-based materials. Even though the initial pore sizes of cements containing fly ash are larger than OPC, after a sufficiently long hydration time (1–3 months) this tendency is reversed (Wesche 2004) and the average pore size is reduced (e.g. Boğa and Topçu 2012, Chindaprasirt et al. 2005). For example, Gui et al. (2016) experimentally showed that a 30 % replacement of OPC by FA leads to finer pores than OPC concretes (Figure 3-6) and that the pore structure of the blended concrete has a high tortuosity and low connectivity. Pastor et al. (2016) also reported a clear refinement of the pore size (i.e. a reduction of the contribution of large pores to the total porosity) with time when adding fly ash to samples with w/b ratio of 0.5 with respect to the corresponding OPC samples.

The total porosity is generally not reduced by the addition of fly ash. In fact, total porosity usually increases with FA replacement at a constant w/b ratio (Pastor et al. 2016, Chindaprasirt et al. 2005). Mercury intrusion porosimetry (MIP) measurements conducted by Zeng et al. (2010) showed a systematic and non-negligible increase when increasing the FA replacement from 0 to 20, 40 and 60 % of total porosity in cement pastes at w/b ratio of 0.5 after 90 days of curing. The authors obtained total porosities of 25.8, 31.5, 36.7, and 45.4 %, respectively. However, the nature, shape and fineness of the fly ash particles may play an important role in the total porosity at a given curing time. Sinsiri et al. (2010) showed that the finer the FA particles, the lower the total porosity. Moreover, spherical particles seem to hydrate faster than highly irregular shaped FA, which can be attributed to a better dispersion of the spherical particles and a higher degree of packing, leading to a reduced porosity after 90 days of hydration (Sinsiri et al. 2010), see Figure 3-7.

Yu et al. (2017) also performed MIP measurements of OPC and FA blended cement paste samples with 30 and 50 wt% replacement, using a water-to-binder ratio of 0.4 over a period of 3 years of curing. Their results show that both the total and capillary porosity decrease with increasing curing time (linearly in a semi-log scale for time). Moreover, the effect of adding 30 or 50 wt% of FA is a clear increase in porosity compared to the OPC sample (see also Yu and Ye 2013). A 30 % replacement induces an increase in porosity from 24 % for OPC to 27.5 % for the FA cement after 28 days of curing. After 1000 days of curing the relative increase is even higher (12 % for OPC and 16.5 % for the FA cement).

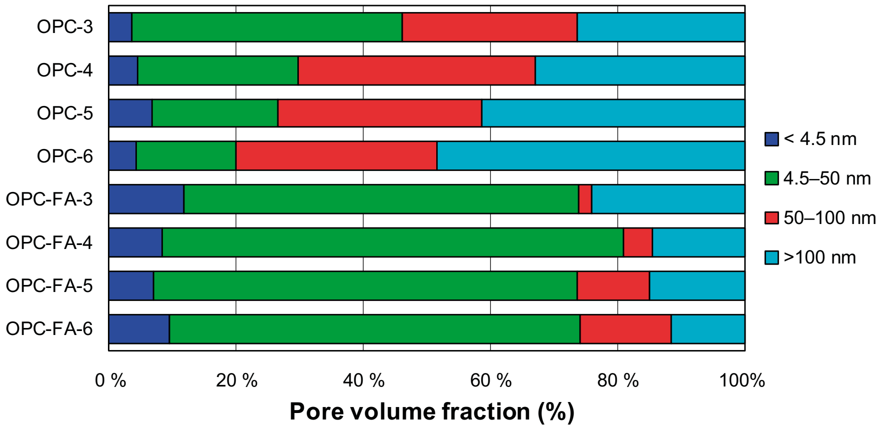

Figure 3-6. *Pore size distribution from mercury intrusion porosimetry (MIP) results for OPC and OPC-FA (30 % replacement) concrete samples with w/b ratios ranging between 0.3 and 0.6 (corresponding to the numbers after the name from 3 to 6) (adapted from Gui et al. 2016).*

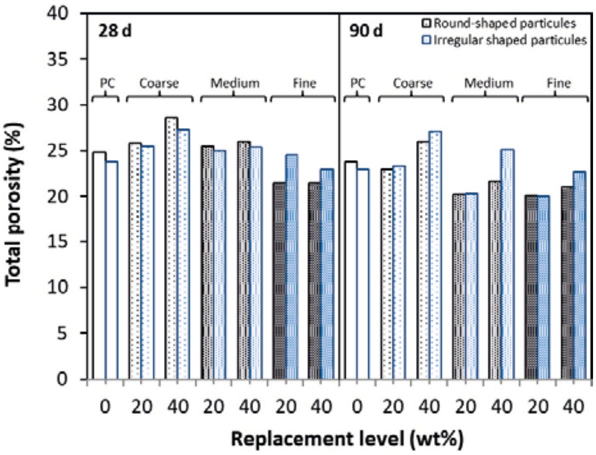

Figure 3-7. *Porosity of Portland cement (PC) pastes and fly ash pastes at 28 and 90 days of curing with w/b = 0.35. (adapted from Sinsiri et al. 2010). Round-shaped and highly irregular shaped FA particles with different sizes (coarse, medium, and fine) are shown in black and blue columns, respectively.*

It should be noted that even though MIP is widely used to measure porosity in cementitious materials, the technique has several limitations (Taylor 1997). Among others, the finest pores (smallest gel pores below a few nm) are not accessible by this technique. In that case, if the effect of fly ash is to produce a more refined pore structure and higher content of C-S-H, it is possible that the results for FA cement pastes do not represent the total porosity.

Transport properties

In concrete technology, permeability and diffusion coefficient are usual indicators for the assessment of durability of concrete structures (e.g. Baroghel-Bouny et al. 2011). It is well accepted that an efficient way to increase the durability of concrete structures is to obtain a dense concrete with reduced permeability and porosity. Numerous studies have been published about the durability of fly ash concrete (Liu et al. 2017, Nath and Sarker 2011, Wesche 2004, and references therein). The incorporation of fly ash in blended cements generally improves the resistance of concrete against the ingress of chlorides or other external ions by reducing its permeability and/or diffusivity (Liu et al. 2017, Boğa and Topçu 2012).

The permeability of concrete is intimately linked to the porosity and pore structure of the hardened cement paste (HCP) and, to a lesser extent, to the interfacial transition zone (ITZ) between HCP and aggregates in mortar or concrete. However, the relationship between porosity and permeability is not straightforward. The most influential parameters on HCP permeability are the degree of hydration and the water-to-dry mass ratio. In general, an increase of the w/c ratio leads to an increase in permeability and a less tortuous path for diffusive solute transport.

There are several experimental studies showing that partial replacement of OPC by fly ash reduces the permeability of concrete due to a refinement in the pore structure (Pastor et al. 2016, Baroghel-Bouny et al. 2011, Boel et al. 2007, Thomas 2007, Wesche 2004, Thomas and Matthews 1992). On the other hand, the experimental results of Gui et al. (2016) do not show any reduction of gas permeability when replacing part of the OPC with FA. Another exception is the experimental study by Hedegaard and Hansen (1992). According to their interpretation of the results, 1 kg of cement would have to be replaced by ~ 3 kg of fly ash to maintain the same water tightness of the fly ash concrete. However, they considered a curing time of 28 days, while as shown in the previous section the refinement of porosity should continue with time. Therefore, it is likely that the benefits associated to longer curing times could not be observed by these authors. Finally, the work by Shi et al. (2008) also reports experimental results that do not show a reduction of gas permeability with increasing FA content. They report an increase in permeability with fly ash content, although it is generally small, especially for a w/b ratio of 0.35 (maximum value studied).

During the hydration process, large voids between the cement grains are filled with hydration products. With time, these hydration products become denser as the pozzolanic effect of fly ash in the concrete mixture creates refined hydration products. A comparison between the permeability of fly ash and OPC concrete samples is presented in Figure 3-8 (Thomas and Matthews 1992). According to Baroghel-Bouny et al. (2011), the beneficial effect of fly ash on the reduction of permeability is larger the longer the curing time. This statement has been recently confirmed using rapid chloride migration tests (Liu et al. 2017). These authors reported systematically lower chloride migration coefficients for longer curing times. They also showed that within the range 0–30 wt% of fly ash replacement, the migration coefficient is lower the higher the FA replacement. A reduction of 20–25 % is reported for a FA replacement of 15 wt% compared to the OPC sample (Liu et al. 2017). According to Krishna and Sabnis (2013), a concrete with 25 wt% FA can have a permeability that is at least one order of magnitude lower than OPC for long enough curing times (Figure 3-9).

As stated in Section 3.1.1, the use of FA reduces the risk of cracking due to shrinkage. This reduction can have a positive impact for improving the durability of concrete, preventing an easy access to deleterious species from the environment.

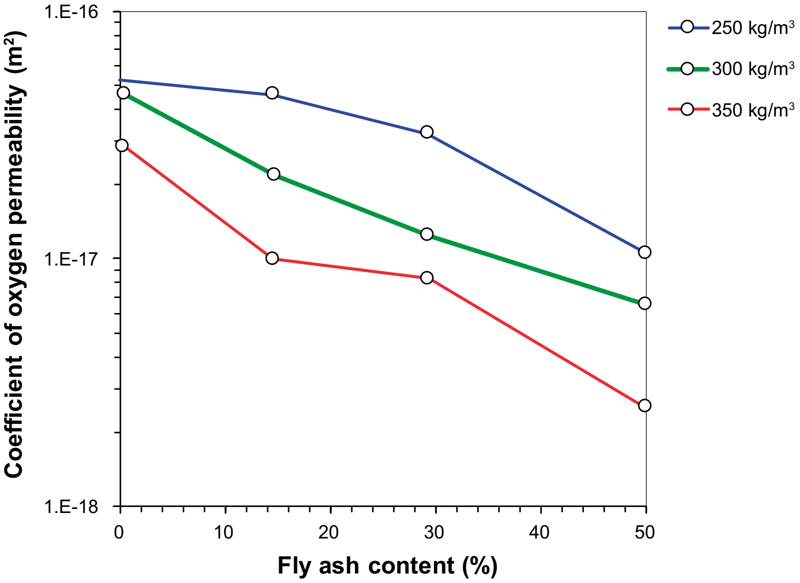

__Figure 3-8.__ Permeability to oxygen of cylindrical concretes samples (15 cm diameter × 30 cm long) with cement contents of 250, 300 and 350 kg/m^3 and cured in water for 28 days (adapted from Thomas and Matthews 1992).

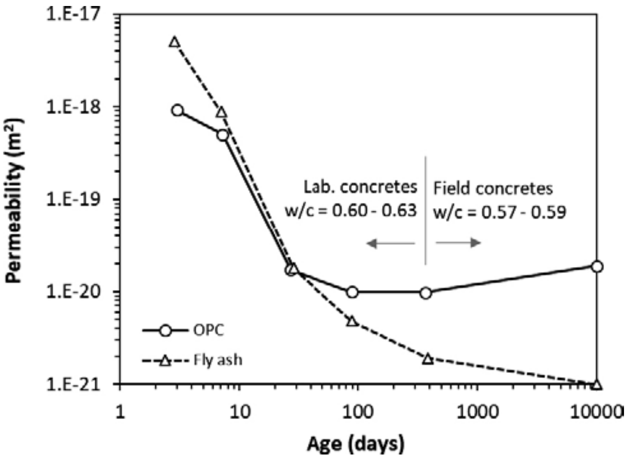

__Figure 3-9.__ Evolution of permeability of OPC and blended cement with 25 wt% of FA replacement with time of curing (adapted from Krishna and Sabnis 2013).

The diffusion coefficient is another important property for long-term performance. In general, pozzolanic concretes are more resistant to e.g. chloride ingress because they are less permeable and less diffusive (Liu et al. 2017, Pastor et al. 2016, Boel et al. 2007). The use of fly ash increases the resistance of concrete to chloride ingress extending the service life of reinforced concrete exposed to a chloride environment. It is noted that chloride ingress also depends on the binding capacity of the cementitious system, which is a function of cement composition and Cl^- concentration. Chlorides can react either with C_3A to form Friedel's salt (Zhang et al. 2013, Lannegrand et al. 2001) or with C_4AF to form an analogous iron-containing salt. The concentration of OH^- ions is the key factor affecting the extent of chloride uptake (Cl^-/OH^- ratio).

Several diffusion experiments using FA concretes are reported in the literature, mostly dealing with chloride ingress (Liu et al. 2017, Thomas 2007 and references therein). Experiments conducted on cement pastes indicate that addition of 20 to 30 % fly ash reduces the chloride diffusion coefficient by between 2.5 to 10 times (Thomas 2007). A replacement of 10 % of OPC with FA can reduce the apparent chloride diffusion coefficient by 20 % (Baroghel-Bouny et al. 2011). This effect becomes more significant with percentage of replacement (Figure 3-10) as well as with the time of curing since the concrete containing fly ash shows substantial reductions in chloride penetrability with time.

Compressive strength

The effect of replacing OPC with increasing amounts of low-calcium FA on compressive strength of concrete samples is illustrated in Figure 3-11(a) (for a constant w/b ratio of 0.35 – Saha 2018). It may be observed that as the level of replacement increases the early-age strength decreases, which agrees with other related studies (e.g. Balakrishnan et al. 2013).

However, samples containing FA reached at least 82 % of OPC compressive strength after one year of curing and thus an improved strength in the long-term is expected due to the pozzolanic reaction (Saha 2018, De Weerdt et al. 2011, Thomas 2007), as shown in Figure 3-11(b).

Alkali-silica reaction (ASR)

Under hyper-alkaline conditions, there is a risk of alkali-silica reactions (ASR) between the hydroxyl ions in the pore solution and reactive silica in the ballast material. These reactions lead to the formation of alkali-silica gels that increase in volume by uptake of water, eventually leading to cracking of the cementitious material. The conditions required for ASR to occur are:

i. Sufficiently high alkali content (it is thought that ASR does not occur with Portland cements containing less than 0.6 % of Na_2O alkali eq., see Massazza 1993);

ii. The presence of reactive aggregates;

iii. A sufficient source of water.

Low-alkali cements and supplementary cementitious materials are frequently used to allow alkali-silica reactive aggregate combinations to be used in concrete without damage. SCMs are known to control ASR expansion mainly by their capacity to reduce the alkalinity of the pore solution by binding alkalis in the C-S-H phases (Thomas 2011, Hong and Glasser 1999). SCMs with high (reactive) silica content and a low amount of CaO and alkalis, such as silica fume (SF), are considered the most effective to reduce ASR (Thomas and Shehata 2004).

In general, the use of low-calcium fly ash reduces the potential for ASR in concrete. According to Thomas (2007), it can control ASR in concrete at moderate levels of replacement (20 to 30 wt%) due to the reduced concentration of alkali hydroxides in the pore solution when FA is present. Figure 3-12 (adapted from Massazza 1993) shows the impact of different pulverised fly ashes on the expansion by ASR. The blends showing lower expansions correspond to the fly ashes with a lower content of alkalis in its oxide composition and a higher surface area (fineness).

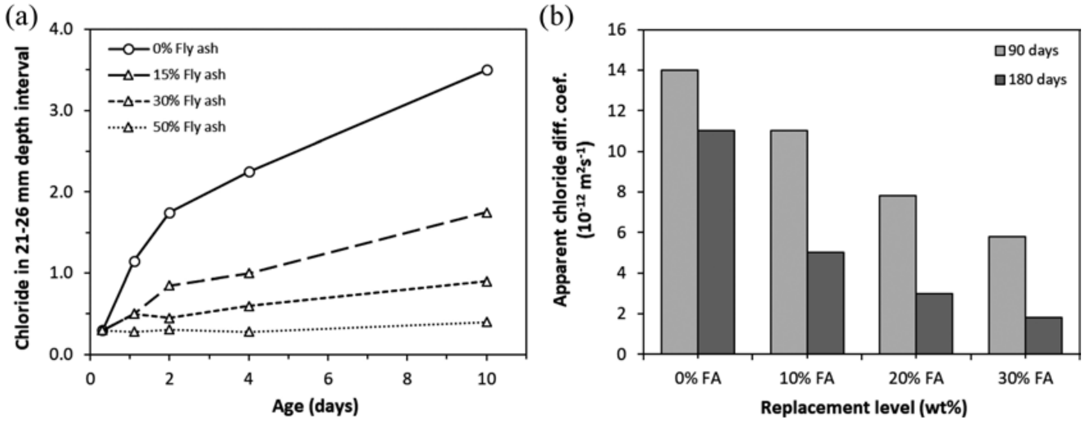

Figure 3-10. *(a) Effect of FA content on (a) the chloride penetration at different ages and percentage of FA replacement (adapted from Thomas 2007). (b) Apparent chloride diffusion coefficient (m^2/s) measured by migration tests under an external electrical field on saturated mortar samples (w/b = 0.45), after 90-day or 180-day water curing (adapted from Baroghel-Bouny et al. 2011).*

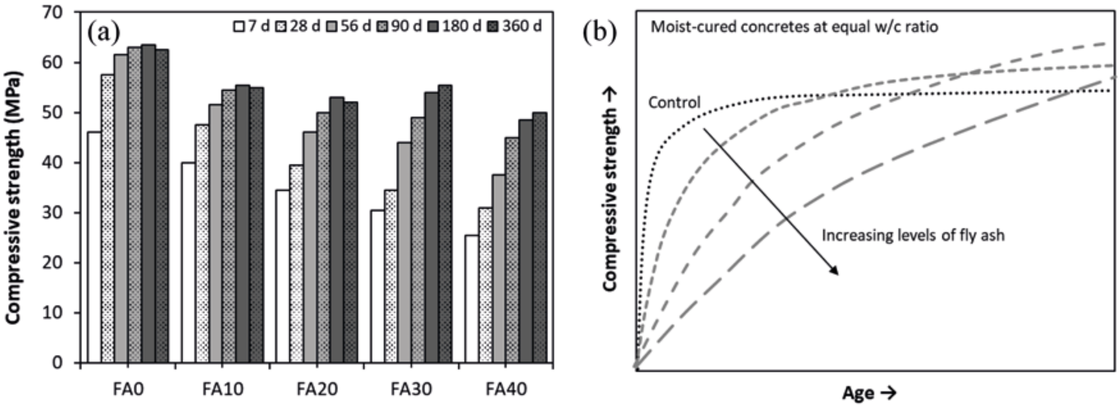

Figure 3-11. *(a) Compressive strength development of concrete samples with several FA replacements (0, 10, 20, 30 and 40 wt%) at the same w/b ratio of 0.35 (from Saha 2018); (b) Theoretical effect of fly ash on compressive strength development of concrete (adapted from Thomas 2007).*

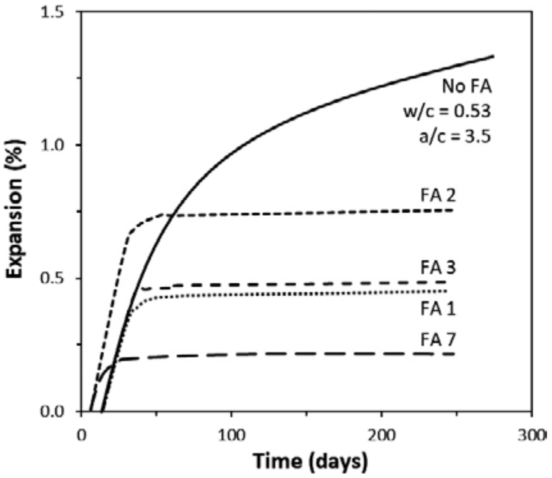

Figure 3-12. *Expansion associated to ASR for specimens in which part of the aggregate is replaced by an equal volume of FA such that FA/(cement + FA) = 0.3 by weight (adapted from Massazza 1993). FA = 1, 2, 3 and 7 correspond to different pulverised fly ashes, with differing oxide composition and fineness. w/c=water-to-cement ratio. a/c=aggregate-to-cement ratio.*

Sulfate attack and carbonation

Sulfate-rich groundwater can impair long-term performance of concrete if it reacts with aluminates and calcium hydrates to form expansive ettringite and/or gypsum. Likewise, severe damage can originate from a combined attack by sulfate and carbonate at low temperature, leading to thaumasite formation by reaction with monosulfate/ettringite (AFm/AFt phases, respectively), where silica from C-S-H gel replaces aluminate.

The use of low-calcium FA can increase the resistance of concrete when exposed to sulfate-rich soils or groundwater. It is well-known that reducing the source of aluminates and portlandite from the cementitious matrix is one of the best ways to minimise the risk of external sulfate attack (Massazza 1993). To this end, low C_3A contents are needed in the clinker. Pozzolanic cements (see Section 3.1.2) reduce the C_3A content of the clinker by dilution with pozzolana and because the pastes contain lower amounts of available portlandite. Moreover, the finer pore structure and reduced transport properties also increase the resistance to external sulfate attack.

Carbon dioxide dissolved in the porewater produces carbonates by consuming OH^- ions, thus lowering the pH. Carbonates react with Ca^{2+} to produce calcite. The required OH^- and Ca^{2+} ions are obtained from portlandite dissolution and C-S-H decalcification. To some extent, carbonation is beneficial to concrete durability because the formation of calcite entails a reduction of porosity and diffusivity, leading in turn to a reduction of the leaching kinetics (Galán et al. 2011, Moranville et al. 2004). In turn, longer exposures or larger concentrations of dissolved carbonates in the groundwater could also lead to gradual dissolution of C-S-H phases, with an associated increase in porosity, and possibly to cracking (Rimmelé et al. 2008, Kutchko et al. 2007).

FA-containing cements are characterised by lower portlandite content. In this regard, it has been reported that fly ash increases the carbonation rate compared to OPC and such increase is more pronounced at higher levels of replacement and in poorly-cured concrete of low strength (Bouzoubaâ et al. 2010, Thomas 2007 and references therein). Liu et al. (2016) reported an increase of the carbonation depth after 28 days from 1.1 mm for OPC to 4.4 and 7.6 mm for samples with 15 and 30 % FA replacement.

3.2 Effect of limestone addition on OPC and fly ash blended cements

Portland–limestone cements are the most widely used cements in Europe. Two classes exist in EN 197-1 designated as CEM II/(A or B)-L and CEM II/(A or B)-LL in which the maximum contents of limestone are 20 and 35 %, respectively. However, limestone is widely used as well in all other European common cement types as a minor additional constituent (0–5 wt%).

Limestone content in standardised cement blends must meet normative requirements such as:

- The purity of the limestone should be greater than 75 wt% of $CaCO_3$.
- Its total clay content must not exceed 1.2 wt% of limestone.
- The organic content analysed by TOC must be below 0.2 and 0.5 wt% for L and LL types, respectively.

3.2.1 Impact on the properties of fresh concrete

Workability and water segregation (bleeding)

There are conflicting results in the published literature regarding the effect of limestone additions on water demand and workability. Much of these effects can be related to the particle size distribution of the limestone in relation to the cement. Generally, fine limestone particles can enhance the overall particle packing of the binder materials resulting in less space for water between the solid grains.

Bleeding has a strong dependence on binder particles surface area. As the surface area increases, the affinity for water absorption increases. Thus, independently of the limestone replacement, increasing fineness of limestone decreases tendency for bleeding (Hooton et al. 2007 and references therein).

Setting time and kinetics of hydration

In general, the addition of limestone accelerates the hydration reactions and thus the setting time of the OPC and cement blends with FA (Georgescu and Saca 2009, Péra et al. 1999). There is a consensus about the fact that limestone particle size is a key factor affecting setting time of cement pastes.

Tanesi et al. (2013) observed that both initial and final setting times of mixtures with 30 wt% of FA and 10 wt% of limestone were equivalent to OPCs. A combination of limestone and fly ash in blended cements seems to have beneficial effects with respect to both early and late strength development.

The presence of limestone in cementitious systems amplifies the main peak of the rate of heat of hydration corresponding to the accelerating period. The reason is that the limestone can also participate in reactions of the aluminate phases in these systems, producing carboaluminates in contrast to the conventional formation of sulfoaluminate hydrates (De Weerdt et al. 2011). Péra et al. (1999) observed a doubled heat production when 50 % of $CaCO_3$ replaces OPC. The cumulative heat release is higher in the presence of limestone, which has been associated to the increased filler effect, i.e. additional surfaces are provided for the nucleation and growth of reaction products (Tanesi et al. 2013).

Shrinkage

Experimental evidence shows that Portland cements containing limestone (PLC) have similar early-age shrinkage, stress development, and cracking behaviour as OPC despite the higher fineness of the PLC (Barrett et al. 2014). In turn, the replacement of 5 wt% by limestone results in a higher chemical shrinkage compared to FA-containing blends (Figure 3-13). This increase was observed by several authors, who attributed it to the influence of limestone powder on the type of hydrates formed, which in turn affects the strength development and porosity. (Deschner et al. 2012, De Weerdt et al. 2011, Hirao et al. 2007).

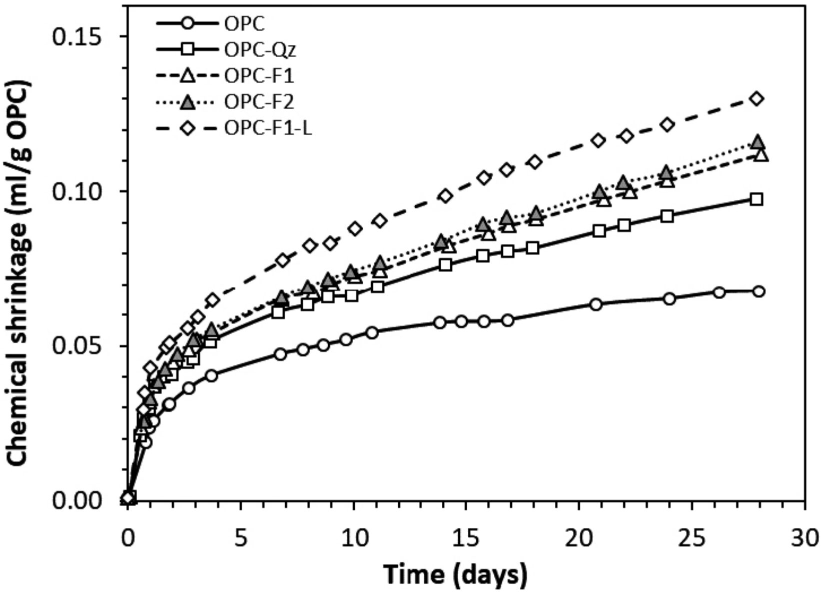

Figure 3-13. *Chemical shrinkage of OPC, OPC–F1, OPC–F2 and OPC–F1 with limestone, normalised to the mass of OPC (adapted from Deschner et al. 2012).*

3.2.2 Chemical aspects

Hydration products

The replacement of 5 wt% by limestone does not result in a significant change of the portlandite content (Deschner et al. 2012, De Weerdt et al. 2011). A substantial increase of bound water has been observed, which is more significant at longer hydration times. This seems to be related to the stabilisation of water-rich hydration products, i.e. ettringite and monocarbonate.

Thermodynamic calculations as well as experimental observations indicate that in the presence of small amounts of limestone, monocarbonate forms instead of monosulfoaluminate (Deschner et al. 2012, De Weerdt et al. 2011, Lothenbach et al. 2008a, Catinaud et al. 2000). Experimental measurements on PLC with 50 % of limestone substitution indicate the presence of carboaluminate and carbosilicate after 60 days of hydration, and disappearance of signals corresponding to monosulfoaluminate (Péra et al. 1999). Therefore, it can be expected that hydroxide and sulfate anions could be released from AFm phases in the presence of limestone or other calcium carbonate form even at low carbonate activity (Matschei et al. 2007a).

Figure 3-14 shows thermodynamic modelling results of the hydration evolution over time for OPC, PC-containing fly ash or limestone, and PC-fly ash-lime ternary blend (De Weerdt et al. 2011). The effect of limestone powder on the hydration of OPC and OPC-FA systems is noticeable already after 1 day of hydration. The type and amount of AFm and AFt phases are different in this case. In the absence of limestone, ettringite eventually destabilises to form monosulfoaluminate, followed by hydrogarnet. On the other hand, addition of limestone leads to the formation of monocarbonate at the expense of monosulfoaluminate, thus indirectly promoting ettringite formation. This is due to the reaction of CO_3^{2-} with monosulfoaluminate in the presence of portlandite to produce ettringite and hemicarbonates. Further reaction with CO_3^{2-} transforms hemicarbonates into monocarbonates (Taylor 1997).

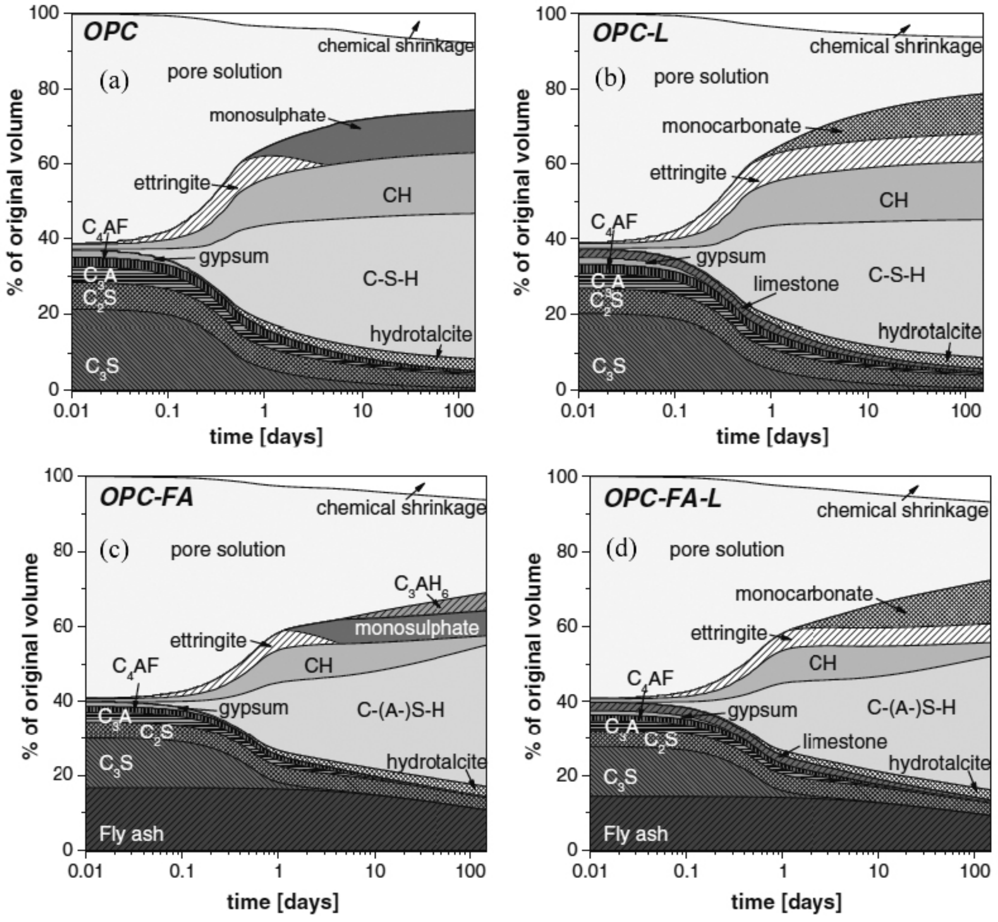

Figure 3-14. *The volume of the different phases as function of time in hydrating cement pastes modelled by GEMS (a) OPC; (b) OPC-L 95/5; (c) OPC-FA 65/35; (d) OPC-FA-L 65/30/5 (from De Weerdt et al. 2011).*

The effect of limestone powder is amplified in the FA-containing cement as limestone interacts with the AFm phases, which content is higher (due to its lower SO_3/Al_2O_3 ratio arising from the additional alumina). The changes in AFm phases are clearly reflected in the sulfate concentrations of the pore solution (see next section).

Pore solution

According to consulted literature, the evolution of the system pH does not seem to be affected by limestone additions up to 5 wt% (De Weerdt et al. 2011 – Figure 3-15a). The main difference in pore solution composition between OPC and OPC-FA, and the limestone containing equivalents is the sulfate concentration. Including 5 wt% of limestone in the mixture significantly increases SO_3 concentration, which indicates a change in the sulfate containing AFm and AFt phases. These observations agree with previous reports (Lothenbach et al. 2008a).

3.2.3 Impact on the properties of hardened concrete

Porosity and transport properties

According to Schmidt et al. (2009), the addition of small amounts of limestone (≤ 5 %) decreases porosity of hardened concrete as it stabilises ettringite in the hydrated cement. On the other hand, higher fractions of substitution of cement (with or without FA) by limestone lead to an increase in porosity (Elgalhud et al. 2016, da Silva and de Brito 2015). Figure 3-16 presents a large compilation on experimental data of the effect of limestone replacement on cement paste samples (Elgalhud et al. 2016). It may be observed that limestone replacement levels smaller than approximately 30 % have the effect of reducing porosity, while larger values have the opposite effect on porosity. The minimum porosity values are reached for a replacement of ~ 15 %. The experiments by Tsivilis et al. (2000) on cement mortars confirm this tendency with porosities of 15.3, 11.6, 12.2, 12.5, and 13.1 % for limestone replacements of 0, 10, 15, 20, and 35 %, respectively. Figure 3-18b shows porosities for large additions of limestone in binary and ternary systems, showing higher values than the reference OPC samples in all cases (da Silva and de Brito 2015).

One plausible reason for this change in tendency has been explored by means of thermodynamic modelling in Matschei et al. (2007b) and Zajac et al. (2014). Their results, presented in Figure 3-17, indicate that there is a minimal porosity for a threshold value of limestone addition to the mix (represented in the figure by the CO_2/Al_2O_3 solid molar ratio (C-S-H not included in the figure due to little variation with limestone addition). The additional ettringite (AFt) formed during carbonation increases the total molar volume of cement hydrates for small amounts of limestone replacement. This results in an enhanced space-filling and a reduction of porosity of hardened cement pastes (Figure 3-17). Additional replacement of limestone leads to an increased porosity in the model (Zajac et al. 2014, Matschei et al. 2007b).

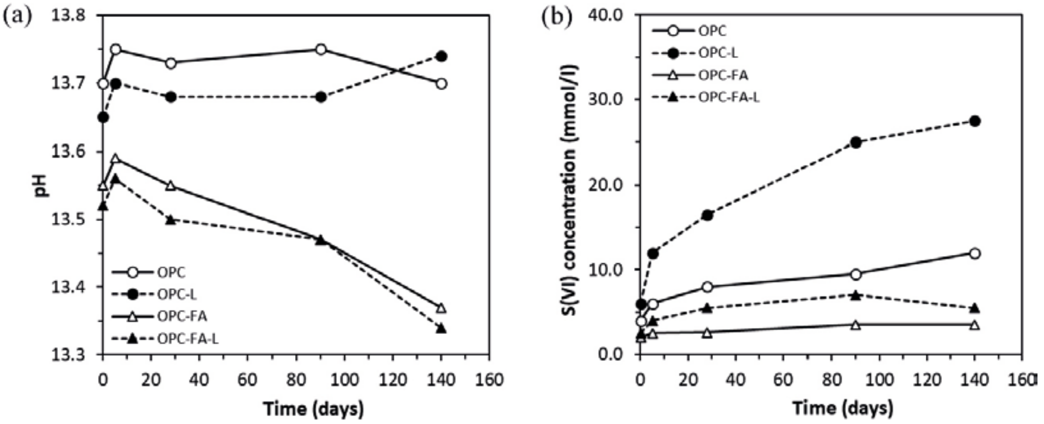

Figure 3-15. *(a) Evolution of pH of the system and (b) SO_3 concentration in the pore solution as a function of curing time. OPC stands for plain cement; OPC-L stands for cement with lime additions of 5 wt%; OPC-FA stands for cement with FA additions of 35 wt%; OPC-FA-L stands for cement with FA and lime additions of 30 wt% and 5 wt%, respectively (adapted from De Weerdt et al. 2011).*

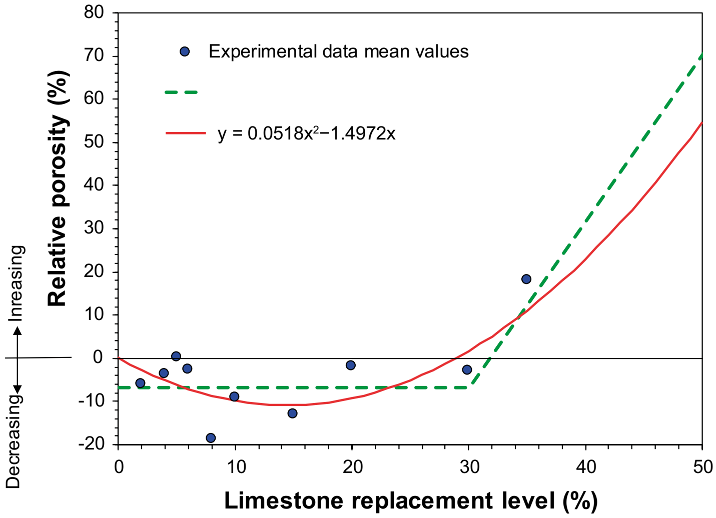

Figure 3-16. Relative porosity changes (e.g. a 10 % relative change of an initial porosity of 15 % results in a porosity of 16.5 %) in % as a function of different limestone replacement levels. Experimental data for cement paste samples from different studies (compilation and figure adapted from Elgalhud et al. 2016).

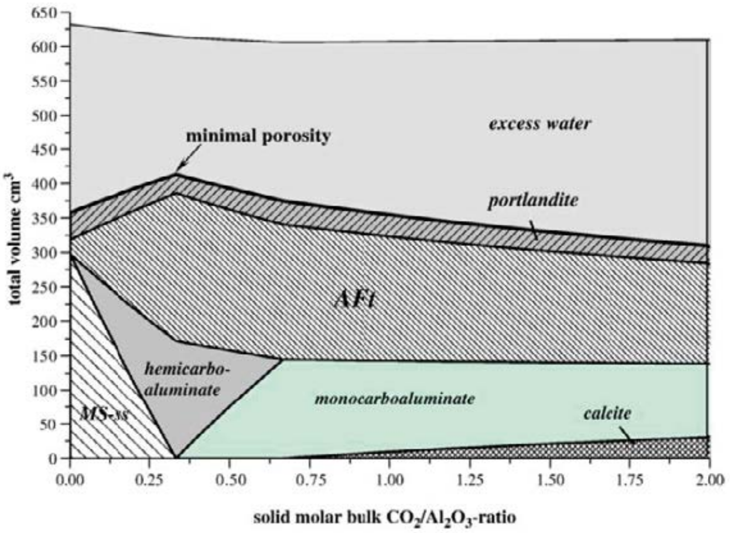

Figure 3-17. Volume changes of hydrate phases of a hydrated model mixture consisting of C_3A, CH and fixed SO_3/Al_2O_3 ratio (= 1) against changing carbonate ratios (CO_2/Al_2O_3) at 25 °C. MS-ss stands for monosulfate solid solution (from Matschei et al. 2007b).

Permeability of concrete is linked to the pore structure and depends on the degree of hydration and the water-to-dry mass ratio. According to published results, small amounts of limestone addition (< 30 %) have a positive effect in reducing the water permeability of concrete, both in binary systems with OPC and in ternary systems with OPC and FA (Figure 3-18a). Other studies have found little impact in gas and liquid permeability (< 50 % changes) for limestone replacements between 10 and 35 % compared to the OPC reference sample (Tsivilis et al. 2003). According to Ingram and Daugherty (1991), an addition lower than 10 to 15 wt% does not have a significant effect on permeability.

In the study conducted by Tanesi et al. (2013) a significant improvement was observed in the transport properties of fly ash concrete when limestone was added. The authors indicated that with 10 wt% of limestone addition the measured resistance to chloride penetration increased by 50 % compared with FA-containing mixtures with the same cement replacement but no limestone powder. On the other hand, Irassar et al. (2001) measured chloride profiles from immersion tests in 3 % NaCl solution of concretes samples made of OPC with 0, 10, and 20 wt% limestone replacements. The apparent chloride diffusion coefficients determined from these profiles showed a clear increase with increasing limestone content (up to 2 to 3 times, depending on the w/c ratio).

The review of Tennis et al. (2011) presents experimental results from other researchers that tend to confirm that small limestone additions (< 15 wt%) can be beneficial in decreasing the diffusion coefficient and/or the permeability of concrete. However, larger additions generally lead to an increase in the (chloride) diffusion coefficient (Tennis et al. 2011 and references therein). This is also confirmed by Ramezanianpour et al. (2009) on the basis of rapid chloride ions permeability tests.

Compressive strength

The compressive strength tends to increase slightly when 5 wt% of limestone is added to either OPC or OPC-FA (Figure 3-19a). This is in line with the observations on the molar volume explained in the previous section. Likewise, limestone addition also proves to affect the velocity of strength development compared to OPC-FA, which agrees with the faster kinetics of hydration observed for these mixtures (see Section 3.1.1). Further, in a comprehensive study by Bentz et al. (2012), a direct relationship between compressive strength development and cumulative heat release is clearly observed. Other works (e.g. Tanesi et al. 2013) pointed that the addition of limestone serves to partly regain the loss in compressive strength at all ages of FA-containing blends (Figure 3-19b).

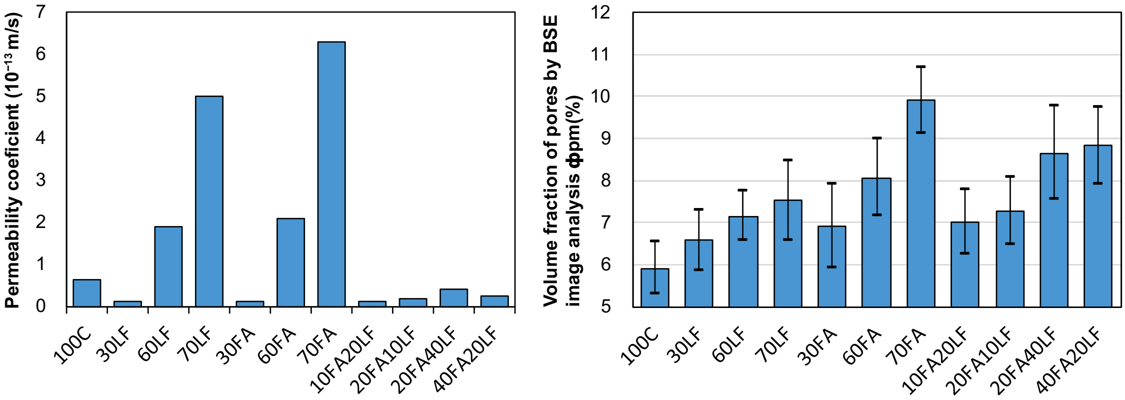

Figure 3-18. *(a) Permeability (10^{-13} m/s) and (b) volume fraction of pores (%) obtained from scanning electron microscopy (SEM) with backscattered electrons (BSE) image analysis for different self-compacting concrete (SCC) mixes after 91 days of curing (adapted from da Silva and de Brito 2015). 100C: 100 % OPC; 30LF, 60LF, and 70LF: 30, 60 and 70 wt% limestone filler; 30FA, 60FA, and 70FA: 30, 60 and 70 wt% fly ash; 10FA20LF: 10 % fly ash and 20 % limestone filler; 20FA10LF: 20 % fly ash and 10 % limestone filler; 20FA40LF: 20 % fly ash and 40 % limestone filler; 40FA20LF: 40 % fly ash and 20 % limestone filler.*

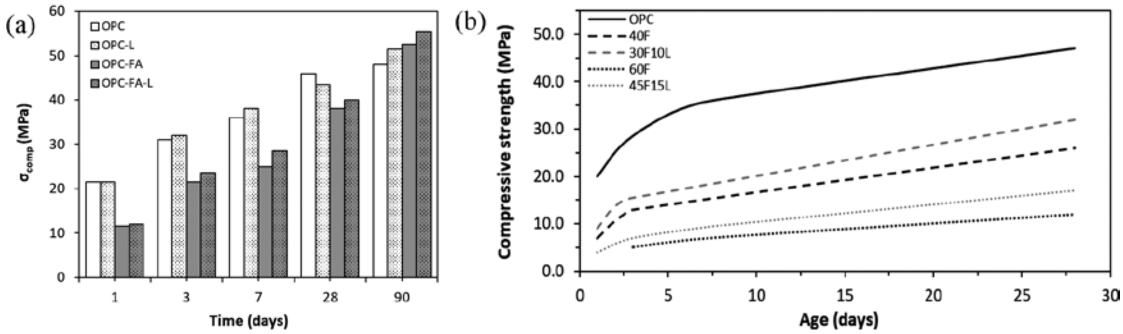

Figure 3-19. *(a) Compressive strength of mortar samples of different composition at different curing times. OPC-L: cement with 5 wt% lime addition; OPC-FA: cement with 35 wt% FA addition; OPC-FA-L: cement with 30 wt% FA and 5 wt% lime additions (adapted from De Weerdt et al. 2011); (b) Compressive strength development for mixtures containing Class F (low Ca content) fly ash (adapted from Tanesi et al. 2013).*

The strength can be maintained or even increased in pastes containing up to 10 wt% limestone (Péra et al. 1999). However, lower compressive and flexural strengths are obtained for cement systems with higher limestone replacement (Bederina et al. 2011, Péra et al. 1999 – Figure 3-20a). Lollini et al. (2014) studied the compressive strength properties of OPC with ground limestone replacements of 15–30 wt% of binder at different w/b ratios (0.42–0.61) and binder content (250–400 kg/m^3). They reported lower compressive strengths for PLC with 15 and 30 % compared to OPC at the same curing time and w/b ratio (Figure 3-20b). Such decrease is maintained in limestone containing mixtures even at different w/b ratios compared to OPC.

Sulfate attack and carbonation

According to Irassar (2009), the risk of external sulfate attack of mixtures containing limestone filler is associated with the resistance to the ingress of sulfate ions, the same as in OPC samples. This means that the governing factor is the transport properties of concrete. Therefore, when a low proportion (< 15 wt%) of limestone is used, no significant changes occur in sulfate resistance mixes compared to OPC. On the other hand, a large proportion (> 15 wt%) can impair sulfate resistance (Irassar 2009). The reaction sequence in cement blends with limestone is essentially the same as in the case of OPC, with the main difference that, at later stages, thaumasite is formed from the decomposition of the ettringite first formed at ambient temperature. Schmidt et al. (2009) indicate that Portland cements containing a few percent of limestone show a better resistance against sulfate attack. The availability of aluminate hydrates and calcium hydroxide in the paste is similar to the samples with no limestone. However, at low levels of filler replacement, porosity is reduced, leading to a lower diffusivity and thus to a better resistance against sulfate attack.

Regarding carbonation, limestone-containing binary cements tend to slightly reduce the buffering capacity towards external subsequent carbonation (e.g. atmospheric carbonation) as a result of lower portlandite content (Matschei et al. 2007b). Dhir et al. (2007) reported a considerable negative impact of the addition of limestone on carbonation depth (Figure 3-21a). Lollini et al. (2014) also observed that higher degree of carbonation is obtained in Portland-limestone cement (PLC) systems compared to OPC. They reported more than double carbonation in specimens with 30 wt% of limestone additions compared to OPC at 28 days of hydration (Figure 3-21b). These results are comparable to the ones reported by Liu et al. (2016) for FA-containing cement samples (see Section 3.1.3).

Although the present literature review has not found related works on ternary PC-FA-L blends, it is expected that the combination of FA and limestone leads to materials with a reduced portlandite content and thus with higher sensitivity towards carbonation. Nonetheless, the reduced porosity from calcite formation could at least in part compensate the loss in buffering capacity.

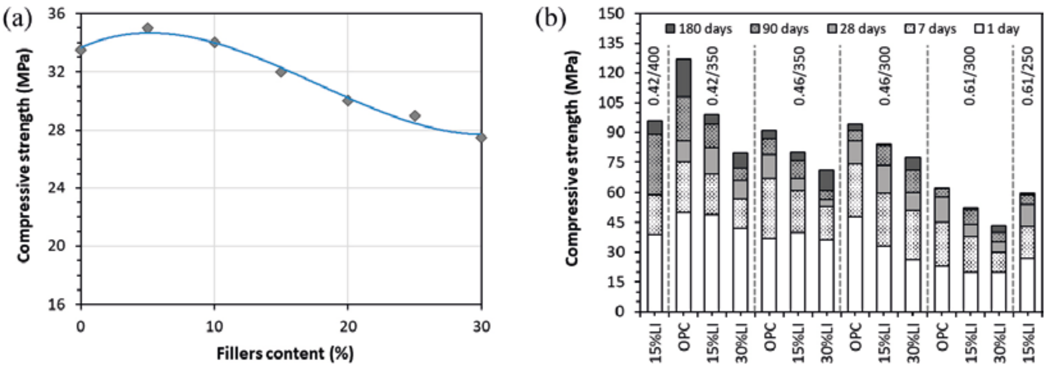

Figure 3-20. *(a) Compressive strength as a function of the limestone wt% replacement (adapted from Bederina et al. 2011). (b) Compressive strength of concrete as a function of curing time, w/b ratio, type of binder and binder dosage (e.g. 0.42/400 means w/b = 0.42 and b = 400 kg/m^3) (adapted from Lollini et al. 2014).*

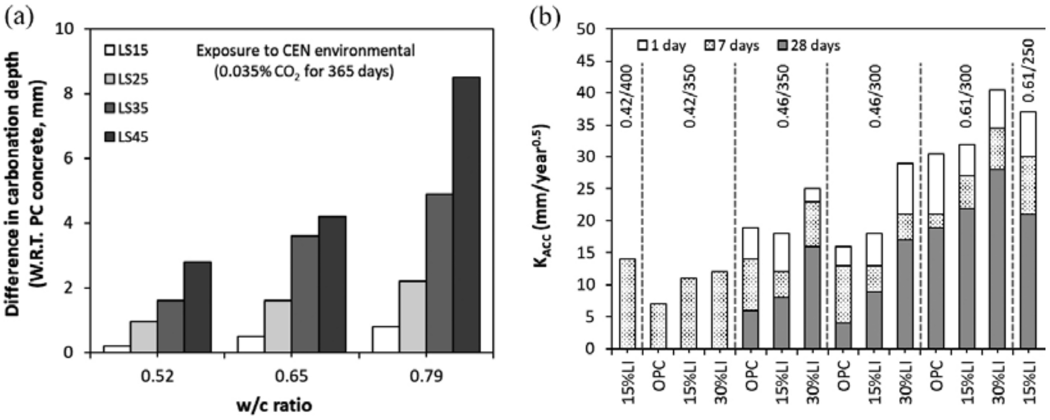

Figure 3-21. *(a) Carbonation resistance of OPC concretes with different levels of replacement by limestone at equivalent w/c ratio considering an exposure to 0.035 % CO_2 for 1 year (adapted from Dhir et al. 2007). (b) Accelerated carbonation coefficient of concrete (K_{ACC} accounting for carbonation depth from accelerated tests) as function of curing time, w/b ratio, type of binder and dosage: 0.42/400 means w/b = 0.42 and b = 400 kg/m^3 (adapted from Lollini et al. 2014).*

3.3 Effect of water-to-cement ratio on concrete properties

The concrete with w/c ratio of 0.63 has different mixing proportions to the previously modelled concretes for the BHK vault. To characterise its transport properties, a literature review is presented here that is based on referenced methodologies in previous SKB reports and recent experimental data as well as analytical models available.

3.3.1 Porosity

There is a large body of experimental data relating the w/c ratio of a concrete mix to its resulting porosity after hydration. However, this relation can be significantly affected by the concrete mix design: mass of water, cement, and aggregates, chemical composition of cement, or possible additions and additives. The focus here is on the effect of w/c ratio on porosity. To this end, a review of different available porosity models that use the w/c ratio as a parameter is presented below.

First, the semi-empirical model presented by Höglund (1992) for OPC is presented. The model is based on a set of equations to calculate the capillary (cap), gel (gel), and contraction (cont) porosity values:

$$\phi_{\text{cap}} = \frac{(w_0 - 0.39 \cdot \alpha \cdot c)}{\rho_{\text{water}}} \tag{3-1}$$

$$\phi_{\text{gel}} = 0.15 \cdot 0.90 \cdot \frac{\alpha \cdot c}{\rho_{\text{water}}} \tag{3-2}$$

$$\phi_{\text{cont}} = 0.0625 \cdot \frac{\alpha \cdot c}{\rho_{\text{water}}} \tag{3-3}$$

In the above equations, α is the degree of hydration, c the cement content (kg/m^3), w_0 the water content (kg/m^3), and ρ_{water} the density of water (kg/m^3). It is noted that the total capillary porosity is the sum of $\phi_{\text{cap}} + \phi_{\text{cont}}$. The density of the cement clinker is assumed to be 3100 kg/m^3. The parameter 0.39 is the minimum w_0/c ratio for complete hydration after Höglund (1992). The total porosity is given by:

$$\phi_{\text{tot}} = \phi_{\text{cap}} + \phi_{\text{gel}} + \phi_{\text{cont}} \tag{3-4}$$

The parameters used for the concrete mix from the 1BMA vault in the SFR repository presented e.g. in (Höglund 2001, 2014) are $w_0/c = 0.47$, $w_0 = 164.5$ kg/m^3, $c = 350$ kg/m^3. These values yield a total porosity of 0.0991 (similar to Höglund 2001) when $\alpha = 0.97$.

The second porosity model is the well-known Powers model (Powers 1960, Jensen and Hansen 2001b). This model for OPC cement pastes is based on a mass and volumetric balance of the components (water, hydrated phases and unhydrated binder) and calculates porosity as the sum of gel, capillary and chemical shrinkage contributions, yielding:

$$\phi_{\text{tot}} = \frac{\frac{w}{c}}{\frac{w}{c} + 0.32} - 0.53 \cdot \alpha \cdot (1 - \frac{\frac{w}{c}}{\frac{w}{c} + 0.32}) \tag{3-5}$$

This model results in a porosity of 0.38 for a hardened cement paste with a w/c ratio of 0.47 and considering full hydration ($\alpha = 1$). This results in a value of 0.1132 for the studied concrete mix (see Equation 4-14).

The third model is based on volume differences between reactants and reaction products (Lothenbach et al. 2010b) and the hydration model presented by Höglund (1992). The hydration model is based on a set of predefined chemical reactions with sequential corrections to calculate the volume of hydrates from the unhydrated cement composition (clinker phases). This approach uses as input the aggregate and unhydrated cement volume in the mixture. Porosity is evaluated as the empty volume left considering aggregates and unhydrated and hydrated cement phases. Thus, this third model is more complete in the sense that it accounts for a higher number of parameters (aggregates and unhydrated clinker volumes, see Equation 3-6).

$$\phi_{\text{tot}} = \frac{V_{\text{clinker},0} + V_{\text{water},0} - V_{\text{clinker},h} - V_{\text{hydrates},h}}{V_{\text{clinker},0} + V_{\text{water},0} + V_{\text{aggregate}}} \qquad (3\text{-}6)$$

First, the hydration model is used to calculate the volume of hydrates from the concrete mix (using the Degerhamn Anläggningscement presented in Chapter 4 and previously by Höglund 2001). Porosity is simply the difference between total and solid volume fractions. The results of the hydration model are presented in Table 3-5. The resulting porosity is 0.105.

Porosity values resulting from the three models presented above are summarised in Table 3-4 for comparison purposes. A relatively good agreement is found between the three models.

Table 3-4. Summary of porosity values (m^3/m^3) for an OPC concrete with w/c = 0.47, as obtained with different models, and comparison with previously reported values. Total capillary porosity is the sum of capillary and contraction pores.

Model for estimating porosity	Modelled results*
Capillary pores	0.032 (0.03)
Gel pores	0.046 (0.047)
Contraction pores	0.021 (0.022)
Total porosity	0.099 (0.099)
Powers model	**0.113**
Volume difference model	**0.105**

* In parentheses, the values reported by Höglund (2014).

Table 3-5. Results of the hydration model presented by Höglund (1992) in terms of cement hydrates. Composition of OPC before and after hydration. Values in parentheses extracted from Höglund (2014).

Clinker composition (wt%)		Hydrated products (mol/L porewater)		
C_3S	64.4	C_3FH_6	1.0184	(1.020)
C_2S	10.9	C_3AH_6	0.2422	(0.2424)
C_3A	2.5	Monosulfoaluminate	0.9714	(0.9722)
C_4AF	13.9	Ettringite	0	(0)
$C\hat{S}H_2$	3.7	C-S-H1.8	12.3573	(12.39)
$CaCO_3$	0.9	Portlandite	10.4382	(10.48)
		Brucite	0.6140	(0.6149)
		Calcite	0.31791	(0.6367)

The relation between w/c ratio and porosity as calculated with the models presented above is plotted in Figure 3-22. Porosity is calculated using the three different cement contents (280, 320, and 350 kg/m^3). The volume differences model (third model) is used to calculate porosity for w/c ratios of 0.47 (Table 3-4) and 0.63 for due to the fact that the hydration model (Höglund 1992) needs to be calculated on a case-by-case basis. Calculations related with the concrete mixes with w/c = 0.63 can be found in Appendix D.

A nearly linear relation can be observed in Figure 3-22 for w/c ratios higher than 0.4. The calculations consider a degree of hydration equal to 1. The different models yield comparable values, although at high w/c ratio (0.63) the volume differences model predicts a lower porosity compared to the other two models. This may be due to a larger volume of hydrates in this case compared to what is assumed in the semi-empirical models.

3.3.2 Permeability

Numerous studies about the impact of water-to-cement ratio on cement paste and concrete permeability can be found in the literature (Ahmad et al. 2012, Nokken and Hooton 2008, Halamickova et al. 1995, Lagerblad and Trägårdh 1995). The common trend between these different studies is the increase of permeability with an increase in w/c ratio. However, a significant dispersion can be observed in the results when comparing different sources. This is due to the different experimental conditions considered in each study, the different setups to measure permeability, and the different materials (cement paste or concrete, mineral additions, etc). The compilation of recent experimental data presented below relating permeability of concrete to w/c ratio is based on the studies presented by Nokken and Hooton (2008) and Ahmad et al. (2012). Using an exponential type fitting curve on the average values, a concrete with w/c ratio of 0.63 should be around 1×10^{-11} m/s (Figure 3-23).

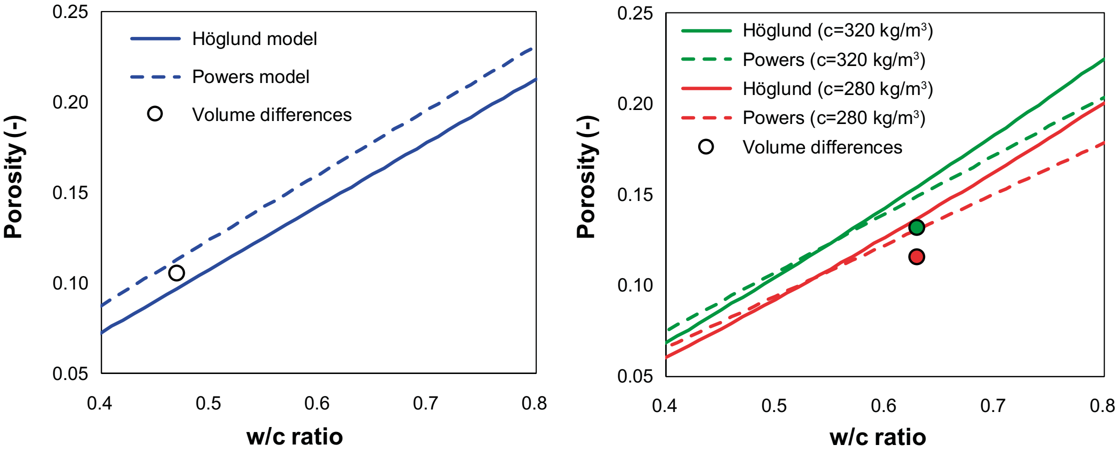

Figure 3-22. *Porosity (-) as a function of w/c ratio for concrete mixes with different cement contents as calculated with three different models.*

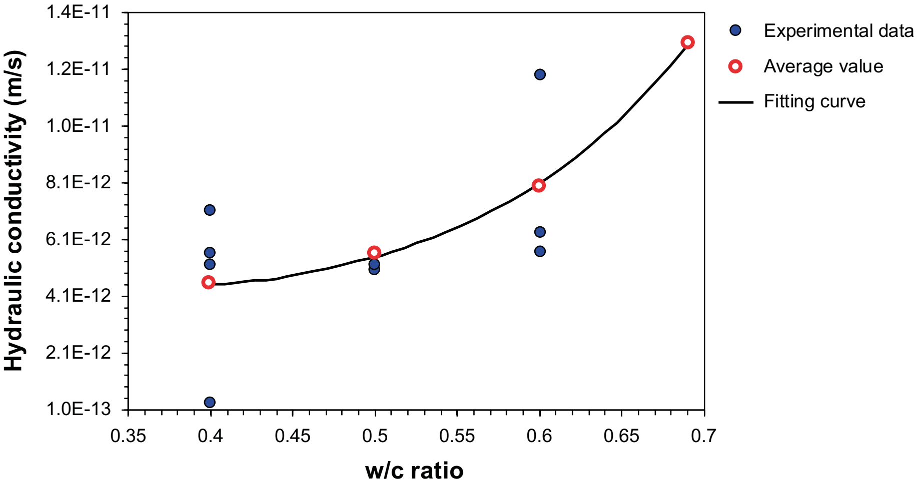

Figure 3-23. *Hydraulic conductivity (m/s) as a function of w/c ratio: experimental data from Nokken and Hooton (2008) and Ahmad et al. (2012) and curve fitting (this work).*

This value is close to that defined for intact concrete (1 × 10^{-11} m/s) in previous SKB reports (Höglund and Bengtsson 1991). Modelled values for the BHK vault take into consideration the effect of traversing fractures in the concrete structure from the beginning, yielding an initial value of 8.30 × 10^{-10} m/s. The formulation used to calculate the hydraulic conductivity of the fractured concrete is detailed elsewhere (Höglund 2014). This formulation is sensitive to the presence of fractures due to their very high hydraulic conductivity (1.0 × 10^{-5} m/s or higher) compared to intact concrete. This fact reduces the impact of the hydraulic conductivity of intact concrete to the value of fractured concrete. The hydraulic conductivity value considered at present by SKB for intact concrete is 1 × 10^{-11} m/s.

3.3.3 Effective diffusion coefficient

In general, the effect of increasing the w/c ratio of cementitious materials is an increase in the effective diffusion coefficient (Patel et al. 2016). Reviewed experimental data are based on the works of Larbi et al. (2016), Spiesz and Browers (2013), and Yeih et al. (1994); all of them showing an increase in diffusion coefficient with increasing w/c ratio. Irassar et al. (2001) also determined the apparent chloride diffusion coefficient from immersion tests of concrete samples for different w/c ratios. The diffusion coefficient values for w/c ratios of 0.4, 0.5, and 0.6 were 5.0 × 10^{-12}, 6.9 × 10^{-12}, and 25.7 × 10^{-12} m^2/s, respectively. This means an increase of 3.7 times when increasing the w/c ratio from 0.5 to 0.6. Larbi et al. (2016) measured the effective diffusion coefficient of tritiated water (used as conservative tracer) in cement mortars with a sand volume fraction of 50 % and different w/c ratios. The effective diffusion coefficient values for w/c ratios of 0.3, 0.35, 0.4, and 0.5 were 7.21 × 10^{-13}, 1.50 × 10^{-12}, 1.45 × 10^{-12}, and 2.68 × 10^{-12} m^2/s, respectively. This means an increase of 1.84 times when increasing the w/c ratio from 0.4 to 0.5.

The recent review of diffusivity experimental data carried out by Patel et al. (2016) confirm these findings. They compiled experimental data on hardened cement pastes, mortar, and concrete for different w/c ratios measured by different techniques. Clear trends between diffusivity and w/c ratio were determined, fitted using an exponential law. For example, fitting of the data obtained on cement pastes using the through-diffusion technique show an increase from 3.3 × 10^{-12} to 1.2 × 10^{-11} m^2/s (assuming a diffusivity in free solution of 1 × 10^{-9} m^2/s) for an increase of the w/c ratio from 0.47 to 0.63, i.e. an increase of 3.6 times. For mortar and concrete, relatively larger scatter of experimental data as compared to cement paste is observed. This scatter, more significant at low w/c ratios was attributed to differences in cement compositions, curing, maturity and experimental protocols and techniques (Patel et al. 2016).

An interesting study is the compilation of diffusion coefficients by Deby et al. (2009). They proposed a simple expression to fit a set of 40 experimentally determined chloride diffusion coefficients as a function of porosity of cement paste (Figure 3-24).

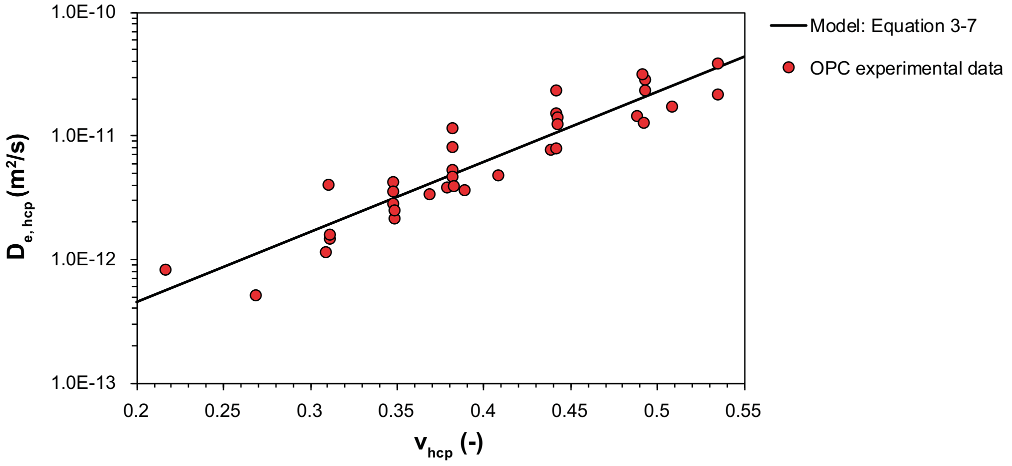

Figure 3-24. *Effective diffusion coefficient (m^2/s) of cement paste as a function of porosity: experimental data for OPC (see references in Deby et al. 2009) and empirical Equation 3-7 (adapted from Deby et al. 2009).*

This empirical relation reads

$$D_{\mathrm{e,hcp}} = e^{13\phi_{\mathrm{hcp}} - 31} \tag{3-7}$$

where $D_{\mathrm{e,hcp}}$ and ϕ_{hcp} are the effective diffusion coefficient and porosity of hardened cement paste, respectively. Deby (2008) calculated porosity as a function of the w/c ratio (see also Section 3.3.1) of each sample using the well-known Powers model (e.g. Taylor 1997):

$$\phi_{\mathrm{hcp}} = \frac{w/c}{w/c\ + 0.32} - 0.53[1 - exp(-3.3 \cdot w/c\,)]\left(1 - \frac{w/c}{w/c + 0.32}\right) \tag{3-8}$$

They furthermore calculated the diffusion coefficient of concrete from the cement paste value (assuming a non-diffusive ballast) and the relation previously proposed by Bruggeman (1935):

$$D_{\mathrm{e,conc}} = D_{\mathrm{e,hcp}} \mathrm{v}_{\mathrm{hcp}}^{3/2} \tag{3-9}$$

where v_{hcp} (-) is the solid volume fraction of hardened cement paste. It is noted that other researchers have found that the exponent in Equation 3-9 is much closer to 1 than to 3/2, resulting in a linear relation between diffusivity and ballast content (Larbi et al. 2016, Patel et al. 2016).

Plugging in Equations 3-7 and 3-8 into Equation 3-9, an expression of the diffusion coefficient of concrete as a function of w/c ratio and aggregate volume fraction $(1 - v_{\mathrm{hcp}})$ is obtained. This expression is plotted in Figure 3-25 considering an aggregate volume fraction of 0.7 $\mathrm{m}^3/\mathrm{m}^3$ of concrete, which is a typical value for concrete. This empirical function agrees well not only with the experiments reported by Deby et al. (2009), but also with more recent available experimental data compiled as part of the present study (Yeih et al. 1994, Irassar et al. 2001, Spiesz and Brouwers 2013, Kim et al. 2014, Larbi et al. 2016). Following the approach by Spiesz and Brouwers (2013), the data from Irassar et al. (2001) has been transformed into effective diffusivity by multiplying by concrete porosity and assuming a retardation factor of 1. Concrete porosity is estimated from w/c ratio using Equation 3-8 and an aggregate volume fraction (assumed to be non-porous) of 0.7. In turn, the results of Kim et al. (2014) are also multiplied by concrete porosity (reported in the paper) to obtain the effective diffusivity.

The value of the effective diffusivity for a w/c ratio of 0.6 given by this empirical function is approximately 3.5×10^{-12} m^2/s. This value is only slightly higher than the one used in previous studies (Höglund 2014, Idiart and Shafei 2019) for an intact concrete with a w/c ratio of 0.47, i.e. 3×10^{-12} m^2/s. Höglund (2014) proposed a simple model to account for the effect of traversing fractures and calculated a value of 3.5×10^{-12} m^2/s for concrete with one traversing fracture per metre with an aperture of 10 microns.

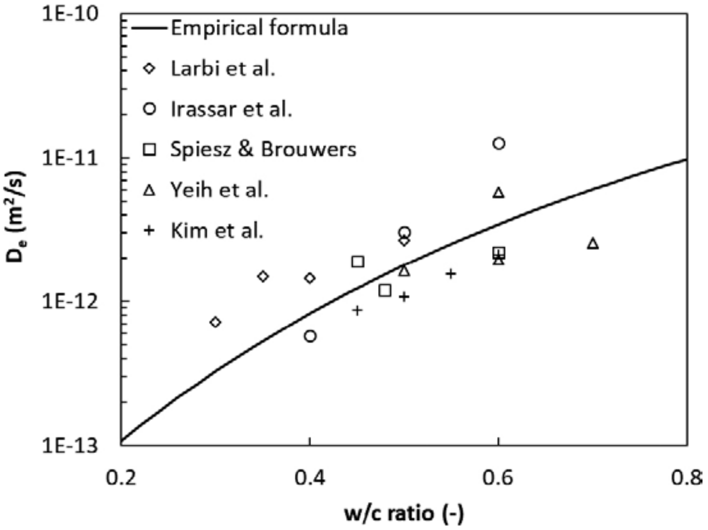

Figure 3-25. *Effective diffusion coefficient (m^2/s) of cement paste as a function of w/c ratio: experimental data from Larbi et al. (2016), Irassar et al. (2001), Yeih et al. (1994), Spiesz and Brouwers (2013) and Kim et al. (2014), and empirical formula by Deby et al. (2009).*

In previous studies by SKB (Höglund and Bengtsson 1991), the effective diffusion coefficient of concrete was characterised by the following equation:

$$D_e = \phi \cdot D_0 \cdot \delta_d / \tau^2 \tag{3-10}$$

where ϕ is the porosity (-), D_0 (m^2/s) the diffusivity in unconfined water, δ_d (-) is a constrictivity factor describing the number of narrow passages in the pore structure, and τ (-) is a tortuosity factor. Höglund and Bengtsson (1991) assumed a porosity of 0.15, a value of δ_d/τ^2 of 0.01, and $D_0 = 2 \times 10^{-9}$ m^2/s, resulting in an effective diffusion coefficient of 3×10^{-12} m^2/s for intact concrete. However, the w/c ratio is not specified in that work.

In 2000 and 2011, two inspections of the concrete structures of the SFR repository were undertaken (see Höglund 2014 and references therein). Based on the fractures data from the inspections and the model presented by Höglund (2014) to account for the effect of traversing fractures on diffusivity, an overall effective diffusivity of the concrete walls in 1BMA between 3.14 and 3.5×10^{-12} m^2/s was found (assuming that intact concrete has a D_e of 3×10^{-12} m^2/s).

The experimental data and calculated values of the effective diffusion coefficient for different w/c ratios presented above show a relatively large dispersion. This analysis seems to indicate that the value of 3.0×10^{-12} m^2/s used so far for an intact concrete with a w/c ratio of 0.47 may also be suited for a w/c ratio of 0.63.

3.4 Conclusions

Table 3-6 provides a summary of the impact of fly ash addition, when used at moderate levels of replacement, on the properties and durability performance of concrete. For comparison, the effects of adding limestone to cementitious systems (with or without FA) are also included to highlight the most remarkable differences expected between cement compositions.

Overall, the effect of increasing the water-to-cement ratio of an OPC mix is to increase porosity and decrease the amount of cement hydrates per unit volume of concrete. As a result of the more porous microstructure, the hydraulic conductivity and effective diffusivity are also increased. Consequently, durability of mixes with high w/c ratios is lower.

Table 3-6. Summary of the impact of fly ash addition (moderate levels of replacement) and limestone on the properties and durability performance of concrete.

Property / Parameter	Effect of siliceous fly ash addition on PC	Effect of limestone addition on PC and PC-FA
Rheological properties and water demand	Improved workability and reduced water demand	Effect related to particle size distribution
Water segregation (bleeding)	Reduced rate and amount of bleeding	Effect related to particle size distribution
Shrinkage	Reduced plastic, drying and autogenous (at w/c ratio approx. > 0.4) shrinkage; increased chemical shrinkage	Slightly increases chemical shrinkage on PC-FA systems. No significant influence on PC
Setting time	Extended setting time and delayed initial and final set of concrete	Limestone powder accelerates PC setting time and mitigates the excessive setting time delays produced in PC-FA cement blends
Heat of hydration	Lowered maximum heat dissipation rate and total amount of heat evolved	Limestone amplifies the maximum heat dissipation rate and the total amount of heat evolved in binary and ternary blends
Portlandite content	Decreased portlandite content in the long term compared to OPC	No significant changes in PC or PC-FA cements
Bound water	Increased bound water	Increased bound water
Hydration products	− Increased formation of more polymerised C-S-H gels with low Ca/Si ratio − Higher A/S ratios: Al enters C-S-H forming C-A-S-H gels − Reduction of ettringite content in favour of AFm precipitation − Other Al-containing phases are stable: hydrogarnet phase at longer curing time and strätlingite at higher FA content	− Limestone stabilises AFm-CO_3 phases: hemicarbonate at early ages and monocarbonate at longer times. − Destabilization of AFm-SO_4 and promotion of ettringite − Formation of solid solutions from the partial replacement of hydroxyl anions by sulfate and carbonate
Pore solution	− Decreased Ca concentrations and pH after few days of hydration by pozzolanic reaction. − Decreased Na, K, and OH^- concentrations by C-S-H and C-A-S-H formation − Decreased sulfate conc. due to increased total Al_2O_3/SO_3 ratio − Increased Al and Si concentrations	− Significantly increased of sulfate concentration compared to PC and PC-FA blends due to changes in the sulfate-containing AFm and AFt phases − No relevant changes are noticed for other cations or pH
Compressive strength	Reduces early strength development and increases the long-term strength	− Increases compressive strength with ≤ 5 wt% limestone and decreases it above this value of replacement − Improves early strength development lacking in FA-bearing cement
Permeability and porosity	Reduces the permeability of concrete due to a refinement in the pore structure	Limestone addition up to 5 wt% reduces permeability and porosity due to a volume increase of hydrate phases. Higher additions have an opposite effect
Chloride penetration	Increase the resistance to chloride diffusion and reduces potential steel corrosion in reinforcements	Significant improvement of the resistance of fly ash concrete when limestone is added
Alkali-silica reaction (ASR)	Reduces the potential ASR in concrete and its potential expansion	No significant change reported
Sulfate attack	Increase the resistance to sulfate attack	Similar resistance against sulfate attack than OPC. Low level of replacement (≤ 5 wt%) can increase resistance to sulfate attack.
Carbonation	Fly ash increases the carbonation rate compared to OPC being more pronounced at higher levels of replacement	Limestone addition decreases the resistance to carbonation, but it is overweighed by a reduced permeability at low levels of replacement.

4 Thermodynamic modelling of cement hydration

Modelling of cement hydration from its fresh state towards hardened cement paste is a challenging task. Different methods and approaches have been proposed in the past and are currently used to determine the chemical composition of the material and its microstructure. A comprehensive review of models that simulate the development of cement paste microstructure during hydration is presented elsewhere (Thomas et al. 2011).

In this work, focus is on long-term performance of hardened concrete used as engineered barriers. In this context, the motivation of using a hydration model is to predict the mineral phase assemblage and porewater composition of the hardened material starting from a concrete mix design. Calculation of the development of the microstructure during hydration is thus not an essential feature in this work. If a different concrete mix is used, for example replacing part of the cement by a supplementary cementitious material or changing the water-to-cement ratio, the hydration model can be used to estimate the chemical composition of the hardened material.

Several models have been proposed in the past to estimate the mineral phase assemblage of the hardened material starting from the mix design (e.g. Jennings and Tennis 1994, Höglund 1992). These models provide concentrations of the main cement hydrates of the hardened material as a function of time and the composition of the cement clinker and w/c ratio. They are based on a pre-defined sequence of chemical reactions starting from clinker dissolution and ending up in formation of cement hydrates. However, these models do not solve these chemical reactions based on the law-of-mass-action, as in traditional geochemical simulators (Parkhurst and Appelo 2013). Consequently, they do not provide any information on the porewater composition.

More recent advances in thermodynamic modelling applied to cement science have significantly increased confidence in the prediction of cement hydration chemical processes. To this end, geochemical simulators, such as GEMS or PHREEQC can be used, coupled to cement-specific thermodynamic data. Reviews of recent advances in this field can be found elsewhere (Lothenbach et al. 2011, Damidot et al. 2011, Lothenbach et al. 2010a). For instance, Lothenbach et al. (2008b) studied the influence of temperature on cement hydration using thermodynamic modelling. Their results compared very well with experimental data of hydration experiments. The effects of supplementary cementitious materials (SCM) on cement hydration have also been addressed with thermodynamic modelling (e.g. Elakneswaran et al. 2016, De Weerdt et al. 2011, Lothenbach et al. 2011). An attempt to couple thermodynamic modelling of cement hydration to a microstructure development model has been proposed by Bullard et al. (2011).

The basic principle of thermodynamic modelling of cement hydration is to consider that the clinker phases and SCM dissolve under kinetically-controlled conditions when contacted with water. The formation of cement hydrates is generally much faster than the dissolution of the clinker. Therefore, precipitation reactions are considered under thermodynamic equilibrium conditions. The advantages of this approach are that not only the concentrations of cement hydrates are obtained, but also the porewater composition. Moreover, these models can be more easily adapted to variations in the cement mix design. Finally, the outcome of the model at a given hydration time can be directly used as input for reactive transport models of long-term performance of cementitious barriers, as in this work.

4.1 Conceptual models and numerical implementation

Different models can be found in the literature to quantify the dissolution rates of the clinker phases of unhydrated cement. The phenomenological approach developed by Parrot and Killoh (1984) is used in the present work, based on the extensive work performed by Lothenbach and co-workers on this topic (e.g. Lothenbach et al. 2008a, b, Lothenbach and Winnefeld 2006). With this approach, the dissolution of the four main clinker compounds (i.e. C_3S, C_2S, C_3A and C_4AF using cement chemistry notation) is described independently. The overall hydration degree is calculated from the degree of hydration of each clinker phase (α_i) and its mass fraction (f_i) as follows:

$$\alpha_t(\mathrm{hyd}) = f_{C_3S}\alpha_{C_3S} + f_{C_2S}\alpha_{C_2S} + f_{C_3A}\alpha_{C_3A} + f_{C_4AF}\alpha_{C_4AF} \tag{4-1}$$

The overall degree of hydration α_t(hyd) of cement – defined as the ratio of mineral reacted to its initial content – is assumed to be the sum of the degree of hydration of the single cement constituents. Based on X-ray measurements, Parrot and Killoh (1984) derived empirical expressions to explain the controlling rate of hydration of a single clinker compound. The dissolution rate at a given time is set as the minimum from a set of three rates corresponding to different mechanisms and defined as:

Nucleation and growth: $\mathrm{R_1} = \frac{\mathrm{K_1}}{\mathrm{N_1}}(1-\alpha_t)[-\ln(1-\alpha_t)]^{(1-\mathrm{N_1})}$ (4-2)

Diffusion: $\mathrm{R_2} = \frac{\mathrm{K_2}(1-\alpha_t)^{2/3}}{1-(1-\alpha_t)^{1/3}}$ (4-3)

Shell formation: $\mathrm{R_3} = \mathrm{K_3}(1-\alpha_t)^{\mathrm{N_3}}$ (4-4)

In these equations, the empirical parameters $\mathrm{K_i}$ and $\mathrm{N_i}$ are based on the work by Parrot and Killoh (1984) and optimised by Lothenbach et al. (2008b). The rate of hydration degree (days^{-1}) for a single clinker constituent is calculated as:

$$\mathrm{R_{hyd}} = \min(\mathrm{R_1},\mathrm{R_2},\mathrm{R_3}) \cdot \mathrm{f_{w/c}} \cdot \beta_{\mathrm{RH}} \cdot \frac{A}{A_0} \cdot e^{\frac{E_\mathrm{a}}{RT}\left(\frac{1}{T_0}-\frac{1}{T}\right)} \quad (4\text{-}5)$$

In the above equation, R is the universal gas constant (8.314 J·mol^{-1}·K^{-1}), T (K) and T_0 (293.15 K) are the absolute and reference temperatures, E_a (J/mol) is the activation energy, and A and A_0 (m^2/kg) are the surface area of the actual cement and a reference value, respectively. The value of A_0 is 385 m^2/kg (Dalziel and Gutteridge 1986), while the value of A for each cement type is given in Table 4-3. Finally, β_{RH} (-) is an empirical parameter that takes into account the influence of relative humidity (RH):

$$\beta_{\mathrm{RH}} = \left(\frac{\mathrm{RH}-0.55}{0.45}\right)^4 \quad (4\text{-}6)$$

In the present study, RH remains equal to 1 throughout the simulation and thus $\beta_{\mathrm{RH}} = 1$. The kinetics of hydration is strongly dependent upon the water-to-cement ratio (w/c). At advanced states of hydration, the lack of larger pores available for hydration products formation may lead to the cease of the process. Therefore, Parrot and Killoh (1984) included a function $\mathrm{f_{w/c}}$ that relates the influence of w/c ratio to the rate of hydration according to the following relation:

$$\mathrm{f_{w/c}} = \begin{cases} \left[1 + 3.333\left(H\frac{\mathrm{w}}{\mathrm{c}} - \alpha_t\right)\right]^4 & | \ \alpha_t > H\frac{\mathrm{w}}{\mathrm{c}} \\ 1 & | \ \text{otherwise} \end{cases} \quad (4\text{-}7)$$

In this equation, H stands for the critical degree of hydration of each clinker constituent (Table 4-1). The degree of hydration at a given time in days for each clinker phase is then expressed as:

$$\alpha_t = \alpha_{t-1} + \Delta t \ \mathrm{R}_{t-1} \quad (4\text{-}8)$$

The overall rate of cement hydration is then calculated by means of weighted averaging as shown in Equation 4-1.

Several hydration models have been developed and implemented in PHREEQC to account for different types of cement compositions and/or mixing conditions. In particular, the following hydration models are presented:

1. *Anläggningscement* (CEM I 42.5 N – SR 3 MH/LA) with a w/c ratio of 0.47.
2. *Anläggningscement* (CEM I 42.5 N – SR 3 MH/LA) with a w/c ratio of 0.63.
3. *Bascement Slite* (CEM II/A-V 52.5 N) with a w/c ratio of 0.47.
4. *Anläggningscement* (CEM I 42.5 N – SR 3 MH/LA) containing limestone and dolomite addition with w/c ratio of 0.49.

Free lime, alkali sulfates, and gypsum initially present in the unhydrated system have no kinetic constraints and their dissolution is defined from thermodynamic equilibrium with the porewater. Clinker minerals are uniformly and progressively dissolved as a function of time according to previously shown equations, releasing chemical species to the pore solution which give rise to precipitation/dissolution reactions of hydrated phases during the course of the hydration process.

Fly ash dissolution is also kinetically controlled. The reaction rate adopted in this study is obtained from the experimental study conducted by Ben Haha et al. (2010):

$$y = -15 + 10\ln(t + 4.5) \tag{4-9}$$

where y stands for the percentage of reacted FA (wt%) and t for time (in days). The composition of the hydrate assemblage was predicted based on the degree of reaction of the cement clinker phases together with that of fly ash as a function of time. It is noted that, all constituents of both the clinker phases and the fly ash are assumed to dissolve homogeneously.

The addition of limestone to the concrete mix is also studied here. Dissolution of limestone (calcite) is assumed under thermodynamic equilibrium.

Numerical calculations are performed at a constant temperature of 25 °C using PHREEQC v.3.3.3 (Parkhurst and Appelo 2013). The reactions described above for dissolution of the clinker phases are implemented as kinetic reactions, while cement hydrates are assumed to form under thermodynamic equilibrium. The thermodynamic database used in the simulations is a PHREEQC-compatible version of Cemdata07 (Lothenbach et al. 2008, Jacques 2009) with supplementary thermodynamic data (for more details, see Sections 4.1.1, 4.1.3 and 4.1.4) and using the extended Debye-Hückel model for ionic strength correction.

4.1.1 Cementitious initial phase composition

The list of parameters used to calculate the kinetics of dissolution of the individual clinker phases as a function of time are gathered in Table 4-1.

Table 4-1. Summary of parameters used in the calculations for the different clinker phase hydration after Parrot and Killoh (1984) and Lothenbach et al. (2008b).

Mechanisms	Parameter	Alite	Belite	Aluminate	Ferrite
Nucleation and growth	K_1	1.50	0.50	1.00	0.37
	N_1	0.70	1.00	0.85	0.70
Diffusion	K_2	0.05	0.02	0.04	0.015
Shell formation	K_3	1.10	0.70	1.00	0.40
	N_3	3.30	5.00	3.20	3.70
	H	2.00	1.55	1.80	1.65
	E_a (J/mol)	41570	20785	54040	34087

Two different cement compositions from the manufacturer CEMENTA are analysed, i.e. *Anläggningscement* – an ordinary Portland cement (CEM-I) and *Bascement Slite* – a blended Portland cement with addition of fly ash (CEMENTA 2015). Compositions of both types of cement as provided by the manufacturer are shown in Table 4-2. The fly ash chemical and crystalline composition is not provided by the manufacturer. Therefore, the composition of fly ash is obtained from De Weerdt et al. (2011), based on class F siliceous fly ash.

The calculated composition and parameters used as input data for modelling the hydration of the different cements is shown in Table 4-3. Note that the mineral composition of Bascement Slite was not fully provided by the manufacturer and thus it was calculated from Bogue's formulas (Bogue 1929). To obtain the initial clinker composition to be used as input data in the model, fly ash chemical composition was deduced from the total oxide cement composition assuming 12.3 % by mass replacement.

Table 4-2. Chemical and mineral composition (wt%) of Anläggningscement and Bascement Slite (data provided by manufacturer). Fly ash chemical and crystalline composition used in Bascement Slite as SCM addition (from De Weerdt et al. 2011).

Component	**Anläggningscement**	**Bascement Slite**	**Fly ash**
Nomenclature (weight%)	**CEM I 42.5 N – SR 3 MH/LA**	**CEM II/A-V 52.5 N**	**Class F siliceous FA**
CaO	64	56.3	6.3
SiO_2	21	23.5	50.0
Al_2O_3	3.5	6.4	23.9
Fe_2O_3	4.6	3.4	6.0
MgO	0.7	2.6	2.1
K_2O	0.62	1.2	1.36
Na_2O	0.07	0.3	0.58
SO_3	2.2	3.5	0.40
Cl	<0.1	<0.1	–
Free $CaCO_3$	0.9	–	–
C_3S	64.4	–	–
C_2S	10.9	–	–
C_3A	2.5	5.4	–
C_4AF	13.9	–	–
$C\hat{S}H_2$	3.7	–	–
$CaCO_3$+$C\hat{S}H_2$	4.6	4.8	–
Alkalis, N+K	0.7	1.1	–
Fly Ash	–	12.3	–
Quartz	–	–	12.3
Calcite	–	–	0.4
Hematite	–	–	0.6
Anhydrite	–	–	0.4
Mullite	–	–	18.3

Table 4-3. Initial cementitious composition and parameters used as input data for the hydration modelling (composition is given in mol/kgw).

Hydration model	**1**	**2**	**3**	**4**
Nomenclature (mol/kg_{water})	**Anläggningscement (w/c = 0.47)**	**Anläggningscement (w/c = 0.63)**	**Bascement Slite**	**Anläggningscement + Limestone/Dolomite**
C_3S	6.001	4.477	5.502	5.756
C_2S	1.347	1.005	0.644	1.292
C_3A	0.197$^{(a)}$	0.147	0.425	0.189
C_4AF	0.609	0.454	0.355	0.584
$K_2O^{(b)}$	0.136	0.101	0.149	0.130
$Na_2O^{(b)}$	0.022	0.016	0.049	0.021
$MgO^{(b)}$	0.369	0.276	1.236	0.355
$SO_3^{(b)}$	–	–	0.332	–
CaO	0.1910	0.1425	–	0.1832
$CaCO_3$	0.1913	0.1427	0.3751	0.1835
$CaSO_4 \cdot 2H_2O$	0.4572	0.3411	0.3751	0.4386
K_2SO_4	0.0042	0.0031	0.0824$^{(c)}$	0.0040
Na_2SO_4	0.0022	0.0017	0.0282$^{(c)}$	0.0022
$CaMg(CO_3)_2^{(d)}$	–	–	–	1.1517
FA	–	–	0.4432	–
Limestone (added)	–	–	–	8.2834
w/c ratio	0.47	0.63	0.47	0.32$^{(e)}$
T (K)	298	298	298	298
RH	1.00	1.00	1.00	1.00
Blaine surface (m^2/kg)$^{(f)}$	310	310	450	310

(a) Maximum value assumed to be close to 100 %. (b) Present in major clinker phases as minor constituents. (c) Included additional 3 wt% (after Taylor 1997) from alkali readily soluble in FA composition. (d) Main composition of Myanit10® product, manufactured from a crystalline dolomite in Sala, Sweden. (e) Limestone and dolomite additions assumed as binder (see Table 4-7). (f) Data from cement producers.

Alkali distribution

The alkali content in the mix is distributed within oxides present in the unhydrated clinker minerals and readily soluble sulfates. According to Taylor (1997), a certain specific percentage of the total Na_2O and K_2O content can be assumed to be readily soluble alkali sulfates (30 and 70 wt%, respectively). However, the amount of gypsum ($CaSO_4 \cdot 2H_2O$) in Anläggningscement, as provided by the manufacturer, is significantly high. Thus, only a small amount of SO_4 was assumed here to be initially present in K_2SO_4 and Na_2SO_4 for Anläggningscement (Table 4-2). Most of the alkali content was included as oxides, specifically distributed between the clinker phases according to Table 4-4. These oxides (Na_2O and K_2O, but also MgO and SO_3) are gradually released in solution during hydration, as clinker minerals dissolve (Equations 4-1 to 4-8).

Note that thermodynamic data of K_2SO_4 and Na_2SO_4 are missing in CEMDATA07 and therefore the equilibrium constants reported by Robie and Hemingway (1995) have been used instead, as included in the new version of CEMDATA (Lothenbach et al. 2018).

Table 4-4. Typical composition of minor constituents in Portland cement clinker (wt%), after Taylor (1997).

Clinker phase	Na_2O	K_2O	MgO	SO_3
Alite	0.1	0.1	1.1	0.1
Belite	0.1	0.9	0.5	0.2
Aluminate	1.0	0.7	1.4	0.0
Ferrite	0.1	0.2	3.0	0.0

4.1.2 Fly ash

The crystalline composition of the type F siliceous fly ash (FA) has been measured by De Weerdt et al. (2011) by means of XRD-Rietveld analysis. As shown in Table 4-2, mullite, quartz, hematite, calcite and anhydrite are present in FA. The composition of the (reactive) glass phase given in Table 4-5 was calculated by subtracting the oxides present in the crystalline phases of FA from the total amount of oxides present in the FA as determined by XRF (Table 4-2). From this composition, the stoichiometry of fly ash was then calculated, and the dissolution reaction was included in the model with an associated kinetic rate (Equation 4-9).

Table 4-5. Composition (in wt% and mol/kg_{water}) of reactive glass phase of the fly ash as obtained from XRD and XRF analyses by De Weerdt et al. (2011).

Nomenclature	Class F siliceous FA	
	wt%	mol/kg_{water}
CaO	5.91	0.443
SiO_2	34.04	2.383
Al_2O_3	9.26	0.382
Fe_2O_3	5.40	0.142
MgO	2.10	0.219
K_2O	1.36	0.061
Na_2O	0.58	0.039
SO_3	0.17	0.009

4.1.3 Cement with limestone and dolomite additions

Composition of this type of cement is based on CEM I 42.5 N with the addition of two commercially available products, i.e. *Omyacarb 2-GU* and *Myanit10* (Table 4-6). The former contains 98 wt% of $CaCO_3$ and the latter is constituted mainly by dolomite ($CaMg(CO_3)_2$).

Table 4-6. Compositions of the commercially available products added to Anläggningscement cement, as given by the manufacturers.

Myanit 10 oxides	Composition (wt%)	Omyacarb 2-GU oxides	Composition (wt%)
CaO	29.4	$CaCO_3$	98.0
MgO	21.0	Fe_2O_3	0.2
SiO_2	3.5	Insoluble	2.0
Fe_2O_3	0.5		
LOI*	44.3		

*LOI: loss of ignition (including CO_2 from carbonates).

Table 4-7 shows the binder composition of this type of cement in kg/m^3 and wt% contribution of each component to the total sum of binder. Note that in this case the water-to-binder ratio is 0.32. The initial composition shown in Table 4-3 was obtained from the chemical composition and mass fraction of each material. A total calcite composition was assumed for Omyacarb 2-GU and added to the $CaCO_3$ content from the clinker phases. In turn, a pure dolomite composition was assumed for Myanit10 due to its low silica and hematite content. Dolomite was included as an initial phase in equilibrium with the pore solution. The equilibrium constant for $CaMg(CO_3)_2$ is not included in CEMDATA and thus the value by Robie and Hemingway (1995) was used (see Appendix B).

Table 4-7. Binder composition in kg/m^3 and wt% from the manufacturer. Note that the quantity of additives was not included in the calculations and thus excluded from the binder.

Binder component	Composition	
	kg/m^3	wt%
Cement (clinker)	320.0	66.2
Omyacarb 2-GU	130.0	26.9$^{(a)}$
Myanit 10	33.3	6.9$^{(b)}$
Additives	3.96	–
Sum binder	483.3	100.0

(a) Considered as $CaCO_3$ in the calculations.
(b) Considered as $CaMg(CO_3)_2$ in the calculations.

4.1.4 Selected phase assemblage

The most common hydrates for an Ordinary Portland Cement are C-S-H phases of different Ca/Si ratios, portlandite (CH), ettringite (AFt-SO_4), monosulfoaluminate (AFm-SO_4), and hydrogarnet (HG), see also Sections 3.1.2 and 3.2.2. Depending on the curing time, unreacted clinker phases are generally also present.

As mentioned in Section 3.1.2, blending cements with supplementary cementitiuos materials (SCM) normally leads to a decrease of the amount of portlandite and the formation of lower C/S ratio C-S-H gels (Lothenbach et al. 2011, Massazza 1993, Fajun et al. 1985). If the additions include high amounts of Al as in the case of fly ash, this favours the formation of Al-containing phases such as strätlingite and hydrogarnet among other hydrated calcium aluminates. A certain amount of Al is also incorporated into C-S-H structures forming the so-called C-A-S-H phases (L'Hôpital et al. 2015, García-Lodeiro et al. 2011). They correspond to solid solutions with a compositional range of $0.72 < CaO/SiO_2 < 1.94$ and $0 < Al_2O_3/SiO_2 < 0.1$, being compatible with portlandite, AFm-type phases, carboaluminates and strätlingite with varying CaO/SiO_2 and Al_2O_3/SiO_2 ratios (García-Lodeiro et al. 2011).

There is little information in the literature concerning what kind of hydrate structures that might form in Portland cement – dolomite – limestone mixtures. In a system containing dolomite (i.e. Myanit 10), a higher magnesium content is expected to favour the precipitation of hydrotalcite-like structures. Under certain conditions, Mg may also partially substitute calcium in C-S-H phases, forming the so-called M-S-H phases (Nocuń-Wczelik et al. 2013). A solid solution model of M-S-H with two end-members is used in the hydration models to account for the potential formation of these phases of variable Mg/Si ratio. To this end, the equilibrium constants reported by Nied et al. (2016) have been included in the thermodynamic database.

Based on the chemical composition, Table 4-8 comprises the total set of minerals allowed to precipitate and dissolve as equilibrium phases and solid solutions during the hydration process for the different cement type or conditions modelled in the present study.

A total of nine (9) solid solutions are used in the models in an attempt to reproduce the study carried out by Lothenbach and co-workers (Lothenbach et al. 2008b, 2006). This is the case of:

- C-S-H phases with two concurrent solid solution systems, i.e. CSH-I, with the end-members SiO_2(am) and tobermorite-I and CSH-II, with the end-members jennite and tobermorite-II;
- AFt solid solution with three end-members, i.e. ettringite, tricarboaluminate and Fe-ettringite;
- AFm-OH-SO_4 solid solution with eight end-members, including strätlingite and monosulfoaluminate (not included in the model with limestone and dolomite additions since it is not expected to form in this system).
- AFm-monocarbo, AFm-hemicarbo and Hydrogarnet solid solutions, with two end-members each, to account for both Al and Fe content.
- In the case of blended cement with FA a C(A)SH-II solid solution model of four end-members is proposed, following the work by Elakneswaran et al. (2016) and De Weerdt et al. (2011). To this end, two end-members with CaO/SiO_2 ratios of 0.125 and 0.85 and Al_2O_3/SiO_2 ratio of ~0.13 were included in the CSH-II(ss) model (ss stands for solid solution hereafter).
- For OPC containing additions of limestone and dolomite, an MSH solid solution is used with two end-members with MgO/SiO_2 ratios of 1.50 and 0.75 (Table 4-8).

Table 4-8. Set of selected phases allowed to precipitate in the models of cement hydration. Solid solutions are defined by two or more end-members after the models proposed by Lothenbach and Winnefeld (2006). Thermodynamic database: CEMDATA07 (the source of thermodynamic data missing in the employed version is provided at the footnote).

Hydration model		**1–2**	**3**	**4**
		Anläggningscement (w/c ratio 0.47 and 0.63)	**Bascement Slite**	**Anläggningscement (with Limestone and Dolomite)**
Equilibrium phases	**Chemical formula**			
Portlandite	$Ca(OH)_2$	✓	✓	✓
Brucite	$Mg(OH)_2$	✓	✓	✓
Hydrotalcite OH	$Mg_4Al_2(OH)_{14} \cdot 3H_2O$	✓	✓	✓
Hydrotalcite C	$Mg_4Al_2(OH)_{12}CO_3 \cdot 3H_2O$	✓	✓	✓
Syngenite	$K_2Ca(SO_4)_2 \cdot H_2O$	✓	✓	✓
CAH_{10}	$CaAl_2(OH)_8 \cdot 6H_2O$	✓	✓	✓
Gibbsite (am)	$Al(OH)_3$	✓	✓	✓
Ferrihydrite (mic)	$Fe(OH)_3$	✓	✓	✓
Solid Solutions	**End-member formula**			
CSH-I		✓	✓	✓
SiO_2 (am)	SiO_2			
CSHtob1	$(CaO)_2(SiO_2)_{2.4}(H_2O)_{3.2}$			
CSH-II		✓	✗	✓
C-S-H jennite	$(CaO)_{1.67}(SiO_2)(H_2O)_{2.1}$			
C-S-H tobermorite	$(CaO)_{0.83}(SiO_2)(H_2O)_{1.3}$			
AFt		✓	✓	✓
Ettringite	$Ca_6Al_2(SO_4)_3(OH)_{12} \cdot 26H_2O$			
Tricarboaluminate	$Ca_6Al_2(CO_3)_3(OH)_{12} \cdot 26H_2O$			
Fe-ettringite	$Ca_6Fe_2(SO_4)_3(OH)_{12} \cdot 26H_2O$			
AFm-OH-SO$_4$		✓	✓	✗(c)
C_4AH_{13}	$Ca_4Al_2(OH)_{14} \cdot 6H_2O$			
C_4FH_{13}	$Ca_4Fe_2(OH)_{14} \cdot 6H_2O$			
C_2AH_8	$Ca_2Al_2(OH)_{10} \cdot 3H_2O$			
C_2FH_8	$Ca_2Fe_2(OH)_{10} \cdot 3H_2O$			
Strätlingite	$Ca_2Al_2SiO_2(OH)_{10} \cdot 3H_2O$			
Fe-strätlingite	$Ca_2Fe_2SiO_2(OH)_{10} \cdot 3H_2O$			
Monosulfoaluminate	$Ca_4Al_2(SO_4)(OH)_{12} \cdot 6H_2O$			
Fe-monosulfate	$Ca_4Fe_2(SO_4)(OH)_{12} \cdot 6H_2O$			
AFm-monocarbo		✓	✓	✓
Monocarboaluminate	$Ca_4Al_2(CO_3)(OH)_{12} \cdot 5H_2O$			
Fe-monocarbonate	$Ca_4Fe_2(CO_3)(OH)_{12} \cdot 5H_2O$			
AFm-hemicarbo		✓	✗	✗
Hemicarboaluminate	$Ca_4Al_2(CO_3)_{0.5}(OH)_{13} \cdot 5.5H_2O$			
Fe-hemicarbonate	$Ca_4Fe_2(CO_3)_{0.5}(OH)_{13} \cdot 5.5H_2O$			
Hydrogarnet		✓	✓	✗
Hydrogarnet OH	$Ca_3Al_2(OH)_{12}$			
Hydrogarnet Fe	$Ca_3Fe_2(OH)_{12}$			
C(A)SH-II(a)		✗	✓	✗
C-S-H jennite(d)	$(CaO)_{1.67}(SiO_2)(H_2O)_{2.1}$			
C-S-H tobermorite(d)	$(CaO)_{0.83}(SiO_2)(H_2O)_{1.3}$			
C-A-S-H 1.25	$(CaO)_{1.25}(Al_2O_3)_{0.125}(SiO_2)(H_2O)_{1.63}$			
C-A-S-H_0.84	$(CaO)(Al_2O_3)_{0.156}(SiO_2)_{1.188}(H_2O)_{1.67}$			
MSH(b)		✗	✗	✓
MSH1.5	$(MgO)_{1.5}(SiO_2)(H_2O)_{1.5}$			
MSH0.75	$(MgO)_{0.75}(SiO_2)(H_2O)_{0.75}$			

(a) Data from Myers et al. (2014) and reported in Elakneswaran et al. (2016).

(b) Data from Nied et al. (2016) and included in CEMDATA18.

(c) Solid solution not included in the hydration model 4 since it is not expected to form in this system.

(d) C-S-H jennite and C-S-H tobermorite correspond to CSHjen and CSHtob2 in CEMDATA07.

4.1.5 Alkali uptake approach

As stated in Chapter 3, alkalis can be incorporated into the C-S-H structure. The alkali retention within the precipitating C-S-H/C-A-S-H gels during cement hydration is modelled here by means of cation exchange processes between Ca^{2+} and K^+/Na^+ as shown in Table 4-9. Modelling of alkali uptake in cement paste by cation exchange reactions has been already proposed in the past by other researchers (Savage et al. 2011, Höglund 2001). As much as possible, the experimental results reported by Vollpracht et al. (2016) have been used as a data source for calibration purposes. The selectivity coefficients reported in Savage et al. (2011) have been modified accordingly to obtain realistic values of pH and Ca concentration, representative of an OPC which can be used later in the reactive transport models.

Table 4-9. Cation exchange selectivity coefficients (log *K*) used in the models to represent alkali uptake. Modified from Savage et al. (2011).

Reaction	log *K*
$2X^- + Ca^{2+} \rightleftharpoons X_2Ca$	0.0
$2X^- + 2K^+ \rightleftharpoons X_2K_2$	−2.6
$2X^- + 2Na^+ \rightleftharpoons X_2Na_2$	−1.8

Likewise, the cation exchange capacity (CEC) for each case was adapted to fit the experimental data, and corresponded to ~ 10 % of the total molar amount of C-S-H (plus C-A-S-H, when present) produced at the end of hydration (Table 4-10). It is worth noting that the CEC in each model is kinetically controlled (i.e. the CEC increases with time). In this way, the CEC is associated to the hydration of the clinker phases, to account for the increasing content of C-S-H/C-A-S-H gels in which alkalis are incorporated.

Table 4-10. Cation exchange capacity (CEC) adopted in the model to account for the alkali binding in the hydration models.

Hydration models	Description	CEC (mol/kg_{water})
1	Anläggningscement (w/c ratio 0.47)	0.717
2	Anläggningscement (w/c ratio 0.63)	0.534
3	Bascement Slite	0.823
4	Anläggningscement + limestone/dolomite	0.688

4.1.6 Porosity and concrete composition

Cement hydration not only defines the chemical composition of the hardened material, but also its physical properties. The results of the hydration models of cement paste in terms of mineral phase assemblage and water consumption can be used to calculate the total porosity as a function of time. These results can be used to calculate the porosity of concrete by considering the dilution effect of adding the aggregates to the mix. Concrete mixes for the different models are presented in Table 4-11. The volume fractions (V_F) of each mineral phase (i) in concrete (conc) is calculated from its respective value in the hardened cement paste (hcp) using the aggregates (aggr) volume fraction:

$$V_{Fi}^{\mathrm{conc}} = V_{Fi}^{\mathrm{hcp}} \cdot \left(1 - V_{F}^{\mathrm{aggr}}\right) \qquad (4\text{-}10)$$

The aggregates volume fraction is calculated with the data in Table 4-11 and is equal to 0.70 ± 0.03, depending on the concrete mix. The total porosity of hardened cement paste (ϕ_{hcp}) can be decomposed at any given time (t) as the sum of capillary (ϕ_{cap}), gel (ϕ_{gel}), and chemical shrinkage (ϕ_{ch}) porosities:

$$\phi_{\mathrm{hcp}}(t) = \phi_{\mathrm{cap}}(t) + \phi_{\mathrm{gel}}(t) + \phi_{\mathrm{ch}}(t) \qquad (4\text{-}11)$$

Total porosity is calculated using the following expression:

$$\phi_{\mathrm{hcp}}(t) = \frac{V_{\mathrm{binder,0}} + V_{\mathrm{water,0}} - V_{\mathrm{binder,h}} - V_{\mathrm{hydrates,h}}}{V_{\mathrm{binder,0}} + V_{\mathrm{water,0}} + V_{\mathrm{additives,0}}} \qquad (4\text{-}12)$$

where V_{water} (L) is the remaining water volume, V_{hydrates} (L) accounts for all the hydrated phases, and V_{binder} (L) corresponds to the volume of the unhydrated binder phases.

Gel porosity is calculated through the volumetric difference between the hydrated and dehydrated amorphous phases C-S-H and C-A-S-H (e.g. Lothenbach et al. 2008b), as predicted by the hydration model. Their molar volumes are listed in Table 4-12. C-S-H values are taken from Lothenbach et al. (2008b), while the molar volumes of C-A-S-H phases are assumed equal to those of C-S-H phases. The molar volumes of all minerals used in the calculations are listed in Appendix B.

Chemical shrinkage (ϕ_{ch}) is the result of the volumetric difference between the reactants (concrete mix before hydration) and the reaction products (concrete composition after hydration). ϕ_{ch} is then calculated as the difference between the total porosity (ϕ_{hcp}) and the volume fraction of the remaining evaporable water after hydration (ϕ_{w}):

$$\phi_{\text{ch}} = \phi_{\text{hcp}} - \phi_{\text{w}} \qquad (4\text{-}13)$$

Once the total, gel and chemical shrinkage porosities are known, capillary porosity is calculated from Equation 4-11. Analogously to Equation 4-10, concrete porosity is calculated (assuming a non-porous aggregate) as:

$$\phi_{conc}(t) = \phi_{hcp}(t) \cdot \left(1 - V_F^{aggr}\right) \qquad (4\text{-}14)$$

Table 4-11. Mixing proportions for concretes (see Table 2-1 for model description), amount given in kg/m³ of concrete, and density assumed for each material.

Component	Density (kg/m³)	Model 1	Model 2a	Model 2b	Model 3	Model 4
Cement	3100$^{(a)}$	350	320	280	307	320
Water	1000	164.5	201.6	176.4	164.5	156.8
Ballast	2600$^{(b)}$	1829	1807.5	1906.5	1829	1751.9
Additives	1120$^{(c)}$	3.087	3.087	3.087	3.087	3.96
Flyash	2490$^{(d)}$	–	–	–	43.05	–
Omyacarb 2-GU	2710$^{(e)}$	–	–	–	–	130
Myanit 10	2850$^{(f)}$	–	–	–	–	33.3
w/c ratio		0.47	0.63	0.63	0.54	0.49
w/b ratio		0.47	0.63	0.63	0.47	0.32

(a) From Höglund (1992), (b) assumed, (c) manufacturer data for Sika Plastiment BV-40, except for model 4, for which no information about additives is available (a value of 1.3 kg/m³ is assumed), (d) De Weerdt et al. (2011), (e) density of calcite, (f) from manufacturer (density of dolomite).

Table 4-12. Molar volumes (cm³/mol) of hydrated and dehydrated amorphous phases used to calculate mineral volumes and porosity. C-S-H values from Lothenbach et al. (2008b). C-A-S-H phases assumed equal to C-S-H phases.

State	C-S-H jennite	C-S-H tobermorite	C-A-S-H 1.25	C-A-S-H 0.84
Hydrated	102	77	102	77
Dehydrated	78	59	78	59

4.2 Results

This section presents the results of the 4 hydration models simulated. To verify the implementation of the modelling approach in PHREEQC, a benchmark case has been simulated and compared with the results of the hydration of an OPC mix presented by Lothenbach and Winnefeld (2006). This benchmark is presented and discussed in Appendix A.

4.2.1 Hydration models 1 and 2 (CEM-I 42.5 N – SR, w/c ratio 0.47 and 0.63)

Figure 4-1 shows a comparison of the evolution of alkalis concentration between experimental data from Vollpracht et al. (2016) and the hydration models 1 and 2 for similar ranges of total mass content (0.07 and 0.62 wt% of Na and K, respectively) and w/c ratios (note that data is compared to the closest w/c ratio reported, i.e. 0.50 and 0.60). Part of the alkalis are adsorbed onto C-S-H phases. However, the consumption of water during hydration, as well as the continuous release of Na and K present in the clinker phases, leads to a net increase in their concentration over time. Alkali concentration is dependent on the w/c ratio: the lower the w/c ratio, the higher the dissolved concentration.

Figure 4-2 compares the chemical aqueous composition obtained with the hydration models 1 and 2 with experimental data (Vollpracht et al. 2016). Figure 4-2a shows that the concentration of hydroxyl ions increases over time as a result of the rise in alkali dissolved content (Figure 4-1). Such increase is slightly lower in the case of the system with higher w/c ratio (0.63) because of the dilution effect, which is evidenced in the pH values as well (e.g. 13.34 vs. 13.30). Calcium fate also depends on the alkali concentration (controlling OH^- content) since its concentration is governed by portlandite solubility. In this way, Ca dissolved content is inversely proportional to OH^- concentrations, and therefore higher for w/c ratio 0.63 (Figure 4-2b). The evolution of sulfate is similar to Ca showing a steep drop in its concentration before one day of hydration due to gypsum total dissolution and AFt (ss) becoming its solubility-limiting phase (Figure 4-2c). A subsequent step in sulfate concentration is observed from approx. 10 days onwards when ettringite is depleted and AFm-OH-SO_4 (ss) governs its solubility in solution. Ca concentration decreases with increasing OH^- concentrations following a logarithmic trend to maintain equilibrium with portlandite and gypsum at early age, and only with portlandite at longer hydration times (Figure 4-2d).

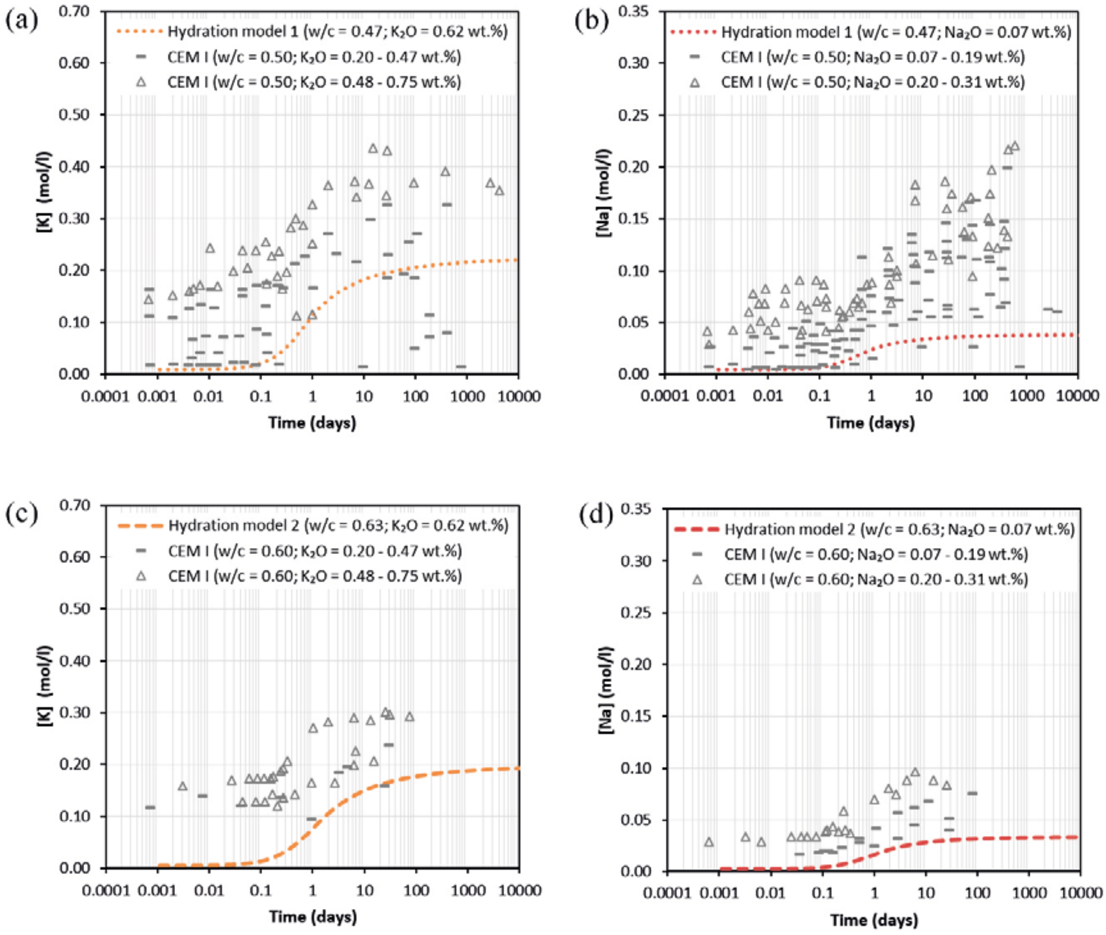

Figure 4-1. *Evolution of alkali concentration during hydration as a function of time for OPC pastes. Symbols stand for analysed concentration in the porewater depending on the total mass content (from Vollpracht et al. 2016). Lines stand for simulated results in the present study for Anläggningscement with w/c ratio 0.47 (a–b) and w/c ratio 0.63 (c–d).*

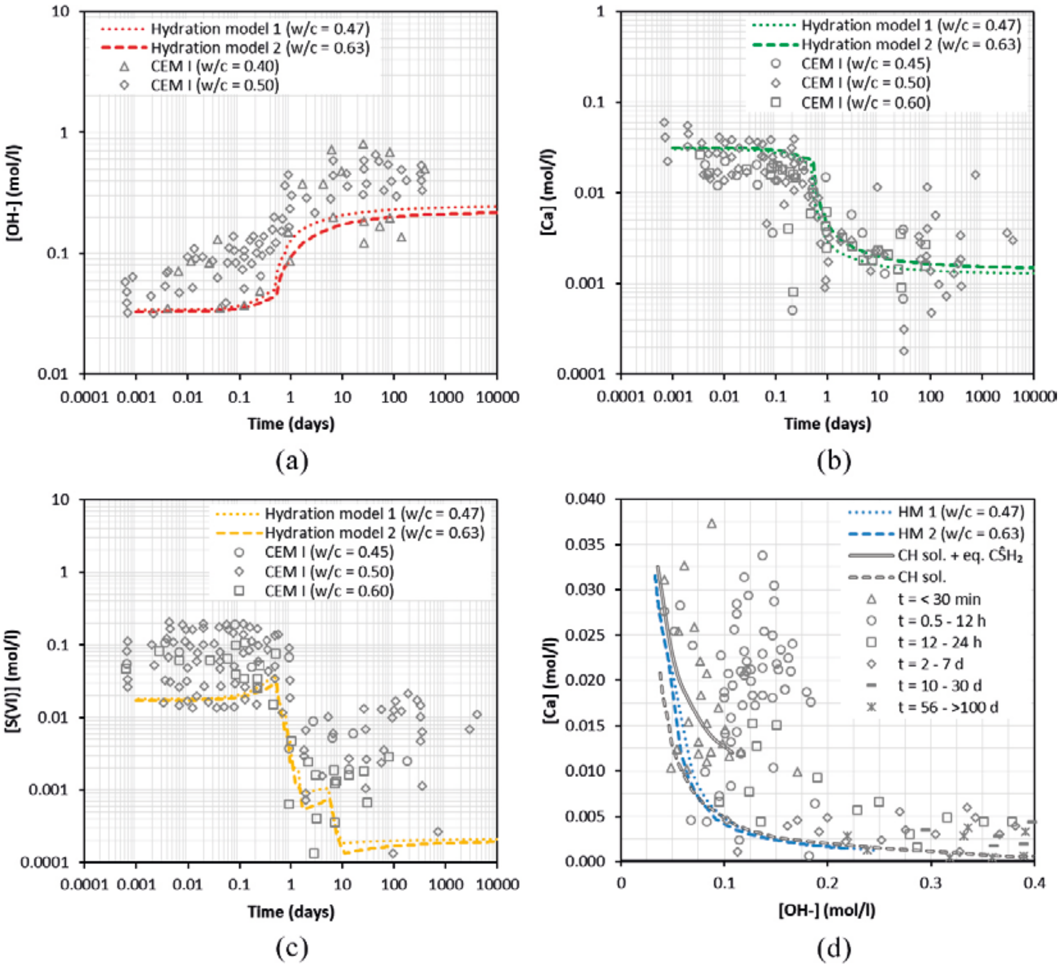

Figure 4-2. *(a–c) Evolution of hydroxyl ions, calcium and sulfate concentration along hydration time for OPC pastes. (d) Calcium concentrations as a function of* OH^- *concentration. Symbols stand for experimentally determined concentrations in the porewater at different hydration times and w/c ratios (from Vollpracht et al. 2016). Results of hydration model 1 (w/c ratio 0.47, dotted lines) and 2 (w/c ratio 0.63, dashed lines).*

The previously shown evolution of the pore solution reflects the changes occurred in the phase assemblage. The results of the hydration model 1 (w/c = 0.47) in terms of the evolution of solid phases are presented in Figure 4-3 and Figure 4-4. Figure 4-5 and Figure 4-6 present the solid phases of the hydration model 2 (w/c = 0.63). During the first instants of cement hydration, there is an oversaturation of gypsum, portlandite, ettringite, C-S-H phases and calcite. Upon further hydration, ettringite destabilises to give rise to monosulfoaluminate (as chief end-member of AFm-OH-SO_4 solid solution) and hydrogarnet(ss). Towards the end of the simulation (e.g. 10 000 days), stable phases/solid solutions are portlandite, CSH-II(ss), AFm-OH-SO_4(ss), hydrogarnet(ss), AFm-monocarbo(ss) and hydrotalcite-OH. In general, these model results agree closely with other reported models found in the literature for similar type of cement and conditions (De Weerdt et al. 2011, Savage et al. 2011, Lothenbach et al. 2008b, Lothenbach et al. 2006 and references therein).

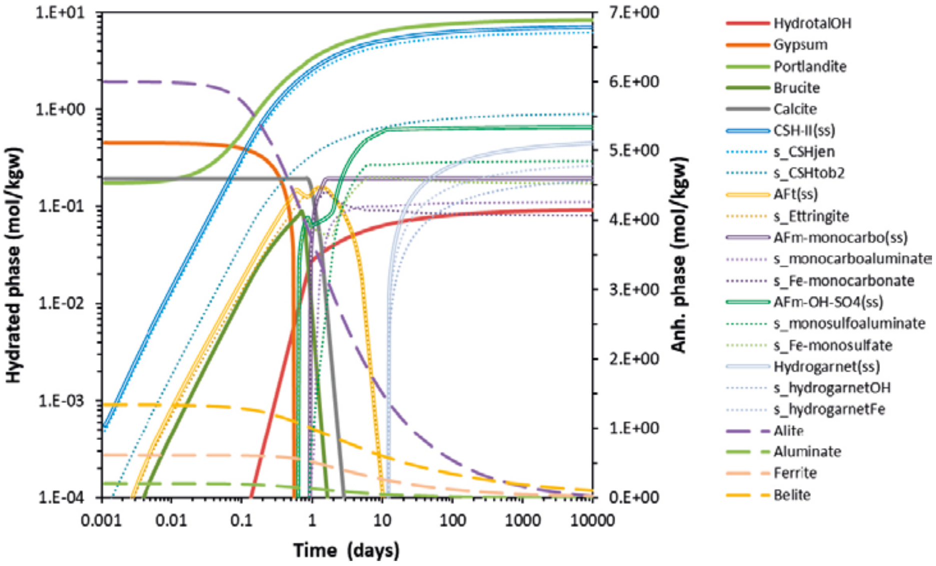

Figure 4-3. *Evolution of the hydrated solid phase assemblage as a function of time in the hydration model 1 (w/c = 0.47). Solid lines stand for discrete equilibrium phases; Double lines stand for solid solution models; Dotted lines stand for end-member associated to solid solution (ss, only the most important contribution is shown); Dashed lines stand for clinker phases (plotted at the secondary axis).*

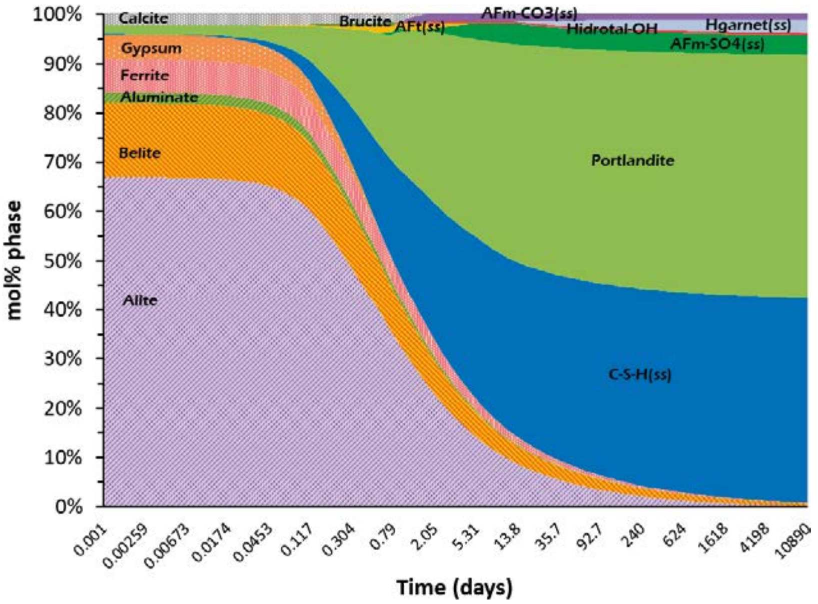

Figure 4-4. *Results of hydration model 1 (Anläggningscement, w/c = 0.47): cumulative mole fraction (%) of solid phases as a function of hydration time.*

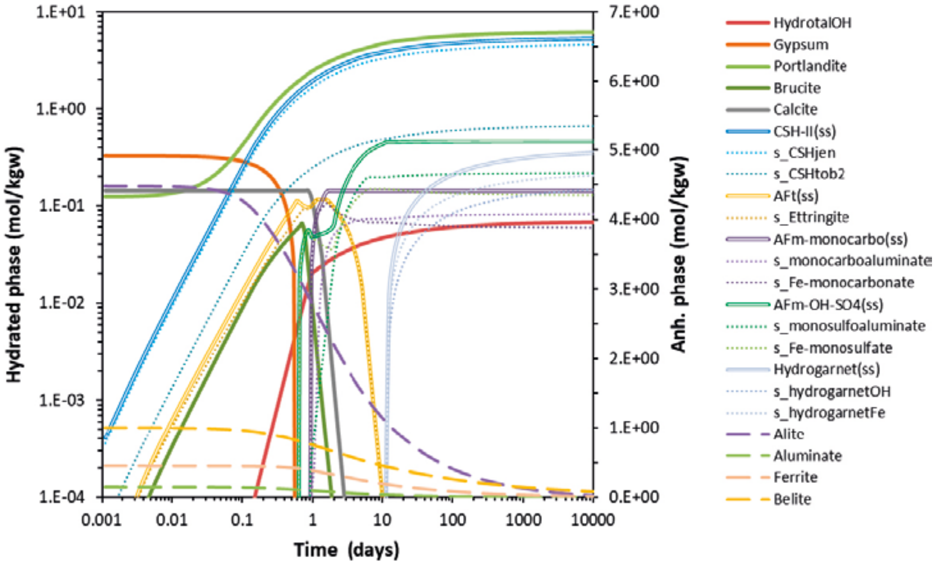

Figure 4-5. *Evolution of the hydrated solid phase assemblage as a function of time in the hydration model 2 (w/c = 0.63). Solid lines stand for discrete equilibrium phases; Double lines stand for solid solution models; Dotted lines stand for end-members associated to solid solution (ss, only the most important contribution is shown); Dashed lines stand for anhydrous clinker phases (plotted at the secondary axis).*

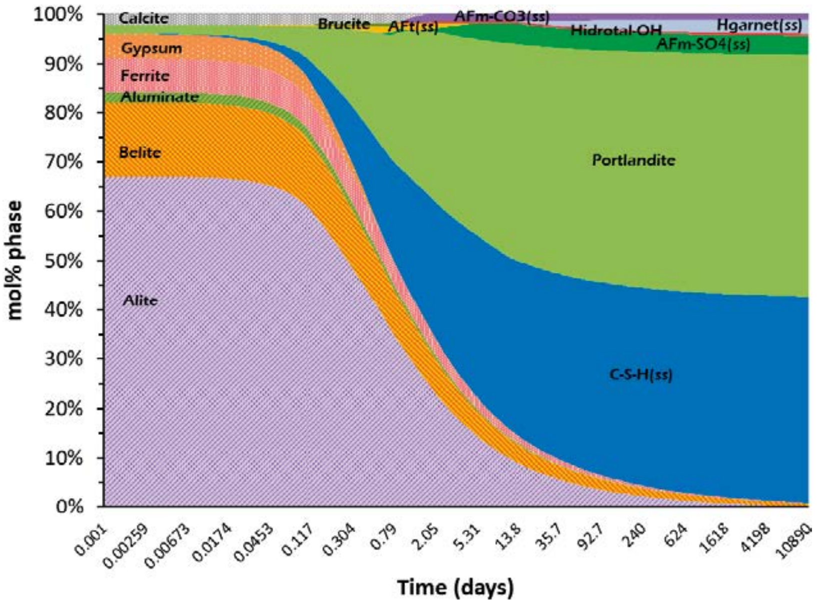

Figure 4-6. *Results of hydration model 2 (Anläggningscement, w/c = 0.63): cumulative mole fraction (%) of solid phases as a function of hydration time.*

The differences between the results of hydration models 1 and 2 are very small in terms of the relative mass fraction proportion of minerals. As result of the dilution effect when increasing the w/c ratio, lower mass content of hydrated phase forms for a w/c ratio of 0.63, representing an averaged 75 % of the molar content (per kg water) formed at w/c ratio of 0.47. The kinetics of hydration is similar in both models. This can be expected, given that the clinker dissolution kinetics used here (Section 4.1) are independent of the w/c ratio, as long as the factor $f_{w/c}$ in Equation 4-7 is equal to 1, which is the case here for hydration degrees lower than ~ 0.74. Readily soluble phases in the unhydrated cement may dissolve faster for higher liquid/solid ratios (or w/c ratios). However, this does not seem to impact the overall hydration kinetics.

4.2.2 Hydration model 3 (CEM II/A-V 52.5 N)

The calculated evolution of Na and K with hydration time falls within the range of reported experimental data for similar w/b ratio at equivalent range of FA addition (Figure 4-7). The model predicts higher concentrations of alkalis in this case compared to the OPC system with the same w/c ratio (hydration model 1) at early hydration times. This is attributed to the relatively higher content of readily soluble alkalis. In turn, at longer hydration times, the concentration is still higher for this type of cement blends. According to the consulted literature (Deschner et al. 2012, De Weerdt et al. 2011, Diamond 1981), the expected outcome is a decrease of the alkali content after some time of hydration due to the formation of C-S-H with lower C/S ratio, as well as C-A-S-H phases, with higher adsorption capacity for alkali than C-S-H with high C/S ratio (Section 3.1.2). The retention of alkalis in this type of cements tends to increase with the curing time as well as the amount of FA replacement. The results obtained in the present case for CEM II/A-V (Bascement Slite) show a pH slightly higher than OPC. This can be attributed to (i) the higher alkali total content in the clinker (0.07 vs. 0.30 wt% of Na_2O and 0.62 vs. 1.20 wt% of K_2O for OPC and OPC-FA, respectively) and (ii) the low level of FA replacement (12.3 wt%).

An increase of the hydroxyl ion content in the porewater limits the solubility of portlandite and consequently Ca concentration is lower than in OPC at early hydration ages (Figure 4-8a-b). At longer times, the dissolved Ca concentration is further reduced due to pozzolanic reaction. Such reduction affects sulfate concentration, which increases accordingly (Figure 4-8c), being higher than in the OPC (hydration model 1). An increase of Al concentration could be expected as a result of FA dissolution, with a high Al content. However, the uptake of Al into the C-S-H to form C-A-S-H phases leads in the model to a very similar concentration compared to OPC (Figure 4-8d).

The results of the hydration model 3 (Bascement Slite cement, w/b = 0.47) are presented in terms of the evolution of solid phases in Figure 4-9 and Figure 4-10. The same solid phases as those observed in the OPC are predicted to precipitate at early hydration times. Upon further hydration, ettringite does not completely dissolve under AFm-OH-SO_4(ss) precipitation since there is enough dissolved sulfate for these two phases to co-exist. The model predicts a reduction of portlandite content over time and an increase of C-(A)-S-H solid solution because of the pozzolanic reaction. The dissolution kinetics of the FA limits this reaction to take place at early times and thus pozzolanic reaction only becomes relevant at longer hydration times. These results are in line with other cement hydration studies of similar systems (Deschner et al. 2013, 2012, De Weerdt et al. 2011, Lothenbach et al. 2011, Massazza 1993, Fajun et al. 1985), which indicate an increase of C-S-H phases with lower C/S ratio and a lowering of portlandite content. These changes in the solid phase assemblage are reflected in the decrease of dissolved calcium concentrations indicated in Figure 4-8b.

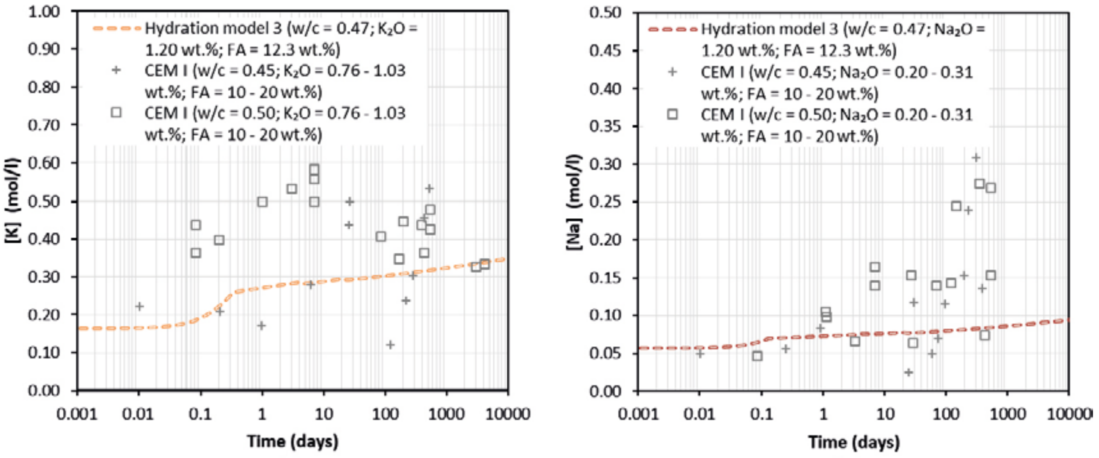

(a) (b)

Figure 4-7. *Evolution of alkalis concentration, K (a) and Na (b), along hydration time for cement pastes containing FA: model results of hydration model 3 (dashed lines) and measured concentrations (symbols). Measured data corresponds to the porewater of CEM I with 10–20 wt% of FA additions and* K_2O *= 0.76–1.03 wt% and* Na_2O *= 0.20–0.31 wt% at different w/b ratio (Vollpracht et al. 2016).*

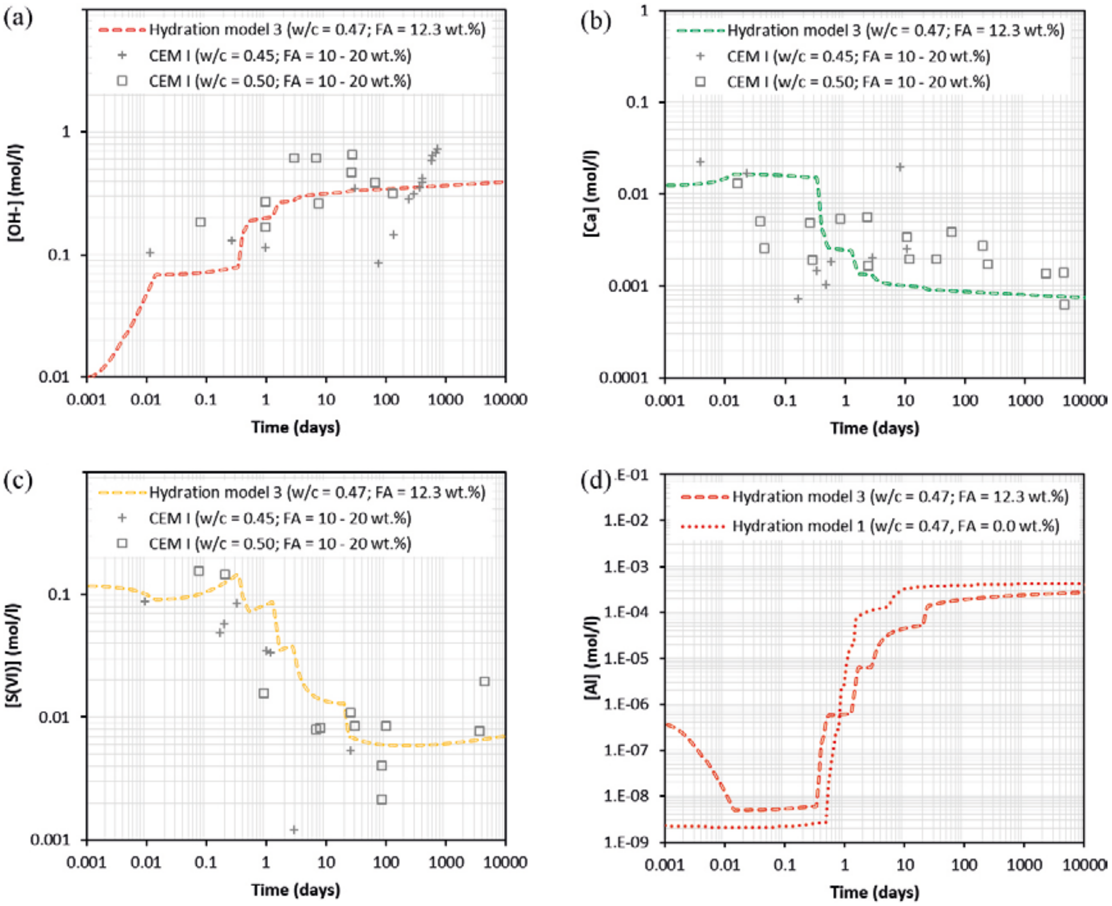

__Figure 4-8.__ Comparison of the evolution of (a) hydroxyl ions, (b) calcium, (c) sulfate, and (d) aluminium concentrations (mol/L) with hydration time (days) between experimental data (symbols, from Vollpracht et al. 2016) and the hydration model 3 (coloured dashed lines). Hydration model 1 (red dotted line) for comparison of aluminium evolution due to lack of experimental data. Experimental results for different water-to-binder ratio and level of FA replacement are shown.

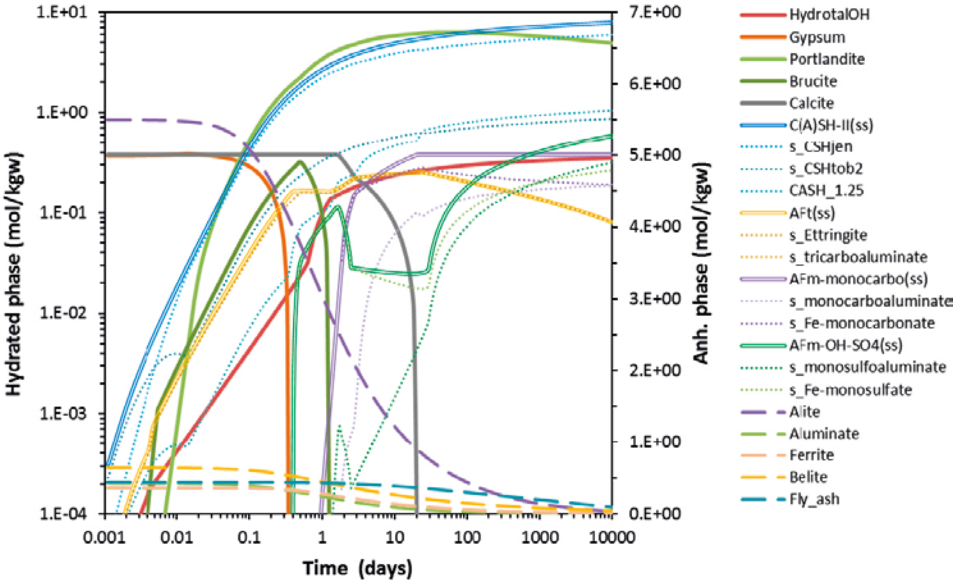

__Figure 4-9.__ Evolution of the hydrated solid phase assemblage as a function of time in the hydration model 3 (Bascement Slite cement, w/b = 0.47). Solid lines stand for discrete equilibrium phases; Double lines stand for solid solution models; Dotted lines stand for end-members associated to SS (only the most important contribution is shown); Dashed lines stand for anhydrous clinker phases (plotted at the secondary axis).

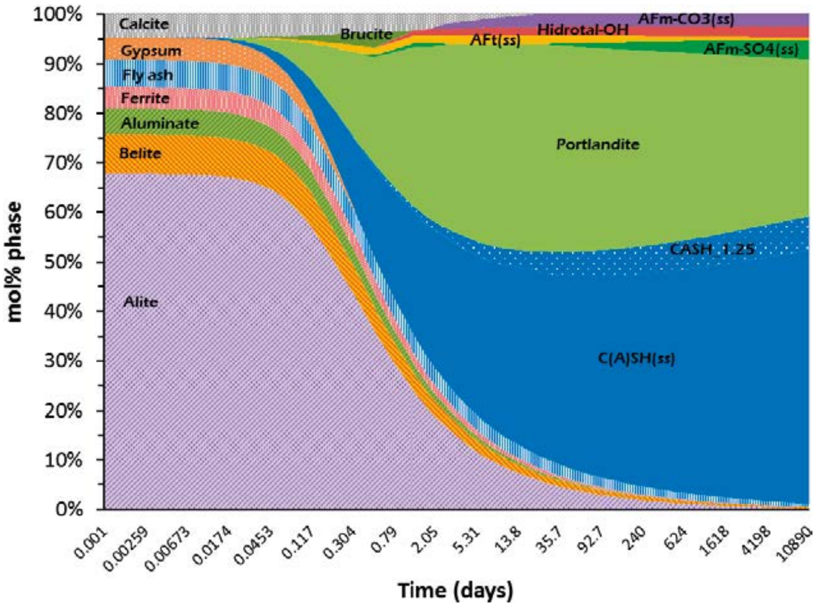

Figure 4-10. *Results of hydration model 2 (Bascement Slite, w/b = 0.47): cumulative mole fraction (%) of solid phases as a function of hydration time (days).*

At the end of simulation (10 000 days), stable phases/solid solutions are portlandite (significantly reduced compared to OPC (8.41 vs. 4.90 mol/kgw), hydrotalcite-OH, AFm-OH-SO_4(ss), AFm-monocarbo(ss), AFt(ss) and C(A)SH-II(ss). Approximately the same C-S-H jennite and C-S-H tobermorite end-members content forms in this case compared to OPC. However, a substantial precipitation of CASH_1.25 end-member can be observed which explains the increased C-(A)-S-H solid solution total content in the system.

4.2.3 Hydration model 4 (CEM I 42.5 N - SR with limestone/dolomite addition)

Figure 4-11a-d shows the simulated evolution of relevant species concentration and pH as a function of time for the hydration model 4, containing Anläggningscement with additions of limestone and dolomite. For comparative purposes, the results obtained with the plain CEM I (OPC - hydration model 1) are also shown in the figures.

Similar evolution of alkalis is predicted in the porewater compared to the OPC system, which is attributed to the similar water-to-cement ratio employed (0.47 in OPC vs. 0.49 in the present case). This is also evidenced in the pH, which evolves similarly from 2–3 hours of hydration onwards. Different values of pH at very early age of hydration (< 0.1 days) are due to calcium concentration, which is controlled by calcite in the present case and by portlandite in the OPC system. Thereafter, Ca dissolved content evolves in a similar way. Regarding sulfate, the concentration at initial times depends on calcium content, while at longer hydration time, different solubility controlling phases can explain the remarkable variation of this anion in solution. Ettringite is the solubility controlling phase in the present case, while in the case of OPC it is monosulfoaluminate.

Likewise, Al concentration differs from the OPC because ettringite (AFt) and monocarbo (AFm-monocarbo) are present instead of monosulfoaluminate (AFm-OH-SO_4), which entails lower Al concentration. With respect to carbonate, there is a sharply different evolution from 2–3 days onwards, i.e. calcite governs C(IV) solubility in this system which increases due to hydroxyl increase, whereas in OPC it undergoes a drop in the concentration when calcite is exhausted and monocarbonate becomes the solubility-controlling phase. The presence of dolomite increases dissolved magnesium concentration compared to OPC, which is especially relevant at initial hydration times, where brucite and MSH(ss) govern its solubility. At longer hydration times, hydrotalcite-OH controls Mg solubility at around 1×10^{-8} M until the end of the simulation. Concentrations of other ions are not affected to a great extent by the presence of limestone and dolomite. These results agree with previous work from the literature (see Section 3.2).

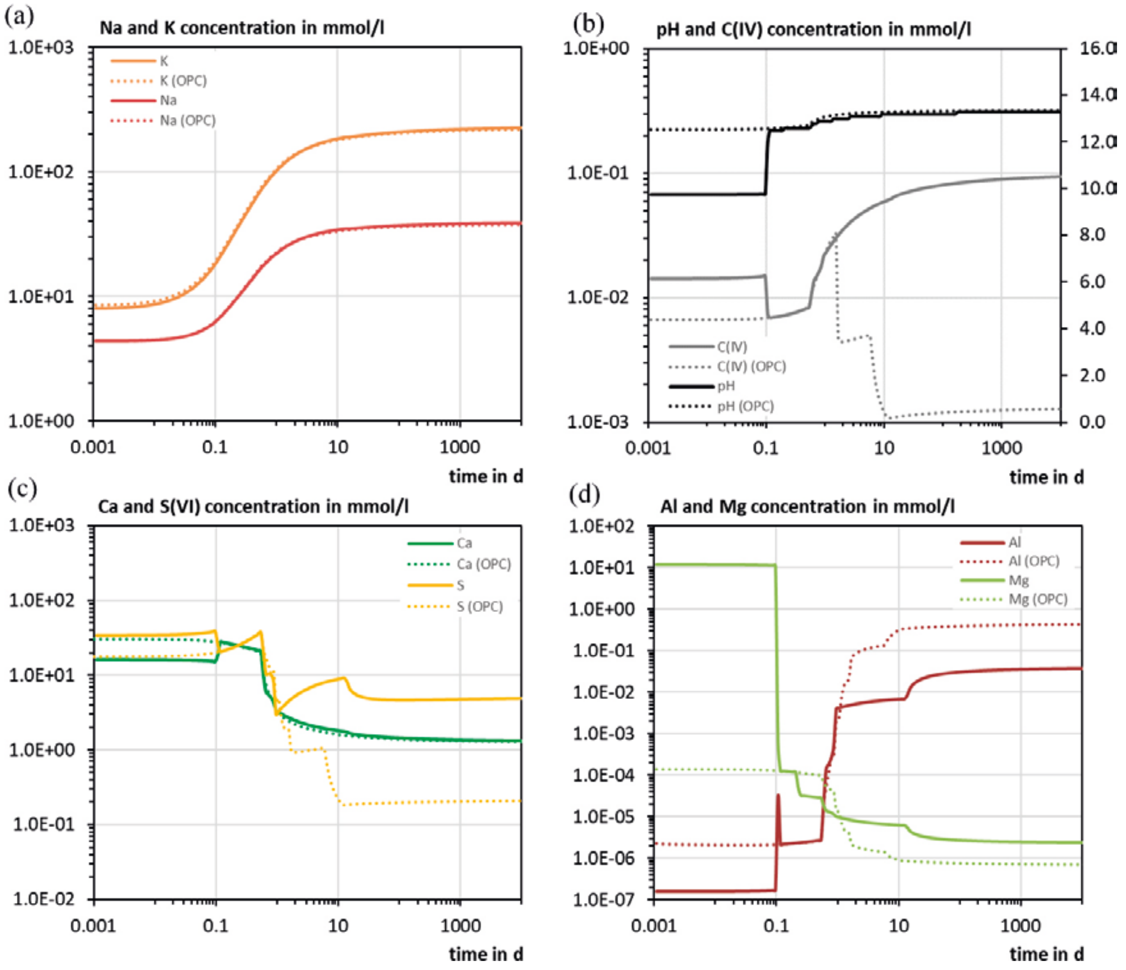

Figure 4-11. *Evolution of alkali (a); pH and carbonate (b); calcium and sulfate (c); aluminium and magnesium (d) concentrations along hydration time (days) for Anläggningscement with limestone and dolomite additions (w/b ratio 0.32 - Solid lines). For comparison purposes, results the hydration model 1 (w/c = 0.47) are also shown (dotted lines).*

These observations in the porewater chemistry are clearly reflected on the evolution of solid phases presented in Figure 4-12 and Figure 4-13. The first instants of this type of cement hydration are governed by calcite, dolomite, gypsum and brucite. The initial content of lime promotes brucite and calcite formation from the beginning of the hydration process. Thus, portlandite formation is slightly delayed by ~ 1 hour. Dolomite continuous dissolution boosts the formation of brucite and MSH(ss) phases until its total depletion within ~ 4.5 hours of hydration. The carbonate released by dolomite dissolution precipitates as calcite, which reaches its maximum content at approx. 2.5 hours of hydration (10.77 mol/kgw). Thereafter, it follows a steady decrease resulting in monocarboaluminate (AFm-monocarbo(ss)) precipitation. The high Mg concentration leads to MSH(ss) formation at initial hydration times. However, after 1 day of hydration, this solid solution destabilises to favour hydrotalcite-OH formation.

Contrary to the OPC system, ettringite (as the main end-member of AFt) remains stable and monosulfoaluminate among other chief end-members of AFm-OH-SO_4 solid solution are not prone to form during the hydration of this type of cement (saturation index below zero). This means that the presence of limestone leads to formation of monocarboaluminate (as the main end-member of AFm-monocarbo(ss)) with an associated destabilization of monosulfoaluminate in favour of ettringite. In absence (or lower content) of limestone, the formation of monosulfoaluminate and a reduction of the amount of ettringite is predicted with time. These results are in agreement with Section 3.2 and with consulted literature (De Weerdt et al. 2011, Lothenbach, et al. 2008a, Matschei et al. 2007a, b).

At the end of simulation (10 000 days), stable phases/solid solutions are portlandite and C-S-H (type II) with 60 to 65 % of the total content formed in OPC. This agrees quite well with the clinker replacement shown in Table 4-7. Other phases are calcite, AFm-monocarbo(ss), AFt(ss) and hydrotalcite-OH, which content has increased compared to OPC due to limestone and dolomite addition.

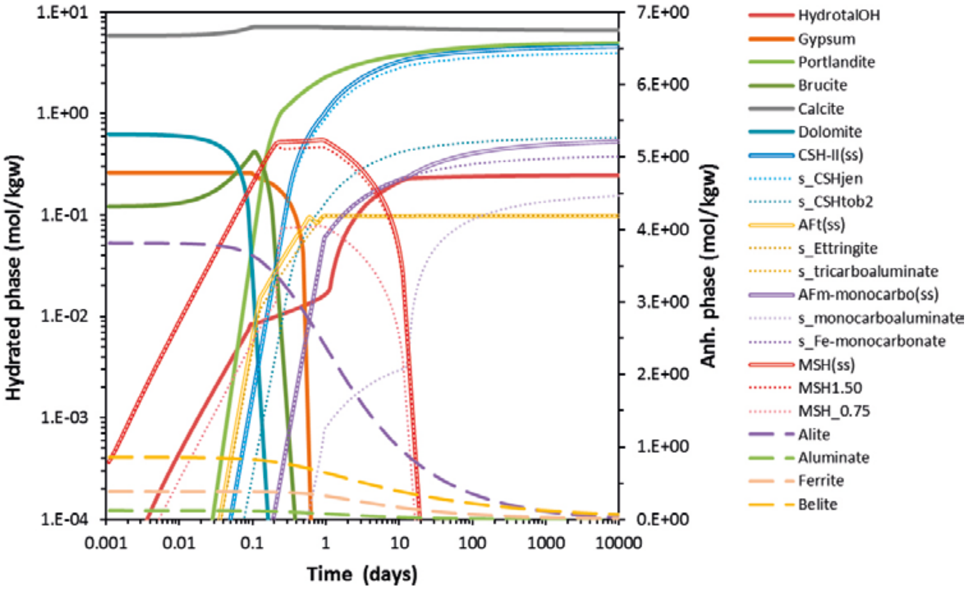

Figure 4-12. *Evolution of hydrated solid phase assemblage as a function of time in the hydration model 4 (Anläggningscement with addition of limestone and dolomite, w/b ratio 0.32). Solid lines stand for discrete equilibrium phases; Double lines stand for solid solution models; Dotted lines stand for end-members associated to SS (only the most important contribution is shown); Dashed lines stand for anhydrous clinker phases (plotted at the secondary axis).*

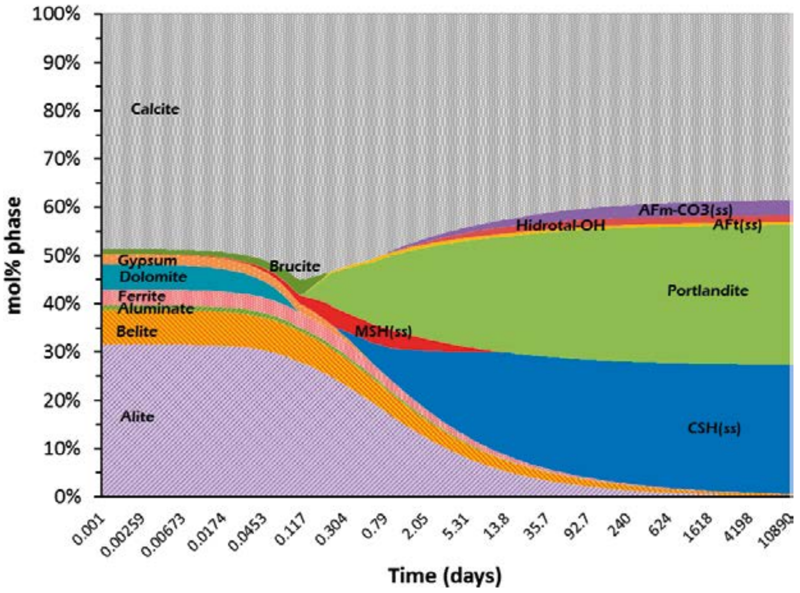

Figure 4-13. *Cumulative mole fraction (%) as a function of hydration time for Anläggningscement hydration with additions of limestone and dolomite (w/b ratio 0.32). Note that Omyacarb content was assumed within calcite composition and Myanit10 assumed as dolomite.*

4.2.4 Evolution of porosity

The results in terms of porosity evolution of all the hydration models calculated as presented in Section 4.1.6 are presented in Figure 4-14. Model 2 corresponds to the case of an OPC system with a w/c ratio of 0.63. Due to the lack of a complete dataset regarding the concrete mix, two different cases are considered, as detailed in Appendix D (different cement contents are used).

A decreasing trend as a function of hydration time is observed in all simulated cases. The final porosity (i.e. after 10 000 days of hydration) is almost half of the initial porosity right after mixing for models 1 and 3. On the other hand, in the rest of hydration models the reduction is smaller and the final porosity represents 65 % of the initial value.

For the hydration model 1 (CEM I with w/c = 0.47), the total porosity after 28 days is 0.1085, while after 10 000 days this value is reduced to 0.0935. Increasing the w/c ratio to 0.63 can have a different impact depending on the mix design (models 2a and 2b). However, both mix designs lead to higher total porosity values (0.1297 and 0.1135 for models 2a and 2b, respectively). Differences between the ratio $\phi_{\mathrm{hcp}}/\phi_{\mathrm{concrete}}$ are clearly shown between these 2 models, highlighting the importance of aggregate volumetric content. Using a binary mix with fly ash (hydration model 3) leads to a slightly lower porosity (i.e. 0.0879) after 10 000 days compared to OPC with similar w/c ratio. The addition of limestone and dolomite also impacts porosity, in this case leading to a significantly lower value after 10 000 days. This is due to the lower volume of cement resulting from the addition of filler. Table 4-13 presents the values of each porosity type for all simulated cases after 10 000 days.

Table 4-13. Porosity values after 10 000 days of hydration for the 5 different concrete mixtures.

Porosities	Model 1	Model 2a	Model 2b	Model 3	Model 4
ϕ_{cap}	0.120	0.266	0.266	0.085	0.076
ϕ_{gel}	0.098	0.081	0.081	0.108	0.079
ϕ_{ch}	0.096	0.073	0.073	0.089	0.086
ϕ_{hcp}	0.314	0.421	0.421	0.283	0.240
ϕ_{concrete}	0.094	0.130	0.114	0.088	0.077

The porosity values obtained after 10 000 days of hydration for models 1, 2a and 2b can be compared to the results of the three models presented in Section 3.3.1 to calculate porosity (Table 3-4 and Appendix D). It may be observed that a relatively good agreement is found between the approach presented in this section and the models in Section 3.3.1. Small differences between models are a consequence of the different hydration models used and the quantification of gel porosity (i.e. if it is directly linked with C-S-H amount or not).

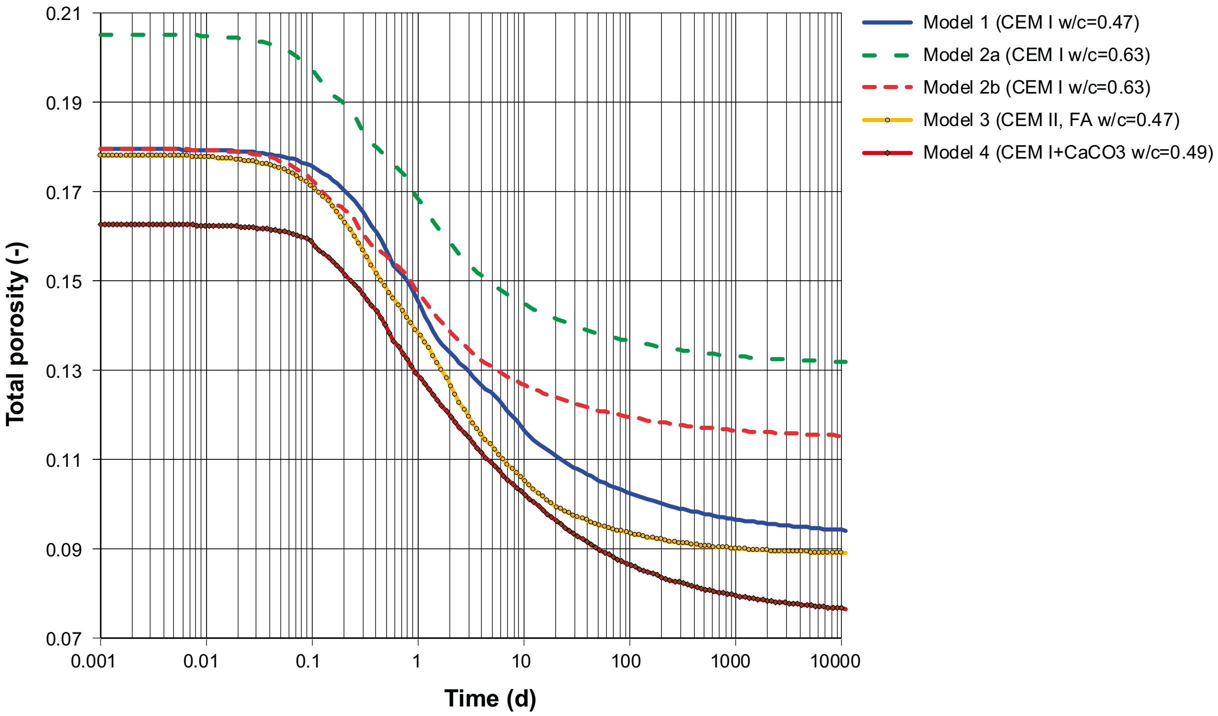

__Figure 4-14.__ Evolution of porosity as a function of time for the five hydration models.

4.2.5 Final mineral assemblages

The results of the hydration models are used as input data for chemical calculations in the long-term reactive transport models of concrete degradation described in Chapter 5. A complete description of the mineralogical phase assemblage of each hydration model is presented in Table 4-14.

Table 4-14. Mineralogical phase assemblage of the concrete backfill: primary minerals and exchanger composition concentration for the 4 hydration models. Units given in mol/kg$_{water}$.

Primary minerals	Model 1	Model 2	Model 3	Model 4
Equilibrium phases				
Portlandite	8.410	6.200	4.896	7.549
Hydrotalcite OH	0.091	0.069	0.349	0.375
Calcite	0	0	0	9.968
C-S-H solid solution				
C-S-H jennite	6.200	4.630	–	6.040
C-S-H tobermorite	0.909	0.677	–	0.884
C-(A)-S-H solid solution				
C-S-H jennite*	–	–	5.990	–
C-S-H tobermorite*	–	–	0.875	–
C-A-S-H 1.25	–	–	1.064	–
C-A-S-H 1.0	–	–	0.026	–
M-S-H solid solution				
M-S-H 1.5	–	–	–	0
M-S-H 0.75	–	–	–	0
AFt solid solution				
Ettringite	0	0	0.078	0.148
Tricarboaluminate	0	0	4.2×10^{-7}	7.3×10^{-5}
Fe-ettringite	0	0	9.4×10^{-7}	4.2×10^{-6}
AFm solid solution I				
Monocarboaluminate	0.110	0.083	0.186	0.234
Fe-monocarbonate	0.081	0.060	0.189	0.569
AFm solid solution II				
C_4AH_{13}	0.043	0.026	–	–
C_4FH_{13}	0.029	0.017	–	–
C_2AH_8	0.002	0.001	–	–
C_2FH_8	0.001	0.001	–	–
Strätlingite	0.070	0.047	0.008	–
Fe-strätlingite	0.048	0.031	0.007	–
Monosulfoaluminate	0.290	0.218	0.318	–
Fe-monosulfate	0.173	0.127	0.264	–
Hydrogarnet solid solution				
Hydrogarnet OH	0.183	0.157	0	0
Hydrogarnet Fe	0.261	0.218	0	0
Un-hydrated phases				
Alite	0.025	0.024	0.031	0.032
Aluminate	0.001	0.001	0.001	0.001
Belite	0.096	0.072	0.041	0.093
Ferrite	0.015	1.8×10^{-9}	0.007	0.015
Exchanger composition				
CaX_2	0.248	0.209	0.100	0.235
K_2X_2	0.094	0.049	0.219	0.093
Na_2X_2	0.017	0.009	0.093	0.017

* C-S-H jennite and C-S-H tobermorite correspond to CSHjen and CSHtob2 in CEMDATA07.

5 Modelling of reactive transport processes

To assess the potential degradation in the long term of the concrete barriers of the BHK vault in SFL, two sets of reactive transport models are presented. The main goal is to compare the long-term performance of different concrete mixtures under repository conditions. Concrete degradation is mainly driven by its interaction with groundwater. Numerical models coupling fluid flow, solute transport and chemical reactions have been performed using iCP (Nardi et al. 2014).

5.1 Conceptual models and numerical implementation

From the results of the cement hydration models of the four different cementitious systems, five concrete mixes are tested using reactive transport modelling. Case I, IIa, IIb, III, and IV correspond respectively to Models 1, 2a, 2b, 3, and 4 (see Table 2-1). Case I corresponds to the CEM I 42.5 N (OPC) mixture with a w/c ratio of 0.47. This concrete mix is equivalent to the concrete studied in Höglund (2014), Idiart and Shafei (2019) and Idiart and Laviña (2019). The difference is that the composition of the hydrated system is obtained in this case using the approach presented in Chapter 4. The goal is to study the influence of different hydration models of a similar concrete mix on the long-term performance of the barrier.

To study concrete degradation, two different sets of models are conceptualised, see Figure 5-1. The first one describes a 2D geometry corresponding to a typical cross-section of the BHK concrete vault of the SFL repository (Idiart and Shafei 2019). The second one is focused on the concrete domain, considering a 1D line across the left-hand side of the concrete backfill (Idiart and Laviña 2019).

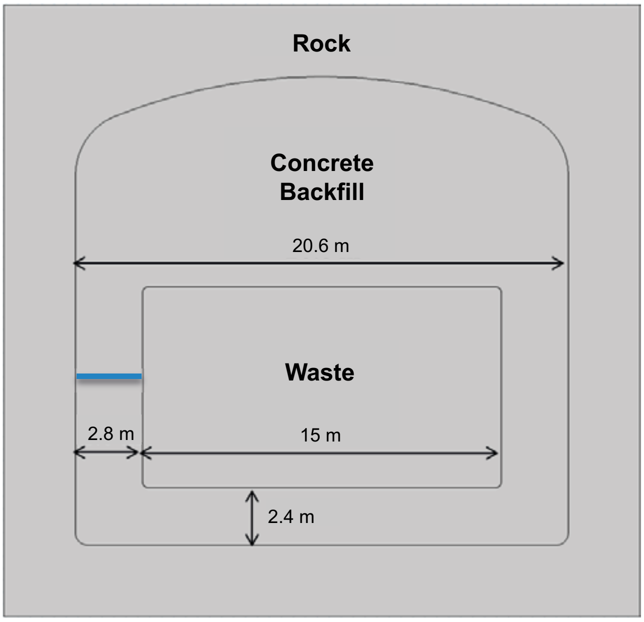

Figure 5-1. *2D cross-section of BHK vault and dimensions in metres (m), including three domains: host rock, concrete backfill and waste. Blue line representing the concrete backfill section modelled in the 1D simulations.*

5.1.1 2D models of a BHK cross-section

The model considers three different domains: the host rock, the concrete backfill and the waste domain. Their distribution and complete geometry is extracted from Idiart and Shafei (2019) and presented in Figure 5-1. The host rock is considered for groundwater flow purposes and therefore chemical reactions and solute transport are not taken into account in this domain. The radioactive waste is modelled as a homogeneous cementitious material, assuming that the only chemically active material in this domain is concrete. Based on the current BHK vault design and its composition, the volume of concrete occupying the waste domain has been calculated (Pękala et al. 2015). Each simulation case considers the same concrete mix in each domain (i.e. backfill and waste), although with different volume fractions to account for the fact that the volume of concrete per unit volume of waste domain is smaller than unity.

Flow and transport initial properties are defined in Table 5-1, summarizing the hydraulic conductivity, K (m/s), and effective diffusion coefficient, D_e (m^2/s). In the rock domain, these values remain constant during the simulation, while in the concrete backfill and waste they may evolve as a function of degradation. The time-dependent evolution of transport properties is the main coupling between chemistry and physics. Changes in transport properties are governed by porosity variations resulting from chemical reactions leading to mineral dissolution and precipitation.

Hydraulic conductivity variation with porosity is modelled through the well-known Kozeny-Carman relation (Carman 1937):

$$K(\phi) = K(\phi_0)\frac{(1-\phi_0)^2}{\phi_0^3}\frac{\phi^3}{(1-\phi)^2} \qquad (5\text{-}1)$$

where, $K(\phi)$ is the hydraulic conductivity (m/s), ϕ is the porosity (m^3/m^3), ϕ_0 is 0.11, and $K(\phi_0)$ is the hydraulic conductivity (m/s) associated with ϕ_0. Dependence of the effective diffusion coefficient (m^2/s) on porosity follows the equation:

$$D_e = \tau\phi_0 D_0\left(\frac{\phi}{\phi_0}\right)^{2.5} \qquad (5\text{-}2)$$

where τ (-) is the tortuosity of the porous medium, ϕ_0 is 0.11, and D_0 (m^2/s) is the diffusion coefficient in free water, assumed to be 1.0×10^{-9} m^2/s. Porosity is updated by mineral dissolution/precipitation reactions:

$$\phi = 1 - \sum_{i=1}^{M} c_i V_{\mathrm{m},i} - V_{\mathrm{inert}} \qquad (5\text{-}3)$$

where c_i is the i^{th} mineral concentration (mol/L of medium), $V_{\mathrm{m},i}$ is the molar volume of i^{th} mineral (L/mol), and V_{inert} (-) is the volume fraction of inert minerals such as the aggregates in concrete. These porosity values do not account for the clogging effects of carbonation (i.e. calcite precipitation). Although clogging is expected to reduce porosity and thus the transport properties, there is a substantial uncertainty on the effectiveness of this process to totally seal the pores and avoid further interaction. Accounting for clogging in this type of modelling scheme could lead to sealing against flow and transport, which may not be a conservative assumption from a safety point of view. However, a sensitivity case accounting for this effect is considered for Case I. For the reference concrete mix, i.e. CEM I with 0.47 w/c ratio (Case I), initial values of porosity, hydraulic conductivity, and effective diffusion coefficient are (e.g. Idiart and Shafei 2019): 0.11, 8.3×10^{-10} m/s and 3.5×10^{-12} m^2/s, respectively.

To allow a more effective comparison, transport properties of all simulated cases follow the same relations (Equations 5-1 to 5-3). This means that the initial transport properties of each case are calculated using its respective initial porosity in Table 5-1, while the parameter ϕ_0 in Equations 5-1 and 5-2 can be interpreted as a reference porosity value, fixed to 0.11. Parameters $K(\phi_0)$ and τ in Equations 5-1 and 5-2, respectively, are also considered as constants.

The use of these equations to scale transport properties of different concrete mixes only on the basis of porosity is considered as a first approximation. This is mainly motivated by the lack of experimental data regarding specific relations between porosity/microstructure and transport properties for the studied concrete mixes under a wide range of degradation states. The models presented in this report would certainly benefit from dedicated studies to assess these relations.

The chemical composition of concrete in each case is based on the results obtained from the hydration models of each cement type presented in Chapter 4. The initial conditions of the cementitious systems in the reactive transport models are based on the final phase assemblages gathered in Table 4-14 resulting from the hydration models. To this end, several simplifications are considered in the final phase assemblages to obtain the initial conditions:

1. Iron is removed from the system to avoid numerical convergence issues (see Idiart and Shafei 2019 or Jacques 2009).
2. The solid solutions where an iron-bearing phase is present are removed from the model and replaced by a single phase lumping the concentrations of the solid solution:
   a. The AFt solid solution is replaced by ettringite, while the concentration of Fe-ettringite is lumped with that of ettringite, and tricarboaluminate is removed from the system (negligible concentrations in all cases).
   b. AFm I solid solution is replaced by monocarboaluminate.
   c. Hydrogarnet solid solution is replaced by hydrogarnet OH.
   d. AFm II solid solution is replaced by the monosulfoaluminate.
3. The rest of end-members of the solid solutions with iron-bearing phases are set to zero concentrations and considered in the reactive transport models as secondary minerals (Table 5-4).
4. The remaining phases and solid solutions (C-S-H, C-A-S-H) remain unaltered.

The initial phase assemblages of the concrete backfill and waste domain in each simulation case are given in Table 5-2 and Table 5-3, respectively. The same thermodynamic database as the one used in Chapter 4 is considered here. The solid solutions involving C-S-H and C-A-S-H phases are kept in the reactive transport models. These two solid solutions are not containing Fe bearing phases and are of major importance to assess concrete degradation. Primary mineral phases and solid solutions for the concrete backfill and waste domain are presented in Table 4-14 and Table 5-3 as well as their cation exchanger composition to represent alkali uptake in cement paste. It is noted that, similar to Idiart and Shafei (2019), the waste domain is assumed to be composed of the same concrete as the backfill domain for modelling purposes. The difference is that the amount of concrete per unit volume of waste domain is lower than in the concrete backfill to take into account the presence of other materials (which are considered as inert in these models).

Secondary minerals, i.e. those allowed to precipitate, are shown in Table 5-4. Concrete porewater compositions for the different cases (in equilibrium with the initial mineral phase assemblage) and groundwater composition are presented in Table 5-5. The granitic groundwater composition is assumed to remain constant in time (as modelled in Idiart and Shafei 2019). This is certainly a simplification for the studied period, and the impact of a variable chemical composition of groundwater should be assessed in future studies. However, this is out of the scope of this work.

Table 5-1. Physical/transport properties for the different concretes, deduced from hydration model results.

	Porosity, ϕ	Tortuosity, τ	D_e (m²/s)	K (ϕ_0) (m/s)	K (m/s)
Host rock	0.3	–	–	–	5.00×10^{-9}
Waste	0.3	1.1600*	3.50×10^{-10}	1.00×10^{-7}	1.00×10^{-7}
Concrete domains for each simulated case					
Case I	0.110	0.0318	3.50×10^{-12}	8.30×10^{-10}	8.30×10^{-10}
Case IIa	0.130	0.0318	5.28×10^{-12}	8.30×10^{-10}	1.42×10^{-9}
Case IIb	0.114	0.0318	3.79×10^{-12}	8.30×10^{-10}	9.19×10^{-10}
Case III	0.088	0.0318	2.00×10^{-12}	8.30×10^{-10}	4.05×10^{-10}
Case IV	0.077	0.0318	1.42×10^{-12}	8.30×10^{-10}	2.60×10^{-10}

* Note that τ is a result of imposing ϕ and D_e values extracted from Idiart and Shafei (2019) in Equation 5-2.

Table 5-2. Mineralogical phase assemblage of concrete backfills, deduced from hydration model results. Concentration units given in mol/L of medium.

Primary minerals	Case I	Case IIa	Case IIb	Case III	Case IV
Equilibrium phases					
Portlandite	1.422	1.198	1.048	0.826	1.205
Hydrotalcite OH	0.016	0.014	0.012	0.059	0.059
Calcite	0.000	0.000	0.000	0.000	1.591
Monocarboaluminate	0.033	0.028	0.025	0.063	0.013
Ettringite	0.000	0.000	0.000	0.013	0.024
Monosulfoaluminate	0.081	0.068	0.060	0.099	0.000
Hydrogarnet OH	0.111	0.098	0.086	0.000	0.000
Solid solutions					
1 C–S–H jennite	1.100	0.930	0.814	–	0.964
C–S–H tobermorite	0.161	0.137	0.120	–	0.141
2 C–S–H jennite	–	–	–	1.000	–
C–S–H tobermorite	–	–	–	0.142	–
C–A–S–H 1.25	–	–	–	0.194	–
C–A–S–H 0.84	–	–	–	0.005	–
Porosity	0.110	0.130	0.114	0.088	0.077
Inert fraction	0.694	0.704	0.741	0.714	0.708
Exchanger composition					
CaX_2	0.04286	0.04150	0.03632	0.01701	0.03734
K_2X_2	0.01657	0.00966	0.00845	0.03680	0.00149
Na_2X_2	0.00292	0.00175	0.00153	0.01560	0.00266

Table 5-3. Mineralogical phase assemblage of waste radioactive domains. Concentration units given in mol/L of medium.

Primary minerals	Case I	Case IIa	Case IIb	Case III	Case IV
Equilibrium phases					
Portlandite	0.742	0.625	0.547	0.431	0.629
Hydrotalcite OH	0.008	0.007	0.006	0.031	0.031
Calcite	0.000	0.000	0.000	0.000	0.831
Monocarboaluminate	0.017	0.015	0.013	0.033	0.007
Ettringite	0.000	0.000	0.000	0.007	0.009
Monosulfoaluminate	0.042	0.036	0.031	0.051	0.000
Hydrogarnet OH	0.058	0.051	0.045	0.000	0.000
Solid solutions					
1 C-S-H jennite	0.5742	0.4855	0.4249	–	0.5032
C-S-H tobermorite	0.08404	0.07151	0.06264	–	0.0736
2 C-S-H jennite	–	–	–	0.5220	–
C-S-H tobermorite	–	–	–	0.07412	–
C-A-S-H 1.25	–	–	–	0.1013	–
C-A-S-H 0.84	–	–	–	0.00245	–
Porosity	0.300	0.300	0.300	0.300	0.300
Inert fraction	0.598	0.613	0.624	0.596	0.588
Exchanger composition					
CaX_2	0.02237	0.02166	0.01896	0.00888	0.01949
K_2X_2	0.00864	0.00504	0.00441	0.01921	0.00078
Na_2X_2	0.00152	0.00091	0.00080	0.00814	0.00139

Table 5-4. List of secondary minerals allowed to precipitate.

Secondary minerals
Brucite
CAH_{10}
Gypsum
Hydrotalcite C
Tricarboaluminate
C_4AH_{13}
C_2AH_8
Strätlingite
Syngenite
Thaumasite
Dolomite*
SiO_2(am)

* Only in Case IV.

Table 5-5. Granitic groundwater (Idiart and Shafei 2019) and concrete porewater compositions (deduced from hydration model results). Temperature is 25 °C.

	Groundwater	Case I	Case IIa	Case IIb	Case III	Case IV
pH	8.64	13.33	13.26	13.26	13.54	13.32
Ionic strength (M)	0.007	0.2482	0.2182	0.2180	0.4070	0.1970
Species (totals)	**Concentration (M)**					
Al	1.21×10^{-6}	6.830×10^{-4}	5.787×10^{-4}	5.787×10^{-4}	4.976×10^{-4}	5.744×10^{-5}
C	6.91×10^{-4}	7.256×10^{-7}	5.254×10^{-7}	5.254×10^{-7}	1.081×10^{-5}	9.438×10^{-5}
Ca	5.26×10^{-4}	1.228×10^{-3}	1.494×10^{-3}	1.494×10^{-3}	7.454×10^{-4}	1.290×10^{-3}
Cl	4.53×10^{-3}	0.0	0.0	0.0	0.0	0.0
K	7.60×10^{-5}	2.164×10^{-1}	1.930×10^{-1}	1.930×10^{-1}	3.506×10^{-1}	2.261×10^{-1}
Mg	1.48×10^{-4}	5.109×10^{-10}	5.932×10^{-10}	5.932×10^{-10}	5.010×10^{-10}	1.786×10^{-9}
Na	4.79×10^{-3}	3.709×10^{-2}	3.334×10^{-2}	3.334×10^{-2}	9.466×10^{-2}	3.892×10^{-2}
S(VI)	3.73×10^{-4}	1.461×10^{-4}	1.024×10^{-4}	1.024×10^{-4}	2.227×10^{-3}	1.877×10^{-3}
Si	1.42×10^{-4}	6.342×10^{-5}	5.532×10^{-5}	5.532×10^{-5}	9.327×10^{-5}	6.222×10^{-5}

Spatial discretization is shown in Figure 5-2. The finite element mesh considers 12 550 triangular elements, divided into: 4 504 for the host rock, 6 284 for the concrete backfill and 1 762 for the waste domain. The maximum element size is 0.6 m in the rock domain near the boundaries of the model (where no chemical reactions are considered) and the centre part of the waste domain (where degradation is expected to be minimal). The minimum size is set to 0.3 m and used in the discretization of the concrete wall.

The total simulation time is set to 100 000 years. Temporal discretization obeys two criteria. The first restriction is the von Neumann stability criterion for preventing numerical oscillations:

$$\Delta t \leq \frac{\Delta x^2}{2D_L} \tag{5-4}$$

where Δt (s) is the time step size, Δx (m) is the finite element size, and D_L (m^2/s) is the dispersion-diffusion tensor. The second criterion limits the time stepping depending on adjacent grid points Δx_i (m) and interstitial velocity v (m/s). The Courant number (C_r) is defined as:

$$C_r = \frac{v\Delta t}{\Delta x_i} < 1 \qquad \text{or} \qquad \Delta t < \frac{\Delta x_i}{v} \tag{5-5}$$

With the current 2D model parameters, time step limiting criteria lead to values presented in Table 5-6. Maximum time steps are calculated for the concrete backfill (smallest element size). The time step selected to define communication steps between Comsol and PHREEQC is set to 3.5 years for the first 50 000 years and to 2.5 years for the second halve of the study period.

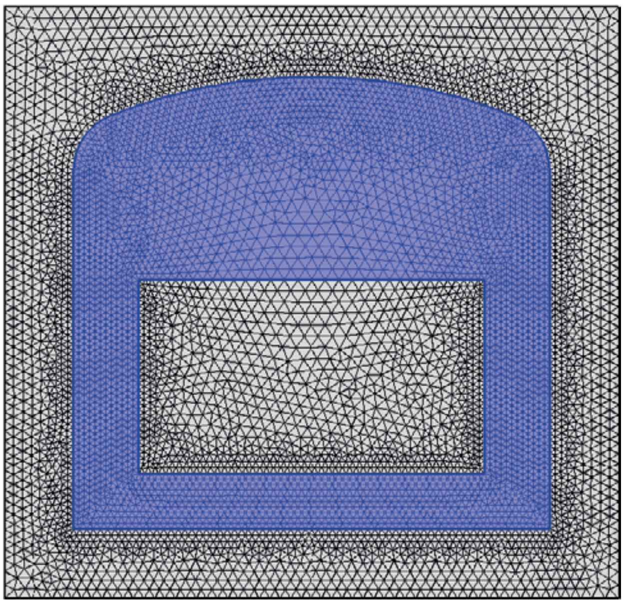

Figure 5-2. Finite element mesh used in the iCP simulations for the 2D cross-section of BHK vault. Including three domains: host rock, concrete backfill (blue) and waste.

Table 5-6. Maximum theoretical time-step size (in years) according to von Neumann and Courant criteria for the given spatial discretization and material properties of the 2D model.

Criterion	Case I	Case IIa	Case IIb	Case III	Case IV
von Neumann	44.8	35.0	42.8	62.7	77.2
Courant	101.6	119.8	104.8	81.3	70.8

Two boundary conditions for groundwater flow are imposed. An inlet boundary condition is set at the left boundary of the rock domains and a fixed hydraulic head condition (0 m) is set at the right boundary. The inlet boundary condition sets a normal inflow velocity equal to 1.03×10^{-11} m/s. This velocity corresponds to an average flow, taken from the results obtained by Abarca et al. (2016). It is consistent with the flow conditions used by Idiart and Shafei (2019). The inlet boundary condition follows the following expression:

$$-\boldsymbol{n}\rho \cdot \boldsymbol{u} = \rho U_0 \tag{5-6}$$

where U_0 is the normal inflow velocity (1.03×10^{-11} m/s), $\boldsymbol{n}$ is the vector normal to the boundary surface, ρ (kg/m^3) is the fluid density, and $\boldsymbol{u}$ (m/s) is the velocity at the boundary.

Reactive transport is only solved for in the concrete and waste domains. The boundary condition for solute transport is then located along the full rock-concrete interface. A Dirichlet boundary condition sets the groundwater composition at this interface (see Table 5-5).

5.1.2 1D models of concrete backfill

The conceptual model of a set of 1D reactive transport simulations of the degradation of the same concrete compositions as for the 2D models is presented here. The main difference is that these 1D models are used to study degradation of the concrete backfill over a 1-million-year time period. These models are focused on the concrete backfill and do not account for the rock or waste domains.

Figure 5-1 shows the 1D geometry and the discretization. It consists of a line cutting the left-hand side of the concrete backfill, bounded by the contact with the rock (left) and the waste domains (right). Flow, transport and chemistry are coupled in the same way as in the 2D models. Chemical dissolution/precipitation processes determine the porosity which, in turn, affects transport properties. Initial values for concrete parameters are shown in Table 5-1.

The mineralogical phase assemblages, resulting from the hydration models, are the same as for the 2D models. Concrete composition, secondary minerals, porewater and groundwater are described in Table 4-14, Table 5-4 and Table 5-5. The groundwater composition is fixed at the left boundary of the model, assuming fast renewal of groundwater. For the right boundary, an outflow boundary condition for concentration is imposed:

$$n \cdot (-D_e \nabla c) = 0 \tag{5-7}$$

where c (M) is the solute concentration vector.

Moreover, a fixed pressure gradient is imposed across the modelled domain so that the initial velocity of Case I is 1.03×10^{-11} m/s. The rest of cases have slightly different initial velocities depending on their initial hydraulic conductivity (Table 5-1**)**. Initial velocities for each 1D case are given in Table 5-7. This assumption is considered to resemble the 2D groundwater flow field, in which the initial Darcy velocities across the left concrete backfill are reduced for lower initial hydraulic conductivities. The Darcy velocity, proportional to the equivalent hydraulic conductivity of the 1D domain, increases as degradation proceeds (Idiart and Laviña 2019).

Table 5-7. Initial hydraulic conductivity (m/s), Darcy velocity (q, m/s) for each 1D case.

	K (m/s)	*q* (m/s)
Case I	8.30×10^{-10}	1.03×10^{-11}
Case IIa	1.42×10^{-9}	1.76×10^{-11}
Case IIb	9.19×10^{-10}	1.14×10^{-11}
Case III	4.05×10^{-10}	5.03×10^{-12}
Case IV	2.60×10^{-10}	3.22×10^{-12}

Spatial discretization consists of a total number of 28 finite elements of 0.1 m size (Figure 5-3), i.e. 3 times more refined than the 2D simulations. The total simulation time of 1 million years is discretised using time steps of 5 years for the operator splitting. This constant communication time steps between Comsol and PHREEQC have been setup considering the von Neumann and Courant criteria. The different spatial discretisation between models lead to different limiting time step values (Table 5-8**)**.

Table 5-8. Maximum theoretical initial time-step size (years)according to von Neumann (Equation 5-4) and Courant (Equation 5-5) criterions for the given spatial discretization and material properties from the 1D model.

Criterion	Case I	Case IIa	Case IIb	Case III	Case IV
von Neumann	5.0	3.9	4.8	7.0	8.6
Courant	33.2	39.9	34.9	27.1	23.6

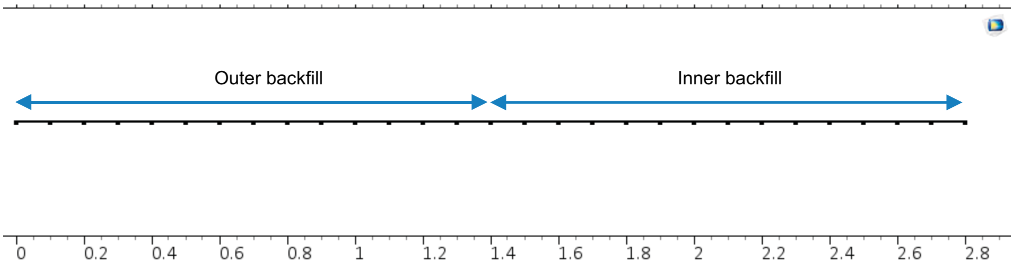

Figure 5-3. *Finite element mesh used in the 1D iCP simulations and control volumes definition. Dimension expressed in metre (m).*

5.2 Results for 2D models of a BHK cross-section

This section presents the results of the five simulation cases of concrete degradation in a typical BHK cross-section. A comparison between the different cases is done to determine the impact of different concrete mixes on long-term performance. First, a complete set of results for Case I is presented and discussed in more detail. Thereafter, the analysis of the remaining simulation cases is focused on the main characteristics and differences compared to Case I.

5.2.1 Case I

The 2D distribution of the mineralogical phase assemblage of Case I after 100 000 years is summarised in Figure 5-4 through Figure 5-6. This case is similar to the base case presented in Idiart and Shafei (2019), with the difference that the mineralogical phase assemblage is calculated using the hydration model of Section 4.2.1 instead of that presented by Höglund (1992). The same degradation patterns can be observed. The mineral dissolution front begins at the rock-concrete interface and evolves towards the interior of the concrete backfill. Degradation proceeds somewhat faster on the left side due to groundwater flow. After 100 000 years, the dissolution depth on the left side of the concrete backfill is 0.94 m for portlandite, 0.24 m for C-S-H jennite, and 0.7 m for hydrogarnet OH. C-S-H tobermorite precipitates in the first 1.16 m, although it completely dissolves at the interface with the rock. Monocarboaluminates and monosulfoaluminates also dissolved completely along the first 0.46 and 0.7 m from the interface with the rock, respectively (Figure 5-5). On the other hand, hydrotalcite OH remains stable after 100 000 years and a small amount precipitates near the interface with the rock.

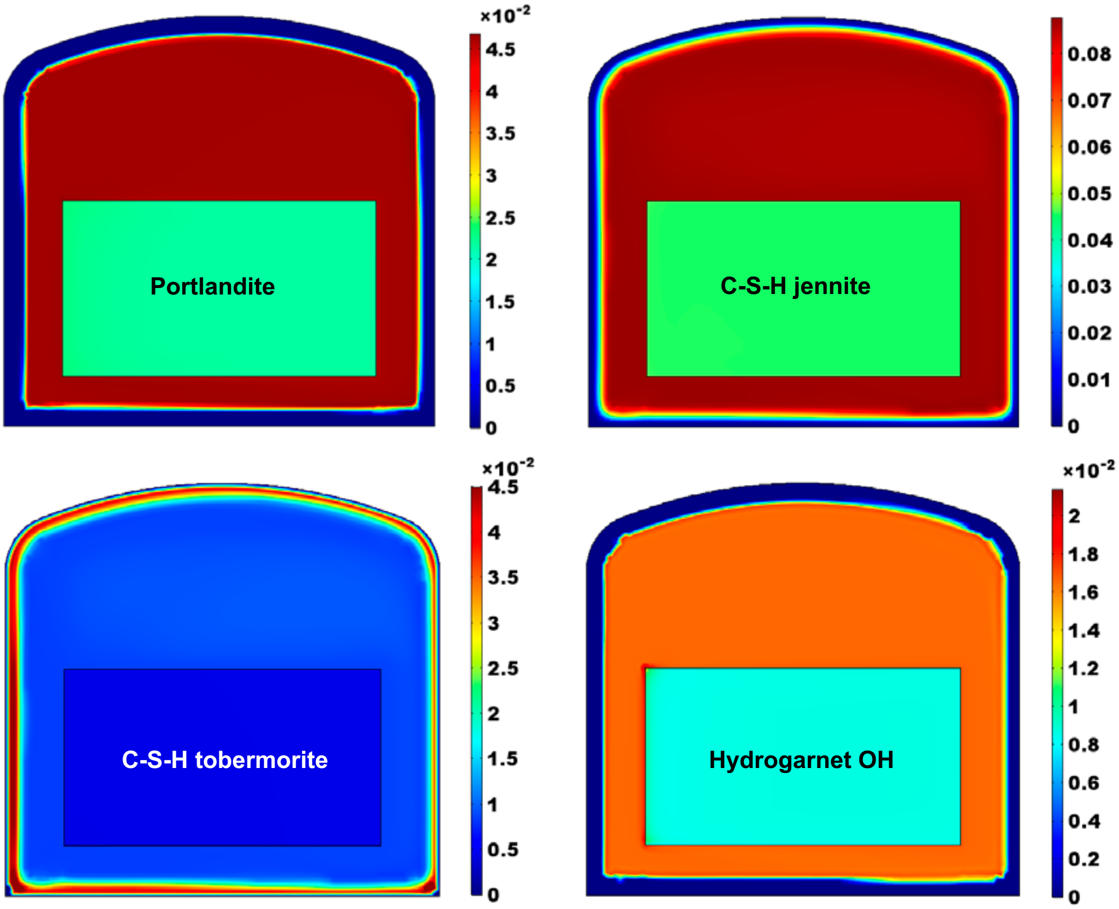

Figure 5-4. *Case I results: 2D spatial distribution of portlandite, C-S-H phases (end members of a solid solution), and hydrogarnet OH after 100 000 years, expressed in volume fraction (-). The dimensions are specified in Figure 5-1.*

Figure 5-5 and Figure 5-6 show the formation of secondary minerals in the concrete backfill after 100 000 years as a result of interaction with groundwater. First, an ettringite precipitation front is observed (up to 0.02 volume fraction), together with an important formation of strätlingite (up to 0.055 volume fraction, given its relatively large molar volume, i.e. 216 cm^3/mol). These phases consume the aluminium released by dissolution of monocarboaluminates and monosulfoaluminates. A small amount of thaumasite forms afterwards, followed by calcite formation at the interface with the rock and extending into the concrete backfill.

Figure 5-7 shows a 1D profile along the concrete backfill (see location in Figure 5-1) of the mineralogical phase assemblage after 100 000 years. This figure shows the sequence of mineral dissolution and precipitation described above. The porosity profile is also shown. In addition, the results of a sensitivity case are also presented in this figure. The only difference with Case I is that in this sensitivity case, porosity is calculated assuming that calcite formation has an impact on porosity clogging. Comparison of the results of Case I and the sensitivity case show that after 100 000 years the results are very similar in terms of degradation sequence and penetration depth of the degradation front. The main difference is of course the porosity profile in the regions where calcite formation is predicted. In the sensitivity case, maximum porosity is around 0.255 due to the effect of calcite, while in Case I it is 0.30.

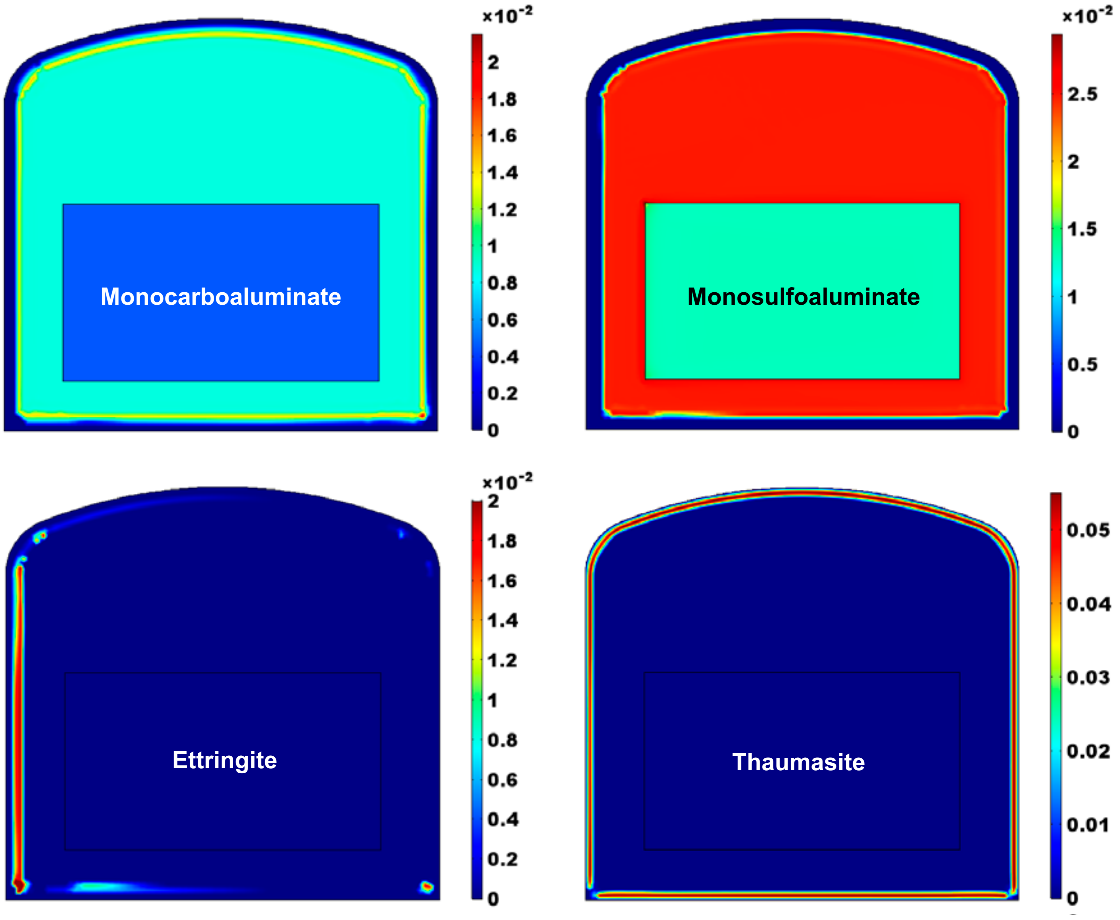

Figure 5-5. *Case I results: 2D spatial distribution of monocarboaluminate, monosulfoaluminate, and hydrotalcite OH after 100 000 years, expressed in volume fraction (-). The dimensions are specified in Figure 5-1.*

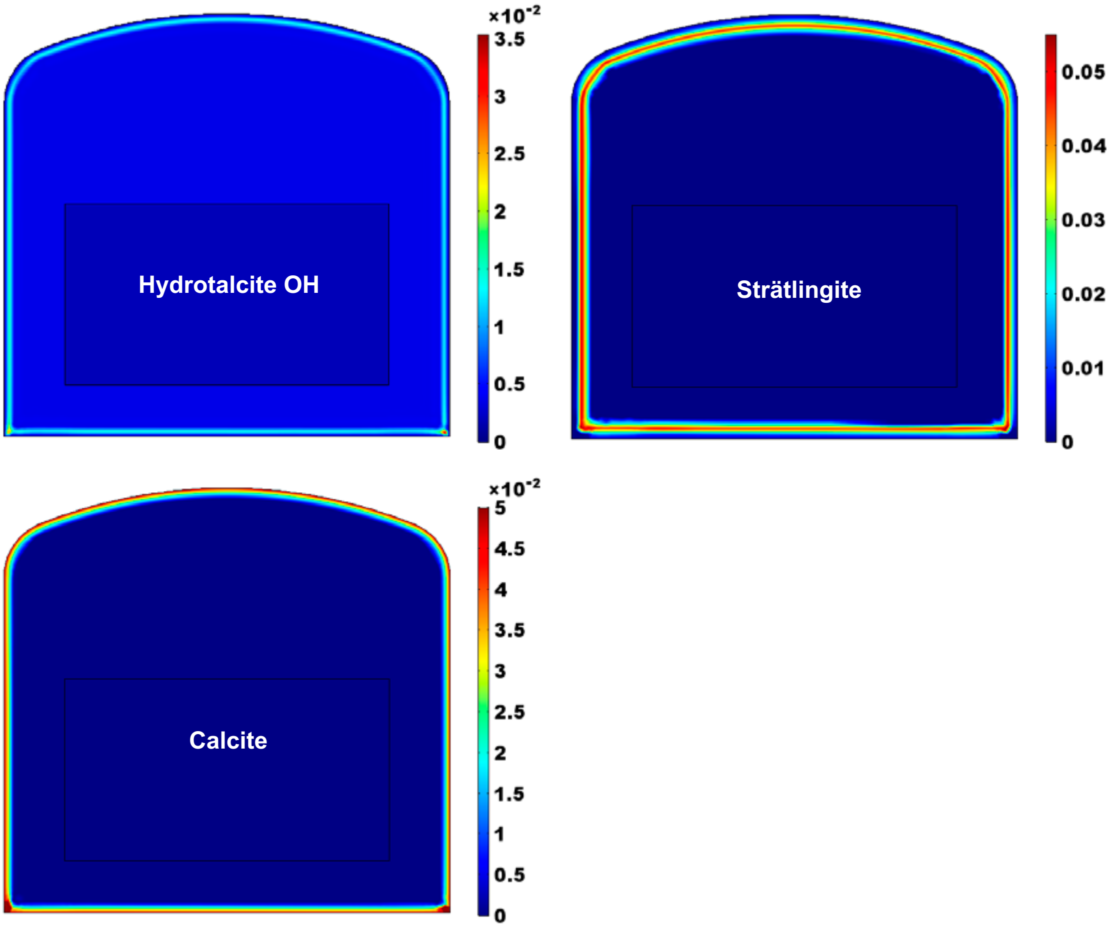

Figure 5-6. Case I results: 2D spatial distribution of ettringite, strätlingite, thaumasite, and calcite after 100 000 years, expressed in volume fraction (-). The dimensions are specified in Figure 5-1.

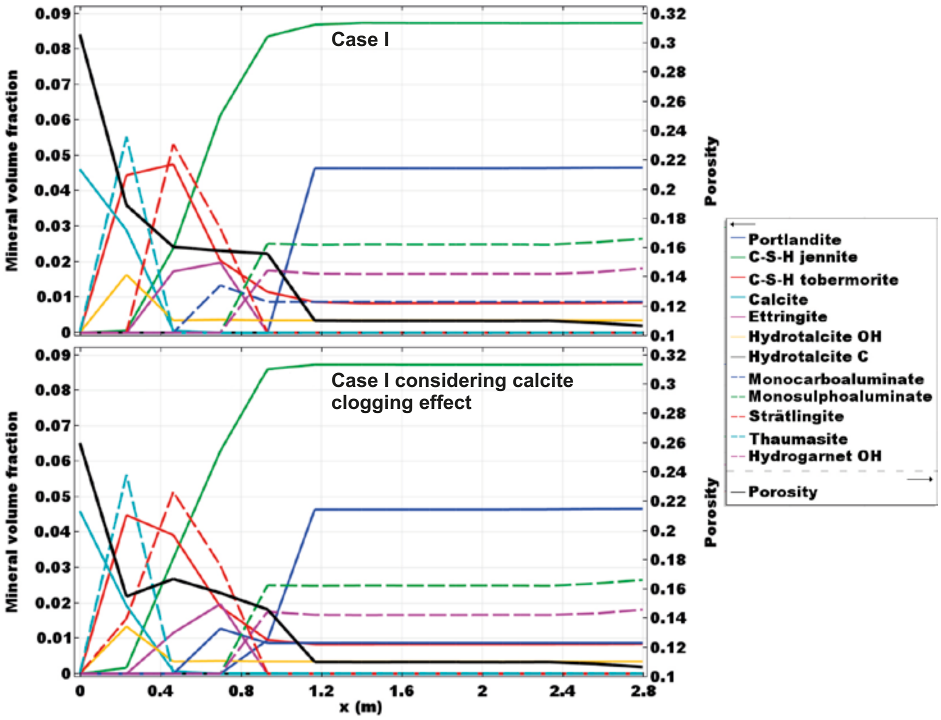

Figure 5-7. Case I results. Mineral volume fractions (-) and porosity after 100 000 years, spatial distribution in the concrete backfill (length in m). Results of a sensitivity case that considers porosity reduction due to calcite formation are also shown.

Mineralogical alteration has an important impact on porosity distribution, as shown in Figure 5-8 (see also Figure 5-20). The initial value of porosity (0.11) increases up to 0.30 at the concrete-rock interface. This is the maximum porosity that can be achieved with the current setup, which considers an inert volume fraction of ~0.7 (Table 5-2). Note that calcite is not accounted for in the calculation of porosity (see discussion in Section 5.1.1). The extent of increase in porosity along the concrete backfill is up to 1.20 m from the interface with the rock. The remaining concrete backfill has a porosity that is equal to the initial value.

The pH distribution after 100 000 years is also shown in Figure 5-8. Total leaching of the alkalis from the pore solution of the concrete backfill and waste domain leads to a maximum pH that is reduced from the initial value of 13.33 to 12.50 after 100 000 years (corresponding to equilibrium with portlandite). On the other hand, the pH at the concrete-rock interface drops to values around 8.5 that correspond to the groundwater composition.

Final values for transport properties are presented in Figure 5-9 in terms of effective diffusion coefficient and hydraulic conductivity. Maximum values at the interface with the host rock are $D_e = 4.5 \times 10^{-11}$ m²/s and $K = 2.9 \times 10^{-8}$ m/s.

In the following, selected results of simulation Cases II to IV are presented and compared with Case I.

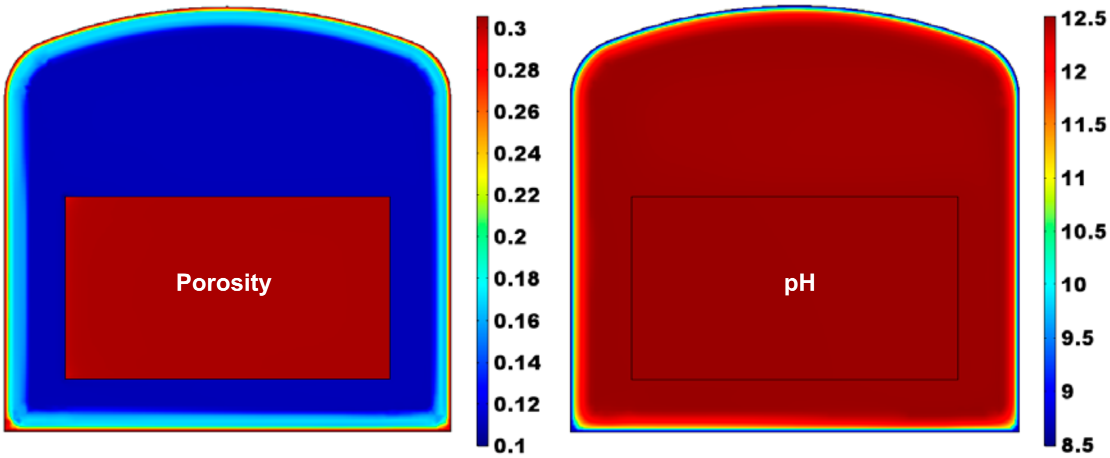

Figure 5-8. *Case I results: 2D spatial distribution of porosity and pH after 100 000 years. The dimensions are specified in Figure 5-1.*

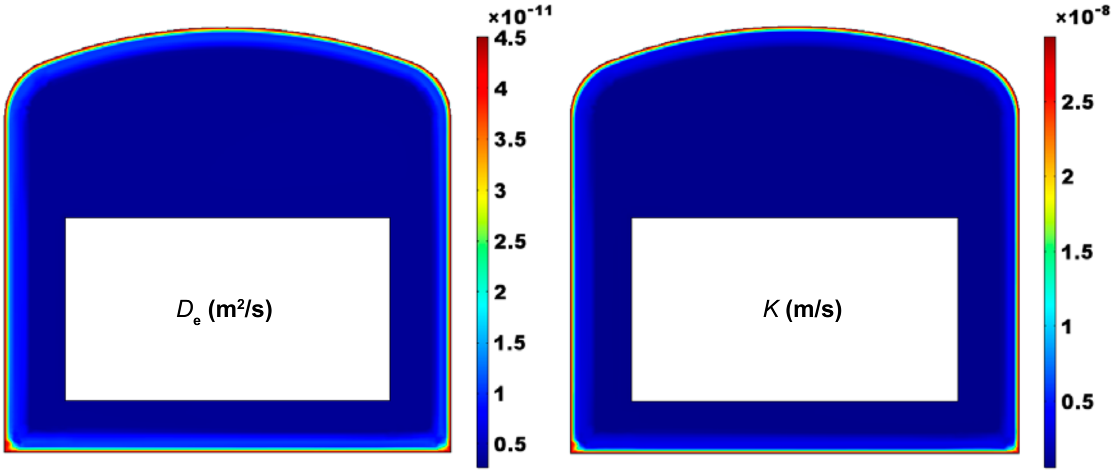

Figure 5-9. *Case I results: 2D spatial distribution of effective diffusion coefficient (m²/s) and hydraulic conductivity (m/s) after 100 000 years. The dimensions are specified in Figure 5-1.*

5.2.2 Case II

Case II considers the same cement composition as Case I, the main difference being the increase in water-to-cement ratio from 0.47 (Case I) to 0.63 (Case II). Two cases with a w/c ratio of 0.63 have been simulated, either using 320 (Case IIa) or 280 (Case IIb) kg of cement per m^3 of concrete in the concrete mix. These cases have the same phase assemblage as Case I, but with a reduction of the mineral concentrations due to a higher w/c ratio (Table 5-2). This reduction is of ~15 % in Case IIa and ~25 % in Case IIb. Different aggregate volume fractions are also used in each case (Table 5-2), which has an impact on concrete initial porosity. Initial porosity values are 0.11, 0.1297 and 0.1135 for Case I, Case IIa and Case IIb, respectively. The inert mineral fraction accounting for ballast content is also different, being ~0.70 for the first two cases and over 0.74 for Case IIb.

The results of Case IIa (Figure 5-10) and Case IIb (Figure 5-11) are therefore very similar to Case I in terms of degradation sequence. The lower volume fraction of the initial cement hydrates compared to Case I also has the effect of reducing the volume fraction of secondary minerals formed. Moreover, higher initial porosities lead to increased values for transport properties, thereby increasing the rate of degradation. As a result, the main effect of increasing the w/c ratio is a larger penetration of the degradation front. However, this is more evident at longer times (see Section 5.3). The differences between Case IIa and Case IIb are small despite the differences in initial porosity and phase assemblage concentrations. Again, larger differences are observed after longer times (see Section 5.3).

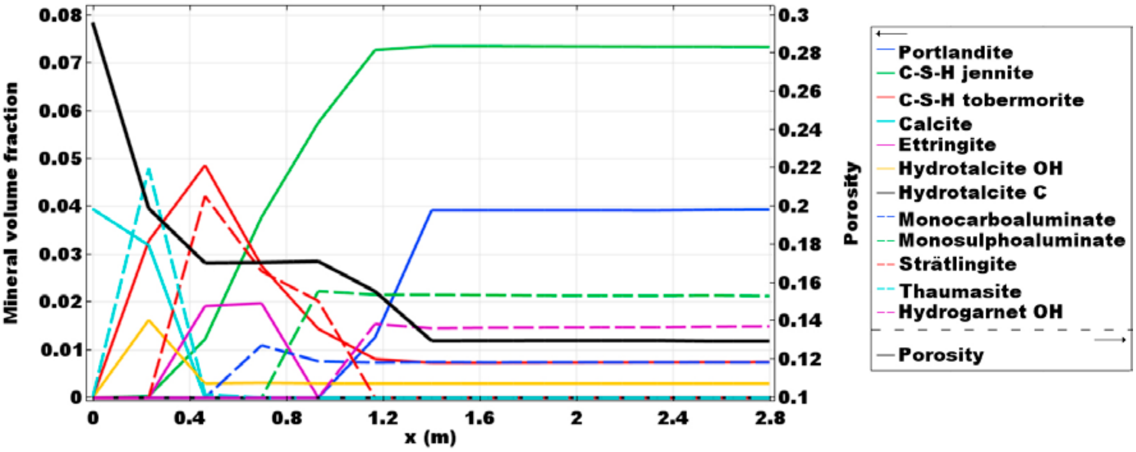

Figure 5-10. Results of Case IIa. Mineral volume fractions (-) and porosity (-) after 100 000 years, spatial distribution in the concrete backfill (length in m).

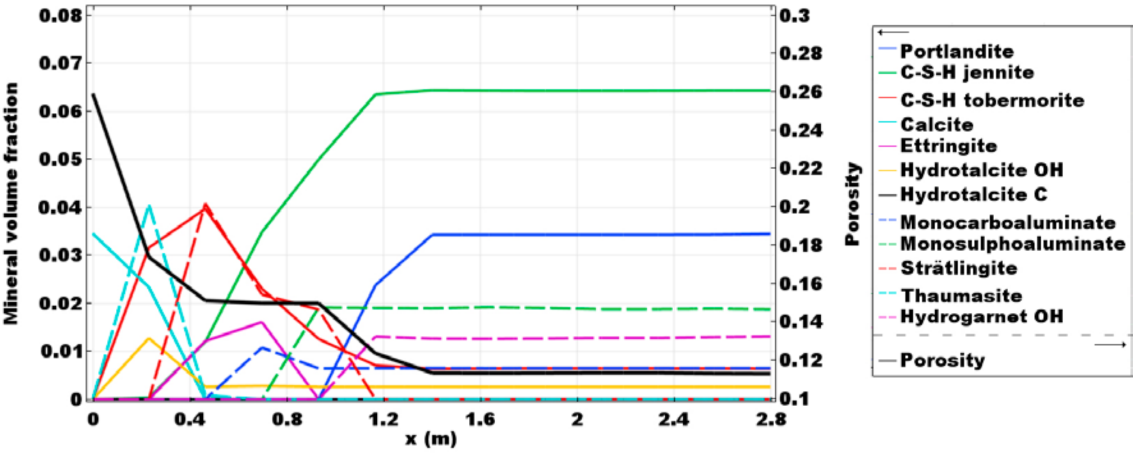

Figure 5-11. Results of Case IIb. Mineral volume fractions (-) and porosity (-) after 100 000 years, spatial distribution in the concrete backfill (length in m).

5.2.3 Case III

Case III considers the use of Bascement Slite, which is a CEM II with 12.3 wt% of fly ash. This case differs from Case I due to its initially different hydrate phase assemblage. Figure 5-12 shows the 2D distribution of minerals of Case III after 100 000 years. The formation of C-A-S-H phases is a distinguishing feature in this case (especially the one with highest Ca/Si ratio). As a result, less strätlingite is formed.

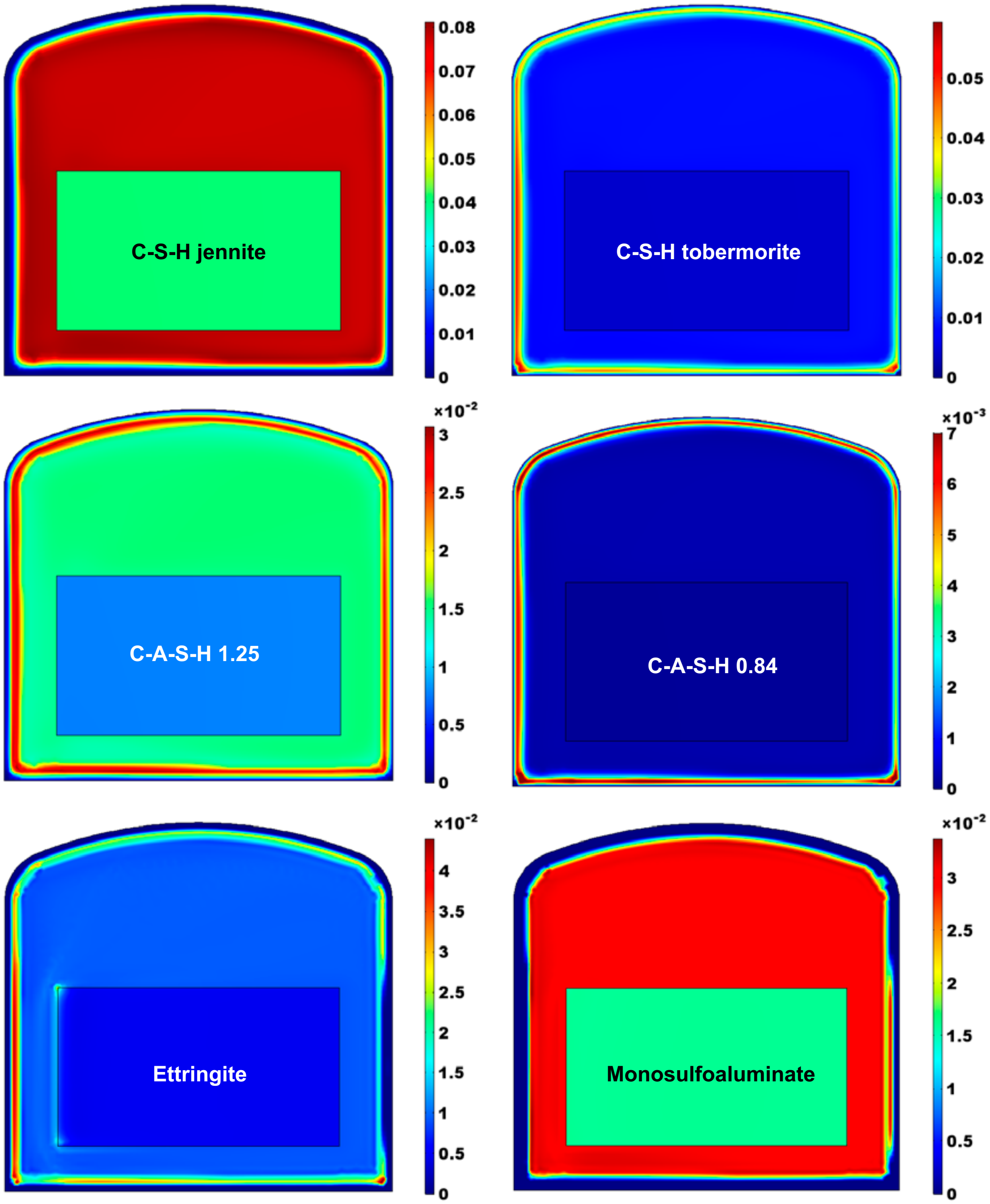

Figure 5-12. *Case III results: 2D spatial distribution of C-S-H and C-A-S-H phases, and ettringite and monosulfoaluminate after 100 000 years, expressed in volume fraction (-). The dimensions are specified in Figure 5-1.*

Monosulfoaluminate and monocarboaluminate are destabilised near the groundwater source, dissolving completely in the first 0.7 m and 0.5 m, respectively (Figure 5-13). As a result, ettringite forms in this region, with larger volume fractions than in Case I (up to 0.044 in this case), although ettringite is initially present in Case III. A very small amount of thaumasite is also formed in a narrow region behind the ettringite precipitation front. Later, ettringite dissolves from the interface with the host rock, with the dissolution front at 0.24 m from this interface. Portlandite also dissolves completely in the first 0.94 m (Figure 5-13). As in Case I, mineral dissolution/precipitation reactions occur to a larger extent on the left side of the concrete backfill, which is due to the effect of groundwater flow.

5.2.4 Case IV

The effect of a large replacement of cement with limestone (26.9 wt%) and dolomite (6.9 wt%) in the concrete mix on long-term degradation is studied in Case IV. The hydrated composition of concrete contains in this case an initial volume fraction of calcite of 0.059 (dolomite is completely dissolved during hydration, partly forming additional calcite, see Section 4.2.3). In this case, important differences can be found with respect to the OPC CEM I cases (Case I and Case IIa and IIb). The addition of limestone filler leads to a lower porosity than the OPC system, resulting in lower hydraulic conductivity and diffusivity values.

The results show an ettringite dissolution front, followed by a thaumasite precipitation front with higher volume fraction (Figure 5-14 and Figure 5-15). However, after 100 000 years this can only be observed on the left-hand side of the concrete backfill (Figure 5-14). On the other hand, ettringite follows a clear non-symmetric pattern and dissolves more slowly on the right side.

Calcite distribution shows a precipitation peak at the interface with the host rock (Figure 5-14 and Figure 5-15). After 100 000 years strätlingite does not form as a result of the degradation sequence, as opposed to Case I. A more detailed comparison is given in the next section.

5.2.5 Comparison of results

The comparison of the different simulation cases is summarised in this section with a set of 1D profiles (see Figure 5-1) of key minerals and parameters after 100 000 years. Figure 5-16 to Figure 5-18 present a comparison between the five models of the distribution of portlandite, C-S-H jennite and C-S-H tobermorite gels, respectively. Note that initial volume fractions are different for each case (Table 5-2). As can be observed, no significant differences in the degradation fronts can be identified for Cases I to III after 100 000 years of interaction with groundwater.

An exception is Case IV, in which the portlandite dissolution front (Figure 5-16) advances slower than in other cases due to the significantly lower porosity (see Figure 5-20). In all cases portlandite is present in more than a half of the backfill thickness.

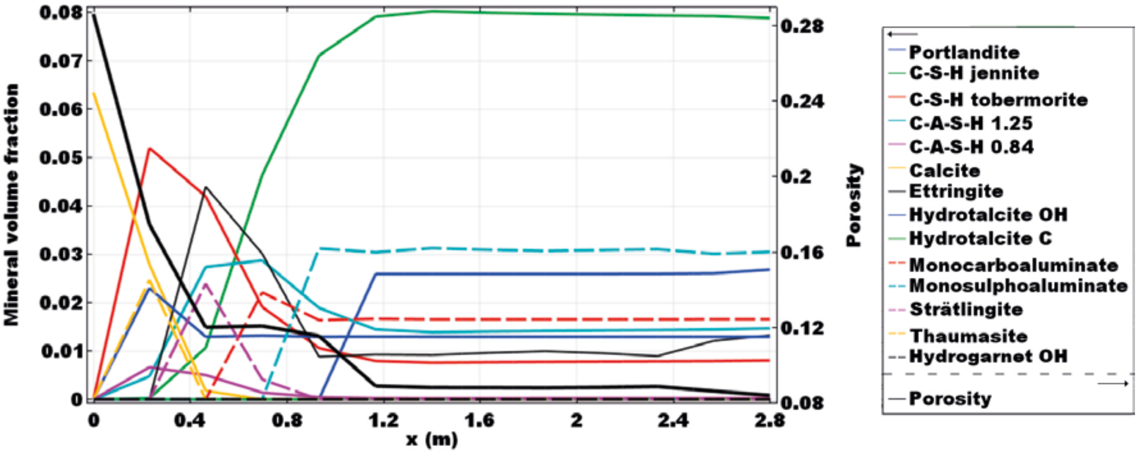

Figure 5-13. *Case III. Mineral volume fractions (-) and porosity (-) after 100 000 years, spatial distribution in the concrete backfill (length in m).*

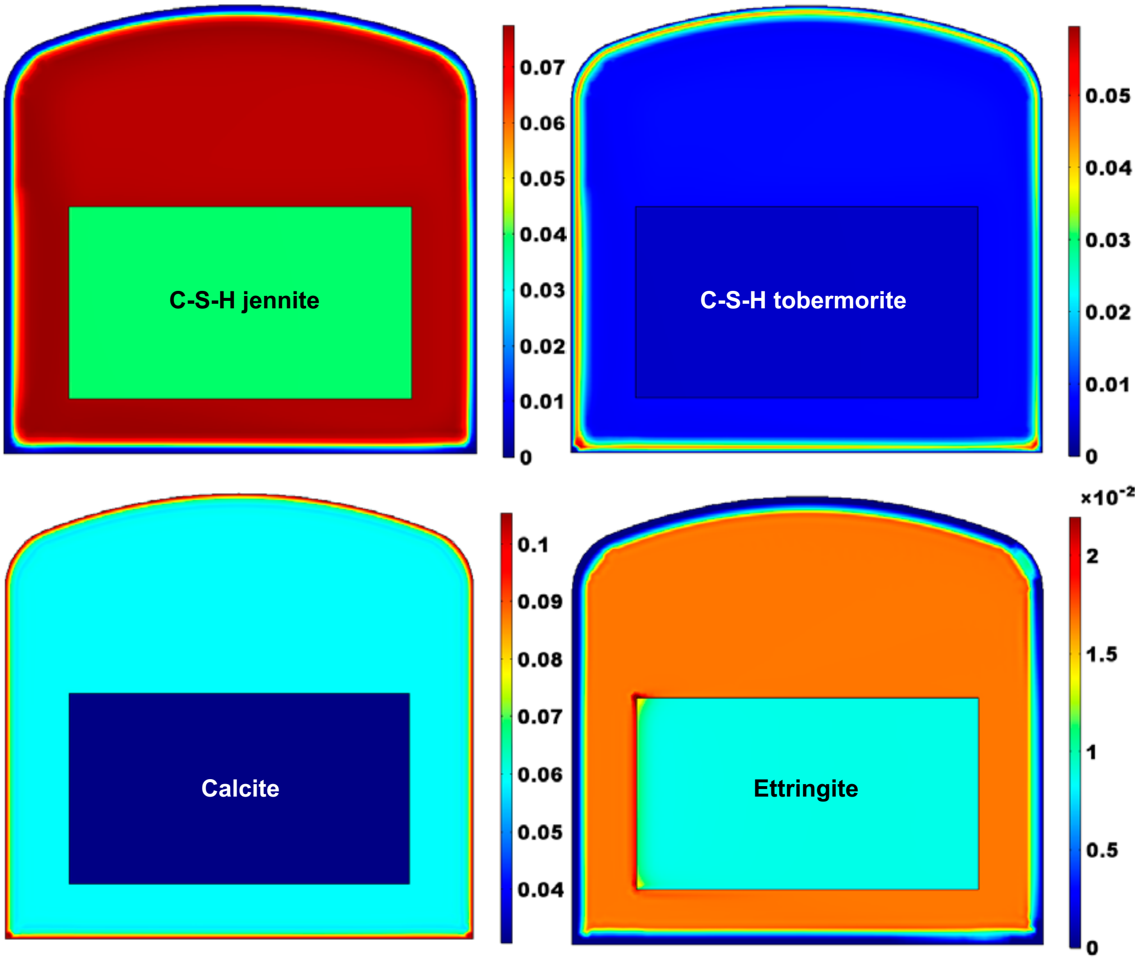

Figure 5-14. Case IV results: 2D spatial distribution of C-S-H phases, calcite and ettringite after 100 000 years, expressed in volume fraction (-). The dimensions are specified in Figure 5-1.

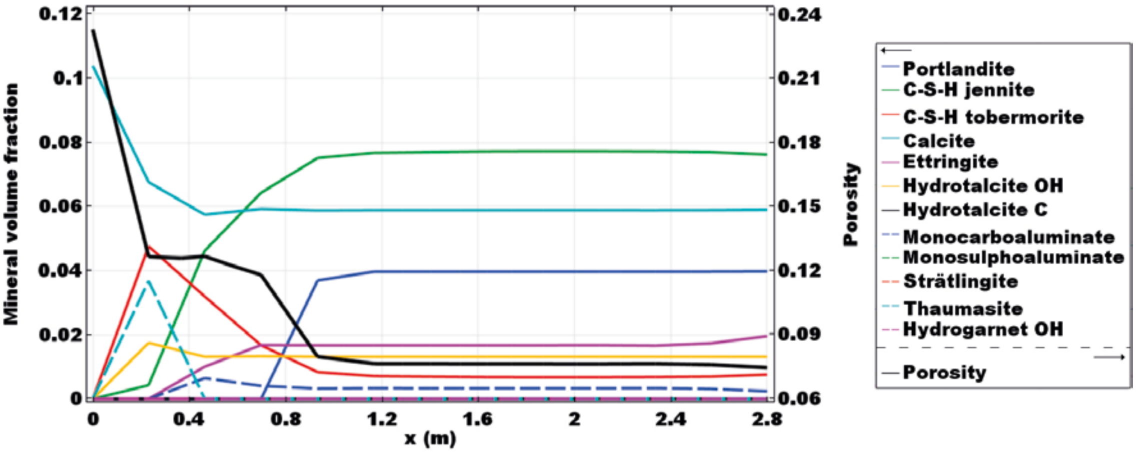

Figure 5-15. Case IV. Mineral volume fractions (-) and porosity (-) after 100 000 years, spatial distribution in the concrete backfill (length in m).

The high Ca/Si ratio end-member of the C-S-H solid solution, i.e. C-S-H jennite, shows a dissolution pattern that is more homogeneously distributed along the backfill thickness in all cases (Figure 5-17). The initial difference in volume fraction between modelled cases does not have a significant impact on the front of complete dissolution. However, the cases with higher initial volume fraction have a sharper dissolution front (Figure 5-17). The profiles of the low Ca/Si ratio end-member of the C-S-H solid solution, i.e. C-S-H tobermorite, are of course linked to jennite dissolution profiles (Figure 5-18). In all cases the peak value is around 0.05 and is located between 0.24 m and 0.48 m from the rock interface. The only case with a smaller peak value is Case IIb, which is due to the lower initial volume fraction of C-S-H gel.

Figure 5-19 presents the 1D profiles of pH after 100 000 years, which shows a remarkable agreement between all the simulation cases despite their different mineralogical compositions. This is not surprising given the similarities between the different portlandite and C-S-H gels profiles. In Case IV, pH values are slightly higher due to the lower values of transport properties.

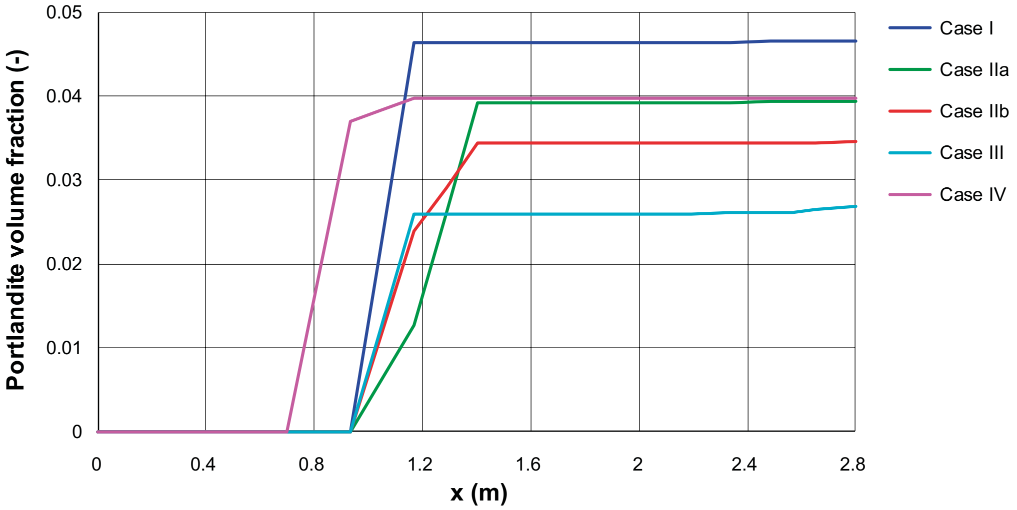

***Figure 5-16.** Portlandite dissolution fronts in terms of volume fraction after 100 000 years, spatial distribution in the concrete backfill (length in m) for the 5 simulated cases.*

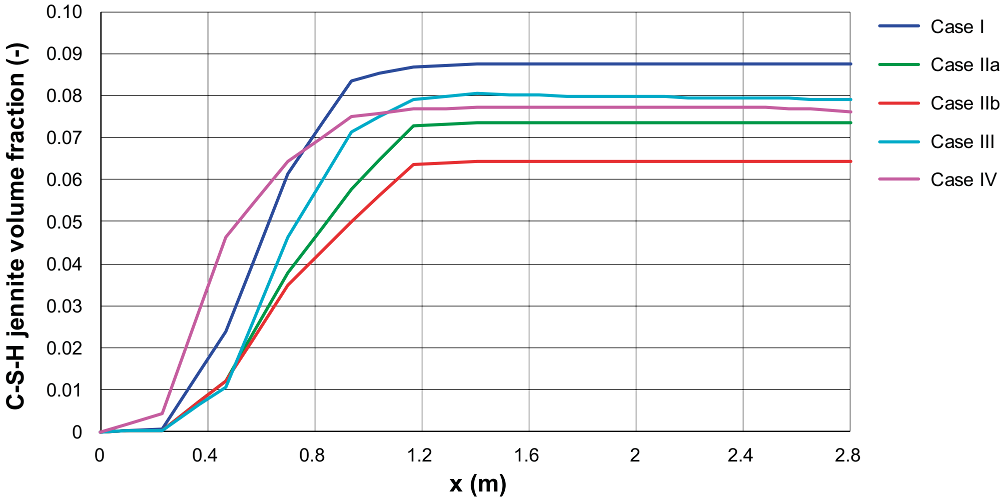

***Figure 5-17.** C-S-H jennite dissolution fronts in terms of volume fraction after 100 000 years, spatial distribution in the concrete backfill (length in m) for the 5 simulated cases.*

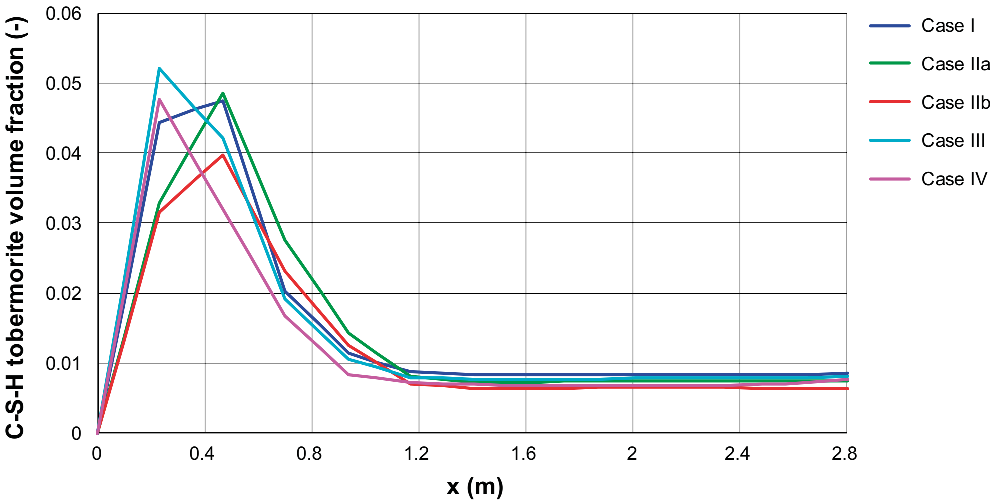

Figure 5-18. *C-S-H tobermorite profiles in terms of volume fraction after 100 000 years, spatial distribution in the concrete backfill (length in m) for the 5 simulated cases.*

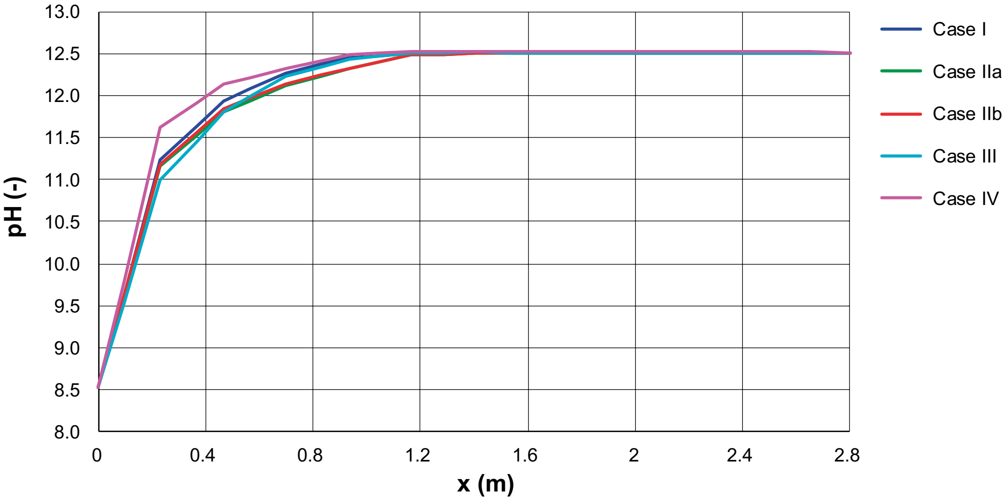

Figure 5-19. *pH (-) spatial distribution in the concrete backfill after 100 000 years, comparison between the results of the 5 simulated cases.*

Comparison plots of porosity and transport properties, i.e. effective diffusion coefficient and hydraulic conductivity, are presented in Figure 5-20, Figure 5-21 and Figure 5-22, respectively. Qualitatively, very similar porosity profiles between modelled cases are observed in Figure 5-20. On the right-hand side, the initial porosity values are shown, and the influence of different concrete mixes is more noticeable. Case IV is the case with initially lowest porosity and thus where the degradation front has the lowest impact on porosity increase. Highest porosity values are observed at the concrete-rock interface, where interaction with groundwater is highest. Values at this interface correspond to the situation where no reactive minerals are left, and only the inert mineral fraction remains (mainly the aggregates). Note that the maximum porosity of Case IIa and Case IIb differs due to their different aggregate volume fractions (0.7 in Case IIa and 0.74 in Case IIb), which result from different concrete mixes. Maximum values reached in Case IV (with limestone addition) are lower due to the substantial volume fraction initially occupied by calcite that remains intact.

The effective diffusion coefficient (m^2/s) in Figure 5-21 and the hydraulic conductivity (m/s) in Figure 5-22 follow a distribution similar to the porosity profiles, which is due to the direct relation between these parameters (Equation 5-1 and 5-2).

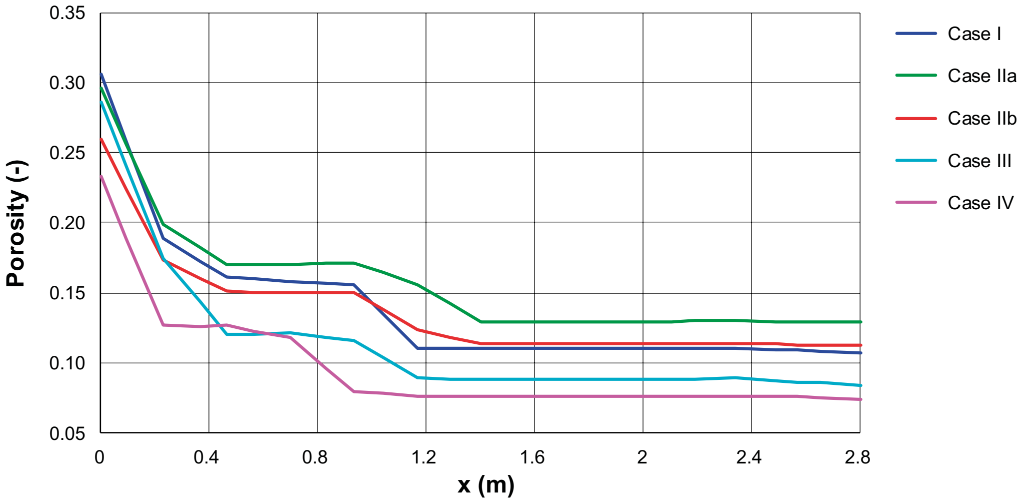

Figure 5-20. *Porosity (-) spatial distribution in the concrete backfill after 100 000 years, comparison between the results of the 5 simulated cases.*

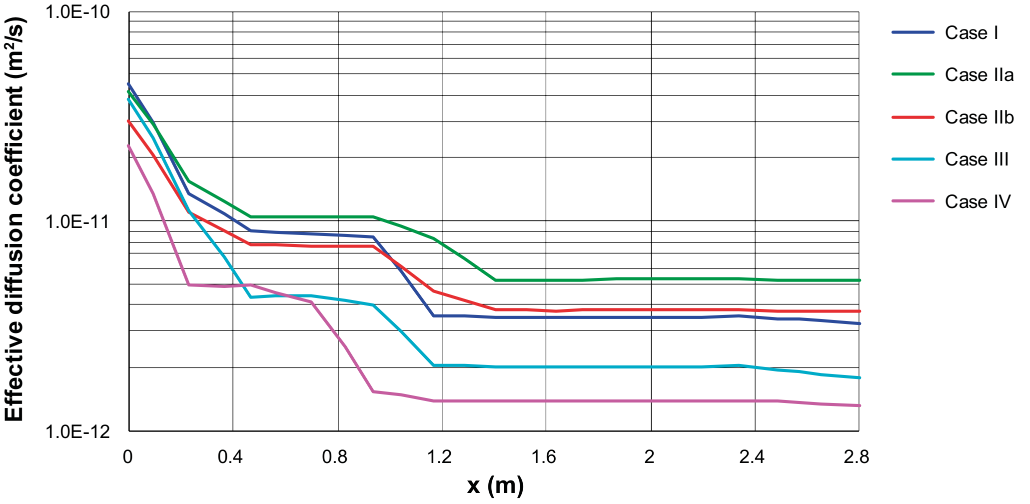

Figure 5-21. *Effective diffusion coefficient (m^2/s) spatial distribution in the concrete backfill after 100 000 years, comparison between the results of the 5 simulated cases.*

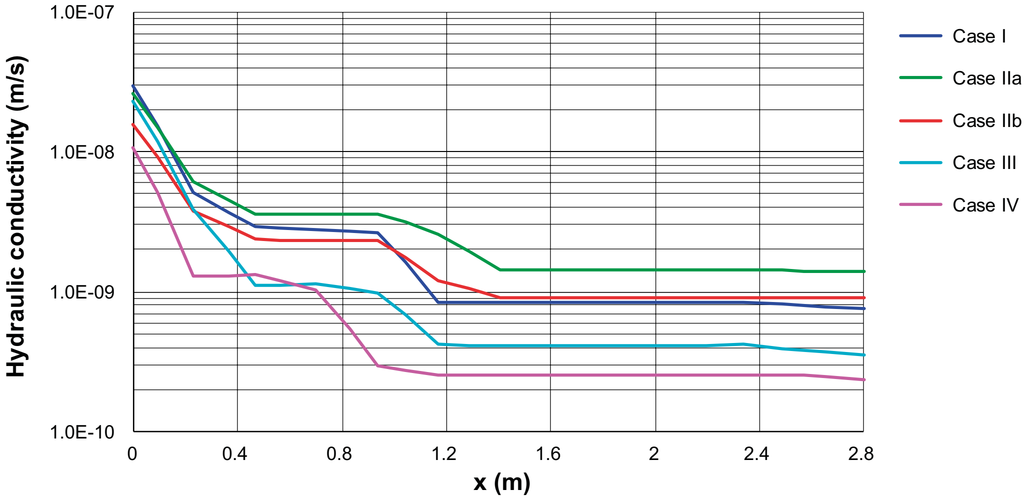

Figure 5-22. *Hydraulic conductivity (m/s) spatial distribution in the concrete backfill after 100 000 years, comparison between the results of the 5 simulated cases.*

5.3 Results for 1D models of concrete backfill

This section presents the results of the 1D reactive transport simulations over 1 million years (Table 2-1). The same modelling cases as in Section 5.2 are simulated in terms of concrete composition, from Case I to Case IV. As in Section 5.2, a complete description of Case I results is shown first. Thereafter, comparison between the five different concretes is made in terms of distribution of specific minerals and equivalent key parameters.

5.3.1 Case I

An in-depth description of the degradation processes for Case I is given from Figure 5-23 to Figure 5-28. First, mineral dissolution/precipitation is analysed. In Figure 5-23 the mineral assemblage in the concrete backfill is shown at different times. After half million years of degradation, portlandite and C-S-H jennite are completely depleted, while C-S-H tobermorite is completely dissolved in the first 0.8 m from the concrete-rock interface.

A large amount of calcite precipitates close to the interface with the host rock. After several hundreds of thousands of years, smaller fractions of calcite also form along almost the entire thickness of the backfill, where also hydrotalcite C forms. It is noted that calcite formation as a result of carbonation is not accounted for in porosity calculations. This assumption is considered to yield a conservative estimate of the fluid flow and transport properties, by not relying on the positive effect of carbonation on decreasing the transport properties (see discussion in Section 5.1.1).

Strätlingite and ettringite formation are also important in the simulation. After 500 000 years, their precipitation fronts reach the backfill-waste interface, while their redissolution fronts are located at 1 m and 2 m from the rock interface, respectively. Hydrotalcites also form at advanced states of degradation, between 0.2 m and 0.6 m after 500 000 years.

The mineral assemblage after 1 million years shows a near complete degradation of the concrete backfill, with a small fraction of C-S-H tobermorite in the last 0.5 m. Otherwise, calcite and small amounts of hydrotalcites and brucite are the only phases present.

Similar conclusions can be drawn from the results in terms of time evolution. Figure 5-24 shows the time evolution of the mineral phases at 1.4 m and 2.8 m from the concrete rock interface.

The degradation sequence can be clearly identified from this figure. This sequence is similar at both observation points, though the time scales are different. The first mineral to dissolve is portlandite, which is completely depleted at 1.4 m after 200 000 years. Complete portlandite dissolution triggers the decalcification process of the C-S-H gel solid solution. C-S-H jennite starts dissolving after 200 000 years and is completely depleted after 420 000 years. On the other hand, C-S-H tobermorite starts precipitating after 200 000 years and continues to form during several hundreds of thousands of years until reaching a volume fraction of 0.094. C-S-H tobermorite volume fraction reaches its maximum with strätlingite depletion and then gradually dissolves until complete depletion after 800 000 years. Portlandite depletion also triggers a rapid dissolution of hydrogarnet OH and strätlingite formation. Following hydrogarnet OH depletion after 230 000 years, monosulfoaluminate also starts dissolving and triggers ettringite formation which lasts for 200 000 more years. A small amount of thaumasite formation is also predicted. Monocarboaluminate dissolves in 300 000 years, followed by a small amount of calcite precipitation. Calcite rapidly redissolves, the dissolved carbon giving rise to thaumasite formation. In turn, after half million years, thaumasite starts dissolving and calcite forms again, but this time as a result of the carbonation process. Hydrotalcite (in its OH and C form) is the most stable mineral of the system and remains throughout the simulated time.

The pH evolution at x = 1.4 m in Figure 5-24 is intimately linked to the dissolution/precipitation sequence described above. After a relatively rapid leaching of alkalis in less than 10 000 years, pH drops from the initial value of 13.3 to 12.5, with the pore solution being in equilibrium with portlandite. After complete portlandite dissolution (at 200 000 years), pH shows a decreasing trend following the evolution of the C-S-H solid solution. A stabilization at pH 10.5 is reached once the C-S-H solid solution is fully composed of C-S-H tobermorite, after 480 000 years. The pH value remains stable at 10.5 as long as there is C-S-H tobermorite present. Complete dissolution of this phase is predicted after 800 000 years. At this point, pH continues its decreasing trend until reaching a value that is the same as the pH of the groundwater.

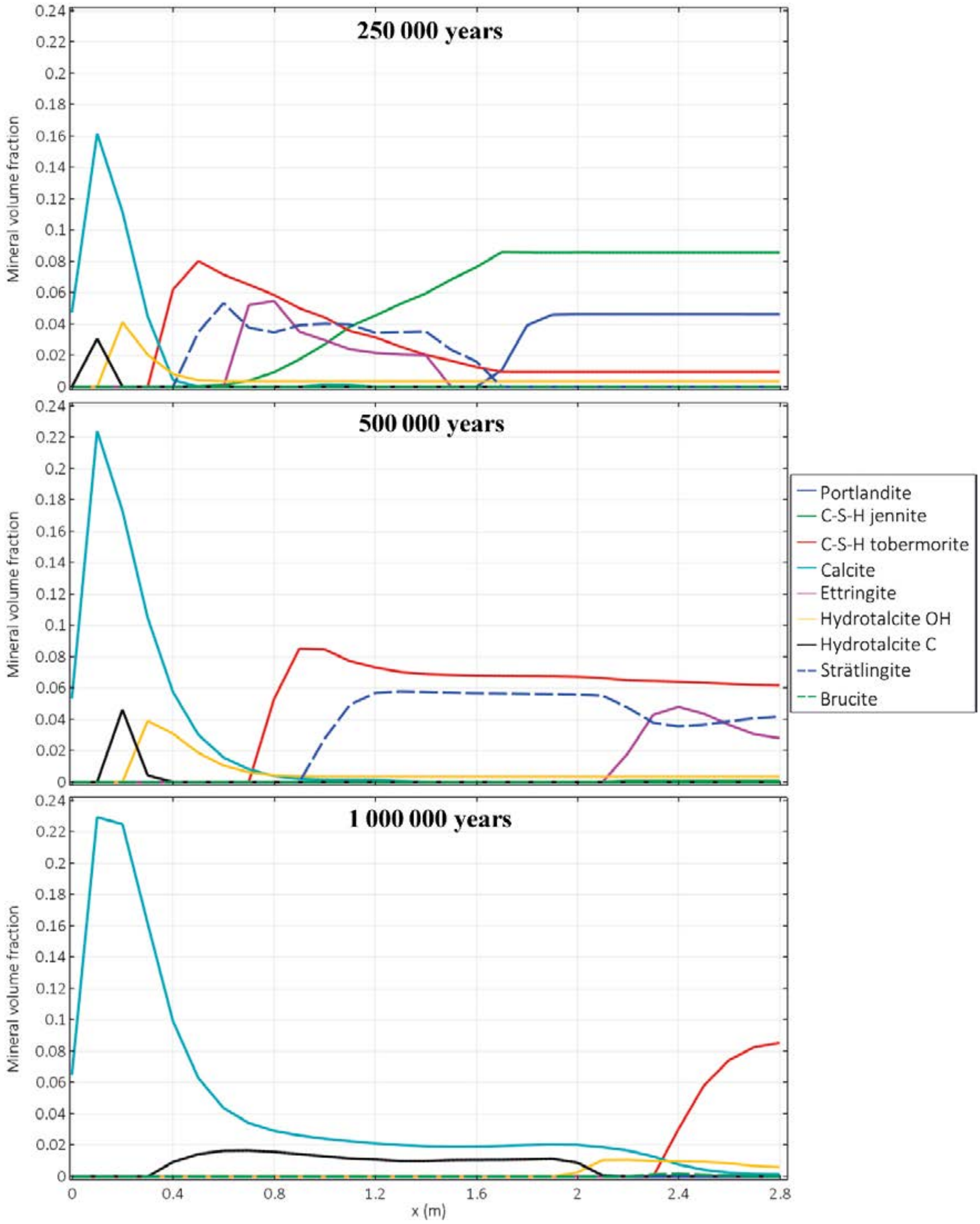

***Figure 5-23.** Case I results. Spatial distribution (length in m) in the concrete backfill of mineral volume fractions at different times (250 000, 500 000 and 1 million years).*

A different temporal evolution of the same sequence of mineral assemblage is observed at x = 2.8 m, i.e. the backfill-waste interface (Figure 5-24). The degradation process is qualitatively the same than at x = 1.4 m, but with two noticeable differences. The distance between the two points results in a lower degree of degradation at x = 2.8 m, and after 1 million years the degradation sequence is not complete at this point. C-S-H tobermorite and hydrotalcite OH do not dissolve and thus small values of calcite are observed. The second and most important difference is the higher degradation rate compared to the first observation point. Although degradation starts later, the time between the start of portlandite dissolution and complete depletion of C-S-H jennite is significantly reduced. Dissolution of the main primary minerals and precipitation of secondary ones occur in a time frame of ~ 50 000 years. This is explained by an increase of the Darcy velocity across the concrete backfill with time. The rate of degradation processes at a given point is closely related to the distance to the groundwater source. The increase of the Darcy velocity is of course a consequence of the increase in porosity and evolution of transport properties. The time frame between complete depletion of portlandite and C-S-H jennite at x = 2.8 m is roughly half of the time needed at x = 1.4 m. In turn, water interstitial velocity duplicates during the time between these two points reach portlandite dissolution.

Figure 5-25 shows 1D profiles of pH values at different times from 0 to 1 million years. pH evolution with time is directly related with the depletion and appearance of the different mineral phases (Figure 5-23). pH values decrease from the initial value of 13.3 to 12.5 in the entire domain, due to leaching of the alkalis before 100 000 years. The value of 12.5 corresponds to the equilibrium with portlandite. Thereafter, progressive decalcification of C-S-H with higher C/S ratio governs the system pH until the total depletion of C-S-H jennite, which gives rise to a period wherein pH is buffered around 10.5 controlled by C-S-H with lower C/S (tobermorite). Dissolution of tobermorite leads to a situation in which pH follows an eventual decrease as it is mainly controlled by calcite and finally groundwater composition.

Porosity evolution resulting from mineral volume changes is shown in Figure 5-26. Maximum values of porosity of 0.3 are reached when all the cement hydrates are dissolved (calcite volume fraction is not accounted for in porosity calculations, see above). As shown in Figure 5-26, porosity increases from left to right and after 500 000 years, only the last 1.6 m presents porosity values under 0.18. After 1 million years, the entire backfill is severely degraded, with a porosity of 0.29, except in the last 0.5 m, with a value of 0.21.

Effective diffusion coefficient and hydraulic conductivity are presented in Figure 5-27 and Figure 5-28, respectively. Transport properties are directly related with porosity and its evolution. Maximum values reached in the concrete domain are 4.5×10^{-11} m²/s and 2.9×10^{-8} m/s, respectively. After 1 000 000 years, minimum values (on the right boundary) are 1.9×10^{-11} m²/s and 7.9×10^{-9} m/s, respectively.

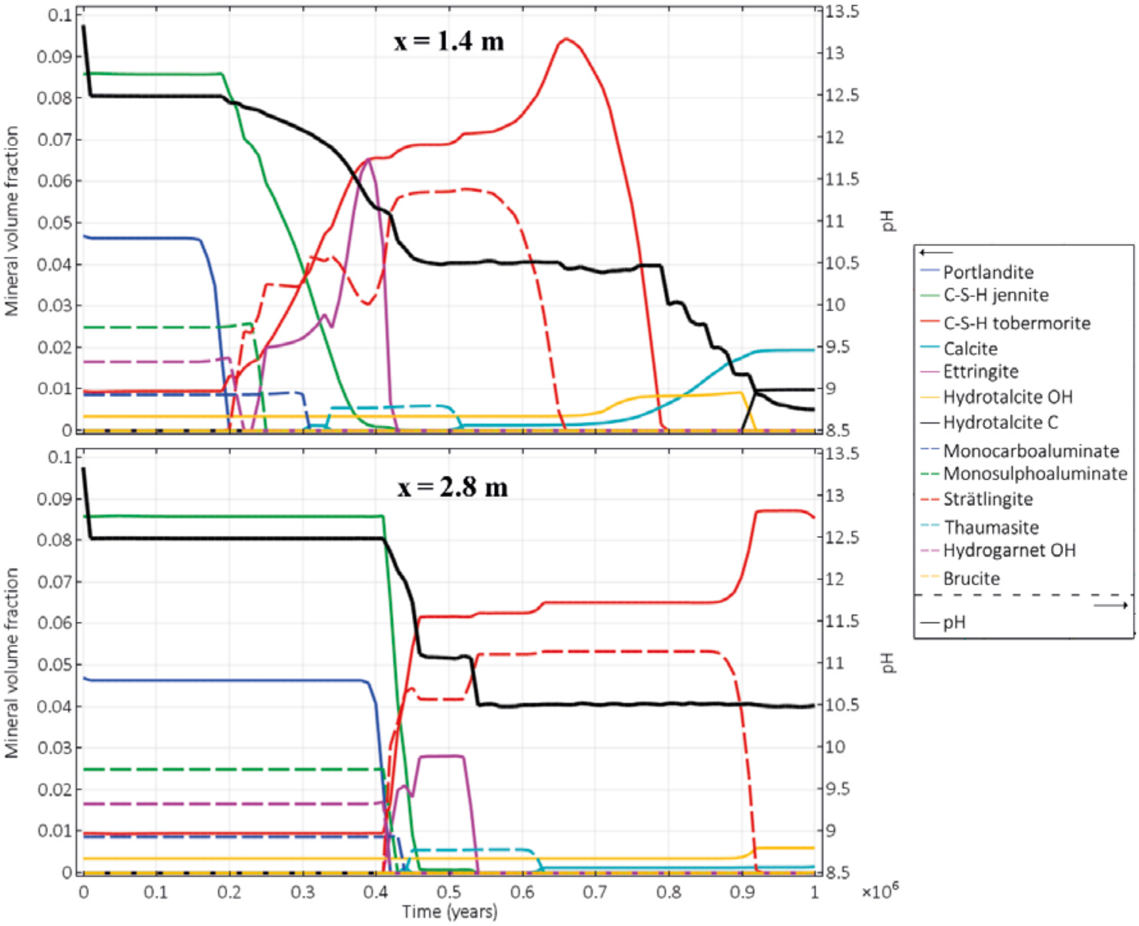

***Figure 5-24.** Mineral volume fractions and pH evolution with time (years) at different point of the concrete backfill. Results for x = 1.4 m (outer-inner interface) in the upper graph and for x = 2.8 m (right boundary) in the lower part.*

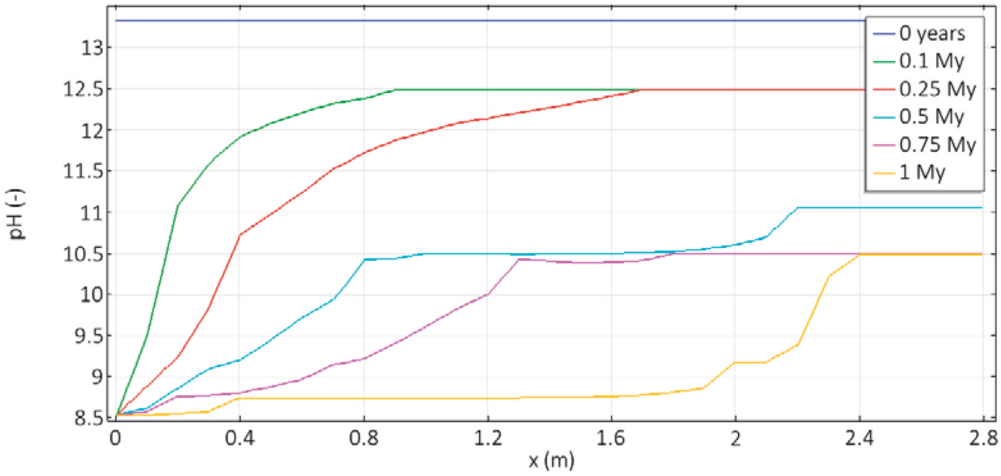

Figure 5-25. pH (-) spatial distribution in the concrete backfill at different times.

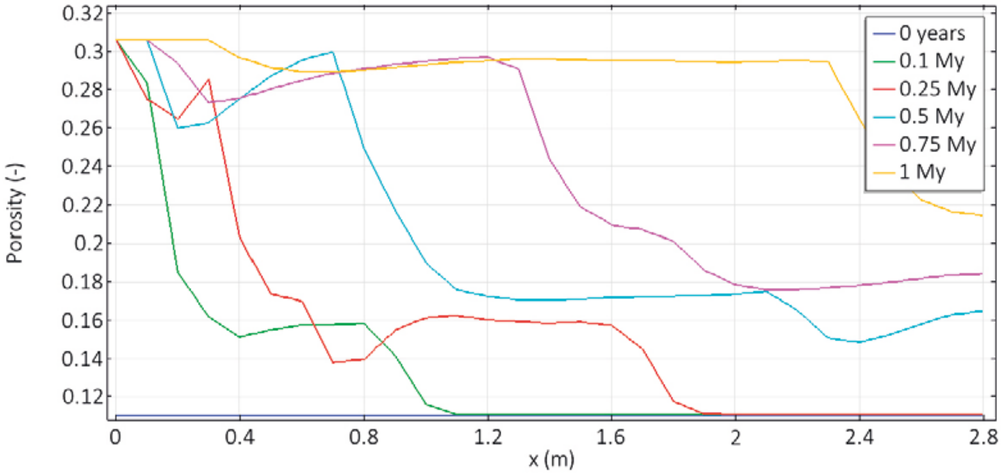

Figure 5-26. Porosity (-) spatial distribution in the concrete backfill at different times.

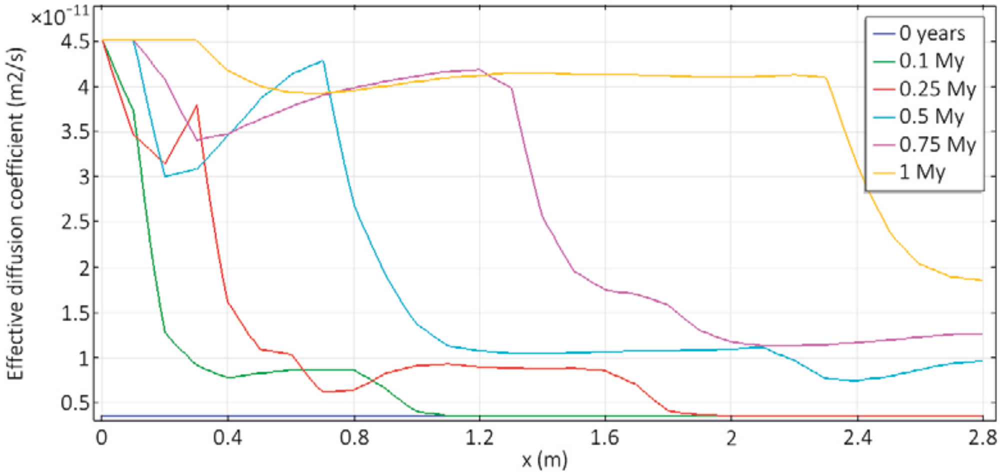

Figure 5-27. Effective diffusion coefficient (m^2/s) spatial distribution in the concrete backfill at different times.

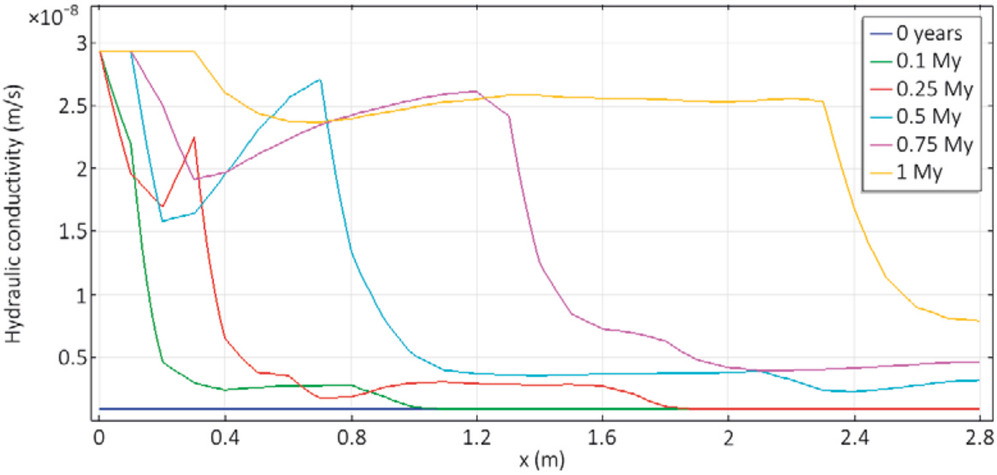

Figure 5-28. *Hydraulic conductivity (m/s) spatial distribution in the concrete backfill at different times.*

5.3.2 Case II

Case II considers the effect of a higher w/c ratio. Case II results are presented in Figure 5-29 to Figure 5-32. The first two figures correspond to Case IIa, while the remaining two figures to Case IIb (see Table 2-1 and Section 5.2.2 for details). The analysis of the results is based on a comparison with Case I in terms of mineralogical variations. As expected, the three cases qualitatively show the same chemical degradation sequence.

Figure 5-29 presents the mineral distribution in the concrete backfill for Case IIa after 250 000, 500 000 and 1 million years. Clearly, the higher porosity and higher values of transport properties resulting from an increase in the w/c ratio leads to a faster degradation process compared to Case I. This is reflected for instance in the advancement of the C-S-H tobermorite dissolution front, which in Case I is positioned at 0.7 m after 500 000 years while for Case IIa it is at ~ 1.2 m. After 1 million years, C-S-H tobermorite is completely absent in the backfill in Case IIa, while in Case I it is still present in the last 0.5 m. Figure 5-37 shows a more detailed comparison of the degradation profiles. Figure 5-30 presents the mineral and pH degradation sequence with time at the same two observation points as in Case I (x = 1.4 m and x = 2.8 m). Compared to Case I (Figure 5-24), the chemical degradation processes are the same, although in Case IIa they occur much earlier. A faster degradation leads to complete portlandite depletion after 130 000 years at x = 1.4 m and 260 000 years for x = 2.8 m. In both cases, only calcite is present after 1 million years, and a minor fraction of hydrotalcite C at x = 2.8 m.

The mineral phase assemblage of Case IIb at different times is presented in Figure 5-31. Case IIb results fall between Case I and Case IIa. The portlandite dissolution depth is at 2 m after 250 000 years, while in Case I it is at 1.6 m and in Case IIb it is almost completely depleted. Evolution of phases with time is shown at x = 1.4 m and x = 2.8 m in Figure 5-32. The most important difference when comparing with Case I results is the amount of hydrates. All mineral volume fractions are smaller in Case IIb.

It is noted that even though the mineral concentrations (expressed in mol/L of medium) of Case IIb are smaller than Case IIa (Table 5-2), the degradation is faster in the latter. This is due to the higher volume fraction of aggregates in Case IIb (0.74 compared to 0.70 in Case IIa), leading to a reduced porosity and transport property values. The impact of the reduction of initial porosity is greater than the effect of reducing the amount of hydrates.

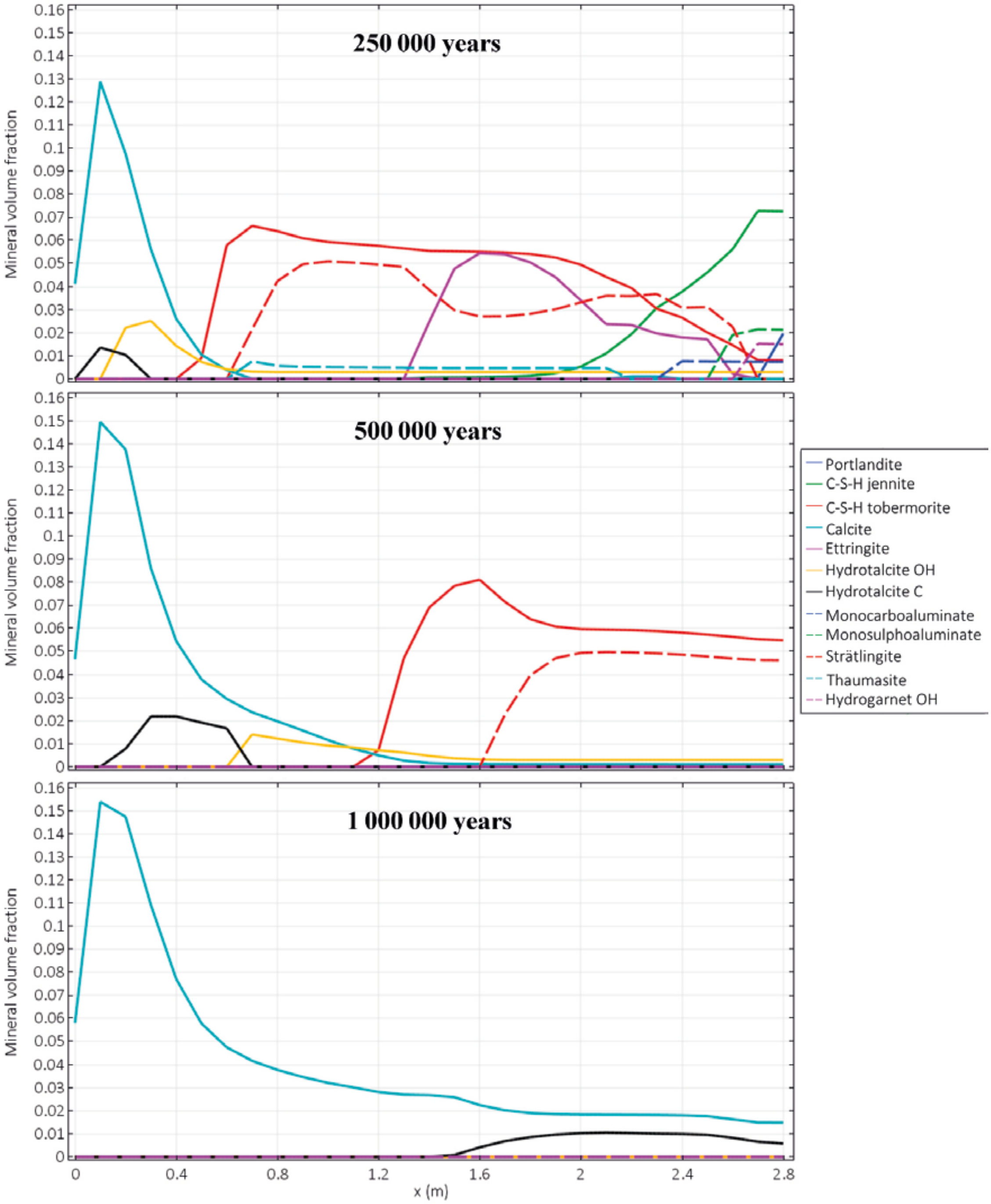

Figure 5-29. *Case IIa results. Mineral volume fractions at different times, spatial distribution in the concrete backfill (length in m).*

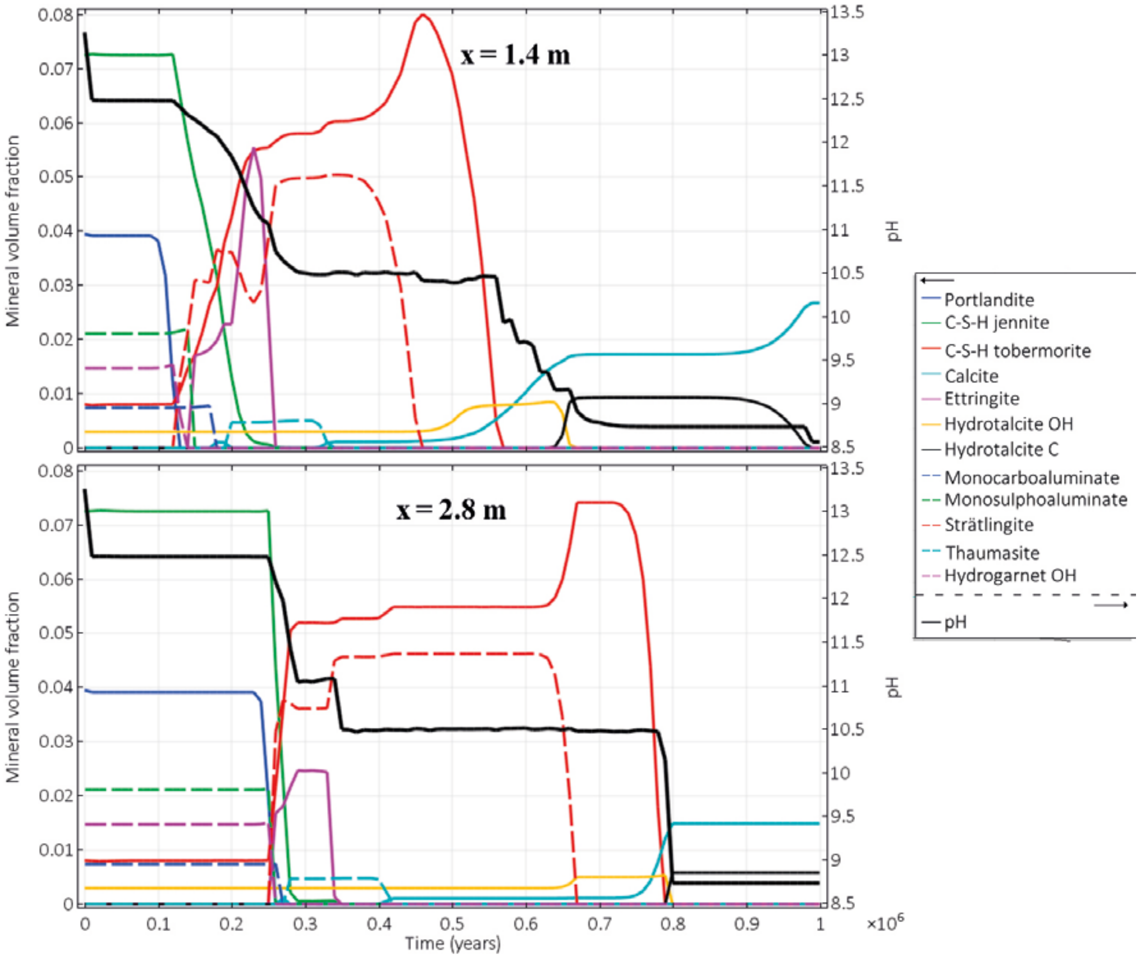

***Figure 5-30.** Case IIa results. Mineral volume fractions and pH evolution with time (years) at different point of the concrete backfill. Results for x = 1.4 m (outer-inner interface) in the upper graph and for x = 2.8 m (right boundary) in the lower part.*

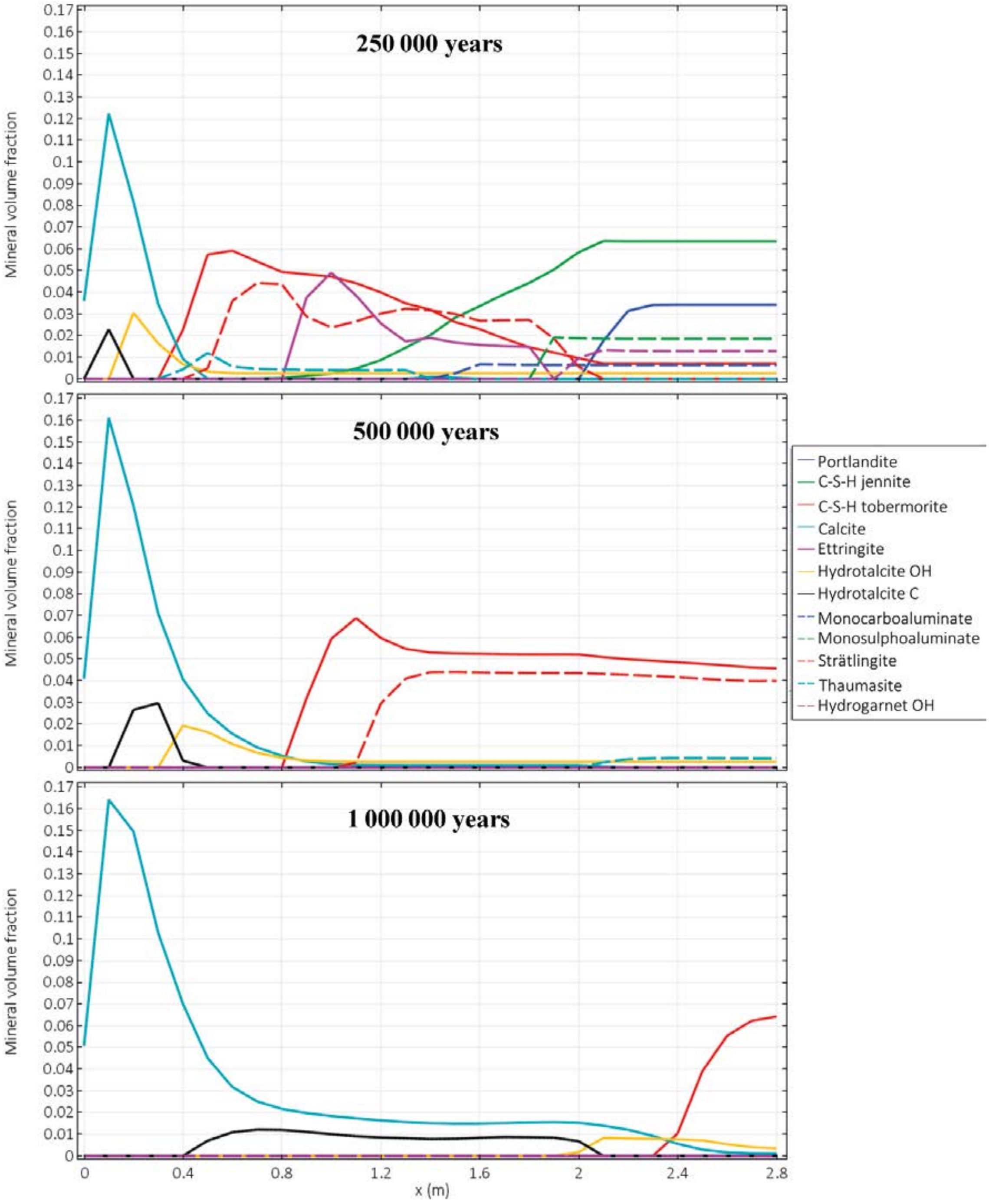

Figure 5-31. *Case IIb results. Mineral volume fractions at different times, spatial distribution in the concrete backfill (length in m).*

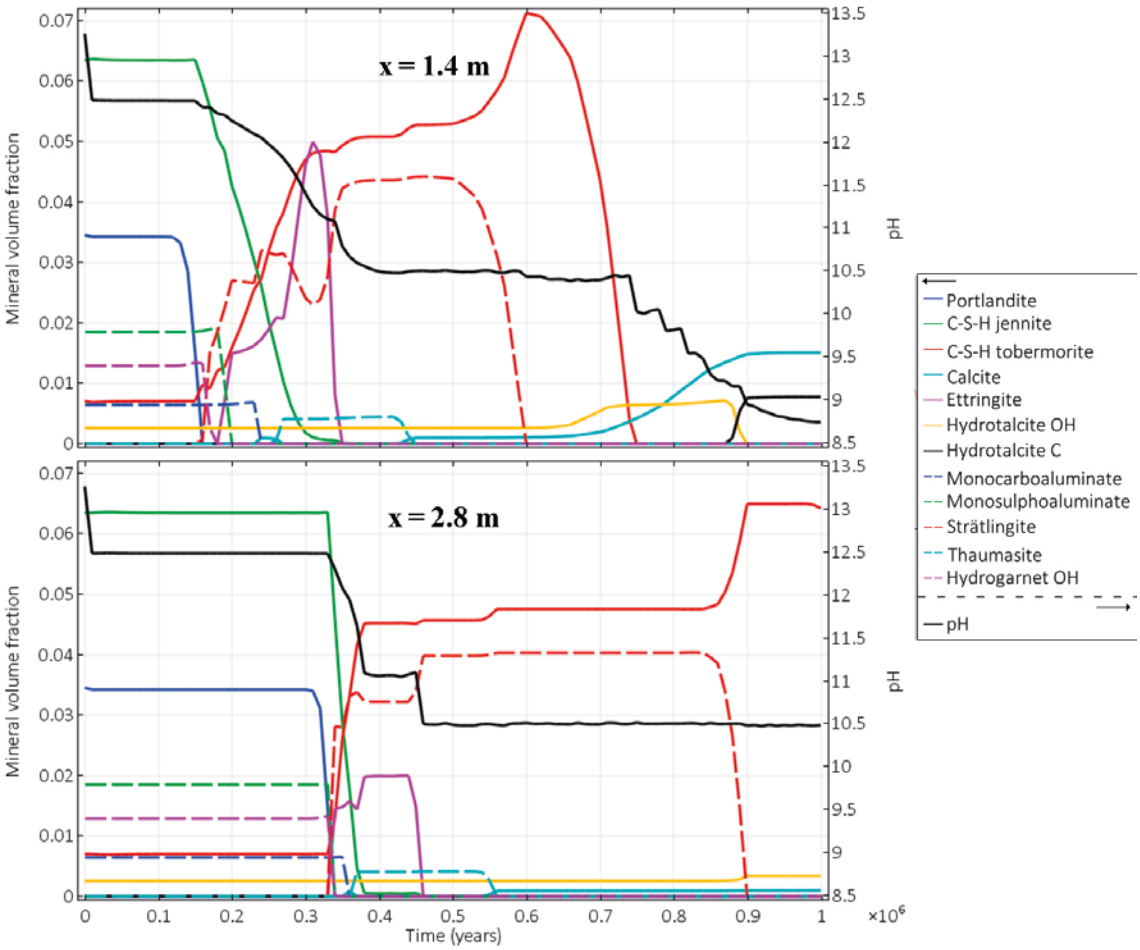

Figure 5-32. *Case IIb results. Mineral volume fractions and pH evolution with time (years) at different point of the concrete backfill. Results for x = 1.4 m (outer-inner interface) in the upper graph and for x = 2.8 m (right boundary) in the lower part.*

5.3.3 Case III

Results from Case III degradation are presented in Figure 5-33 and Figure 5-34. Differences with Case I results are due to the initial concrete compositions. The addition of fly ash leads to a different initial mineralogical composition, with less portlandite than Case I and with more C-S-H (solid solution including C-S-H and C-A-S-H phases in this case). Also, ettringite is present as primary mineral (Table 5-2), while no hydrogarnet OH is initially present in Case III.

The distribution of mineral phases along the concrete backfill is shown in Figure 5-33 for three different times. A significantly slower rate of degradation may be observed compared to Case I. In Case III, the initially lower porosity and transport property values have the effect of decreasing the rates of solute transport. As a result, there are important differences in mineral distribution. After 500 000 years, C-S-H jennite is still present in the inner backfill and even portlandite in the last centimetres of the domain. Moreover, C-A-S-H gels are still present in 80 % of the concrete domain (Figure 5-33). After 1 million years, a significant volume fraction of low Ca/Si ratio gels (C-S-H tobermorite and C-A-S-H 0.84) remain in the inner backfill.

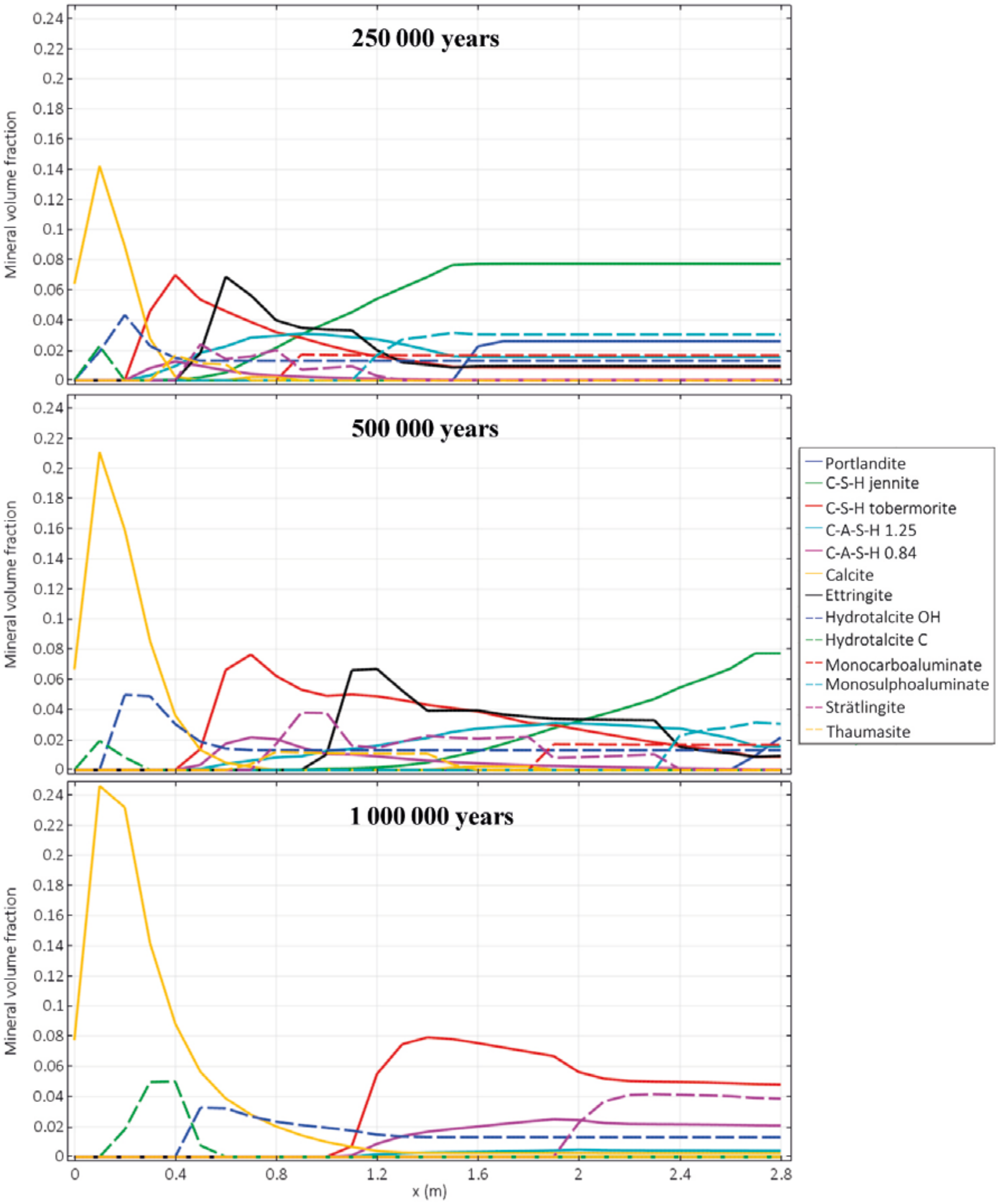

Figure 5-33. *Case III results. Mineral volume fractions at different times, spatial distribution in the concrete backfill (length in m).*

Figure 5-34 presents the mineral dissolution and precipitation sequence with time at two observation points (x = 1.4 m and x = 2.8 m). The pH evolution is also included in the figure. Qualitatively, the chemical sequence is similar to the one presented for Case I. Again, differences due to a slower degradation process are shown. At the middle point, C-S-H tobermorite continues to precipitate for the entire studied period, while C-A-S-H gels are also present. The pH is stabilised at around 10.5 after 1 million years, governed by the solubility of C-S-H gel composition. At x = 2.8 m, the slower degradation leads to portlandite complete depletion after 500 000 years, i.e. 100 000 years later than in Case I.

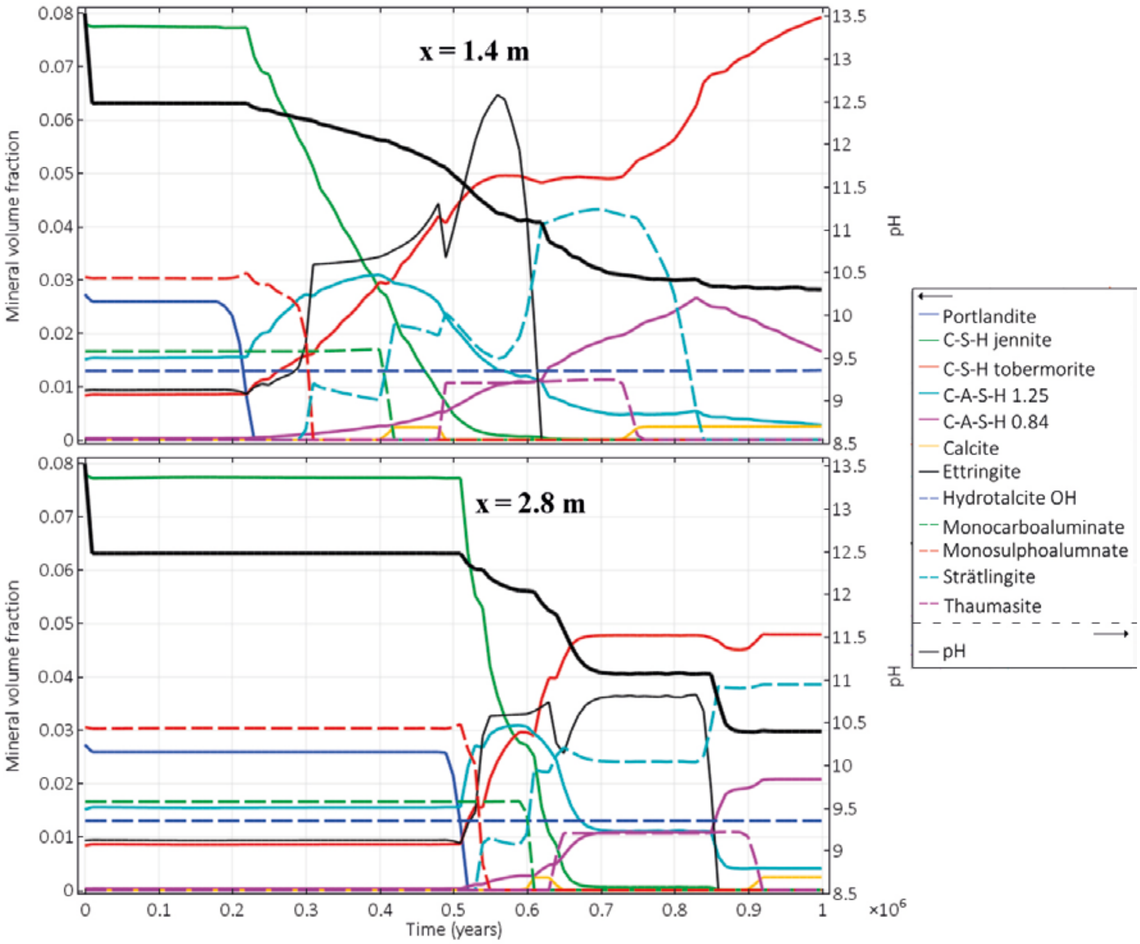

Figure 5-34. *Case III results. Mineral volume fractions evolution with time (years) at different point of the concrete backfill. Results for x = 1.4 m (outer-inner interface) in the upper graph and for x = 2.8 m (right boundary) in the lower part.*

5.3.4 Case IV

Case IV corresponds to the concrete mix containing partial replacement of cement by limestone and dolomite. The results are presented in Figure 5-35 and Figure 5-36 in terms of mineral volume fractions. Compared with Case I, a higher calcite volume fraction is the main difference. Calcite precipitates in the first 0.3 meters, and it is present in the entire domain, due to the initial chemical assemblage. When comparing results after 1 million years, a substantially slower advancement of the degradation fronts can be observed. In particular, not only hydrotalcites, calcite and C-S-H tobermorite remain as in Case I. C-S-H jennite, strätlingite, ettringite and monocarboaluminate are also present in Case IV. An important difference in the degradation process is given by the precipitation of thaumasite, reaching volume fraction values of up to 0.07. These high values could be associated with expansions and cracking (see e.g. Idiart and Laviña 2019). However, it is noted that thaumasite formation in Case IV follows from primary ettringite dissolution (with a 0.02 initial volume fraction) and occurs when the total porosity has increased substantially. Including the effect of thaumasite volume fraction, porosity values at these regions remain above the initial value (not shown). Therefore, expansions and cracking from thaumasite formation are not likely in this context. The formation of thaumasite also affects the stability of strätlingite, showing a lower volume fraction than in other cases.

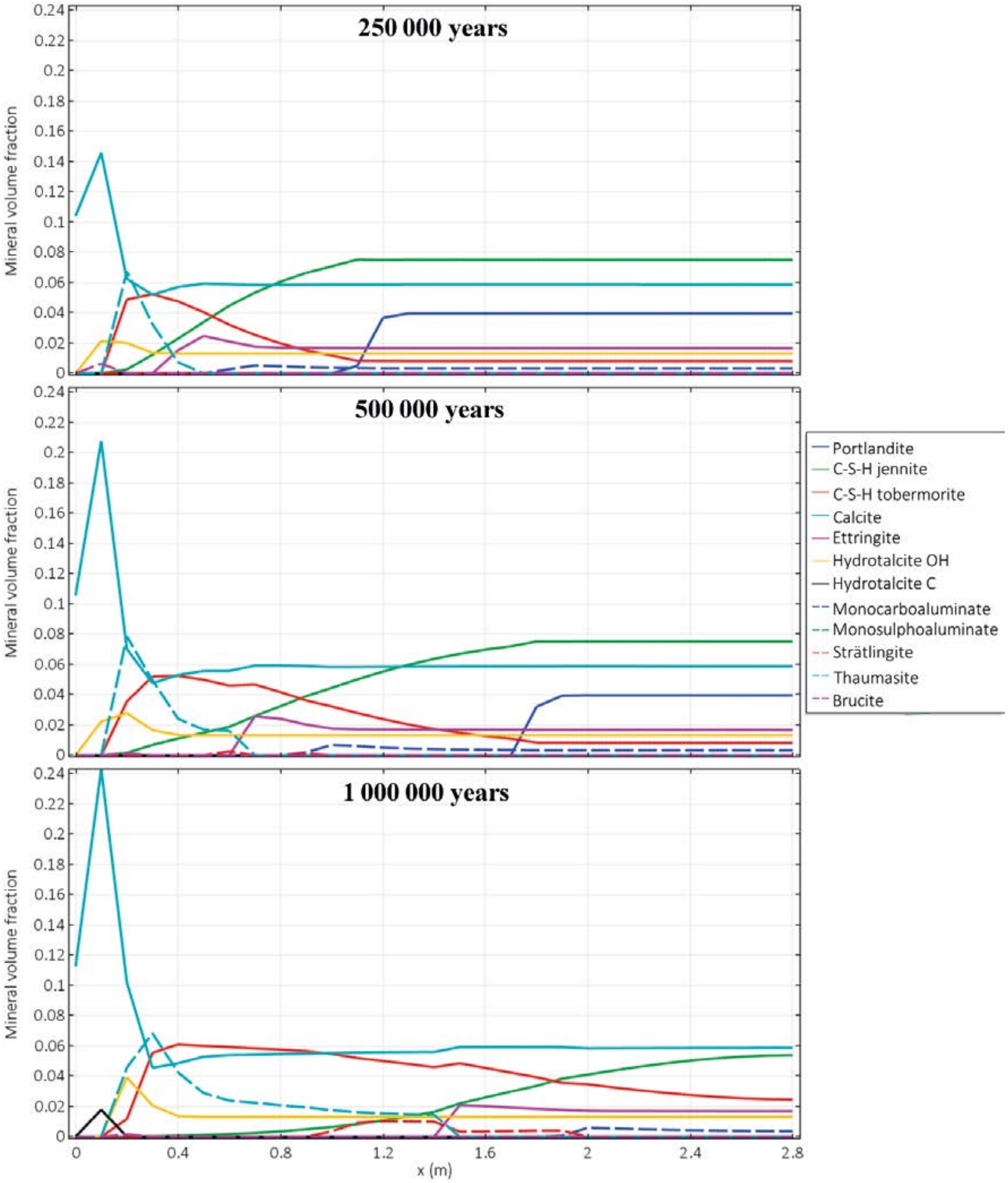

Figure 5-35. *Case IV results. Spatial distribution (length in m) in the concrete backfill of mineral volume fractions at different times (250 000, 500 000 and 1 million years).*

Figure 5-36 shows the evolution of the mineral phase assemblage at the two observation points x = 1.4 m and x = 2.8 m. Degradation is much slower than in Case I, with portlandite depletion completed after 370 000 years for the outer backfill and 950 000 years for the inner one. Portlandite degradation takes approximately double the time compared to Case I. The rest of primary minerals are also dissolved more slowly, such as calcite, hydrotalcite and both C-S-H phases. These minerals are present in the entire study period for x = 1.4 m; and ettringite and monocarboaluminate for x = 2.8 m. The pH distribution profiles reflect the great difference in results: values between 12.0 and 12.5 are observed in the entire study period, as opposed to Case I, where much lower values in equilibrium with groundwater are reached.

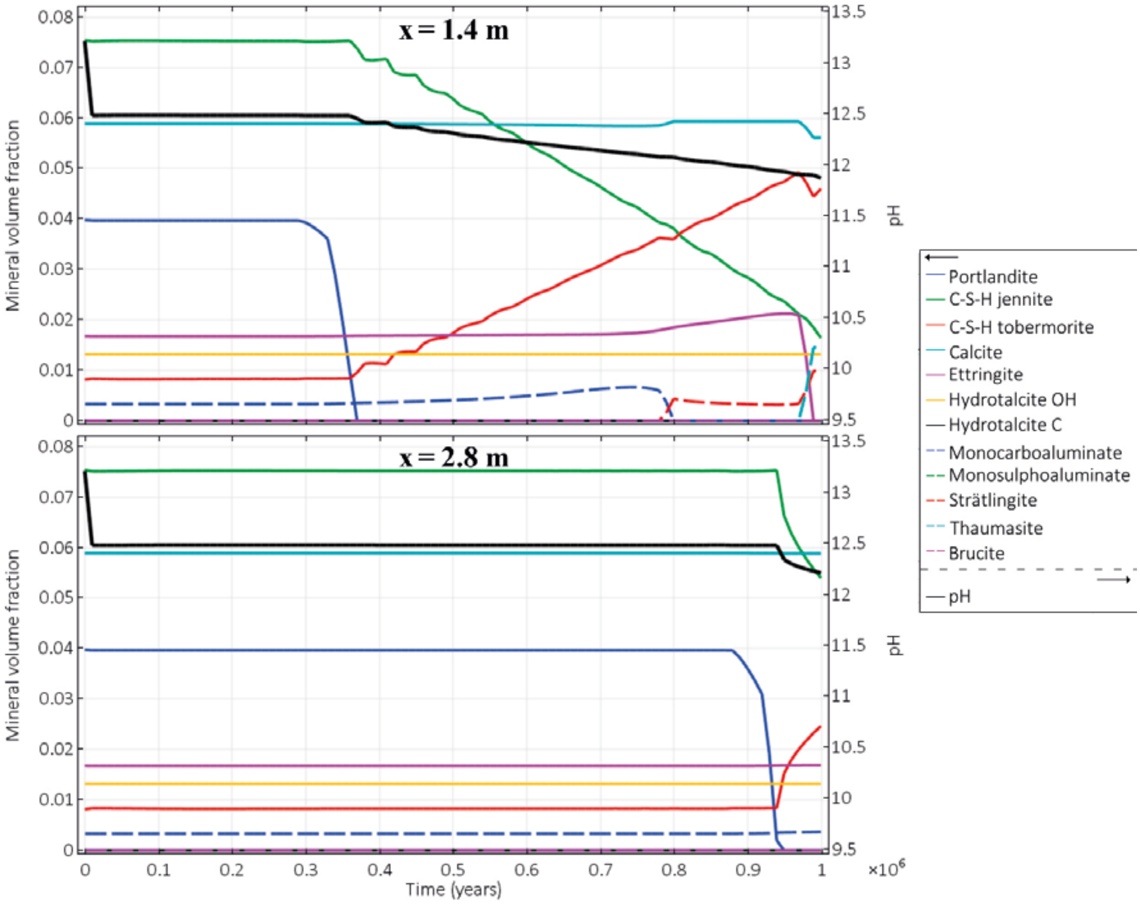

Figure 5-36. *Mineral volume fractions and pH evolution with time (years) at different point of the concrete backfill. Results for x = 1.4 m (outer-inner interface) in the upper graph and for x = 2.8 m (right boundary) in the lower part.*

5.3.5 Comparison of results

Results obtained from Case I to Case IV are compared in more detail in this section. The comparison is made using three sets of plots: (1) dissolution fronts of main buffering cement hydrates after 250 000 years, (2) equivalent key parameters (pH, ϕ, D_e and K) as defined by Idiart and Laviña (2019), and (3) main variables that characterise the degradation processes.

First, the dissolution fronts of the main buffering cement hydrates after 250 000 years are shown in Figure 5-37. The focus is on portlandite and the C-S-H solid solutions. The ideal solid solution used to describe the composition of C-S-H is characterised here using the following equations:

$$CSH_{\text{gel}} = CSH_{\text{jen}} \cdot V_{\text{m}}^{\text{jen}} + CSH_{\text{tob}} \cdot V_{\text{m}}^{\text{tob}} \tag{5-8}$$

$$C/S_{CSH} = \frac{CSH_{\text{jen}} \cdot 1.667 + CSH_{\text{tob}} \cdot 0.833}{CSH_{\text{jen}} + CSH_{\text{tob}}} \tag{5-9}$$

In the above equations, the concentrations of the end members of the solid solution, CSH_{jen} and CSH_{tob}, are given in mol/L of medium, V_{m} (L/mol) correspond to the molar volumes of the end members, CSH_{gel} is the volume fraction of the total C-S-H solid solution, and C/S_{CSH} is the C/S ratio of the C-S-H gel (1.667 and 0.833 are the C/S ratio of the end members). For Case III, Equation 5-9 also includes the C-A-S-H phases with their corresponding Ca/Si ratios (see solid solution 2 in Table 5-2).

A first conclusion is that the position of the portlandite dissolution fronts in Figure 5-37 is not directly related with initial portlandite content. For Case III (blended cement) the lower porosity and transport property values compared to Case I contribute to a slower advancement of the front despite having a much lower initial portlandite content. Comparing Case I with Case IIa and Case IIb (OPC cements) leads to a similar conclusion, i.e. the initial portlandite content is not related with the dissolution depth. Case IIa has a higher initial portlandite content than Case IIb but shows the highest dissolution after 250 000 years.

Total C-S-H gel volume fraction is presented as the addition of the end-members of this solid solution (Equation 5-8) for each case in Figure 5-37. The C/S ratio of the C-S-H solid solutions calculated according to Equation 5-9 is also compared in this figure. Case III shows the lowest portlandite content and highest C-S-H content of the studied systems. This is due to the effect of fly ash addition, consuming portlandite and forming additional C-S-H during hydration. The influence of C-A-S-H phases in Case III is shown in the initial C/S ratio of C-S-H. The 1.25 and 0.84 C/S ratios of the two C-A-S-H end-members of the solution yield a lower C/S ratio in intact concrete. This case is clearly the one with more content of C-S-H after 250 000 years. However, it is in Case IV where the dissolution front of C-S-H is less advanced. This is due to the initially lower porosity and transport property values in Case IV compared to the rest of simulated cases.

The differences between Case I and Cases IIa and IIb are more pronounced, showing a more advanced state of degradation of C-S-H phases (volume fraction and C/S ratio) and especially portlandite.

Similar to Idiart and Laviña (2019), the results of the 1D reactive transport models are post-processed here by spatial integration of key parameters needed in the radionuclide transport model. To this end, the modelled domain is divided into two control volumes of the same size (1.4 m), named as inner and outer backfill (see Figure 5-3). The following time-dependent equivalent properties are calculated:

- pH.
- Porosity.
- Effective diffusivity (m^2/s).
- Hydraulic conductivity (m/s).

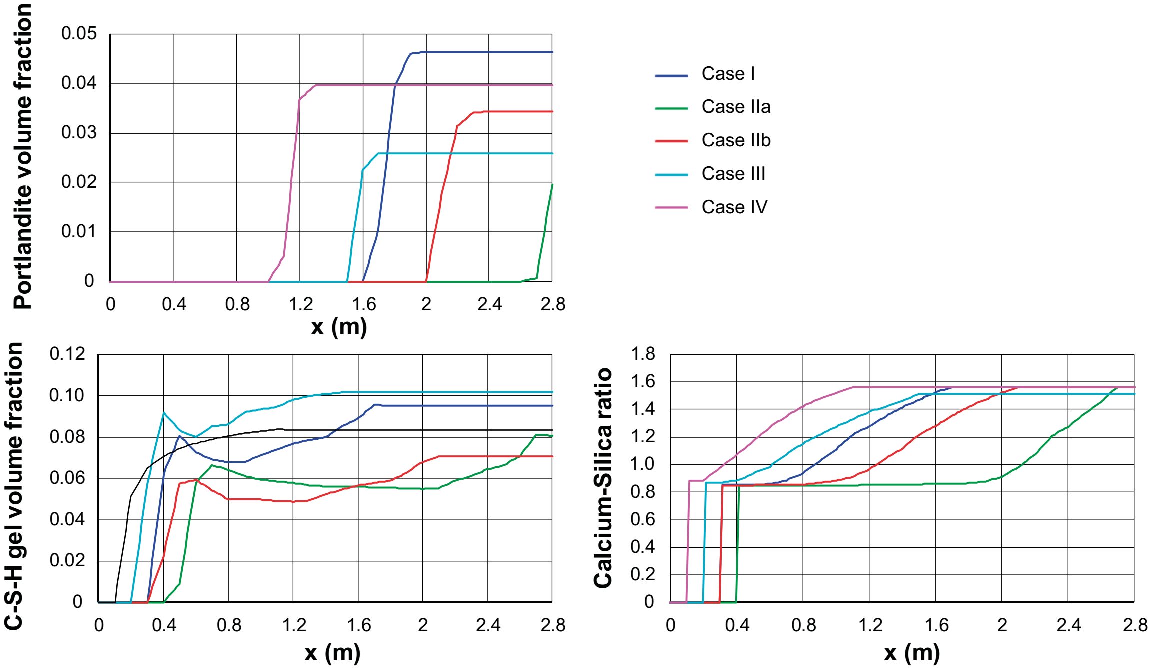

Figure 5-37. *Comparison between modelled cases in terms of spatial distribution of volume fraction of portlandite and C-S-H solid solution and C/S ratio of C-S-H at 250 000 years (length in m).*

Depending on the nature of each variable, either a series model or a model based on the weighted average is used. Equivalent transport properties along the direction of flow are calculated using a series model. On the other hand, mean values of porosity over the control volumes are calculated based on a weighted average.

The equivalent effective diffusion coefficient resulting from the 1D reactive transport simulation is calculated over 1 million years using the following equation:

$$D_e^{eq} = \frac{L}{\int_a^b \frac{1}{D_e(x,t)} dx} \tag{5-10}$$

Above, $D_e(x,t)$ is the local effective diffusion coefficient, a (m) and b (m) correspond to the x coordinate of the boundaries where the integration is calculated and L (m) is the calculated backfill thickness ($b - a$). Thus, L is 1.4 m for the control volumes and 2.8 m for the complete backfill.

Analogously, the equivalent hydraulic conductivity resulting from the reactive transport simulation can be calculated as:

$$K^{eq} = \frac{L}{\int_a^b \frac{1}{K(x,t)} dx} \tag{5-11}$$

The averaged porosity is calculated with the following equation:

$$\phi_{av} = \frac{\int_a^b \varphi(x,t)\, dx}{L} \tag{5-12}$$

Equivalent parameter evolution for the outer and inner backfills are presented from Figure 5-38 to Figure 5-41. Results are presented separately for the outer and inner backfill showing pH values at x = 1.4 and 2.8 m (Figure 5-38), averaged values of porosity (Figure 5-39) and equivalent values for effective diffusion coefficient (Figure 5-40) and hydraulic conductivity (Figure 5-41). In addition, Appendix C includes the tabulated values of the averaged pH plots presented in this section.

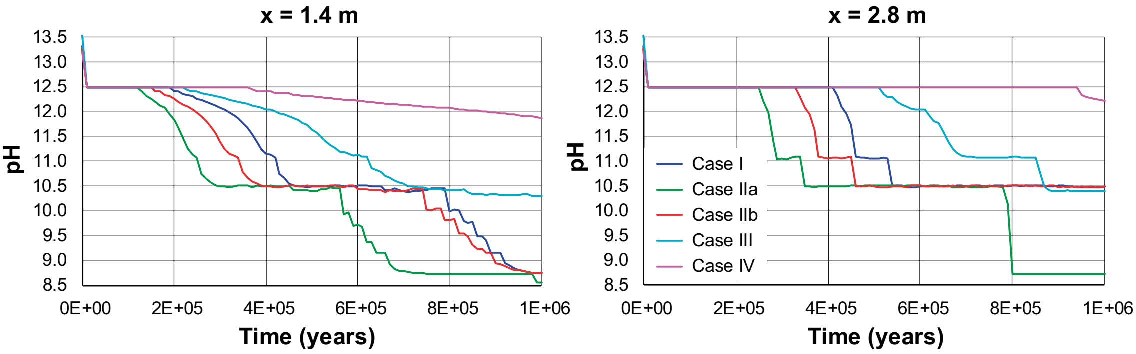

Figure 5-38. *pH values (-) as a function of time (years) at the inner - outer backfill interface (x = 1.4 m) and inner backfill – waste interface (x = 2.8 m) for the 5 simulated cases.*

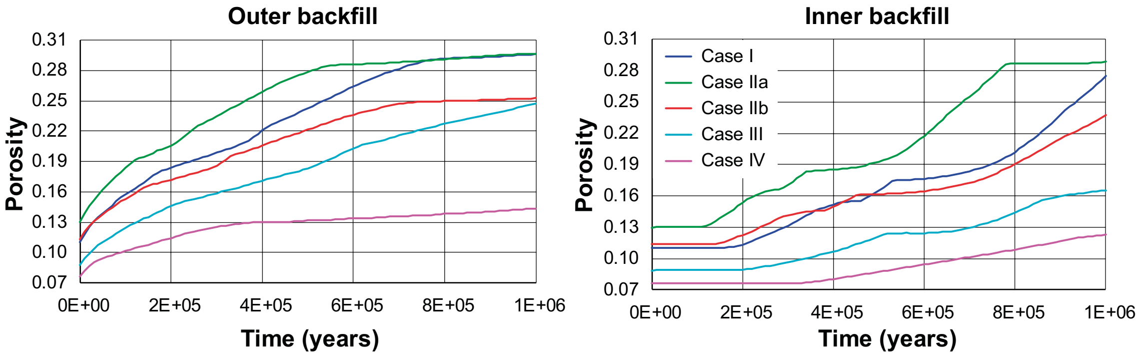

Figure 5-39. *Averaged porosity values (-) as a function of time (years) for the inner and outer backfills for the 5 simulated cases.*

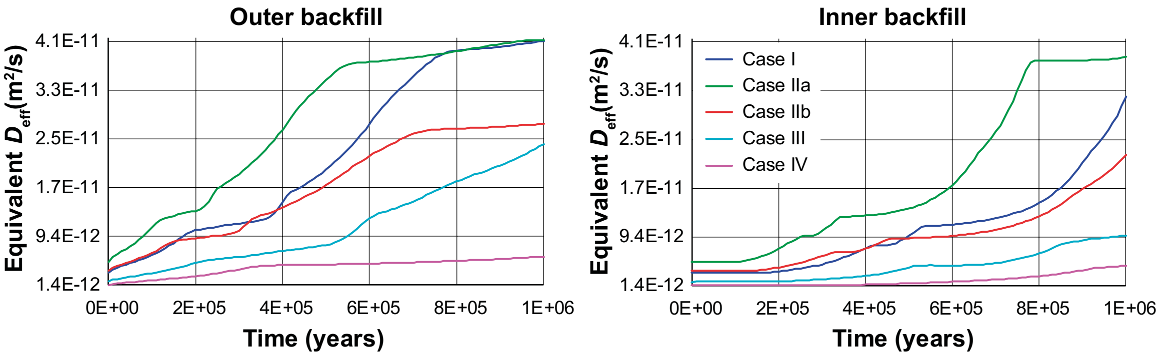

Figure 5-40. Equivalent effective diffusion coefficient (m^2/s) as a function of time (years), representative values for the inner and outer backfills for the 5 simulated cases.

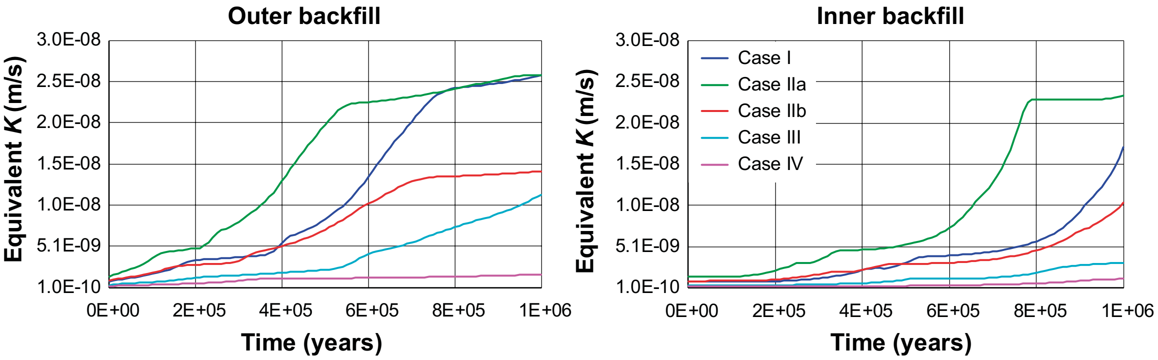

Figure 5-41. Equivalent hydraulic conductivity (m/s) as a function of time (years), representative values for the inner and outer backfills for the 5 simulated cases.

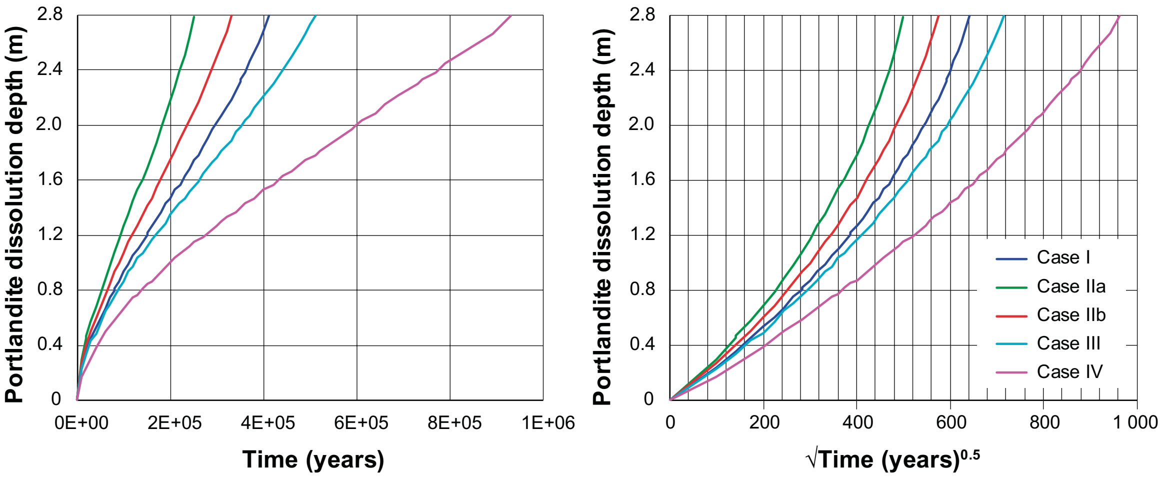

Figure 5-42. Portlandite dissolution depth (m) in the concrete backfill as a function of time (years) and the square root of time ($years^{1/2}$). Results corresponding to the 5 simulated cases.

The differences in the decrease in pH values due to groundwater interaction are more noticeable at x = 1.4 m. This is due to the larger differences between degradation rates in each case for longer times, resulting from the increase in Darcy velocities (Figure 5-43).

The results in terms of averaged porosity values follow a similar monotonously increasing trend in all cases, although starting from different initial values both in the inner and outer backfill volumes (Figure 5-39). The final values reached, especially in the outer backfill, are close to the maximum porosity that can be achieved in each case, which depends on the inert mineral fraction. An exception is Case IV, where only half of the maximum porosity value is attained due to calcite content.

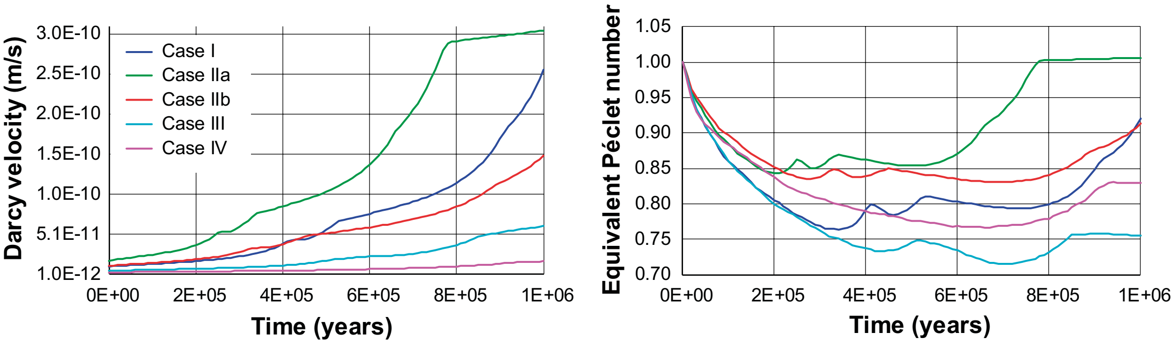

Figure 5-43. *Darcy velocities (m/s) and equivalent Péclet numbers (-), normalised to their respective initial values, as a function of time (years). Results corresponding to the 5 simulated cases.*

The equivalent transport properties in Figure 5-40 and Figure 5-41 are calculated using Equations 5-10 and 5-11. Case IIa shows the highest transport properties due to the higher initial porosity. As a result, degradation is fastest in this case. On the other hand, Case III and Case IV have a lower initial porosity compared to Case I, thus showing lower transport property values and slower degradation rates, especially Case IV.

Figure 5-42 presents the portlandite dissolution depths of all cases (in m), corresponding to the time at which the concentration of portlandite at a given point is half of its initial value. Results are shown as a function of time and the square root of time. There is a significant difference between the simulated cases in the time that the portlandite dissolution front needs to reach the innermost point of the concrete backfill. In Case I, it takes 410 000 years, while in Case III this time increases up to 510 000 years. On the other hand, the time needed in Cases IIa and IIb is reduced to 250 000 and 330 000 years, respectively. Case IV shows the longest time needed by portlandite dissolution front to reach the innermost side of the backfill (930 000 years), which is due to the low initial porosity of the system. Solute transport in the system is more advective-dominated, as indicated by the non-linearity between dissolution depth and square root of time.

The equivalent Péclet number of the 1D model assuming the entire backfill thickness (L_b) can be calculated as:

$$\mathrm{Pe} = \frac{qL_\mathrm{b}}{\phi_\mathrm{av}\, D_\mathrm{e}^\mathrm{eq}} \tag{5-13}$$

where q is the Darcy velocity (m/s). The evolution in time of the Darcy velocity and equivalent Péclet number (normalised to its initial value) is presented in Figure 5-43.

Degradation process can be characterised with the analysis of portlandite dissolution front, water velocity and Péclet number. The initial Péclet numbers of each case are given in Table 5-9. It may be observed that the system is initially dominated by advection. The evolution of the equivalent Péclet number indicates that even though the Darcy velocity increases, the relative impact of diffusion over advection increases with time. The increase of the diffusion coefficient is due to the increase in averaged porosity. In turn, increased porosity also has the effect of decreasing the interstitial velocity (defined as the Darcy velocity divided by porosity). However, the modelled systems are still dominated by advection throughout the studied period.

Table 5-9. Initial equivalent Péclet (Pe) number for each 1D case calculated using Equation 5-13.

Simulation	Pe
Case I	74.9
Case IIa	72.1
Case IIb	74.3
Case III	79.8
Case IV	83.4

6 Summary and conclusions

This work presents a comprehensive study of the effect of using different concrete mixes on the long-term performance of engineered barriers in the BHK vault of SFL. A literature review is presented to summarise the most important differences between the reference concrete composition previously studied (e.g. Idiart and Shafei 2019) and the proposed concrete mixes. Time-dependent cement hydration models have been implemented in PHREEQC to quantify the cement hydrate phase assemblage upon full hydration starting from the cement mix composition. The results of the hydration models are then used as input to a set of ten reactive transport models in 1D and 2D of concrete degradation, implemented in iCP.

The compositions of the cementitious materials considered by SKB include concretes with:

- water-to-cement ratio of 0.63 (instead of 0.47 used previously),
- the addition of fly ash as a supplementary cementitious material (SCM), and
- partial replacement of cement by limestone ($CaCO_3$) filler.

Degradation of concrete in the SFL repository has first been studied using 2D reactive transport models of a cross-section of the BHK vault over a period of 100 000 years. A total of five models are presented considering different concrete compositions. The main concrete degradation process is driven by leaching of calcium in all cases, which leads to gradual dissolution of the main cement hydrates. Calcite precipitation, as a result of the carbonate ingress from groundwater and calcium from hydrates dissolution, is another important process. The rate of this degradation process is shown to be low after 100 000 years in all the simulation cases considered. This is due to the relatively small flow of water into the repository, together with a low initial diffusion coefficient of the concrete backfill. Comparison of the results of the different cases over this time scale shows that the impact of changing the concrete composition to the studied alternatives does not have a significant effect on the performance of the barriers. The depth of the penetration front of degraded concrete is relatively sensitive to concrete composition, although the results indicate that the governing factors are the initial porosity and transport properties.

A set of 1D reactive transport models of the same five cases described for the 2D models is presented, considering an extended period of 1 million years. These models are also implemented in iCP. The focus has been put on evaluating and comparing the pH, porosity, effective diffusivity and hydraulic conductivity of the BHK concrete backfill over 1-million-year time span. The differences between different modelled cases are much larger over these longer time periods in terms of penetration of degradation fronts. After 1 million years, the full thickness of the concrete backfill (2.8 m) is near complete degradation in all cases, with calcite precipitating in most of the thickness. An exception is Case IV, in which degradation proceeds much slower than in the other cases. This is due to the lower initial porosity, which results in lower transport property values and thus slower solute transport. In the 1D models, there is a constant increase in the Darcy velocity with time. This is in part due to the assumed boundary condition, which is based on a constant hydraulic head gradient. As a result, fluid flow increases monotonously with time.

The main conclusion of the work is that the extent of degradation of the concrete backfill over long time-scales is governed by the porosity and transport properties, rather than the chemical composition of the cementitious material, at least for the studied systems. Case IV, which considers the addition of limestone filler, is clearly the concrete mix that has the best performance. According to the model results, this improvement is more related with the initially lower porosity compared to the rest of cases than to the chemical composition of the cementitious system.

The coupling between dissolution/precipitation reactions involving mineral phases and physical properties considered in the models is based on the use of total porosity. Empirical relations between porosity and either hydraulic conductivity (Kozeny-Carman equation) or effective diffusivity (Archie's law type) are assumed in the reactive transport models. However, there is a lack of specific experimental data regarding the relation between porosity and transport properties for the different concrete compositions. Therefore, a limitation of the models is clearly related to the validity of the coupling strategy and the definition of these empirical relations, especially in the long term.

References

SKB's (Svensk Kärnbränslehantering AB) publications can be found at www.skb.com/publications. SKBdoc documents will be submitted upon request to document@skb.se.

Abarca E, Sampietro D, Miret M, von Schenck H, 2016. Initial modelling of the near-field hydrogeology. Exploring the influence of host rock characteristics and barrier properties. Report for the safety evaluation SE-SFL. SKB R-16-02, Svensk Kärnbränslehantering AB.

Ahmad S, Azad A K, Loughlin K F, 2012. Effect of the key mixture parameters on tortuosity and permeability of concrete. Journal of Advanced Concrete Technology 10, 86–94.

Andersen M D, Jakobsen H J, Skibsted J, 2006. A new aluminium-hydrate species in hydrated Portland cements characterized by ^{27}Al and ^{29}Si MAS NMR spectroscopy. Cement and Concrete Research 36, 3–17.

Atiş C D, 2003. High-volume fly ash concrete with high-strength and low drying shrinkage. Journal of Materials in Civil Engineering 15, 153–156.

Balakrishnan B, Abdul Awal A S M, Shehu I A, 2013. Influence of high volume fly ash in controlling heat of hydration of concrete. International Journal of Engineering Research and Applications 3, 932–936.

Baroghel-Bouny V, Kinomura K, Thiery M, Moscardelli S, 2011. Easy assessment of durability indicators for service life prediction or quality control of concretes with high volumes of supplementary cementitious materials. Cement and Concrete Composites 33, 832–847.

Barrett T, Sun H, Villani C, Barcelo L, Weiss J, 2014. Early-age shrinkage behavior of Portland limestone cement. Concrete international 36, 51–57.

Bederina M, Makhloufi Z, Bouziani T, 2011. Effect of limestone fillers the physic-mechanical properties of limestone concrete. Physics Procedia 21, 28–34.

Ben Haha M, De Weerdt K, Lothenbach B, 2010. Quantification of the degree of reaction of fly ash. Cement and Concrete Research 40, 1620–1629.

Bentz D P, Sato T, De la Varga I, Weiss W J, 2012. Fine limestone additions to regulate setting in high volume fly ash mixtures. Cement and Concrete Composites 34, 11–17.

Boel V, Audenaert K, De Schutter G, Heirman G, Vandewalle L, Desmet B, Vantomme J, 2007. Transport properties of self compacting concrete with limestone filler or fly ash. Materials and Structures 40, 507–516.

Boğa A R, Topçu I B, 2012. Influence of fly ash on corrosion resistance and chloride ion permeability of concrete. Construction and Building Materials 31, 258–264.

Bogue R H, 1929. Calculation of the Compounds in Portland Cement. Industrial & Engineering Chemistry Analytical Edition 1, 192–197.

Bouzoubaâ N, Bilodeau A, Tamtsia B, Foo S, 2010. Carbonation of fly ash concrete: laboratory and field data. Canadian Journal of Civil Engineering 37, 1535–1549.

Brooks J J, Johari M M, Mazloom M, 2000. Effect of admixtures on the setting times of high-strength concrete. Cement and Concrete Composites 22, 293–301.

Bruggeman D A G, 1935. Berechnung verschiedener physikalischer Konstanten von heterogenen Substanzen. I. Dielektrizitätskonstanten und Leitfähigkeiten der Mischkörper aus isotropen Substanzen (The calculation of various physical constants of heterogeneous substances). Annalen der Physik 416, 636–664. (In German.)

Bullard J W, Lothenbach B, Stutzman P, Snyder K A, 2011. Coupling thermodynamic and digital image models to simulate hydration and microstructure development of Portland cement pastes. Journal of Materials Research 26, 609–622.

Carman P, 1937. Fluid flow through a granular bed. Transactions of the American Institute of Chemical Engineers 15, 150–167.

Catinaud S, Beaudoin J J, Marchand J, 2000. Influence of limestone addition on calcium leaching mechanisms in cement-based materials. Cement and Concrete Research 30, 1961–1968.

CEMENTA, 2015. Bascement. CEM II/A-V 52.5 N Technical data sheet. Available at: https://www.cementa.se/en/bascement-eng

Chindaprasirt P, Jaturapitakkul C, Sinsiri T, 2005. Effect of fly ash fineness on compressive strength and pore size of blended cement paste. Cement and Concrete Composites 27, 425–428.

da Silva P R, de Brito J, 2015. Experimental study of the porosity and microstructure of self-compacting concrete (SCC) with binary and ternary mixes of fly ash and limestone filler. Construction and Building Materials 86, 101–112.

Dalziel J A, Gutteridge W A, 1986. The influence of pulverized-fuel ash upon the hydration characteristics and certain physical properties of a Portland cement paste. London: Cement and Concrete Association. (Technical report 560).

Damidot D, Glasser F P, 1995. Investigation of the CaO-Al_2O_3-SiO_2-H_2O system at 25 °C by thermodynamic calculations. Cement and Concrete Research 25, 22–28.

Damidot D, Lothenbach B, Herfort D, Glasser F P, 2011. Thermodynamics and cement science. Cement and Concrete Research 41, 679–695.

De Weerdt K, Haha M B, Le Saout G, Kjellsen K O, Justnes H, Lothenbach B, 2011. Hydration mechanisms of ternary Portland cements containing limestone powder and fly ash. Cement and Concrete Research 41, 279–291.

Deby F, 2008. Approche probabiliste de la durabilité des bétons en environnement marin. PhD thesis. Université Toulousse III, France. (In French.)

Deby F, Carcassès M, Sellier A, 2009. Probabilistic approach for durability design of reinforced concrete in marine environment. Cement and Concrete Research 39, 466–471.

Deschner F, Lothenbach B, Winnefeld F, Neubauer J, 2013. Effect of temperature on the hydration of Portland cement blended with siliceous fly ash. Cement and Concrete Research 52, 169–181.

Deschner F, Winnefeld F, Lothenbach B, Seufert S, Schwesig P, Dittrich S, Goetz-Neunhoeffer F, Neubauer J, 2012. Hydration of Portland cement with high replacement by siliceous fly ash. Cement and Concrete Research 42, 1389–1400.

Dhir R K, Limbachiya M C, McCarthy M J, Chaipanich A, 2007. Evaluation of Portland limestone cements for use in concrete construction. Materials and Structures 40, 459–473.

Diamond S, 1981. Effects of two Danish flyashes on alkali contents of pore solutions of cement-flyash pastes. Cement and Concrete Research 11, 383–394.

Elakneswaran Y, Owaki E, Miyahara S, Ogino M, Maruya T, Nawa T, 2016. Hydration study of slag-blended cement based on thermodynamic considerations. Construction and Building Materials 124, 615–625.

Elfwing M, Evins L Z, Gontier M, Grahm P, Mårtensson P, Tunbrant S, 2013. SFL concept study. Main report. SKB TR-13-14, Svensk Kärnbränslehantering AB.

Elgalhud A A, Dhir R K, Ghataora G, 2016. Limestone addition effects on concrete porosity. Cement and Concrete Composites 72, 222–234.

Escalante-Garcia J-I, Sharp J H, 2004. The chemical composition and microstructure of hydration products in blended cements. Cement and Concrete Composites 26, 967–976.

Fajun W, Grutzeck M W, Roy D M, 1985. The retarding effects of fly ash upon the hydration of cement pastes: the first 24 hours. Cement and Concrete Research 15, 174–184.

Galan I, Andrade C, Castellote M, Rebolledo N, Sanchez J, Toro L, Puente I, Campo J, Fabelo O, 2011. Neutron diffraction for studying the influence of the relative humidity on the carbonation process of cement pastes. Journal of Physics: Conference Series 325, 012015. doi:10.1088/1742-6596/325/1/012015

García-Lodeiro I, Palomo A, Fernández-Jiménez A, Macphee D E, 2011. Compatibility studies between N-A-S-H and C-A-S-H gels. Study in the ternary diagram Na_2O–CaO–Al_2O_3–SiO_2–H_2O. Cement and Concrete Research 41, 923–931.

Gebler S H, Klieger P, 1986. Effect of fly ash on the durability of air-entrained concrete. In Proceedings, 2nd International Conference on Fly Ash, Silica Fume, Slag, and Natural Pozzolans in Concrete, ACI SP-91, Vol. 1. Farmington Hills, MI: American Concrete Institute, 483–519.

Georgescu M, Saca N, 2009. Properties of blended cements with limestone filler and fly ash content. Scientific Bulletin B Chemistry and Materials Science 71, 11–22.

Girão A V, Richardson I G, Taylor R, Brydson R M D, 2010. Composition, morphology and nanostructure of C-S-H in 70 % white Portland cement-30 % fly ash blends hydrated at 55 °C. Cement and Concrete Research 40, 1350–1359.

Glasser F P, Macphee D E, Lachowski E E, 1987. Modelling approach to the prediction of equilibrium phase distribution in slag-cement blends and their solubility properties. In Apted M J, Westerman R E (eds). Scientific basis for nuclear waste management XI: symposium held in Boston, Massachusetts, USA, 30 November – 3December 1987. Pittsburgh, PA: Materials Research Society. (Materials Research Society Symposium Proceedings 112)

Gui Q, Qin M, Li K, 2016. Gas permeability and electrical conductivity of structural concretes: impact of pore structure and pore saturation. Cement and Concrete Research 89, 109–119.

Halamickova P, Detwiler R J, Bentz D P, Garboczi E J, 1995. Water permeability and chloride ion diffusion in portland cement mortars: Relationship to sand content and critical pore diameter. Cement and Concrete Research 25, 790–802.

He J-Y, Scheetz B E, Roy D M, 1984. Hydration of fly ash-portland cements. Cement and Concrete Research 14, 505–512.

Hedegaard S E, Hansen T C, 1992. Water permeability of fly ash concretes. Materials and Structures 25, 381–387.

Hirao H, Yamada K, Hoshino S, Yamashita H, 2007. The effect of limestone addition on the optimum sulphate levels of cements having various Al_2O_3 contents. In Proceedings of the 12th International Congress on Chemistry of Cement (ICCC), Montreal, Canada, 8–13 July 2007.

Holt E E, 2001. Early age autogenous shrinkage of concrete. Espoo, Finland: Technical Research Centre of Finland. (VTT Publications 446)

Hong S-Y, Glasser F P, 1999. Alkali binding in cement pastes: Part I. The C–S–H phase. Cement and Concrete Research 29, 1893–1903.

Hooton R D, Nokken M, Thomas M D A, 2007. Portland-limestone cement: state-of-the-art report and gap analysis for CSA A 3000. University of Toronto.

Hummel W, Berner U, Curti E, Pearson F J, Thoenen T 2002. Nagra/PSI chemical thermodynamic data base 01/01. Radiochimica Acta 90, 805–813.

Höglund L O, 1992. Some notes on ettringite formation in cementitious materials; Influence of hydration and thermodynamic constraints for durability. Cement and Concrete Research 22, 217–228.

Höglund L O, 2001. Project SAFE. Modelling of long-term concrete degradation processes in the Swedish SFR repository. SKB R-01-08, Svensk Kärnbränslehantering AB.

Höglund L O, 2014. The impact of concrete degradation on the BMA barrier functions. SKB R-13-40, Svensk Kärnbränslehantering AB.

Höglund L O, Bengtsson A, 1991. Some chemical and physical processes related to the long-term performance of the SFR repository. SKB SFR 91-06, Svensk Kärnbränslehantering AB.

Idiart A, Laviña M, 2019. Modelling of concrete degradation in a one-million-year perspective – Hydro-chemical processes. Report for the safety evaluation SE-SFL. SKB R-19-13, Svensk Kärnbränslehantering AB.

Idiart A, Shafei B, 2019. Modelling of concrete degradation – Hydro-chemical processes. Report for the safety evaluation SE-SFL. SKB R-19-11, Svensk Kärnbränslehantering AB.

Idiart A, Laviña M, Coene E, 2019. Modelling of concrete degradation – Hydro-chemo-mechanical processes. Report for the safety evaluation SE-SFL. SKB R-19-12, Svensk Kärnbränslehantering AB.

Ingram K D, Daugherty K E, 1991. A review of limestone additions to Portland cement and concrete. Cement and Concrete Composites 13, 165–170.

Irassar E F, 2009. Sulfate attack on cementitious materials containing limestone filler – A review. Cement and Concrete Research 39, 241–254.

Irassar E F, Bonavetti V L, Menéndez G, Donza H, Cabrera O, 2001. Mechanical properties and durability of concrete made with portland limestone cement. In Malhotra V M (ed). Proceedings of 3rd CANMET/ACI International Symposium: Sustainable Development of Cement and Concrete. Detroit: American Concrete Institute. (Special Publication 202), 431–450.

Jacques D, 2009. Benchmarking of the cement model and detrimental chemical reactions including temperature dependent parameters. Project near surface disposal of category A waste at Dessel. NIROND-TR 2008–30 E, ONDRAF, Belgium.

Jennings H M, Tennis P D, 1994. Model for the developing microstructure in portland cement pastes. Journal of the American Ceramic Society 77, 3161–3172.

Jensen O M, Hansen P F, 2001a. Autogenous deformation and RH-change in perspective. Cement and Concrete Research 31, 1859–1865.

Jensen O M, Hansen P F, 2001b. Water-entrained cement-based materials I. Principles and theoretical background. Cement and Concrete Research 31, 647–654.

Khairallah R S, 2009. Analysis of autogenous and drying shrinkage of concrete. PhD thesis. McMaster University, Canada.

Kim Y-Y, Lee K-M, Bang J-W, Kwon S-J, 2014. Effect of W/C ratio on durability and porosity in cement mortar with constant cement amount. Advances in Materials Science and Engineering 2014, 273460. doi:10.1155/2014/273460

Krishna V, Sabnis, G M, 2013. Utilization of waste products and by-products in concrete: the key to a sustainable construction. In Proceedings of International Conference on Civil and Architecture Engineering (ICCAE'2013), Kuala Lumpur, Malaysia, 6–7 May, 2013.

Kulik D, 2002. GEMS-PSI 2.0. Villigen, Switzerland: Paul Scherrer Institut. Available at: http://gems.web.psi.ch/

Kutchko B G, Strazisar B R, Dzombak D A, Lowry G V, Thaulow N, 2007. Degradation of well cement by CO_2 under geologic sequestration conditions. Environmental Science & Technology 41, 4787–4792.

L'Hôpital E, Lothenbach B, Le Saout G, Kulik D, Scrivener K, 2015. Incorporation of aluminium in calcium-silicate-hydrates. Cement and Concrete Research 75, 91–103.

Lagerblad B, Trägårdh J, 1995. Conceptual model for concrete long time degradation in a deep nuclear waste repository. SKB TR 95-21, Svensk Kärnbränslehantering AB.

Lagerblad B, Rogers P, Vogt C, Mårtensson P, 2017. Utveckling av konstruktionsbetong till kassunerna i 2BMA. SKB R-17-21, Svensk Kärnbränslehantering AB. (In Swedish.)

Lannegrand R, Ramos G, Talero R, 2001. Condition of knowledge about the Friedel's salt. Materiales de Construcción 51, 63–71.

Larbi B, Dridi W, Dangla P, Le Bescop P, 2016. Link between microstructure and tritiated water diffusivity in mortars: impact of aggregates. Cement and Concrete Research 82, 92–99.

Liu L, Qiu Q, Chen X, Wang X, Xing F, Han N, He Y, 2016. Degradation of fly ash concrete under the coupled effect of carbonation and chloride aerosol ingress. Corrosion Science 112, 364–372.

Liu L, Ou G, Qiu Q, Chen X, Hong J, Xing F, 2017. Chloride transport and microstructure of concrete with/without fly ash under atmospheric chloride condition. Construction and Building Materials 146, 493–501.

Lollini F, Redaelli E, Bertolini L, 2014. Effects of Portland cement replacement with limestone on the properties of hardened concrete. Cement and Concrete Composites 46, 32–40.

Lothenbach B, Winnefeld F, 2006. Thermodynamic modelling of the hydration of Portland cement. Cement and Concrete Research 36, 209–226.

Lothenbach B, Le Saout G, Gallucci E, Scrivener K, 2008a. Influence of limestone on the hydration of Portland cements. Cement and Concrete Research 38, 848–860.

Lothenbach B, Matschei T, Möschner G, Glasser F P, 2008b. Thermodynamic modelling of the effect of temperature on the hydration and porosity of Portland cement. Cement and Concrete Research 38, 1–18.

Lothenbach B, Damidot D, Matschei T, Marchand J, 2010a. Thermodynamic modelling: state of knowledge and challenges. Advances in Cement Research 22, 211–223.

Lothenbach B, Bary B, Le Bescop P, Schmidt T, Leterrier N, 2010b. Sulfate ingress in Portland cement. Cement and Concrete Research 40, 1211–1225.

Lothenbach B, Scrivener K, Hooton R D, 2011. Supplementary cementitious materials. Cement and Concrete Research 41, 1244–1256.

Lothenbach B, Kulik D A, Matschei T, Balonis M, Baquerizo L, Dilnesa B, Miron G D, Myers R J, 2018. Cemdata18: A chemical thermodynamic database for hydrated Portland cements and alkali-activated materials. Cement and Concrete Research. doi:10.1016/j.cemconres.2018.04.018

Lura P, Jensen O M, Van Breugel K, 2003. Autogenous shrinkage in high-shrinkage cement paste: an evaluation of basic mechanisms. Cement and Concrete Research 33, 223–232.

Malhotra V M, Mehta P K, 2005. High-performance, high-volume fly ash concrete. supplementary cementing materials for sustainable development. Ottawa, Canada: Suppementary Cementing Materials for Sustainable Development.

Manzano H, Dolado J S, Ayuela A, 2009. Aluminum incorporation to dreierketten silicate chains. The Journal of Physical Chemistry B 113, 2832–2839.

Massazza F, 1993. Pozzolanic cements. Cement and Concrete Composites 15, 185–214.

Matschei T, Lothenbach B, Glasser F P, 2007a. The AFm phase in Portland cement. Cement and Concrete Research 37, 118–130.

Matschei T, Lothenbach B, Glasser F P, 2007b. The role of calcium carbonate in cement hydration. Cement and Concrete Research 37, 551–558.

Moranville M, Kamali S, Guillon E, 2004. Physicochemical equilibria of cement-based materials in aggressive environments – experiment and modelling. Cement and Concrete Research 34, 1569–1578.

Myers R J, Bernal S A, Provis J L, 2014. A thermodynamic model for C-(N-)A-S-H gel: CNASH_ss. Derivation and validation. Cement and Concrete Research 66, 27–47.

Nagataki S, Sakai E, Maeda M, 1982. Effect use of fly ash in precast concrete produced by autoclave curing. In Cabrera J G, Cusens A R (eds). The use of PFA in concrete: proceedings of international symposium, 14–16 April 1982, Vol. 1. University of Leeds, 201–208.

Naik T R, Singh S S, 1997. Influence of fly ash on setting and hardening characteristics of concrete systems. Materials Journal 94, 355–360.

Nardi A, Idiart A, Trinchero P, de Vries L M, Molinero J, 2014. Interface COMSOL-PHREEQC (iCP), an efficient numerical framework for the solution of coupled multiphysics and geochemistry. Computers & Geosciences 69, 10–21.

Nath P, Sarker P, 2011. Effect of fly ash on the durability properties of high strength concrete. Procedia Engineering 14, 1149–1156.

Nehdi M, Soliman A M, 2011. Early-age properties of concrete: overview of fundamental concepts and state-of-the-art research. Proceedings of the Institution of Civil Engineers – Construction Materials 164, 57–77.

Nied D, Enemark-Rasmussen K, L'Hôpital E, Skibsted J, Lothenbach B, 2016. Properties of magnesium silicate hydrates (M-S-H). Cement and Concrete Research 79, 323–332.

Nocuń-Wczelik W, Trybalska B, Żugaj E, 2013. Application of calorimetry as a main tool in evaluation of the effect of carbonate additives on cement hydration. Journal of Thermal Analysis and Calorimetry 113, 351–356.

Nokken M R, Hooton R D, 2008. Using pore parameters to estimate permeability or conductivity of concrete. Materials and Structures 41. doi:10.1617/s11527-006-9212-y

Pardal X, Pochard I, Nonat A, 2009. Experimental study of Si–Al substitution in calcium-silicate-hydrate (C-S-H) prepared under equilibrium conditions. Cement and Concrete Research 39, 637–643.

Pardal X, Brunet F, Charpentier T, Pochard I, Nonat A, 2012. ^{27}Al and ^{29}Si solid-state NMR characterization of calcium-aluminosilicate-hydrate. Inorganic Chemistry 51 1827–1836.

Parkhurst D L, Appelo C A J, 2013. Description of input and examples for PHREEQC version 3 – a computer program for speciation, batch-reaction, one-dimensional transport, and inverse geochemical calculations: U.S. Geological Survey Techniques and Methods, book 6, chap. A43. Available at: https://pubs.usgs.gov/tm/06/a43/

Parrot L J, Killoh D C, 1984. Prediction of cement hydration. British Ceramic Proceedings 35, 41–53.

Pastor J L, Ortega J m, Flor M, Pilar López M, Sánchez I, Climent M A, 2016. Microstructure and durability of fly ash cement grouts for micropiles. Construction and Building Materials 117, 47–57.

Patel R A, Phung Q T, Seetharam S C, Perko J, Jacques D, Maes N, De Schutter G, Ye G, Van Breugel K, 2016. Diffusivity of saturated ordinary Portland cement-based materials: a critical review of experimental and analytical modelling approaches. Cement and Concrete Research 90, 52–72.

Pękala M, Olmeda J, Grivé M, Bruno J, 2015. Assessment of redox state and its impact on the solubility and speciation of selected radionuclides in the SFL repository. Amphos 21. SKBdoc 1533627 ver 1.0, Svensk Kärnbränslehantering AB.

Péra J, Husson S, Guilhot B, 1999. Influence of finely ground limestone on cement hydration. Cement and Concrete Composites 21, 99–105.

Powers T C, 1960. Physical properties of cement paste. In Chemistry of cement: Proceedings of Fourth International Symposium, Washington 1960. U. S. Department of Commerce, National Bureau of Standards, 577–613.

Puertas F, Santos H, Palacios M, Martínez-Ramírez S, 2005. Polycarboxylate superplasticiser admixtures: effect on hydration, microstructure rheological behaviour in cement pastes. Advances in Cement Research 17, 77–89.

Rahhal V, Talero R, 2004. Influence of two different fly ashes on the hydration of Portland cements. Journal of Thermal Analysis and Calorimetry 78, 191–205.

Ramezanianpour A A, Ghiasvand E, Nickseresht I, Mahdikhani M, Moodi F, 2009. Influence of various amounts of limestone powder on performance of Portland limestone cement concretes. Cement and Concrete Composites 31, 715–720.

Rayment P L, 1982. The effect of pulverised-fuel ash on the c/s molar ratio and alkali content of calcium silicate hydrates in cement. Cement and Concrete Research 12, 133–140.

Rimmelé G, Barlet-Gouédard V, Porcherie O, Goffé B, Brunet F, 2008. Heterogeneous porosity distribution in Portland cement exposed to CO_2-rich fluids. Cement and Concrete Research 38, 1038–1048.

Robie R A, Hemingway B S, 1995. Thermodynamic properties of minerals and related substances at 298.15 K and 1 bar (10^5 pascals) pressure and at higher temperatures. Washington: U.S. Government Printing Office.

Saha A K, 2018. Effect of class F fly ash on the durability properties of concrete. Sustainable Environment Research 28, 25–31.

Sánchez de Rojas M S, Luxán M P D, Frías M, García N, 1993. The influence of different additions on portland cement hydration heat. Cement and Concrete Research 23, 46–54.

Savage D, Soler J M, Yamaguchi K, Walker C, Honda A, Inagaki, M, Rueedi J, 2011. A comparative study of the modelling of cement hydration and cement–rock laboratory experiments. Applied Geochemistry 26, 1138–1152.

Schmidt T, Lothenbach B, Romer M, Neuenschwander J, Scrivener K L, 2009. Physical and microstructural aspects of sulfate attack on ordinary and limestone blended Portland cements. Cement and Concrete Research 39, 1111–1121.

Sharma R C, Jain N K, Ghosh S N, 1993. Semi-theoretical method for the assessment of reactivity of fly ashes. Cement and Concrete Research 23, 41–45.

Shehata M H, Thomas M D A, Bleszynski R F, 1999. The effects of fly ash composition on the chemistry of pore solution in hydrated cement pastes. Cement and Concrete Research 29, 1915–1920.

Shi H, Xu B, Shi T, Zhou X, 2008. Determination of gas permeability of high performance concrete containing fly ash. Materials and Structures 41, 1051–1056.

Sinsiri T, Chindaprasirt P, Jaturapitakkul C, 2010. Influence of fly ash fineness and shape on the porosity and permeability of blended cement pastes. International Journal of Minerals, Metallurgy, and Materials 17, 683–689.

Spiesz P, Brouwers H J H, 2013. The apparent and effective chloride migration coefficients obtained in migration tests. Cement and Concrete Research 48, 116–127.

Sun G K, Young J F, Kirkpatrick R J, 2006. The role of Al in C–S–H: NMR, XRD, and compositional results for precipitated samples. Cement and Concrete Research 36, 18–29.

Tanesi J, Bentz D P, Ardani A, 2013. Enhancing high volume fly ash concretes using fine limestone powder. ACI SP-294: Advances in Green Binder Systems. Farmington Hills, MI: American Concrete Institute.

Taylor H F W, 1997. Cement chemistry. 2nd edition. London: Thomas Telford.

Tazawa E I (ed), 2014. Autogenous shrinkage of concrete: proceedings of the international workshop, organised by the JCI (Japan Concrete Institute), Hiroshima, 13–14 June 1998. New York: Routledge.

Tennis P D, Thomas M D A, Weiss W J, 2011. State-of-the-art report on use of limestone in cements at levels of up to 15 %. SN3148, Portland Cement Association, Skokie, Illinois.

Thomas J J, Jennings H M, Chen J J, 2009. Influence of nucleation seeding on the hydration mechanisms of tricalcium silicate and cement. Journal Physical Chemistry C 113, 4327–4334.

Thomas J J, Biernacki J J, Bullard J W, Bishnoi S, Dolado J S, Scherer G W, Luttge A, 2011. Modeling and simulation of cement hydration kinetics and microstructure development. Cement and Concrete Research 41, 1257–1278.

Thomas M D A, 2007. Optimizing the use of fly ash in concrete. Skokie, IL: Portland Cement Association. Available at: https://www.cement.org/docs/default-source/fc_concrete_technology/is548-optimizing-the-use-of-fly-ash-concrete.pdf

Thomas M D A, 2011. The effect of supplementary cementing materials on alkali-silica reaction: A review. Cement and Concrete Research 41, 1224–1231.

Thomas M D A, Matthews J D, 1992. The permeability of fly ash concrete. Materials and Structures 25, 388–396.

Thomas M D A, Shehata M, 2004. Use of blended cements to control expansion of concrete due to alkali-silica reaction. In Malhotra V M (ed). Proceedings of Eighth CANMET/ACI International Conference on Fly Ash, Silica Fume, Slag, and Natural Pozzolans in Concrete. Farmington Hills, MI: American Concrete Institute. (Special Publication 221), 591–607.

Tsivilis S, Batis G, Chaniotakis E, Grigoriadis G, Theodossis D, 2000. Properties and behavior of limestone cement concrete and mortar. Cement and Concrete Research 30, 1679–1683.

Tsivilis S, Tsantilas J, Kakali G, Chaniotakis E, Sakellariou A, 2003. The permeability of Portland limestone cement concrete. Cement and Concrete Research 33, 1465–1471.

Vollpracht A, Lothenbach B, Snellings R, Haufe J, 2016. The pore solution of blended cements: a review. Materials and Structures 49, 3341–3367.

Wesche K (ed), 2004. Fly ash in concrete: properties and performance. CRC Press. (RILEM Report 7)

Yeih W D, Huang R, Chang J J, 1994. A study of chloride diffusion properties of concrete at early age. Journal of Marine Science and Technology 2, 61–67.

Yu Z, Ye G, 2013. The pore structure of cement paste blended with fly ash. Construction and Building Materials 45, 30–35.

Yu Z, Ma J, Ye G, van Breugel K, Shen X, 2017. Effect of fly ash on the pore structure of cement paste under a curing period of 3 years. Construction Building Materials 144, 493–501.

Zajac M, Rossberg A, Le Saout G, Lothenbach B, 2014. Influence of limestone and anhydrite on the hydration of Portland cements. Cement and Concrete Composites 46, 99–108.

Zeng Q, Li K, Fen-Chong T, Dangla P, 2010. Surface fractal analysis of pore structure of high-volume fly-ash cement pastes. Applied Surface Science 257, 762–768.

Zhang M, Chen J, Lv Y, Wang D, Ye J, 2013. Study on the expansion of concrete under attack of sulfate and sulfate–chloride ions. Construction and Building Materials 39, 26–32.

Appendix A

Verification of the cement hydration model

To verify the implementation of the cement hydration modelling approach in PHREEQC used in Chapter 4, the hydration of the OPC system presented by Lothenbach and Winnefeld (2006) has been simulated. The composition of the cementitious system before hydration is identical to the one used by those authors and can be found in Lothenbach and Winnefeld (2006). Parrot and Kiloh (1984) expressions for clinker dissolution are identical in both models. The thermodynamic database used in the simulations is the CEMDATA07 in both cases. The difference is that a version of CEMDATA07 for PHREEQC is used here (from Jacques 2009), while the GEMS version of CEMDATA07, consistent with Nagra/PSI-Thermodynamic Data Base (Hummel et al. 2002).

The results obtained with the implementation in PHREEQC of the hydration modelling approach are compared to the ones obtained using the GEMS software (Kulik 2002). In their approach, the CEMDATA07 thermodynamic database (Lothenbach et al. 2008a, b) is coupled with the internally consistent thermodynamic data set of Hummel et al. (2002) expanded with additional data for solids that are expected to form under cementitious conditions.

In Lothenbach and Winnefeld (2006), alkali uptake by C-S-H phases was simulated by assuming a distribution ratio (R_d) of 0.42 ml/g applied to C-S-H for both Na and K. In the present model implemented in PHREEQC, cation exchange reactions are used to simulate alkali uptake. The selectivity coefficients of Na, K, and Ca are adjusted to fit experimental data presented in Lothenbach and Winnefeld (2006), while the cation exchange capacity (CEC) increases with time using a kinetic rate.

Figure A-1 and Figure A-2 depict the results of the evolution of the aqueous chemistry and hydrates phase assemblage as a function of hydration time for the OPC system reported by Lothenbach and Winnefeld (2006). Overall, a good agreement is observed between both models. Small discrepancies in the results probably arise from the differences between how alkali uptake is treated in each model and the fact that in PHREEQC the CEMDATA07 database is not coupled to the Nagra database. Some error in the digitalization process of the plots by Lothenbach and Winnefeld (2006) can also affect the comparison.

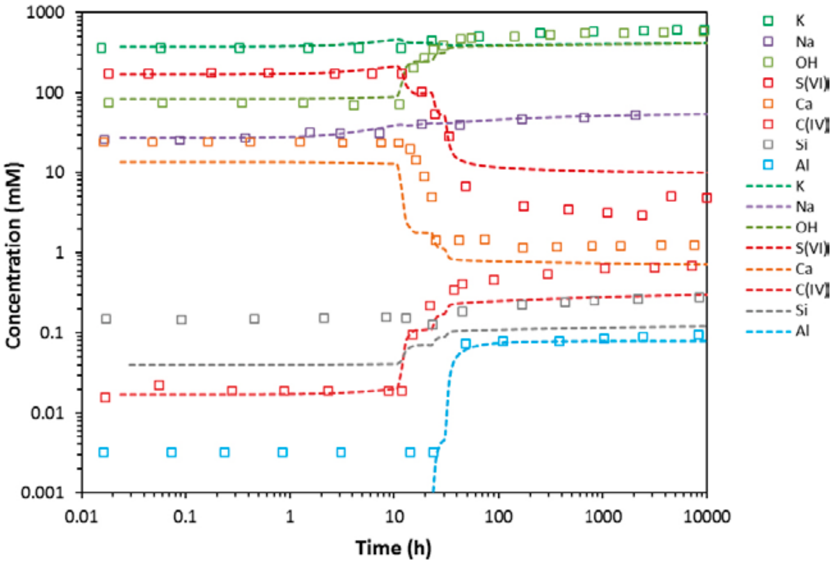

Figure A-1. *Comparison of evolution of aqueous chemistry with hydration time (hours). Square symbols stand for data reported in Lothenbach and Winnefeld (2006) while dashed lines stand for results calculated in the present work.*

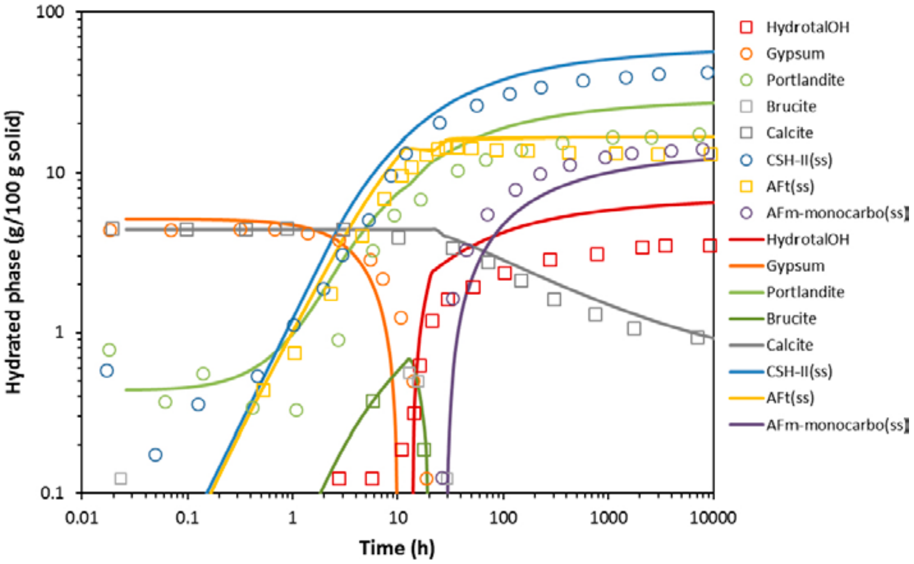

Figure A-2. *Comparison of evolution of phase assemblage with hydration time (hours). Symbols stand for data reported in Lothenbach and Winnefeld (2006) while solid lines stand for results calculated in the present work.*

Appendix B

Minerals

Table B-1. Molar volume (V_m, in L/mol), equilibrium constant of the mineral (log *K*) and its chemical formula are given in the table below.

Mineral	V_m (L/mol)	log *K*	Dissolution reactions used to calculate solubility products log *K*
Brucite	0.024	16.84	$Mg(OH)_2 \rightleftharpoons Mg^{2+} + 2H_2O - 2H^+$
C_2AH_8	0.184	−13.56	$Ca_2Al_2(OH)_{10} \cdot 3H_2O \rightleftharpoons 2Ca^{2+} + 2Al(OH)_4^- + 2OH^- + 3H_2O$
C_2FH_8	0.194	−17.60	$Ca_2Fe_2(OH)_{10} \cdot 3H_2O \rightleftharpoons 2Ca^{2+} + 2Fe(OH)_4^- + 2OH^- + 3H_2O$
C_4AH_{13}	0.274	−25.40	$Ca_4Al_2(OH)_{14} \cdot 6H_2O \rightleftharpoons 4Ca^{2+} + 2Al(OH)_4^- + 6OH^- + 6H_2O$
C_4FH_{13}	0.286	−29.40	$Ca_4Fe_2(OH)_{14} \cdot 6H_2O \rightleftharpoons 4Ca^{2+} + 2Fe(OH)_4^- + 6OH^- + 6H_2O$
CAH_{10}	0.194	−7.50	$CaAl_2(OH)_8 \cdot 6H_2O \rightleftharpoons Ca^{2+} + 2Al(OH)_4^- + 6H_2O$
Calcite	0.037	1.85	$CaCO_3 \rightleftharpoons Ca^{2+} - H^+ + HCO_3^-$
C-A-S-H 1.25	0.078	26.19	$(CaO)_{1.25}(Al_2O_3)_{0.125}(SiO_2) \cdot 1.625H_2O + 3.25H^+ - H_2O + OH^- \rightleftharpoons 1.25Ca^{2+} + 0.25Al^{3+} + SiO(OH)_3^- + 1.25H_2O$
C-A-S-H 0.84	0.059	21.57	$(CaO)(Al_2O_3)_{0.156}(SiO_2)_{1.188} \cdot 1.656H_2O + 2.938H^+ - 1.188H_2O + 1.188OH^- \rightleftharpoons Ca^{2+} + 0.313Al^{3+} + 1.188SiO(OH)_3^- + 0.75H_2O$
C-S-H jennite	0.078	−13.16	$(CaO)_{1.6667}(SiO_2)(H_2O)_{2.1} \rightleftharpoons 1.6667Ca^{2+} + SiO(OH)_3^- + 2.3333OH^- - 0.5667H_2O$
C-S-H tobermorite	0.059	−8.00	$(CaO)_{0.8333}(SiO_2)(H_2O)_{1.3333} \rightleftharpoons 0.8333Ca^{2+} + SiO(OH)_3^- + 0.6667OH^- - 0.5H_2O$
Dolomite	0.064	−17.12	$CaMg(CO_3)_2 \rightleftharpoons Ca^{2+} + Mg^{+2} + 2CO_3^{2-}$
Ettringite	0.707	−44.84	$Ca_6Al_2(SO_4)_3(OH)_{12} \cdot 26H_2O \rightleftharpoons 6Ca^{2+} + 2Al(OH)_4^- + 3SO_4^{2-} + 4OH^- + 26H_2O$
Fe-monocarbonate	0.290	−35.50	$Ca_4Fe_2(CO_3)(OH)_{12} \cdot 5H_2O \rightleftharpoons 4Ca^{2+} + 2Fe(OH)_4^- + CO_3^{2-} + 4OH^- + 5H_2O$
Fe-ettringite	0.712	−44.01	$Ca_6Fe_2(SO_4)_3(OH)_{12} \cdot 26H_2O \rightleftharpoons 6Ca^{2+} + 2Fe(OH)_4^- + 3SO_4^{2-} + 4OH^- + 26H_2O$
Fe-monosulfate	0.321	−33.20	$Ca_4Fe_2(SO_4)(OH)_{12} \cdot 6H_2O \rightleftharpoons 4Ca^{2+} + 2Fe(OH)_4^- + SO_4^{2-} + 4OH^- + 6H_2O$
Fe-strätlingite	0.227	−23.70	$Ca_2Fe_2SiO_2(OH)_{10} \cdot 3H_2O \rightleftharpoons 2Ca^{2+} + 2Fe(OH)_4^- + SiO(OH)_3^- + OH^- + 2H_2O$
Gypsum	0.075	−4.58	$CaSO_4 \cdot 2H_2O \rightleftharpoons Ca^{2+} + SO_4^{2-} + 2H_2O$
Hydrogarnet Fe	0.155	−25.16	$Ca_3Fe_2(OH)_{12} \rightleftharpoons 3Ca^{2+} + 2Fe(OH)_4^- + 4OH^-$
Hydrogarnet OH	0.150	−20.84	$Ca_3Al_2(OH)_{12} \rightleftharpoons 3Ca^{2+} + 2Al(OH)_4^- + 4OH^-$
Hydrotalcite C	0.220	−51.14	$Mg_4Al_2(OH)_{12}CO_3 \cdot 3H_2O \rightleftharpoons 4Mg^{2+} + 2Al(OH)_4^- + CO_3^{2-} + 4OH^- + 3H_2O$
Hydrotalcite OH	0.220	−56.02	$Mg_4Al_2(OH)_{14} \cdot 3H_2O \rightleftharpoons 4Mg^{2+} + 2Al(OH)_4^- + 6OH^- + 3H_2O$
Monocarboaluminate	0.262	−31.46	$Ca_4Al_2(CO_3)(OH)_{12} \cdot 5H_2O \rightleftharpoons 4Ca^{2+} + 2Al(OH)_4^- + CO_3^{2-} + 4OH^- + 5H_2O$
Monosulfoaluminate	0.309	−29.24	$Ca_4Al_2(SO_4)(OH)_{12} \cdot 6H_2O \rightleftharpoons 4Ca^{2+} + 2Al(OH)_4^- + SO_4^{2-} + 4OH^- + 6H_2O$
M-S-H 1.5	0.074	−23.57	$(MgO)_{1.5}(SiO_2)(H_2O)_{2.5} + OH^- + H_2O \rightleftharpoons 1.5Mg^{2+} + SiO(OH)_3^- + 3OH^- + H_2O$
M-S-H 0.75	0.095	−28.80	$(MgO)_{1.5}(SiO_2)_2(H_2O)_{2.5} + 2OH^- + 2H_2O \rightleftharpoons 1.5Mg^{2+} + 2SiO(OH)_3^- + 3OH^- + H_2O$
Portlandite	0.033	22.81	$Ca(OH)_2 \rightleftharpoons Ca^{2+} - 2H^+ + 2H_2O$
SiO_2(am)	0.089	1.48	$SiO_2 + OH^- + H_2O \rightleftharpoons SiO(OH)_3^-$
Strätlingite	0.216	−19.70	$Ca_2Al_2SiO_2(OH)_{10} \cdot 3H_2O \rightleftharpoons 2Ca^{2+} + 2Al(OH)_4^- + SiO(OH)_3^- + OH^- + 2H_2O$
Syngenite	0.152	−7.20	$K_2Ca(SO_4)_2H_2O \rightleftharpoons 2K^+ + Ca^{2+} + 2SO_4^{2-} + H_2O$
Thaumasite	0.332	−49.36	$Ca_6(SiO_3)_2(SO_4)_2(CO_3)_2 \cdot 30H_2O \rightleftharpoons 6Ca^{2+} + 2H_3SiO_4^- + 2SO_4^{2-} + 2CO_3^{2-} + 2OH^- + 26H_2O$
Tricarboaluminate	0.650	−46.51	$Ca_6Al_2(CO_3)_3(OH)_{12} \cdot 26H_2O \rightleftharpoons 6Ca^{2+} + 2Al(OH)_4^- + 3CO_3^{2-} + 4OH^- + 26H_2O$

Table B-2. Saturation indices (S.I.) for meteoric groundwater composition used in the simulations are given in the table below, together with the saturation indices for all concrete porewater simulated (the absence of iron in water compositions provokes the non-appearance of ferritic phases).

Mineral	S.I. for groundwater	S.I. for concrete I porewater	S.I. for concrete IIa porewater	S.I. for concrete IIb porewater	S.I. for concrete III porewater	S.I. for concrete IV porewater
Brucite	−3.56	−1.52	−1.52	−1.52	−1.34	−0.99
C_2AH_8	−16.35	−2.10	−2.10	−2.10	−2.78	−4.23
C_4AH_{13}	−32.85	−0.65	−0.66	−0.66	−1.31	−2.78
CAH_{10}	−8.24	−2.98	−2.99	−2.99	−3.70	−5.11
Calcite	0.12	−2.13	−2.12	−2.12	−1.45	0
C-A-S-H 1.25	−6.57	−0.68	−0.68	−0.68	−0.84	−0.95
C-A-S-H 0.84	−4.85	−2.23	−2.23	−2.23	−2.44	−2.57
C-S-H jennite	−10.15	−0.06	−0.06	−0.06	−0.13	−0.06
C-S-H tobermorite	−3.50	−0.89	−0.89	−0.89	−0.98	−0.89
Dolomite	−0.15	–	–	–	–	−6.81
Ettringite	−20.43	−1.23	−1.24	−1.24	0	0
Gypsum	−2.48	−3.81	−3.80	−3.80	−3.14	−2.69
Hydrogarnet OH	−23.24	0	0	0	−0.64	−2.13
Hydrotalcite C	−3.50	−10.30	−10.30	−10.30	−9.65	−8.18
Hydrotalcite OH	−4.43	0	0	0	0	0
Monocarboaluminate	−20.98	0	0	0	0	0
Monosulfoaluminate	−21.9	0	0	0	0	−1.01
Portlandite	−8.98	0	0	0	0	0
SiO_2(am)	−1.17	−6.04	−6.04	−6.04	−6.14	−6.04
Strätlingite	−9.90	−0.52	−0.53	−0.53	−1.31	−2.66
Syngenite	−11.80	−7.38	−7.59	−7.59	−5.28	−5.12
Thaumasite	−9.22	−8.24	−8.24	−8.24	−5.86	−1.74
Tricarboaluminate	−22.69	−6.28	−6.30	−6.30	−5.07	−2.03

Appendix C

Tabulated key parameter results

Table C-1. Evolution of pH at x = 1.4 m and x = 2.8 m (right boundary of the control volumes) for the 5 different 1D cases.

	Case I		Case IIa		Case IIb		Case III		Case IV	
Time (years)	x = 1.4 m pH	x = 2.8 m pH	x = 1.4 m pH	x = 2.8 m pH	x = 1.4 m pH	x = 2.8 m pH	x = 1.4 m pH	x = 2.8 m pH	x = 1.4 m pH	x = 2.8 m pH
0	13.331	13.331	13.265	13.265	13.264	13.264	13.539	13.539	13.214	13.214
5	13.331	13.331	13.265	13.265	13.264	13.264	13.539	13.539	13.214	13.214
10000	12.487	12.484	12.489	12.485	12.489	12.484	12.486	12.484	12.485	12.483
20000	12.488	12.484	12.486	12.487	12.487	12.486	12.486	12.483	12.485	12.483
30000	12.487	12.485	12.485	12.487	12.486	12.487	12.486	12.483	12.486	12.484
40000	12.486	12.486	12.484	12.486	12.485	12.487	12.487	12.484	12.487	12.484
50000	12.485	12.486	12.484	12.485	12.484	12.486	12.487	12.484	12.487	12.484
60000	12.485	12.486	12.484	12.484	12.484	12.485	12.487	12.484	12.487	12.484
70000	12.484	12.486	12.484	12.484	12.484	12.484	12.486	12.484	12.487	12.485
80000	12.484	12.485	12.484	12.484	12.484	12.484	12.486	12.485	12.487	12.485
90000	12.484	12.485	12.484	12.484	12.484	12.484	12.486	12.485	12.487	12.485
100000	12.484	12.484	12.483	12.484	12.484	12.484	12.486	12.485	12.487	12.486
110000	12.484	12.484	12.483	12.484	12.484	12.484	12.486	12.485	12.487	12.486
120000	12.484	12.484	12.483	12.484	12.483	12.484	12.485	12.485	12.487	12.486
130000	12.484	12.484	12.407	12.484	12.483	12.484	12.485	12.485	12.487	12.486
140000	12.484	12.484	12.321	12.484	12.483	12.484	12.485	12.486	12.486	12.486
150000	12.483	12.484	12.266	12.484	12.483	12.484	12.485	12.486	12.486	12.486
160000	12.483	12.484	12.203	12.484	12.407	12.484	12.485	12.486	12.486	12.486
170000	12.483	12.484	12.131	12.484	12.407	12.484	12.485	12.486	12.486	12.486
180000	12.483	12.484	12.075	12.484	12.335	12.484	12.485	12.486	12.486	12.486
190000	12.483	12.484	11.957	12.484	12.318	12.484	12.483	12.485	12.486	12.486
200000	12.407	12.484	11.842	12.484	12.250	12.484	12.483	12.485	12.486	12.486
210000	12.407	12.484	11.676	12.484	12.201	12.484	12.483	12.485	12.486	12.486
220000	12.355	12.484	11.463	12.484	12.150	12.484	12.483	12.485	12.486	12.486
230000	12.334	12.484	11.256	12.483	12.096	12.484	12.432	12.485	12.486	12.486
240000	12.318	12.484	11.128	12.483	12.055	12.484	12.409	12.485	12.486	12.486
250000	12.267	12.484	11.071	12.483	11.978	12.484	12.405	12.485	12.486	12.486
260000	12.234	12.484	10.751	12.195	11.904	12.484	12.373	12.485	12.486	12.486
270000	12.196	12.484	10.647	11.978	11.816	12.484	12.352	12.485	12.486	12.486
280000	12.160	12.484	10.575	11.428	11.705	12.484	12.335	12.485	12.486	12.486
290000	12.122	12.484	10.514	11.046	11.570	12.484	12.311	12.485	12.486	12.486
300000	12.077	12.484	10.502	11.058	11.406	12.484	12.297	12.485	12.483	12.486
310000	12.038	12.484	10.489	11.046	11.255	12.483	12.281	12.485	12.483	12.486
320000	11.982	12.484	10.486	11.068	11.161	12.483	12.242	12.485	12.483	12.486
330000	11.926	12.484	10.488	11.086	11.106	12.483	12.223	12.485	12.483	12.486
340000	11.868	12.484	10.511	11.087	11.082	12.302	12.201	12.485	12.483	12.486
350000	11.780	12.484	10.513	10.503	10.790	12.083	12.173	12.485	12.483	12.485
360000	11.676	12.484	10.508	10.499	10.670	11.943	12.154	12.485	12.483	12.485
370000	11.538	12.484	10.481	10.469	10.598	11.643	12.130	12.485	12.454	12.485
380000	11.395	12.484	10.509	10.497	10.560	11.092	12.101	12.485	12.415	12.485
390000	11.244	12.483	10.502	10.491	10.522	11.069	12.083	12.485	12.413	12.485
400000	11.149	12.483	10.502	10.491	10.498	11.061	12.053	12.484	12.414	12.485
410000	11.129	12.483	10.515	10.503	10.488	11.067	12.048	12.485	12.417	12.485
420000	11.071	12.318	10.497	10.497	10.483	11.068	12.012	12.484	12.379	12.485
430000	10.757	12.097	10.498	10.498	10.482	11.050	11.966	12.485	12.371	12.485
440000	10.666	11.974	10.492	10.492	10.500	11.078	11.944	12.484	12.370	12.485
450000	10.559	11.727	10.513	10.513	10.506	11.103	11.904	12.484	12.370	12.485
460000	10.521	11.104	10.417	10.508	10.509	10.501	11.865	12.485	12.344	12.485

	Case I		Case IIa		Case IIb		Case III		Case IV	
Time (years)	**x = 1.4 m pH**	**x = 2.8 m pH**	**x = 1.4 m pH**	**x = 2.8 m pH**	**x = 1.4 m pH**	**x = 2.8 m pH**	**x = 1.4 m pH**	**x = 2.8 m pH**	**x = 1.4 m pH**	**x = 2.8 m pH**
470 000	10.500	11.066	10.414	10.490	10.503	10.494	11.826	12.485	12.332	12.485
480 000	10.488	11.066	10.410	10.507	10.505	10.494	11.772	12.484	12.326	12.485
490 000	10.477	11.061	10.411	10.508	10.514	10.513	11.731	12.483	12.323	12.485
500 000	10.496	11.058	10.392	10.506	10.503	10.491	11.646	12.483	12.311	12.485
510 000	10.496	11.051	10.396	10.508	10.495	10.483	11.578	12.483	12.296	12.485
520 000	10.496	11.082	10.437	10.507	10.495	10.483	11.499	12.362	12.288	12.485
530 000	10.498	11.060	10.436	10.507	10.496	10.484	11.408	12.301	12.283	12.485
540 000	10.500	10.490	10.468	10.508	10.512	10.500	11.336	12.297	12.277	12.485
550 000	10.517	10.507	10.465	10.510	10.512	10.501	11.271	12.194	12.263	12.485
560 000	10.519	10.508	10.461	10.494	10.489	10.490	11.200	12.141	12.252	12.485
570 000	10.491	10.478	9.935	10.513	10.481	10.482	11.186	12.101	12.245	12.485
580 000	10.492	10.479	9.973	10.513	10.507	10.507	11.150	12.070	12.240	12.485
590 000	10.493	10.480	9.708	10.516	10.508	10.508	11.110	12.051	12.231	12.485
600 000	10.507	10.495	9.721	10.517	10.439	10.514	11.126	12.048	12.220	12.485
610 000	10.508	10.496	9.673	10.502	10.438	10.503	11.094	12.037	12.210	12.485
620 000	10.508	10.497	9.370	10.505	10.440	10.503	11.094	11.907	12.203	12.485
630 000	10.503	10.503	9.369	10.514	10.409	10.510	10.872	11.816	12.197	12.485
640 000	10.503	10.503	9.161	10.510	10.409	10.499	10.821	11.772	12.189	12.485
650 000	10.504	10.504	9.162	10.497	10.411	10.500	10.788	11.592	12.179	12.485
660 000	10.426	10.498	9.167	10.516	10.388	10.497	10.700	11.405	12.170	12.485
670 000	10.427	10.499	8.918	10.481	10.410	10.515	10.676	11.258	12.163	12.485
680 000	10.451	10.518	8.839	10.484	10.391	10.499	10.615	11.164	12.156	12.485
690 000	10.419	10.512	8.799	10.480	10.401	10.497	10.571	11.119	12.149	12.485
700 000	10.401	10.496	8.790	10.487	10.400	10.497	10.546	11.092	12.141	12.485
710 000	10.381	10.494	8.767	10.482	10.423	10.516	10.502	11.086	12.133	12.485
720 000	10.402	10.511	8.755	10.476	10.457	10.514	10.491	11.076	12.125	12.485
730 000	10.403	10.512	8.747	10.479	10.435	10.499	10.480	11.079	12.116	12.485
740 000	10.412	10.496	8.743	10.475	10.455	10.501	10.472	11.072	12.111	12.485
750 000	10.411	10.496	8.742	10.492	10.031	10.518	10.456	11.081	12.106	12.485
760 000	10.464	10.512	8.741	10.495	10.006	10.504	10.441	11.078	12.096	12.485
770 000	10.463	10.512	8.741	10.486	10.045	10.504	10.430	11.082	12.088	12.485
780 000	10.462	10.507	8.740	10.480	10.059	10.504	10.432	11.084	12.079	12.485
790 000	10.463	10.498	8.740	10.152	9.810	10.507	10.426	11.072	12.077	12.485
800 000	9.997	10.516	8.740	8.740	9.821	10.507	10.416	11.086	12.075	12.485
810 000	10.034	10.517	8.740	8.740	9.838	10.507	10.421	11.089	12.060	12.485
820 000	10.010	10.502	8.740	8.740	9.547	10.510	10.424	11.074	12.049	12.485
830 000	9.803	10.523	8.740	8.740	9.552	10.510	10.429	11.073	12.040	12.485
840 000	9.759	10.508	8.740	8.740	9.488	10.496	10.376	11.079	12.032	12.485
850 000	9.770	10.507	8.740	8.740	9.305	10.514	10.348	11.075	12.028	12.486
860 000	9.485	10.512	8.740	8.740	9.231	10.501	10.346	10.755	12.019	12.486
870 000	9.487	10.514	8.740	8.740	9.228	10.501	10.348	10.485	12.009	12.485
880 000	9.417	10.500	8.740	8.740	9.163	10.505	10.328	10.419	11.998	12.483
890 000	9.169	10.504	8.740	8.740	9.164	10.506	10.337	10.403	11.989	12.483
900 000	9.160	10.505	8.740	8.740	8.954	10.483	10.340	10.399	11.983	12.483
910 000	9.165	10.511	8.740	8.740	8.932	10.489	10.322	10.396	11.974	12.483
920 000	8.937	10.497	8.740	8.740	8.879	10.475	10.322	10.414	11.962	12.483
930 000	8.911	10.488	8.740	8.740	8.856	10.492	10.325	10.407	11.949	12.483
940 000	8.848	10.481	8.740	8.740	8.818	10.479	10.317	10.406	11.941	12.483
950 000	8.806	10.478	8.740	8.740	8.809	10.488	10.328	10.406	11.933	12.343
960 000	8.795	10.484	8.740	8.740	8.782	10.482	10.334	10.406	11.919	12.301
970 000	8.770	10.481	8.740	8.740	8.776	10.492	10.333	10.406	11.904	12.272
980 000	8.757	10.475	8.740	8.740	8.761	10.485	10.309	10.406	11.904	12.249
990 000	8.747	10.479	8.566	8.740	8.752	10.481	10.310	10.406	11.899	12.229
1 000 000	8.745	10.489	8.566	8.740	8.750	10.487	10.309	10.406	11.871	12.212

Table C-2. Case I porosity and effective diffusion coefficient representative values for inner and outer backfills. Values tabulated for each leaching event.

Time (years)	Porosity outer backfill	Porosity inner backfill	D_e (m^2/s) outer backfill	D_e (m^2/s) inner backfill	Leaching event
0	0.110	0.110	3.500×10^{-12}	3.500×10^{-12}	Initial values
200 000	0.184	0.113	1.046×10^{-11}	3.700×10^{-12}	CH depletion in outer backfill
420 000	–	0.154	–	7.946×10^{-12}	CH depletion in inner backfill
800 000	0.292	0.202	3.996×10^{-11}	1.498×10^{-11}	C-S-H depletion in outer backfill
1 000 000	0.296	0.275	4.156×10^{-11}	3.238×10^{-11}	Final values

Table C-3. Case IIa porosity and effective diffusion coefficient representative values for inner and outer backfills. Values tabulated for each leaching event.

Time (years)	Porosity outer backfill	Porosity inner backfill	D_e (m^2/s) outer backfill	D_e (m^2/s) inner backfill	Leaching event
0	0.130	0.130	5.285×10^{-12}	5.285×10^{-12}	Initial values
130 000	0.193	0.133	1.244×10^{-11}	5.595×10^{-12}	CH depletion in outer backfill
260 000	–	0.165	–	9.543×10^{-12}	CH depletion in inner backfill
570 000	0.286	0.208	3.795×10^{-11}	1.628×10^{-11}	C-S-H depletion in outer backfill
790 000	–	0.287	–	3.839×10^{-11}	C-S-H depletion in inner backfill
1 000 000	0.296	0.288	4.164×10^{-11}	3.895×10^{-11}	Final values

Table C-4. Case IIb porosity and effective diffusion coefficient representative values for inner and outer backfills. Values tabulated for each leaching event.

Time (years)	Porosity outer backfill	Porosity inner backfill	D_e (m^2/s) outer backfill	D_e (m^2/s) inner backfill	Leaching event
0	0.114	0.114	3.786×10^{-12}	3.786×10^{-12}	Initial values
160 000	0.167	0.116	8.765×10^{-12}	3.944×10^{-12}	CH depletion in outer backfill
340 000	–	0.145	–	6.865×10^{-12}	CH depletion in inner backfill
750 000	0.249	0.180	2.698×10^{-11}	1.147×10^{-11}	C-S-H depletion in outer backfill
1 000 000	0.253	0.237	2.792×10^{-11}	2.284×10^{-11}	Final values

Table C-5. Case III porosity and effective diffusion coefficient representative values for inner and outer backfills. Values tabulated for each leaching event.

Time (years)	Porosity outer backfill	Porosity inner backfill	D_e (m^2/s) outer backfill	D_e (m^2/s) inner backfill	Leaching event
0	0.088	0.088	2.000×10^{-12}	2.000×10^{-12}	Initial values
230 000	0.151	0.091	5.486×10^{-12}	2.151×10^{-12}	CH depletion in outer backfill
520 000	–	0.124	–	4.700×10^{-12}	CH depletion in inner backfill
1 000 000	0.247	0.166	2.455×10^{-11}	9.616×10^{-12}	Final values

Table C-6. Case IV porosity and effective diffusion coefficient representative values for inner and outer backfills. Values tabulated for each leaching event.

Time (years)	Porosity outer backfill	Porosity inner backfill	D_e (m^2/s) outer backfill	D_e (m^2/s) inner backfill	Leaching event
0	0.077	0.077	1.413×10^{-12}	1.413×10^{-12}	Initial values
370 000	0.130	0.078	4.638×10^{-12}	1.472×10^{-12}	CH depletion in outer backfill
950 000	–	0.121	–	4.396×10^{-12}	CH depletion in inner backfill
1 000 000	0.143	0.123	6.058×10^{-12}	4.594×10^{-12}	Final values

Appendix D

Porosity calculations

The porosity models presented in Section 3.3.1 are used to calculate the porosity of a concrete with a water-to-cement ratio of 0.63. A very important parameter needed in these models is the aggregate (ballast) content. Given the lack of information on the ballast content, in the new concrete mixes it is computed as the volume not accounted for by water and cement. This assumption implies some uncertainty in concrete final porosity value. Due to the lack of a complete dataset regarding the concrete mix, two different cases are considered. The difference between the two cases is the cement content, which according to SKB is equal to either 320 (concrete A) or 280 (concrete B) kg/m^3 concrete. The w/c ratio is the same in both mixes. Therefore, the aggregate volume fraction is adjusted in each case to complete the mix volume.

Table D-1 presents the concrete phase assemblages after hydration, computed using the hydration model presented by Höglund (1992). Table D-2 shows the porosity values obtained with the three different porosity models presented in Section 3.3.1. A relatively good agreement is found between the three models.

Table D-1. Hydrated phases content for concretes A and B according to the hydration model presented by Höglund (1992). Units given in mol/L concrete.

Mineral	Concrete A	Concrete B
C_3FH_6	0.0919	0.0806
C_3AH_6	0.0218	0.0192
Monosulfoaluminate	0.0876	0.0769
Ettringite	0	0
C-S-H1.8	1.1146	0.9785
Portlandite	1.0864	0.9537
Brucite	0.0554	0.0486
Calcite	0.0287	0.0252

Table D-2. Porosity values (m^3/m^3) obtained by different methods for both concretes.

	Concrete A	Concrete B
Cement content (kg/m^3)	320	280
Model for estimating porosity		
Capillary pores	0.081	0.070
Gel pores	0.101	0.088
Contraction pores	0.019	0.017
Total porosity	0.142	0.124
Powers model	0.149	0.131
Volumetric differences model	0.133	0.116

Arkitektkopia AB, Bromma, 2019

SKB is responsible for managing spent nuclear fuel and radioactive waste produced by the Swedish nuclear power plants such that man and the environment are protected in the near and distant future.

skb.se